Sensor System Design To Determine Position and Orientation of Articulated Structures

By

Alexander H. Slocum

Submitted to the Department of Mechanical Engineering In Partial Fulfillment of the Requirements

For the Degree of

Doctor of Philosophy

at the

Massachusetts Institute of Technology

May 1985

Signature of Author ....
Department of Mechanical Engineering
May 1985

Certified by ....
Professor David Hardt
Chairman, Thesis Committee

Accepted by ....
Professor Ain A. Sonin, Chairman
Departmental Graduate Committee
Department of Mechanical Engineering

Sensor System Design To Determine Position and Orientation of Articulated Structures

By

Alexander H. Slocum

Submitted to the Department of Mechanical Engineering In Partial Fulfillment of the Requirements

For the Degree of

Doctor of Philosophy

Abstract

This thesis focuses on methods of increasing the accuracy of articulated structures. Sources of measurement error in articulated structures were first identified. Various state of the art motion measuring methods were reviewed and none were found to be entirely suitable for use with articulated structures. Accordingly, a six degree of freedom motion measuring system was developed that relied directly (only) on the stability and accuracy of non-contact displacement measuring sensors. The design is also flexible enough to allow for the introduction of new types of sensors as they become available. A model was tested on a simulated one degree of freedom robot and the measured errors were predicted by the error analysis. On the model tested, which had the same error amplification factor as a robot with a 90" reach, endpoint error was on the order of .000625". Subsequently, the errors present in the test system were identified, and recommendations made to correct them. A conceptual robot design was then presented which showed that a five axis robot with a 76" reach and 200 pound payload could be designed to have a payload to weight ratio of 4:1 and an endpoint feedback accuracy of .000284", which is sufficient for most manufacturing processes the robot may be required to perform. Thus by using the concepts developed, an order of magnitude increase in structural performance and a two to three order of magnitude increase in accuracy over existing robots was attained.

Thesis Committee: Professor David Hardt (Chairman)
Professor Woodie Flowers
Professor Carl Peterson
Professor Warren Seering

Table of Contents Page

LIST OF FIGURES

List of Tables:

(this page left blank)

Chapter 1

State of the Art Methods for Increasing

Accuracy of Articulated Structures

1.1 Introduction

This thesis addresses the issues of accuracy and repeatability of articulated structures. Articulated structures are chosen for study because they are the most versatile type of manipulator. Presently, large articulated robotic manipulators (>36" (1 m) reach and 20 pound (10 kg) payload) can only be used to repeat previously taught positions to within .010" (.3 mm) (somewhat better performance can be achieved after an extensive warm up period). Also most systems do not offer the option of off line programming. Thus articulated robots are used mainly in dedicated systems where special fixtures have been designed to allow the robot to manipulate a particular part or perform a specific function.

Accuracy is defined as how closely measurements are with respect to an absolute reference standard. Repeatability (often referred to as "precision'), on the other hand, is defined as the average difference among a group of measurements. Resolution is defined as the smallest detectable incremental measurement that the system can make. With regard to robots, accuracy is the ability to use remote control to direct a tool's motion along a desired path, or to position the tool at any desired point in the work envelope. Repeatability is the ability of the robot to perform a previously taught task. At present, no large, accurate articulated robots are available.

Current research is attempting to substitute vision and/or compliance devices for accuracy in pick and place operations (used as an aid in the manufacturing process); however, they cannot provide accuracy which is required when performing machining operations such as laser and water jet machining and hole drilling (used as part of the manufacturing process). At present, accuracy of the former operations, when performed by articulated robots, is limited to about ± .10" (2.5 mm). The development of an accurate articulated robot system thus would lead to large productivity gains in the areas of low reaction force machining.

Accordingly, the objective of this thesis is to develop and test a sensor system that can determine the true position and orientation of an articulated structure's joints and endpoint. The system design must satisfy the following: 1) system accuracy must be limited only by that of the electronic systems, and 2) the system must not restrict the motions of the supporting structure. Conceptual designs which employ the sensor system are also discussed.

This document is organized into chapters which describe the general design methodology for the sensor system. The design of a specific test system is also discussed in order to help test the developed concepts. A brief summary of chapter content is given below:

Chapter 1 (Sections beginning with 1.2) Establishes the background necessary to identify a region of design space that will lead to a solution of the robot accuracy problem. First the state of the art and projected research for increasing accuracy in articulated structures is discussed. Then the main sources of the problem, mechanical positioning and sensor system error, are identified. With the cause of the problem in mind, some of the more "promising" ideas, such as inertial guidance systems and goniometers, are then discussed in greater detail. Based on this background information, the "most promising" region of design space is identified for detailed study, and is the subject of the remainder of this document. Appendix 1A discusses the effect that the availability of a sensor system to determine precise endpoint location of articulated structures could have on robot design.

Chapter 2. Discusses the design principle of the goniometer as a method of performing measurements of an articulated structure's position and orientation. Relevant literature and patents are cited, and are used as a starting point for development of a high accuracy multi degree-of-freedom goniometer for articulated structures.

Chapter 3. Formulates design methodology for a high accuracy multi degree-of-freedom goniometer to provide precise position information for articulated structures. A brief overview of available sensor system building blocks is made and two possible sensor system configurations are presented (each design is flexible enough to allow new sensors to be used as they are developed). Methods of incorporating the sensor system into a robot are also discussed to illustrate applicability of the sensor system design.

Chapter 4. Presents a detailed discussion of high resolution mechanical metrology sensor building blocks including: optical devices, LVDT's, impedance probes, and capacitance probes. Methods of achieving accuracy in high resolution sensors by the process of mapping are also discussed. Then a sensor system is chosen to illustrate the concepts presented in Chapter 3 and following chapters formulate the analytical tools necessary for implementation of this design.

Chapter 5. Formulates methods of error analysis necessary to arrive at a "Total Error Budget" for predicting the accuracy of a mechanical metrology system. Sensor linearization, placement and alignment are discussed for the general case, and also in detail for the goniometer to be used to illustrate the concepts presented in Chapter 3.

Chapter 6. Formulates analytical models necessary for "optimum" design of measuring system mechanical components. The methodology described is not only useful for the design of the test goniometer, but also for the design of any precision measuring instrument. The detailed design of the test goniometer is also presented.

Chapter 7. Discusses the methods and results of calibration experiments performed to calibrate and test the test goniometer components. Photographs of the experimental system are shown along with detailed "how and why" explanations of the mechanical metrology procedures.

Analysis of data is performed using the results of Chapter 5 to determine the expected accuracy of the test system.

Chapter 8. Discusses the methods and results of the final tests to determine test system performance. Error analysis of the results is compared to that predicted by the error budget of Chapter 5.

Chapter 9. To illustrate the use of the design methodologies discussed throughout this thesis, a conceptual design for a five degree-of-freedom robot is presented. Back of the envelope calculations for performance of the robot's structural and measuring systems are also presented. The overall conclusions of the thesis are then presented.

1.2 State of the Art Robot Technology

Assessment of current robotics technology is sometimes difficult because standards for robot metrology do not yet exist. As a result, claims of robot performance are often inflated. Table 1.1 lists some 'popular' robots and their performance characteristics based on product literature and observations. A review of current literature, patents, and products indicates that no solutions to the robot accuracy problem will become available in the near future, although various studies indicate that solutions are possible.

For example, the National Academy of Sciences (NAS) made a comprehensive study [1.1] to determine the state of the art and projected future developments in robotics and artificial intelligence. The study

Table 1.1 Comparison of Robot Performance Specifications*

Robot	Weight (lbs)	Payload (lbs)	Reach (in)	Claimed Rep. (in)	Actual Rep. (in)
Bendix AA-160	3000	45	60	.002	.020
Puma 760	650	22	49	.008	.015
Cincinnati Milicron:					
T^3-746	5250	150	99	.010	Not tested
T^3-586	5000	225	102	.050	.060
T^3-726	960	14	41	.004	Not tested

*Observed at the National Bureau of Standards' Automated Manufacturing Research Facility.

points out that for many operations compliance or vision can be substituted for accuracy. However, there are some operations such as hole drilling or laser machining which require accuracy. Moreover, most compliant systems have a small payload bandwidth, and work well only in a vertical mode. Vision is expensive, has reliability problems, is hard to maintain, and has trouble with shiny parts and secondary light sources. The study also anticipates that in five to ten years robot payload to weight ratio and accuracy will improve enough so robots will be mobile and will be able to perform most assembly operations. The NAS projections are also corroborated by the Society of Manufacturing Engineers [1.2].

1.3 Sources of Machine Error and Methods of Compensation

It would be desirable for robots to achieve endpoint accuracies on the order of .001" (25 μm) over 60" (1.5 m) which requires 16 bit accuracy. Bear in mind that few rotational systems are capable of achieving this type of accuracy unless they use a pulse counting method (optical encoder or resolver). Accordingly this section will identify the major problems that cause robots to be inaccurate and give a specific example of why the problem cannot be overcome by brute force (specifying the most accurate components available for present designs). How accuracy problems in machine tools are solved is also discussed to provide insight into the emerging field of accuracy enhancement of mechanical systems.

Robots are inaccurate because they have no sensors to detect errors caused by, for example, gear backlash or structural deflections. Thus when calculating position from joint angles, robot controllers presently assume the structure is rigid. Methods are beginning to be developed to compensate for some of these motions [1.3, 1.4, 1.5]. The first reference describes a method and apparatus for calibrating a robot to increase its repeatability and accuracy; however, the reliability of the method seems doubtful, and requires periodic updating. The second reference describes a "manually manipulated teaching robot" whose motions a large robot are to later follow, but the method addresses the problem of repeatability, not accuracy. The third reference describes a method for allowing repeatable adjustment of gear backlash. The above approaches may help improve repeatability, but will not provide the breakthrough necessary for significantly increasing robot accuracy and hence utilization.

As an example of the effect of even small errors on robot accuracy, consider the effect of the following errors from high precision components: 1) gear backlash ε (10 arc-sec [1.5]), and 2) misalignment ζ between encoder shaft and axis of bearing rotation (5 arc-sec [1.6]). Assume a robot with two 30" (.8 m) articulating arms ℓ_1 and ℓ_2 and two degrees of freedom as shown in Figure 1.1. The endpoint error $\Delta\xi$ is:

$$\Delta\xi = (\varepsilon + \zeta)(2\ell_2 + \ell_1) \qquad (1.1).$$

With the above values, $\Delta\xi$ = .0065" (.17 mm). Even for this rigid link model, a reasonable size robot (reach 60", payload 50 lbs (1.5 m, 23

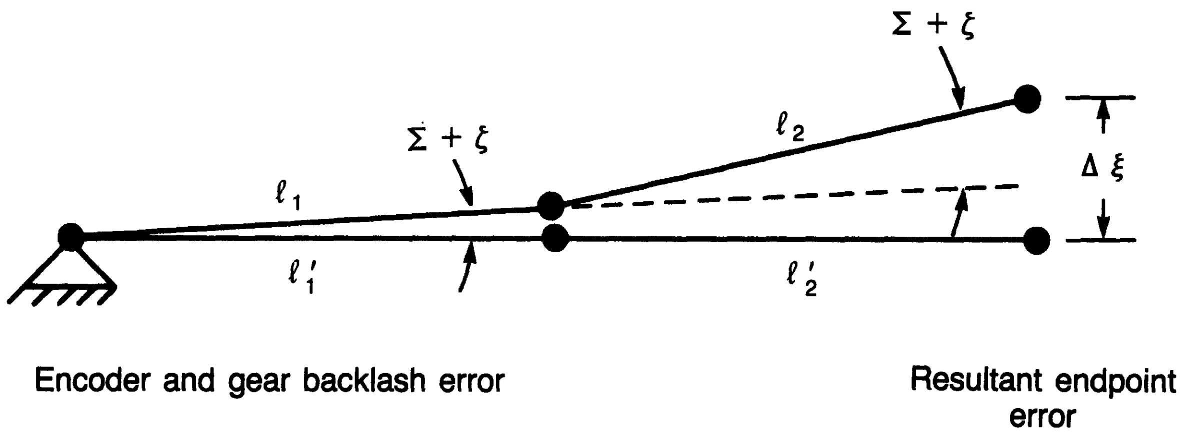

Figure 1.1 Schematic representation of endpoint error caused by gear backlash and encoder errors

kg)) would have trouble inserting parts into collets (requires ±.003" (.08 mm)). Note that remote robot programability (as opposed to teach mode) is a key to a truly flexible manufacturing system because it is impractical to re-teach the robot every time a new part is added to the line. With the above in mind, consider how accurate machine tools are built:

Physics seems to have taught us that whenever a lower limit on size is reached, a smaller limit is then discovered. Similarly, no mechanical system is perfect, and each axis of motion of a tool will contain the one large degree of intended freedom, and five small error motions. Simple geometric calculations yield the tolerances and environmental (temperature in particular) conditions necessary to achieve the required accuracy. When the tolerances necessary to reduce the error motions below a threshold are tighter than can be provided by existing machine tools, extensive finishing by hand is required (scraping and lapping). An alternative is to make the system repeatable and map the errors (which may be temperature dependent), or sense and then compensate for them in real time. This approach can be simply thought of as feedback control, but the real difficulty is in providing the feedback signal which may require 16 - 20 bit accuracy. Obtaining high accuracy feedback signals by mapping or specialized sensing is known as "Deterministic Metrology".

The term "Deterministic Metrology" can be interpreted as meaning "silicon is cheaper than cast iron and it doesn't wear". For example, in 1979 the errors of all three axes' ballscrews and ways of a Brown and

Sharp vertical mill with a 100" (2.5 m) bed were mapped with a laser, and the controller modified to use this information to achieve positioning accuracies of .0002" (.0051 mm) [1.7]. Work in progress is attempting to increase the accuracy of a three axis slantbed lathe from 1 milli-inch to 50 microinches (25 μm to 1.2 μm) [1.7]. The necessary measurements, however, can take months to perform and quantify and the machine must be recalibrated every few years; thus for the general machine tool industry it is not feasible to map and compensate for simultaneous ballscrew and way errors in all axes. At present, ballscrew backlash and nonlinearity (the latter is only compensated for along one axis) are the only errors in commercial machine tools that are compensated for by software corrections. Since machine tools are sliding mass structures where load is not a strong function of position and errors are not amplified by extended distances, the prospect of error mapping an articulated structure is not technically feasible; therefor direct sensing of all the structure's motions will be required.

1.4 Methods for Increasing Robot Accuracy and Repeatability

It is apparent that some robot manufacturers have been trying to increase structural stiffness in an effort to increase accuracy [1.8]. But robots are typically cantilevered structures where loads and joint errors are amplified by arm lengths. In contrast, machine tools are sliding mass structures where load is not a strong function of position; thus accuracy in machine tools is attained by building a massive structure with the predominant deformations due to shear and axial loads. Adding more metal to robots, in an attempt to increase stiffness, can reduce deformations due to applied loads, but it creates a slow, reach limited tool, not a fast, dexterous robot. If a robot is to be accurate, it will require a sensor system, which can measure all the motions of the structural system, to feedback signals to the servo-actuator system.

The above suggests that a position sensing system that is insensitive to load, age, bearing runout, etc. be developed to sense true endpoint position. This information can be used as an error signal for the robot to home in on a desired position either with its own servos, or it could use a "micromanipulator", as described by Sharon [1.9], for final positioning.

In order to determine true endpoint position, two types of sensor systems must be considered, external and internal. The external systems include tracking lasers, millimeter radar, acoustic pingers, and inertial guidance systems. The internal systems include the class of systems broadly known as goniometers. In choosing the best system, note that relative position information of the robot's links will also be needed to compute optimum paths.

In addition to accuracy, a major design requirement is that the sensor system must not restrict the working environment of the robot; thus most external systems would be difficult to implement because if a robot were to reach behind a large metal object, an electromagnetic or acoustic pulse could be blocked. This can be overcome by the use of many sensors around the work area, but then the versatility and mobility of the robot is lost. The characteristics of an external laser based tracking system were studied by Bechek [1.10] and Washington [1.11] confirming the above, although the system has been found to be ideal for purposes of robot metrology. Even if an array of sensors was feasible, acoustic pingers are wavelength limited, and are accurate at best to one part in 1000. Also, as accuracy is enhanced, they become very sensitive to environmental conditions [1.12]. The main use for acoustic pingers is in small digitizing machines (2D and 3D) and several relevant patents have been issued [1.13, 1.14, 1.15]. Millimeter Radar, which operates in the GHz range, offers better performance, but requires large (10" D sphere) antennas [1.16, 1.17]. Note that even if a suitable electromagnetic pinger system were found, two such pingers would be required on each link to provide position and orientation information necessary for path planning and control.

Weckenmann and Linhart [1.18] have suggested that gyroscopes would be able to provide absolute angular positions for robots, but they did not provide data on sensitivity requirements; thus gyroscopes will be investigated in some detail below. Gyroscopes and accelerometers have become the backbone of most navigation systems and an excellent overview of their history, development, and operation is given by Kuritsky and Goldstein [1.19]. For application to robots, the true endpoint position would have to be periodically updated to compensate for drift. The minimum rotation rate sensitivity is thus governed by the time between updates of actual robot position. With the assumption of update time = 30 minutes, robot arm length of 100" (2.5m), and required accuracy of .001", (25 μm) the maximum allowable drift rate is 5.6×10^{-9} rad/sec.

Because gyroscope sensitivities are geared toward navigation, they are measured in nautical miles per hour (nmi/h). For purposes of determining their sensitivity, a speed of 600 nmi will be assumed. Typical (mechanical) navigational grade gyroscope (jewelled bearings) will have a sensitivity on the order of $.008^{\circ}/h$ (3.9×10^{-8} rad/s) and high precision gyros (air or magnetic bearings) will have sensitivities of $.0003^{\circ}/h$ (.2 nmi/h) (1.5×10^{-9} rad/s) [1.19]. The size and cost of the high precision units (10" (.25 m) diameter, cost on order of $500 K) make them impractical for robot use, as well as the fact that they are generally available only for strategic missile applications. Thus only optical gyroscopes can be considered.

The fiber optic gyro operates by having two light beams travel in opposite directions in a fiber optic coil. As the coil rotates about its longitudinal axis, the optical path length between the two changes, which leads to a phase shift Φ between the two counter-propagating beams [1.20]:

$$\Phi = \frac{8\pi A\Omega}{\lambda_o c} \qquad (1.2).$$

λ_o is the vacuum wave length, A is the total area enclosed by the fiber coil, Ω is the angular rotation rate, and c is the speed of light. As of August 1983, the slowest rate of rotation detectable has been

9.7×10^{-7} radians per second [1.20] which is two orders of magnitude less than is needed. Rates of 4.4×10^{-9} rad/sec are predicted by Lin and Giallorenzi [1.21]; however they are based on the temperature being held to within .0067°C as calculated to be necessary by Shupe [1.22].

Ring laser gyroscopes have the potential of becoming the least expensive inertial navigation devices. In a laser ring gyro, light travels around a triangular path and a phase shift is seen between the clockwise and counterclockwise beams as the unit rotates about an axis perpendicular to the plane of the triangle. In 1978, a commercial ring laser gyro 17" (.4 m) on a side gave 4.8×10^{-6} rad/sec accuracy [1.23] which is three orders of magnitude less than is needed. Accuracies of 5×10^{-8} rad/sec are predicted; however they will be difficult to achieve because a phenomenon known as the "lock-in effect" limits the minimum rotation rate (not accuracy) that the gyro can sense [1.24]. The lock-in effect produces coupling between the counter propagating light waves which does not allow a phase shift to occur below minimum rotation rates.

To measure linear motions, an accelerometer would be needed. The most sensitive accelerometer is a Mach-Zehnder interferometer. The MZ interferometer splits a laser beam and transmits its halfs along a reference fiber optic cable and a sensing cable. The reference cable is left undisturbed and a physical effect (temperature, acceleration, sound, etc.) is imposed on the sensor cable. Accelerations as low as 6×10^{-6}g have been detected [1.25]. This translates into .0023"/sec^2 (58 μm/sec^2). Assume that a robot can be "reset" every t seconds, and the allowable drift during this time is $\Delta\xi$, then the minimum detectable acceleration is

$$a_{min} \leq \frac{2\Delta\xi}{t^2} \qquad (1.3).$$

If t = 30 minutes, and δ = .001" (25 μm), then $a_{min} = 6.2\times10^{-10}$ in/sec² (1.6×10^{-11} m/sec²).

From the above, it does not seem that inertial guidance technology will be applicable to robot guidance problems in the forseeable future. It should be noted that the accuracies which are required, 1 part in 100,000, are similar to those needed for strategic missile applications so any major advances in gyro technology are likely to be classified.

1.5 Conclusions

In accordance with the above, this thesis will formulate a general design methodology for sensing motions of articulated structures which will relieve the burden of achieving accuracy from the structural system. The basic design premise will be to remove dependence upon mechanical precision from sensor system accuracy. Thus accuracy must only be limited by the sensors and the electronics. The device also must be able to use a variety of sensors so the system can be upgraded as more accurate sensors become available.

A key to achieving accuracy is realizing that "good" sensor accuracy is usually limited to 12 bits (14 - 16 bit accuracy can be obtained in controlled environments). Thus to accurately measure the large motions of a robot, which requires at least 16 bit accuracy, some sort of encoder device (bit accuracy of sensor is enhanced by counting of regularly spaced perturbations) which excludes the use of commercially available visual, radar, sonar, and inertial guidance systems (whose accuracy is on the order of 12 - 14 bits). In order to implement an "encoder" type system, the sensors will have to be located near each joint which will require a goniometer type device to support the sensors that will prevent non-measurable structural deformations from introducing errors into the measurements. This type of system, however, will require all small degrees of freedom to be measured directly at the joints using 12 - 14 bit sensors. A conceptual design of this type of system is shown in Figure 1.2 and is discussed further in following chapters.

For application to multi-link articulated structures, ideally each link of the goniometer type device must track its associated structural link without interfering with the motions of the structural link. Thus each goniometer link must have six degrees of freedom which will require six measurements to be made to determine the relative position of each goniometer link. In general, at each joint the system must be able to sense two small angular, three small translational, and one large angular degree-of-freedom (the latter measuring the articulation). Coordinate transformations between the links will give endpoint position and orientation of each link. This type of feedback information will

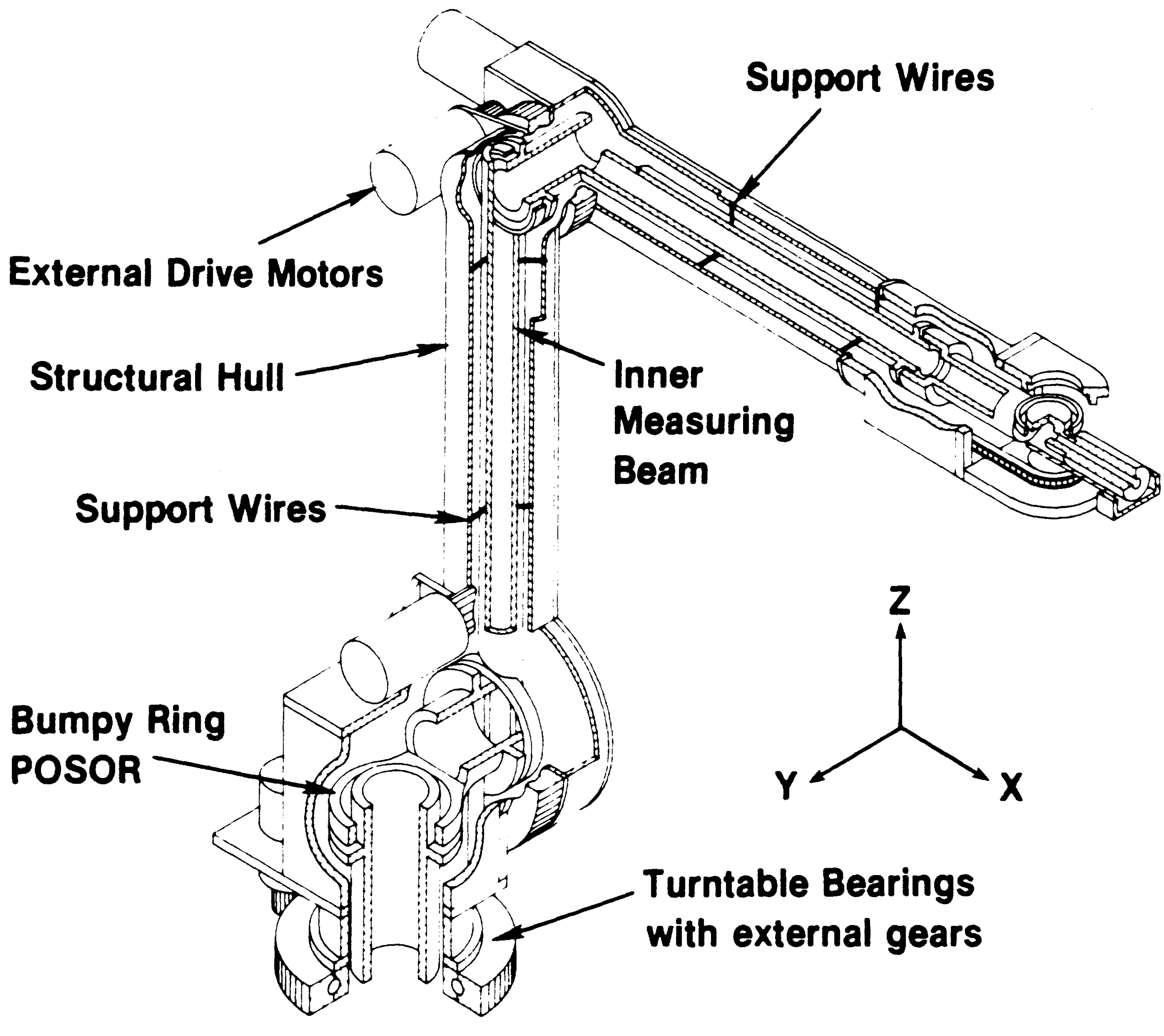

Figure 1.2 Conceptual design of a five degree of freedom, high payload, high accuracy robot. (impedance probes not shown here for clarity)

also raise the possibility of using joint actuators to help damp lower mode structural vibrations.

The next chapter discusses the state of the art of goniometers and their application as metrology systems for articulated structures in greater detail.

References

[1.1] Committee on Army Robotics and Artificial Intelligence, Manufacturing Studies Board, Commission on Engineering and Technical Systems, National Council of the National Academy of Sciences: `Applications of Robotics and Artificial Intelligence to Reduce Risk and Improve Effectiveness, A Study for the United States Army'. 1983.

[1.2] Society of Manufacturing Engineers. `Directory of Manufacturing Research Needed by Industry'. 1982.

[1.3] M.J. Harjar, J.S. Noss, 'Apparatus for Calibrating Link Position Transducers of a Teaching Robot and a Work Robot', U.S. Patent #4,372,721 Feb. 1983

[1.4] R. C. Evans et al, 'Method and Apparatus for Calibrating a Robot to Compensate for Inaccuracy of the Robot', U.S. Patent #4,362,977, Dec. 7, 1982.

[1.5] N. C. Dagalakis, D. R. Meyers, 'Adjustment of Robot Joint Gear Backlash with the Use of the Robot Joint Test Excitation Technique', accepted for publication in Trans. of ASME; Jou. Dynamic Sys. Meas. and Con.

[1.6] Heidanhain Corporation. Product literature. 19??.

[1.7] Charleton, T. `Machine Tool Accuracy Enhancement'. National Bureau of Standards internal document. 1979.

[1.8] Bendix Robotics. The Bendix AA-160 CNC Industrial Robot System. Bendix Corp., Southfield, Michigan. 1981.

[1.9] A. Sharon, 'Enhancement of Robot Accuracy Using Endpoint feedback and a Macro/Micro Manipulator System', 1984 American Control Conference, Vol3, pp 1836-1842

[1.10] R. Bechek, 'Robot End Effector Position and Orientation Measurement Using Laser Triangulation for Improved Accuracy' M.I.T. BSME Thesis. 1981.

[1.11] L. Washington, 'Receiver Evaluation for Laser Triangulation System for Accurate Robot End Effector Position and Orientation Measurement', M.I.T. BSME Thesis. 1983.

[1.12] D. Blomquist, Personal Communication. Leader Sensor Systems Group, National Bureau of Standards, Washington, D. C. 1983-84.

[1.13] T. Uchiyama et al, 'Device for Measuring Three Dimensional Coordinates of Models', U.S. Patent #3,924,450, Dec. 1975

[1.14] W.E. Hunt, 'Position Locating Systems', U.S. Patent #3,731,273, May 1973

[1.15] J.A. Howells, S.J. Sindeband, 'Distance Ranging Apparatus and Method', U.S. Patent #4,357,672, Nov. 1982

[1.16] S.L. Johnston, 'Some Aspects of Millimeter Radar', Proc. Intl. Conference on Radar. Paris, France, December 1978, pp. 148-159.

[1.17] V.J. Falcone, L.W. Abreu, 'Atmospheric Attenuation of Millimeter and Submillimeter Waves', IEEE EASCON 1979 Conference. Rec. Vol. 1, pp. 36 - 41.

[1.18] Weckenmann, A.: Linhart, C. "Absolute Angular Sensor For Controlling Robots", Tech. Mess. TM (Germany) Vol. 51, No. 5, May 1984, pp165-170.

[1.19] M.M. Kuritsky, M.S. Goldstein, 'Inertial Navigation', Proc. IEEE, Vol. 71, No. 10, Oct. 1983 pp 1156-1176

[1.20] K.H. Wanser, R.E. Wagoner, 'Making Sense of Fiber Optic Sensors', Photonics Spectra, oct. 1983 pp 61-66

[1.21] S. Lin, T.G. Giallorenzi, 'Sensitivity Analysis of the Sagnac-effect Optical-fiber Ring Interferometer', Applied Optics, Vol. 18, No. 6, March 1979, pp915-931

[1.22] D.M. Shupe, 'Thermally Induced Nonreciprocity in the Fiber-Optic Interferometer', Applied Optics, Vol. 19, No. 5 March 1980, pp 654-655

[1.23] H.J Engebretson, 'Ring Laser Gyro Program at Honeywell', Proc. SPIE, Vol. 157, August 1978, pp34-40

[1.24] H. Greenstein, 'Progress on Laser Gyros Stimulates New Interest', Laser Focus, Feb. 1978 pp60-67

[1.25] Anonymous, 'Technology Report: Fiberoptic Technology', Laser Focus/Electro-Optics, July 1984, pp 50.

[1.26] W.J. Book, O. Maizza-Neto, D.E. Whitney, 'Feedback Control of Two-Beam Two-Joint Systems with Distributed Flexibility', ASME Jou. Dynamic Sys. Meas. and Con. Dec. 1975 pp 424-431.

[1.27] R.C. Burrows, T.P. Adams, 'Control of a Flexibly mounted Stabilized Platform', ASME Jou. Dynamic Sys. Meas. and Con. Sept. 1977,pp 174-182.

[1.28] L. Meirovitch, Elements of Vibration Analysis, McGraw-Hill 1975, pp269

APPENDIX 1A

Effects of Sensor System Design on Structural System Design

If a sensor system were available that could sense all errors (that produce endpoint errors greater than $\Delta\xi$), then in addition to having a remotely programmable robot, substantial reductions in the number of required precision robot parts could be realized. The resultant savings would be invested in the silicon of the sensors which does not change with time. Thus robot design could be based on a maximum stress criteria similar to aircraft. Note that one of the keys to implementing automated production facilities on a widespread scale is to reduce the amount of required initial capital investment and future operating costs.

As an example of a maximum stress criteria design, let it be assumed that a ten foot long, cantilevered aluminum box beam is to be used to support 300 pounds (136 kg) with a maximum design stress of 5,000 psi (34.4 ksi). This would require a box beam seven inches high, four inches wide with a wall thickness of three-sixteenths inch (178×102×4.8 mm) The beam would have a section moment of inertia of 26 in^4 ($1.08\times10^{-5} m^4$), weigh 4.5 lbs/ft (6.7 kg/m), and deflect .67" (17 mm). On the other hand, a design for minimum deflection of .020" (.51 mm) would require a beam whose cross section is on the order of 20"×8"×5/16" (508×203×7.93). It would have a section moment of inertia of 864 in^4 ($3.59\times10^{-4} m^4$) which would weigh approximately 20 lbs/ft (29.8

kg/m). The resultant savings would be realized not only in structural materials, but also in drive components. A snowball effect occurs with the end result of a stress criteria design being a very fast lightweight accurate robot.

As a robot becomes faster and lighter, the question of controllability arises. Book et al [1.26], Burrows and Adams [1.27], and others have studied control of flexible systems for some time and although the controls problem is difficult, it does not seem insurmountable. Also the availability of a robot with endpoint feedback would certainly stimulate new research, as there would be immediate financial benefits for those who are successful.

As a first look at the controllability of the system relative to existing robots, compare the natural frequencies of the two former beam designs. The relative magnitude of the natural frequencies can be determined by dimensional analysis and use of the Rayleigh Ritz method [1.28]. The natural frequency ω_n of a cantilever beam is a function of: 1) Youngs modulus E, 2) mass per unit length m, and endpoint mass M, 3) length ℓ, 4) and section moment of inertia I.

$$\omega_n \propto \left(\frac{EI}{m\ell^4 + M\ell^3}\right)^{1/2} \qquad (1.1A).$$

As shown in Figure 1A.1, the ratio of the natural frequencies of the deflection versus stress designed beams are about .3 which are not high; however, more research in this area will be necessary to determine limits on controllability of flexible structures.

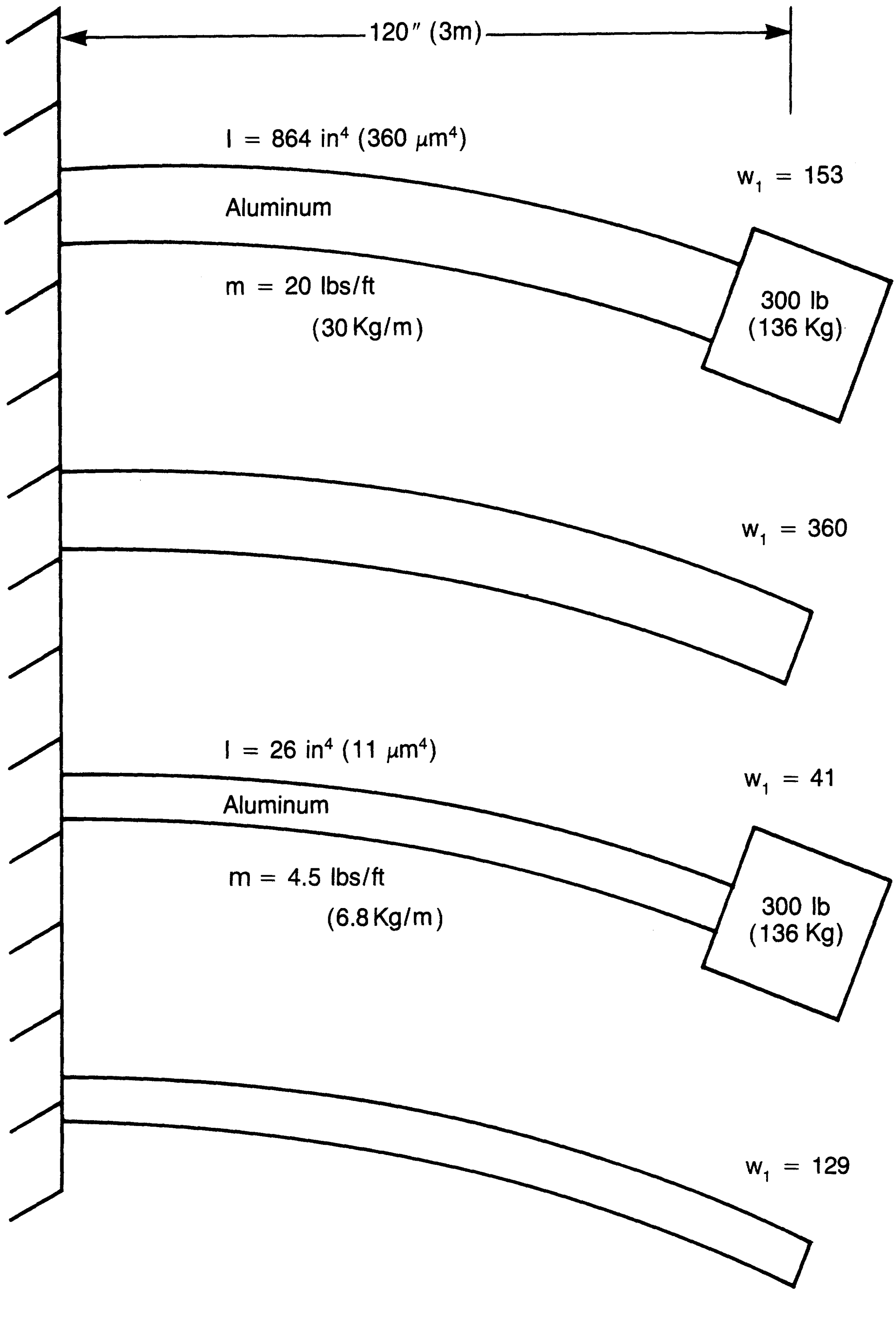

Figure 1A.1 Natural frequencies of stress and deflection criteria designed beams

(this page left blank)

Chapter 2

Goniometers as Devices for Determining Position of Articulated Structures

2.1. Introduction

Webster's defines:

goni- or **gonio-** comb form [Gk gōnia]: corner: angle <goniometer>

goniometer\gō-nē-ˋåṁ-et-er\ n 1: an instrument for measuring angles 2: DIRECTION FINDER

This chapter will review current literature describing state of the art of goniometers used in bio-medical, physics, and manufacturing fields. Existing devices, although crude in the number of measurements they can make, may provide insight into design methods. Note that in most applications, the term goniometer is meant to include angle measuring systems that can also measure small changes in length.

2.2 Goniometers Used in Bio-Medical Applications

Chao [2.1] gives convenient definitions for three types of goniometers: 1) planar goniometer - which only measure angles in one plane, 2) triaxial goniometer - which can measure angles as a line traces out a sphere, and 3) spatial goniometer - which can detect position and orientation. The latter is the most effective for determining the actual motion of skeletal linkages because measurements must be made from points not directly on the bone; thus algorithms are used to convert goniometer readings into readings of the actual motions of the bones. These studies are used to determine effectiveness of prostheses.

Note that some of the problems associated with medical goniometry (study of bio-mechanical motions) are directly applicable to goniometers for robots. The three types of measuring systems: mechanical, optical and electromagnetic each have their good and bad points. Mechanical systems such as described by Chao [2.1] or Townsend [2.2] strap onto a appendage and straddle the joint. Since their mechanical links and joints are not colinear with the structural members (bones), their sensors must measure rotations and translations in order to obtain accurate measurements. The motion of the tissue is analogous to bearing runout and structural deflections. The mechanical versions offer the advantage that signal processing is kept to a minimum and that they are easier to calibrate; however their size precludes their use from any environment other than in a laboratory. Thus a patient's progress cannot be monitored during a normal day. In a similar way, a robots performance must not be hindered by its sensor system.

Optical systems involve stroboscopic photography, infra-red [2.3] and visible light movies, and tracking lasers. An example of the latter is given by de Vries [2.4] where a rapidly moving spot of light scans a field which contains one or more photosensitive devices. Note that a similar system is being developed for robot metrology but it is not practical for use in a manufacturing environment. The vision systems are limited in the planes which they can simultaneously view and do not provide accurate dimensional measurements. For three dimensional resolution, a stereoscopic system, such as described by Antonsson [2.5], would be needed, although the system resolution is two orders of magnitude too low (limited to 10 - 12 bits, while 16 bit accuracy is required)

Electromagnetic goniometers use radio waves or acoustic "pingers" to determine relative sensor position. The interesting feature is that the pingers and receivers are all mounted on the patient. This is the logical thing to do for it allows the patient (or structure) greater mobility. Such pinging goniometers for medical use are described for example by Jackson [2.6]; however, they have very nonlinear responses and are limited to about a degree of accuracy when installed on a patient (accuracy also limited to about 10 bits).

2.3 Goniometers for Use in the Physical Sciences

Goniometers for use in measuring photo-scattering property experiments and other optical calibration procedures are actually precision rotational stages. Examples in the literature can be found from: 1) large (two meters cube) four axis stages for determining properties of retroreflectors (a device which reflects rays parallel to the incident rays) with milli-radian accuracy [2.7], to 2) precision rotary tables with unlimited rotary motion and micro-radian accuracy [2.8], to 3) monolithic linkage nanoradian accuracy stages (which are range limited to milli-radians of motion) [2.9].

The first example is a precision index table. The second example uses a direct drive motor with integral optical encoder and high precision bearings to achieve arc-second accuracy. They note that runout of the optical scales, which are photo-etched in place, produce error in the interpolation of the fringe counting process. The third example is a clever system of levers connected by thin section springs such that a large motion on one terminal lever produces very small motion on the other terminal lever. The levers and springs are all machined from a single block so hysteresis and backlash are not a problem. Unfortunately such a system does not provide the 360° range needed for robots.

2.4 Goniometers Used in Manufacturing Environments

Many of the goniometers used in manufacturing environments are similar to those previously described such as precision turntables and the like. Two interesting patents are cited here. The first is a mechanism to determine position and orientation of a line in space, and the second is a planar goniometer attached to a robot. Each of these is discussed in greater detail below.

The 'Spatial Mechanism and Method' [2.10] is a clever device shown in Figure 2.1. It uses a system of gears and racks to record the three Eulerian angles that a single arm can trace out in space (including

U.S. Patent Dec. 6, 1983 Sheet 4 of 4 4,419,041

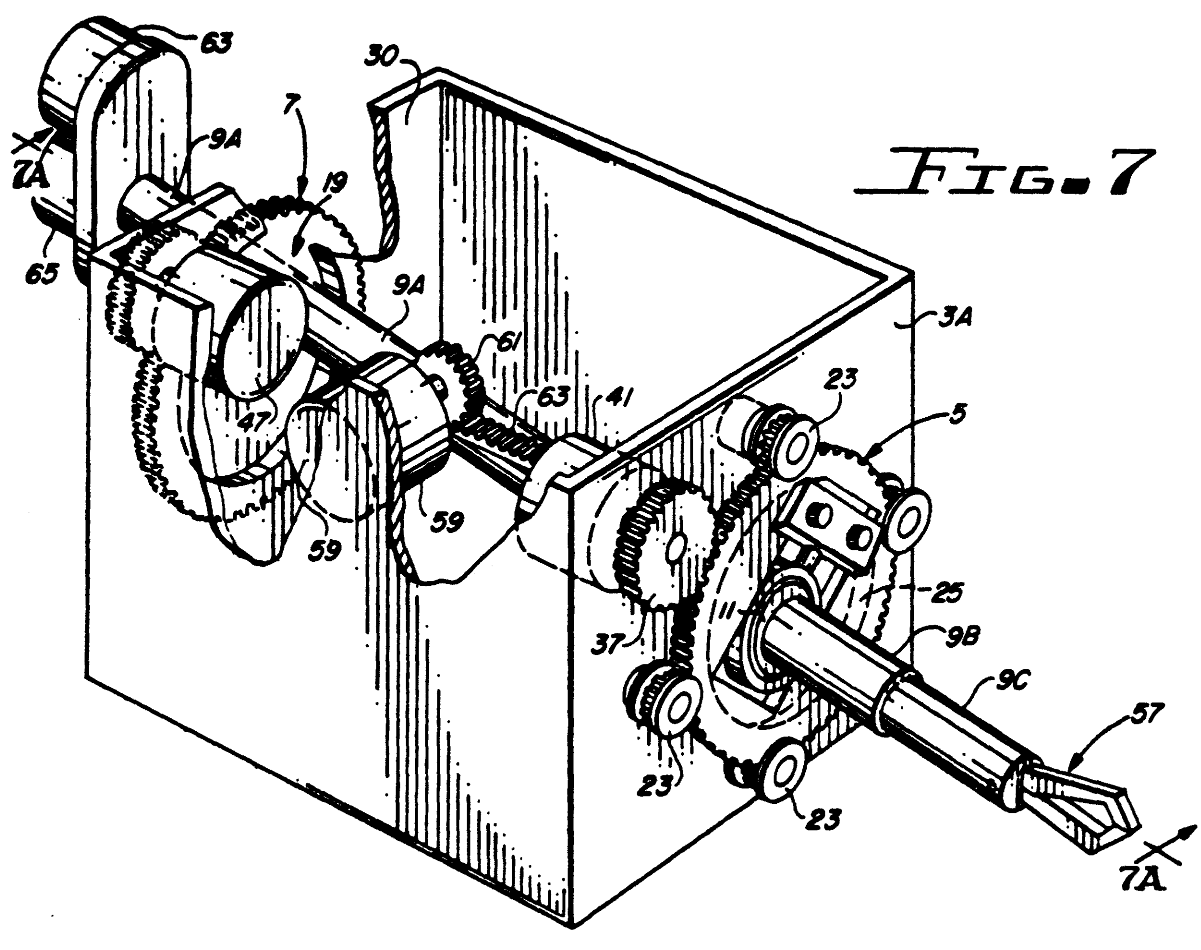

Figure 2.1* Spatial mechanism for determining endpoint position.

*Reprinted from U.S. Patent 4,419,071

twist of the arm about its length) and the extension of the arm via a telescoping tube. Accuracy on the order of one part in 7000 is claimed which is an order of magnitude less than required for robotic applications. The device seems to be a miniature portable coordinate measuring machine. Examples of the latter in full scale can have accuracies in the 50 microinch range when mapped with laser interferometers, but they are too big and inflexible for robotic applications.

The 'Monitoring the Location of a Robot Hand' [2.11] patent, shown in Figure 2.2, describes a knee joint with a planar goniometer attached. However, it is apparent that if constructed as shown, a large static error would occur when the linkage is straightened out and gravity applied normal to its length and the axis of joint rotation. Since the two links are connected via an angular measuring device (#39 on Fig 2.2), (which is only supported by the links) and supported at their ends by angular measuring devices #35 and #37, no bending moments can be transferred about the joint axis. Since no length adjustment is allowed for, the links will sag until static equilibrium is reached.

As an example, consider the case where each link is of length ℓ and the weight of the measuring system is M. The linkage will sag by a small angle ε which will cause the links to stretch to a new length of $\ell + \delta$. Using the small angle approximation for the cosine of ε, the angle ε is found:

$$\varepsilon = \left(\frac{\delta}{\ell + \delta} \right)^{1/2} \qquad (2.1).$$

U.S. Patent Oct. 10, 1978 4,119,212

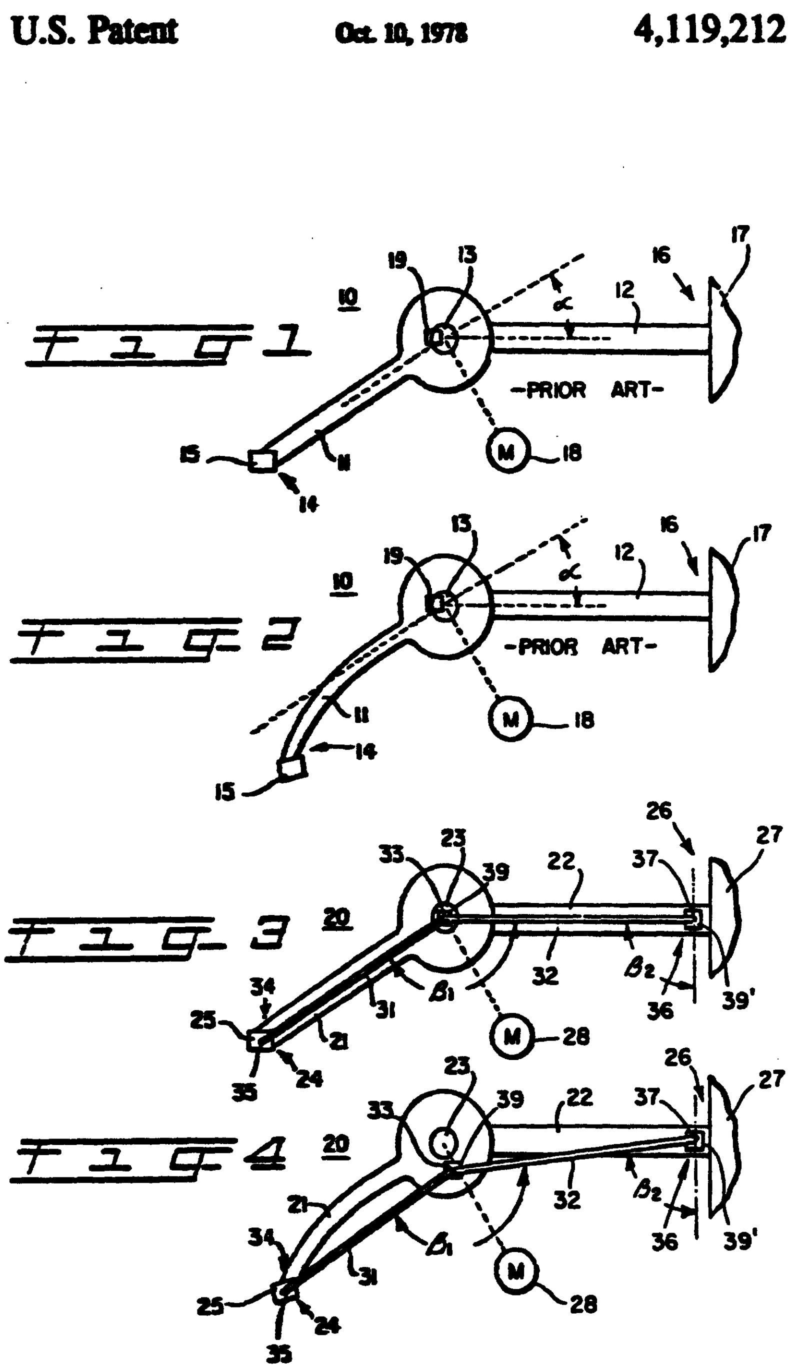

Figure 2.2* Robot goniometer as applied for in U.S. Patent 4,119,212

*Reprinted from U.S. Patent 4,119,212

The stretch δ in terms of the tension T, link cross section area A, modulus of elasticity E, and length ℓ is:

$$\delta = T\ell/AE \qquad (2.2).$$

The tension times the sine of the angle ε must balance the weight. Using this, (2.1), (2.2), and $\sin\varepsilon \approx \varepsilon$ (for ε small) the tension is found from:

$$T^3 = TM^2 + M^2AE \qquad (2.3).$$

To solve (2.3), let $a = M^2/3$, and $b = M^2AE/2$, then:

$$T = \left(b + \sqrt{b^2 - a^3} \right)^{1/3} + \left(b - \sqrt{b^2 - a^3} \right)^{1/3} \qquad (2.4).$$

As an example, consider the static case where the links are made from steel tubing with a 2" (50.8 mm) OD and a 1.75" (44.5 mm) ID and are each 30" long (762 mm) (weight = 6.625 pounds (3.01 kg) each). With an angular measuring device weight of 2 pounds (.91 kg), the tension and stretch are 862 pounds (391 kg) and .0012" (.031 mm) per link. The latter validates the small angle assumptions. The error is marginally acceptable; however, the tension would destroy the angular measuring devices' bearings. Thus any accuracy would soon be lost.

Figure 2.3 shows the type of mechanical linkage that would be necessary to avoid the above stated problems with Figure 2.2. It shows

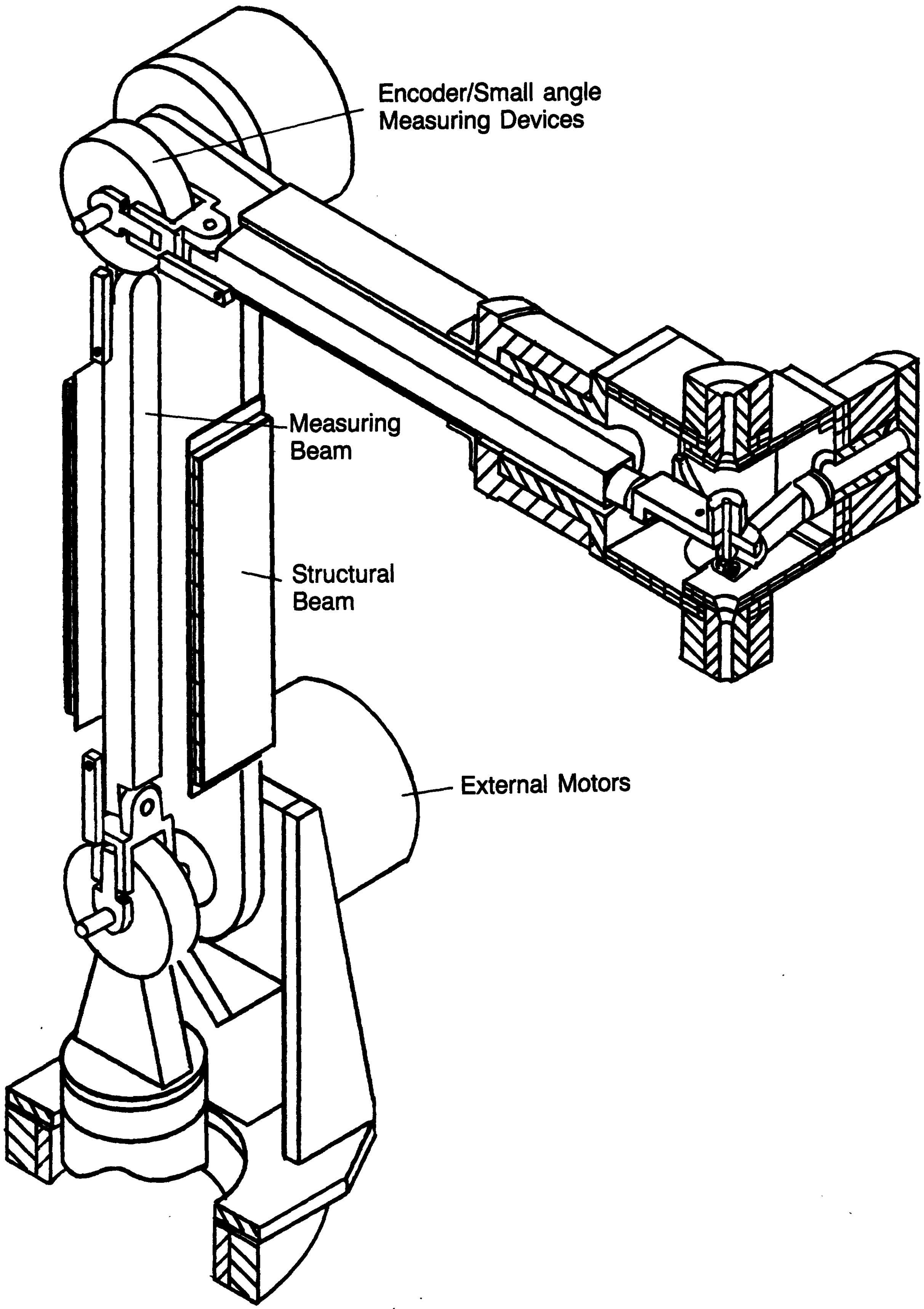

Figure 2.3 Six degree of freedom measuring beam, mechanical goniometer inside robot

an inner system of measuring beams and linear and angular measuring devices contained within a series of articulating structural beams. All the degrees of freedom measured are necessary to accurately determine the robot's endpoint position and orientation. Accordingly, the system is very complex and there is much room for manufacturing error to create inaccuracies in the various sliding joints. As an example of how a small error can disrupt the system, consider a four inch long slide near one of the joint encoders. If a gap of only .0001" (2.5 μm) opens up, then over a distance of 100" (2.5 m), an error of .0025" (100 μm) is created. There are too many similar potential sources of error to make the system practical.

2.5 Metrology Frames

For high accuracy cartesian motion, high precision diamond turning centers and coordinate measuring machines are evolving with accuracies in the micro and sub-micro inch range. To achieve such high accuracies, the concept of metrology frames has evolved. A metrology frame consists of dimensionally stable platforms mounted on moving parts of the machine. The platforms hold optics which allow high precision laser interferometers to measure large linear and small angular displacements. The concept of using laser interferometery is discussed further in Chapter 3.

2.5 Conclusions

The idea of using a goniometer to determine robot endpoint position is a logically correct one; however, since endpoint accuracies of 16 bits are necessary and each robot link can have up to six degrees of deformation and loads are not always vertical (as in the case of a human walking), a very complex goniometer will be required. It is important to note that intuition doesn't work well when applied to measuring very small distances. Each possible motion must be carefully modeled to ensure that it will be measured by the system. The design of such a goniometer will be discussed in greater detail in the following chapters.

References

[2.1] E.Y.S. Chao, 'Justification of Triaxial Goniometer for the Measurement of Joint Rotation', Jou. Biomechanics, Vol. 13, pp989-1066

[2.2] M.A. Townsend, M. Izak, R.W. Jackson, 'Total Motion Knee Goniometry', Jou. Biomechanics, Vol. 10, pp183-193

[2.3] F.C. Conati, 'Real Time Measurement of Three Dimensional Multiple Rigid Body Motion', MSME thesis, MIT, Cambridge Mass. 1977

[2.4] J.H. de Vries, 'A Concept for a Floating Circle Target Tracker', Medical and Biological Engineering and Computing, March 1980 pp213-219

[2.5] E.K. Antonsson, 'A Three Dimensional Kinematic Aquisition and Intersegmental Dynamic Analysis System for Human Motion', MIT Ph.D. Thesis, Dept. Mech. E. June 1982.

[2.6] K.M. Jackson, 'Monitoring of Movement With Radio Frequency Transducers', Jou. Biomedical Eng. Vol. 5, No. 2, pp117-124

[2.7] N.L Jachson, 'The Photometry of Retroreflectors Using a Computer Controlled Four Axis Goniometer', COLOR Research and Application, Vol. 7, No. 4, 1982 pp319-326

[2.8] A.R. Robertson, 'A high Resolution Servo Controlled Goniometer' Precision Engineering Vol. 1, No. 4, 1979 pp130-135

[2.9] M. Tanaka, K. Nakayama, 'Precision Goniometer for Fine Adjustment in the Nanoradian Range', Jpn. Jou. of Applied Physics, Vol. 71, No. 7, 1982 ppL399-L401

[2.10] S.E. Rose, 'Spacial Mechanism and Method', U.S. Patent # 4,419,041, Dec. 1983

[2.11] J.P.W. Flemming, 'Monitoring the Location of a Robot Hand', U.S. Patent # 4,119,212, Oct. 1978

(this page left blank)

Chapter 3

Methodology for Achieving High Endpoint Accuracy in Articulated Structures

3.1 Introduction

Consistent with the conclusions of Chapter 1 and 2, this chapter will describe a methodology, centered around goniometers, for designing sensor systems to measure position and orientation of articulated structures with an accuracy on the order of 16 bits. As the example in Chapter 1 showed, since these is a large error amplification associated with cantilevered structures, the basis of the methodology is to eliminate mechanical coupling between sensors and the motion which they are measuring. Thus accuracy shall not depend directly on the accuracy of mechanical components. This is accomplished by requiring that all measurements be made across air gaps, and the sensor system must be designed so that its structure is subject only to acceleration induced loads.

This chapter is organized as follows: In order to develop a high accuracy goniometer type sensor system for articulated structures, the basic mechanical metrology requirements are first described. Then methods of measurement are briefly discussed to provide background on the types of "building blocks" which are available to satisfy these requirements (Chapter 4 discusses individual types of sensors in greater detail). The method of locally arranging appropriate sensors into a geometry that can measure all the required degrees of freedom is then studied conceptually (detailed methods of error analysis are discussed in Chapter 5). Conceptual designs for the goniometer links and support anchors are then discussed (detailed design methods are presented in Chapter 6). In conclusion, a conceptual design of a robot that incorporates the sensor system is presented to illustrate application of the developed principles.

3.2. Identification of Necessary Measurements for Determining Position of Articulated Structures

Chapters 1 and 2 concluded that a joint to joint goniometer would provide the most rugged system for measuring position and orientation of robots without decreasing dexterity. Also discussed was the condition that any single large degree-of-freedom is always accompanied by five small error motions. Thus for articulated structures, whose long links greatly amplify these error motions, all six degrees of freedom at each joint will need to be measured. The above implies that there are two unique coordinate systems located at each joint which are separated by the air gaps across the sensors. The principle of goniometery, however, allows each set of coordinate systems in a specific link to be coupled together. This allows the two coordinate systems at each end of a link to be modeled as one.

Hence to determine the position and orientation of one "conglomerated" coordinate system with respect to another, six independent degrees of freedom between them must be measured. If designed properly, the rigidly coupled coordinate systems will track their associated structural links as they move and bend. The robot controller will then have an accurate "stick" model of the robot whose position and orientation are determined from the lengths of the links and the measurements made at the joints.

3.2.1 Methods of Motion Measurement Between Two Coordinate Systems

As previously described, beams (which are loaded only by their own weight) for support of sensors at joints are required to support groups of sensors and to track structural beams' motions. The function of a "measuring beam" is illustrated (see Figure 3.1) as follows: If a connecting line intersects a plane of a coordinate system XYZ at the origin, then two angles (θ and ϕ) will uniquely define the position and orientation of the line with respect to the coordinate system. If two intersection angles (θ' and ϕ') of the line with the origin of another coordinate system X'Y'Z', the length of the line ℓ, and the twist γ of the line along its length are also known, the relative position and orientations of the two coordinate systems with respect to each other will be uniquely determined. These measurements can all be made by sensors at the ends of the lines, and the lines are hereafter referred to as measuring beams.

The measuring beams can be "electromagnetic" or "mechanical", i.e. laser beams or beams made of solid materials, or a combination of the

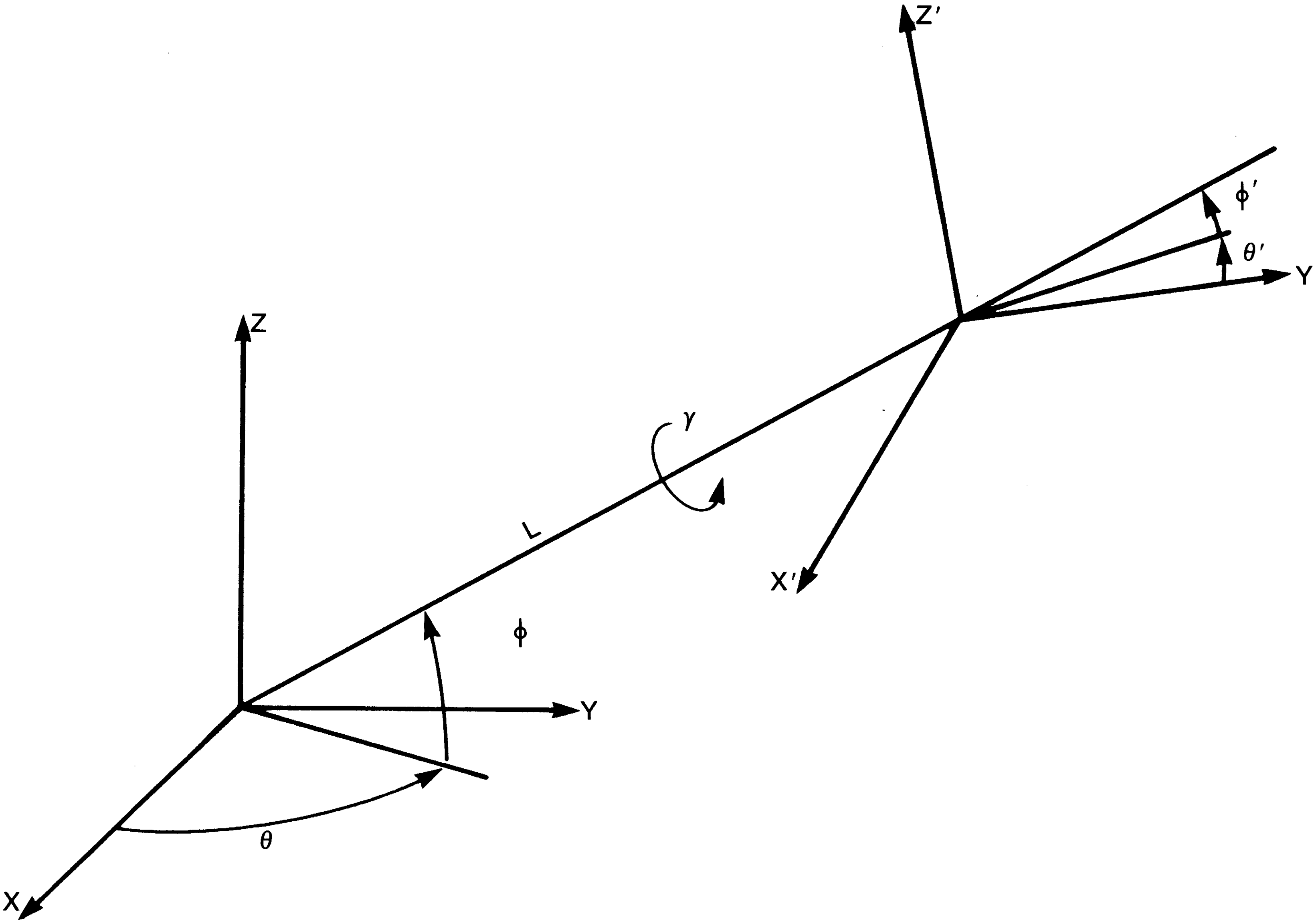

Figure 3.1 Coordinate systems' relative orientation

two. Note that the slightest external load acting on a measuring beam may result in a deflection error which is not necessarily repeatable and which can be magnified up to two orders of magnitude at the end point. Therefore, if mechanical components are incorporated into the design, deflections must be elastic and below a threshold unless provisions are made for their direct measurement. Possible types of measuring beams are discussed below.

Optical measuring beams would be difficult to use, unless an initial reference datum was provided. As an example, consider beaming a laser at a mirror that reflects the light back to the source. The distance of the mirror from the source can be determined by pulsing the laser and measuring the reflection time. This is extremely difficult to do over short distances (on the order of meters), and is impractical for large scale commercial use. On the other hand, changes in position of the mirror can be detected very accurately by interferometery which depends on counting interference fringes. This requires the laser to pass through an interferometer to a retroreflector, and return back through the interferometer into the receiving port for analysis. Note that accuracy is impaired if a count is missed, and the counting speed is limited to one foot per second, but measurement accuracy on the order of one part per million (20 bits) is possible [3.1].

A second problem with laser interferometery is that the laser head is on the order of five inches square by eighteen inches long and costs

$30,000. Since the fringe counting process must be continuous, a minimum of one laser for each degree-of-freedom would be necessary. This would make the cost of a multi-axis system exorbitant.

Even if laser interferometers were used, then the centers of the robot arms would need to be hollow in order to accomodate the laser beams. Thus a logical step is to replace the laser beam with a solid measuring beam and use sensors at the ends of the beams to detect relative motion between the ends. Like the laser beam which must be kept from hitting the walls of the hollow robot arm, the solid measuring beam must be supported in a way that allows it complete freedom to track the motions of a structural beam. To prevent errors associated with deflections, the measuring beam must only be loaded by acceleration of its structure. In addition, the measuring beam geometry should be kept simple so deflections can be accounted for with a software correction (or be kept below a threshold level). Further discussion of the construction of the measuring beams is delayed until after the description of the measuring devices that are to be held at each end of the measuring beam.

With regard to the placement of groups of sensors, in the measuring beam system, where structural beam ends meet at a joint, the ends of successive measuring beams would be located in close proximity to each other (as shown in Figure 3.2). Small range high resolution sensors could provide information to determine the position and orientation of one measuring beam with respect to its neighbor. Examples of this type of sensor include: capacitance and impedance probes, and fiber optic levers. Also lateral effect diodes can be used to measure X - Y coordinates of the center of intensity of a beam of light. (The physics of operation of these types of sensors and a detailed description of laser interferometery is discussed in Chapter 4.) The following section will examine methods for combining these basic types of sensors into a configuration that will allow all the motions at a joint to be measured.

3.2.2 Placement of Sensors to Measure Six Degrees of Freedom at a Joint: The Development of the POSOR

There are three basic motions that adjacent measuring beams' sensor groups will be required to make with respect to each other in order to track a structural beam (as shown in Figure 1): twisting, bending, and translating. For an articulated structure, these motions are comprised of: three small translational, two small rotational, and one large rotational degree-of-freedom. The nature of these motions lends them to be detected by looking at the relative motion between two adjacent (essentially parallel) planes. In order to determine the best method for detecting relative motion between the planes, consider that the tools available are distance sensors and lateral position sensors. Also, if desired, local geometry variations (bumps) can be introduced. Detailed concepts are discussed below.

The combination of sensors to provide accurate determination of one large and five small degrees of freedom is herein referred to as a POSOR (POSition and ORientation) device.

One small translational and two small angular degrees of freedom can be easily determined by looking at the separation between the planes. Since the planes are always essentially parallel and the large degree-of-freedom motion can only cause one plane to rotate above the other, if the separation between the planes is determined at three points, then the relative distance and orientation between the planes will be uniquely defined. This concept is illustrated in Figure 3.2 which shows a plane attached to one measuring beam "looking" at an adjacent plane mounted to another measuring beam. If the relative distance between the three sensors (shown as impedance probes) is known, then combined with the sensor readings, the Y, α, and β motions can be accurately determined.

Since the distance measurements are made across small (.05" (1.3 mm)) gaps, 12 bit sensor resolution with the sensors spaced 5" (127 mm) will allow for the angles α and β to be determined to 2.4 μrad (.5 arc-sec). As will be discussed in Chapter 4, impedance and capacitance probes' measurements will not become distorted by small (1°) motions of the planes. Detailed calibration and error analysis of this system is discussed in Chapter 5.

The Y distance measurements between the planes, however, provide no information about the relative XZ position or θ rotation (i.e. the two remaining small translational and the large rotational degrees of freedom) of the plates (coordinate systems which lie at the ends of the measuring beams). Two systems, for detection of these motions, are presented here: 1) A "Bumpy Ring Sensor" shown in Figure 3.3, and 2) a

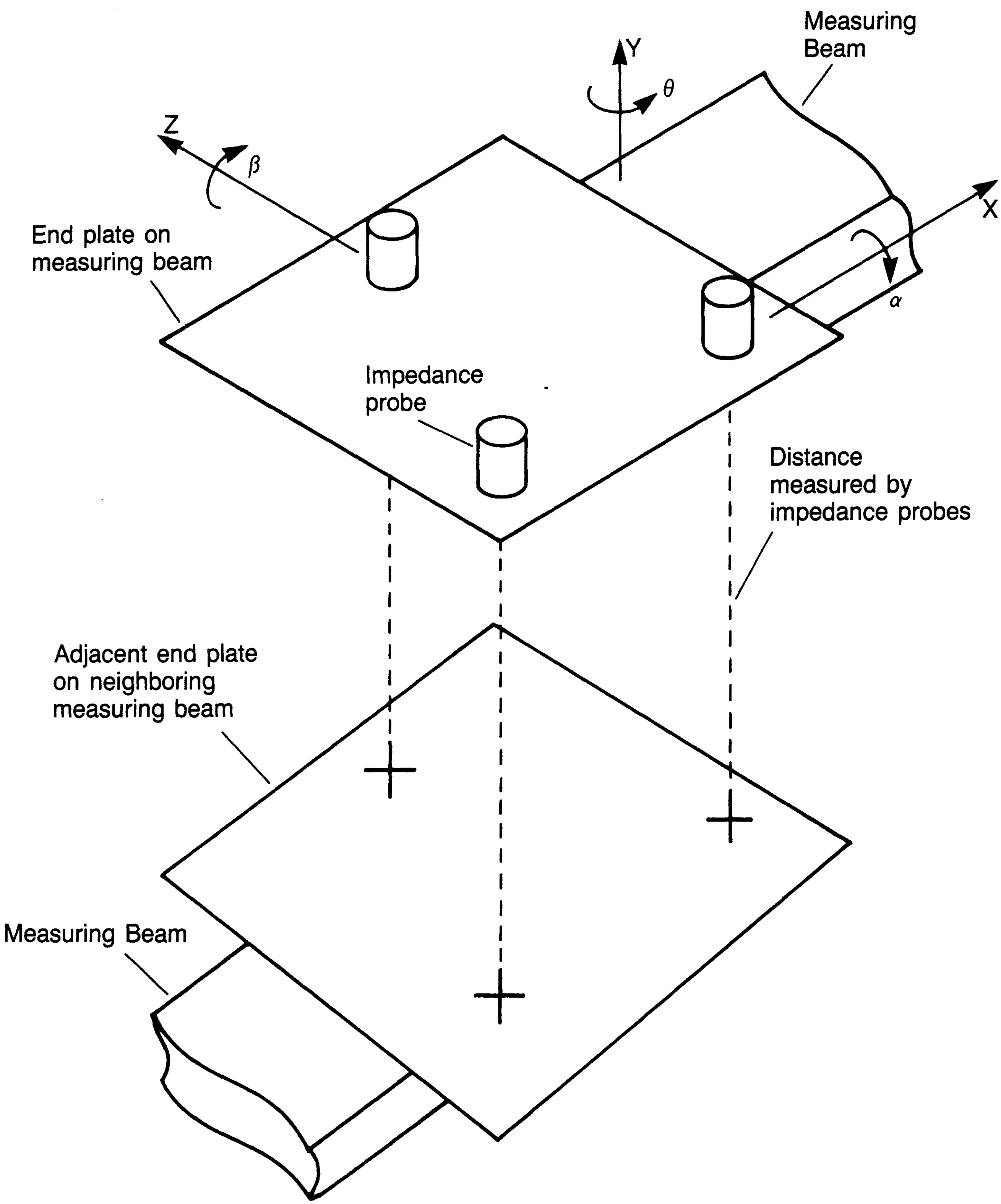

Figure 3.2 Distance-orientation measure using distance measuring probes

"Light source Ring - Lateral Effect Diode Sensor" shown in Figure 3.4. The former has the potential to be the most accurate but will be the most difficult to develop. The latter is the simplest to build and test, but it is more sensitive to contamination. Both systems are discussed in detail below.

The Bumpy Ring sensor shown in Figure 3.3 has three distance measuring sensors (shown as impedance probes) required to measure three degrees of freedom for the holonomic system of the adjacent plates; however the motions are not measured directly. Runout (XZ motion) is not amplified by the distance from joint to endpoint so 12 bit accuracy is sufficient. The rotation Θ is amplified, however, so the 16 bit required accuracy is obtained by the counting of the bumps as they go by the sensors. In order to sense the bumps, the sensors are placed out of phase with each other, so that one sensor looks at the peak, one looks at the ramp, and one looks at the trough of a bump. The shape of the signals from the three sensors should remain the same as the inner ring undergoes small translations, only the amplitudes should change. Thus by starting from a home bump, runout is determined by looking at the relative amplitude, and rotation is determined by counts and looking at the relative phase of the sensor readings.

For angular sensitivity, if the slant is at 45°, angular motion ε at a ring radius R_r will produce a sensor reading εR_r. If fine bumps are used (.05" (1.3 mm)), an impedance probe with 5 μin (.13 μm) resolution can be used. Thus a measuring device 5" (12.7 cm) in diameter could sense rotations of 2 μ radians (.5 arc-seconds). With

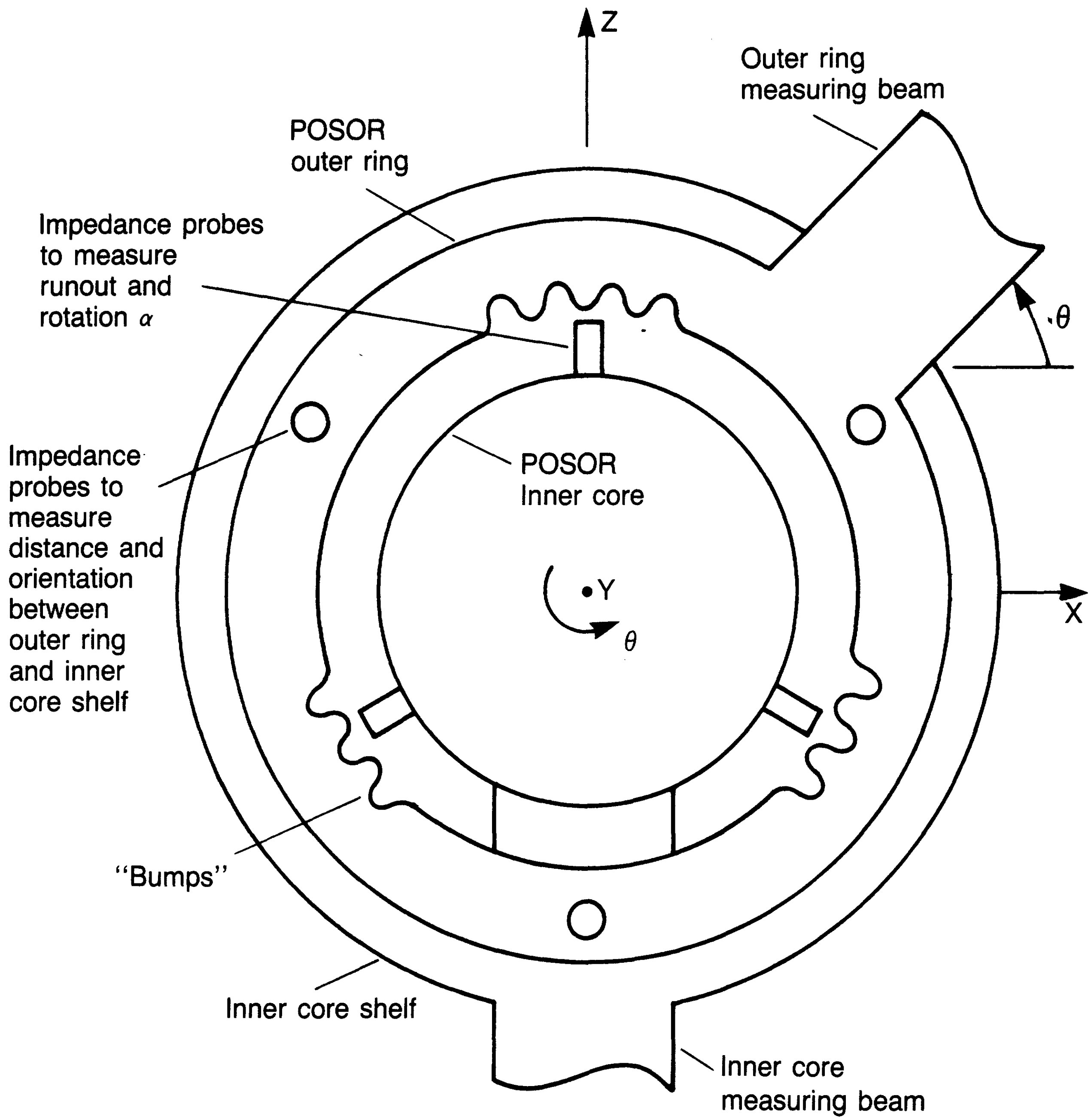

Figure 3.3 "Bumpy Ring Sensor" for measuring XZ position and θ rotation

regard to sensing relative translational motions between the two rings' centers, Whitehouse [3.2] has theoretically shown that it is possible to sense these motions by using three probes of varying sensitivity spaced asymmetrically around the part. Note that this system will have to be initially calibrated to account for mechanical inaccuracies in the shape and position of the bumps.

The lateral effect diode system, shown in Figure 3.4, consists of a ring of light sources and two lateral effect diodes (provide XZ coordinates of a light spot on its surface) arranged on the two plates (which are mounted on the ends of adjacent measuring beams) respectively. To ensure that each photo diode will always have a light source hitting its surface, the spacing $\ell - \delta$ between the light sources must be less than the width ℓ across the diodes. To operate the sensor, the lasers are sequentially pulsed so two light sources do not simultaneously strike the surface of a photo diode (or an erroneous signal will result). Pulsing the light sources also allows for identification of which light source hit which diode, and also allows the use of a lock in amplifier to filter noise. To supply the large number of light sources required, fiber optic cables could lead from all the joints to a central high beam quality laser whose light is multiplexed to the cables by a mechanical chopper. Note that a laser is specified because stability of the beam is important.

From initial calibration measurements the position of each light source and lateral effect diode in its plane is known. When a pulsed light source beam intersects a diode, its XZ coordinates are measured.

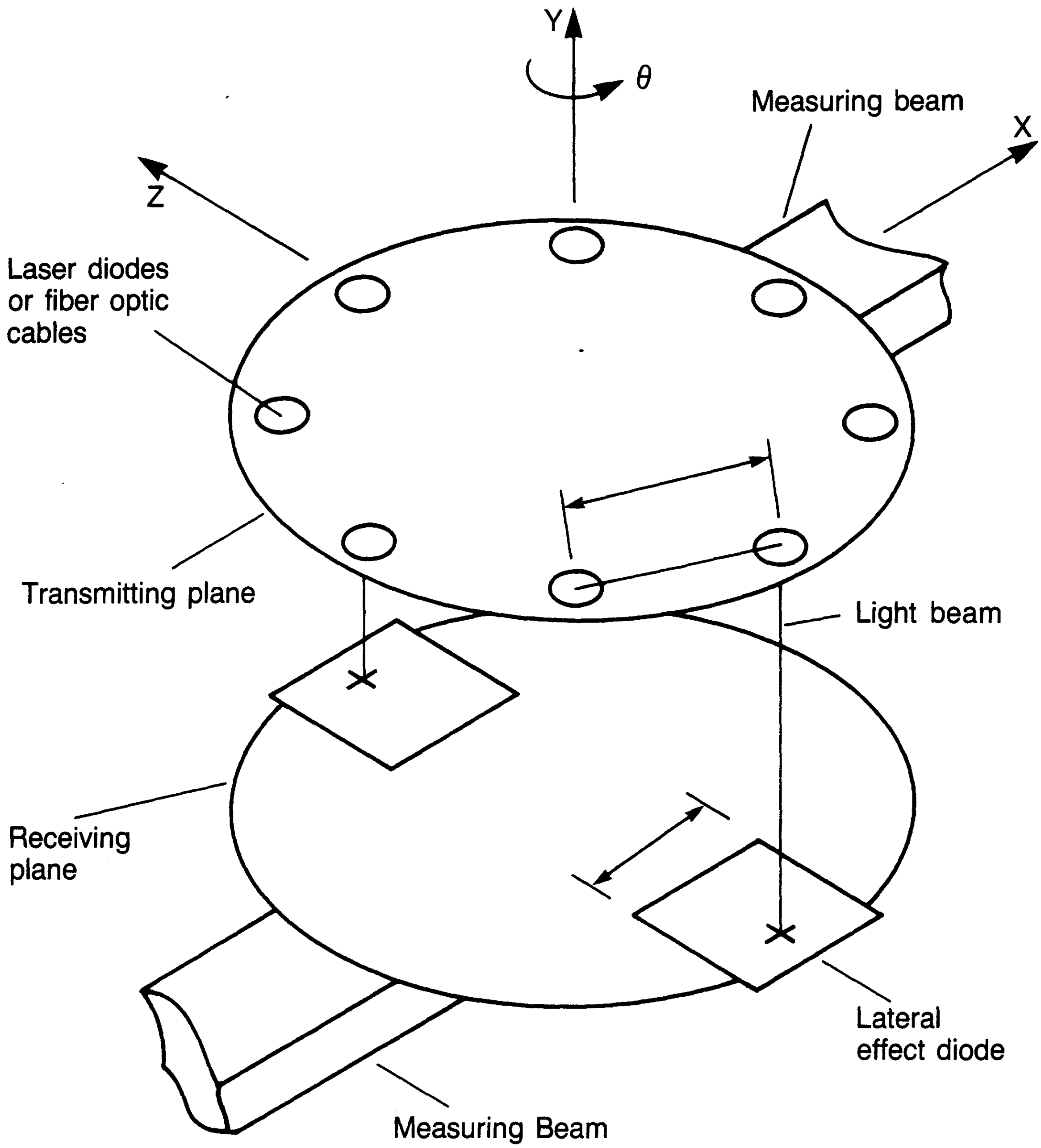

Figure 3.4 "Light source-lateral effect diode sensor" for measuring XZ position and θ rotation

After the XZ coordinates of two light sources are found, a simple coordinate transform will uniquely define the XZ position and Θ rotation of one plane with respect to the other. The key is to design the measuring beam system so at least one light source is always pointed at a lateral effect diode regardless of the deflected shape of the structural beam. Angular resolution is equal to the ratio of diode resolution to diode spacing, and can be on the order of 25 μ/2.5 (10 μrad). A detailed error analysis and calibration methods for the lateral effect diode system are given in Chapter 5.

Other methods for simultaneously determining one large and five small degrees of freedom will undoubtedly become apparent in the future; however, it is the methodology of using the information from a POSOR to determine the position of the measuring beams that is important, not necessarily the method by which it is accomplished.

3.3. Structural Characteristics of the Measuring Beam System to Support POSORs

This section will discuss conceptual methods for the mechanical design of measuring beams and methods for structurally isolating them from the load carrying members of the robot. Since the POSORs described above will only measure relative motions at the ends of measuring beams, any non-rigid body motion of the measuring beams will be amplified by the structures length. This makes accurate calculation of elastic deflections critical, because they must be kept below a threshold value (typically below the resolution of the POSORs) to avoid large contributions to endpoint error. Detailed design calculations for measuring beams and associated components are discussed in Chapter 6.

A long measuring beam must be supported at two points, roughly at each endpoint, in such a way that it cannot deform except under the influence of an acceleration on its own mass (i.e., the beam must not be loaded by external forces or moments). If possible, the supports should be located so as to minimize acceleration induced bending moments and maximize the natural frequencies of the system as shown schematically in Figure 3.5. The support design must take into consideration the fact that the structural beam acts as a free cantilever beam, and can undergo linear and angular motions along and about the X, Y, and Z axes as shown in Figure 3.6.

A structural beam's deflections, shown in Figure 3.6, impose certain restrictions on the gimbal support design. Since the structural beam can deflect sideways in two directions, each end of the measuring beam must be pinned about two orthogonal axes. In addition, since the structural beam can twist about its length, one end of the measuring beam must be pinned about an axis parallel to its length. Furthermore, since the structural beam's length can change, the measuring beam must be held in such a way that one end is free to move along its longitudinal axis. These possible motions form the basic design requirements for the support gimbals.

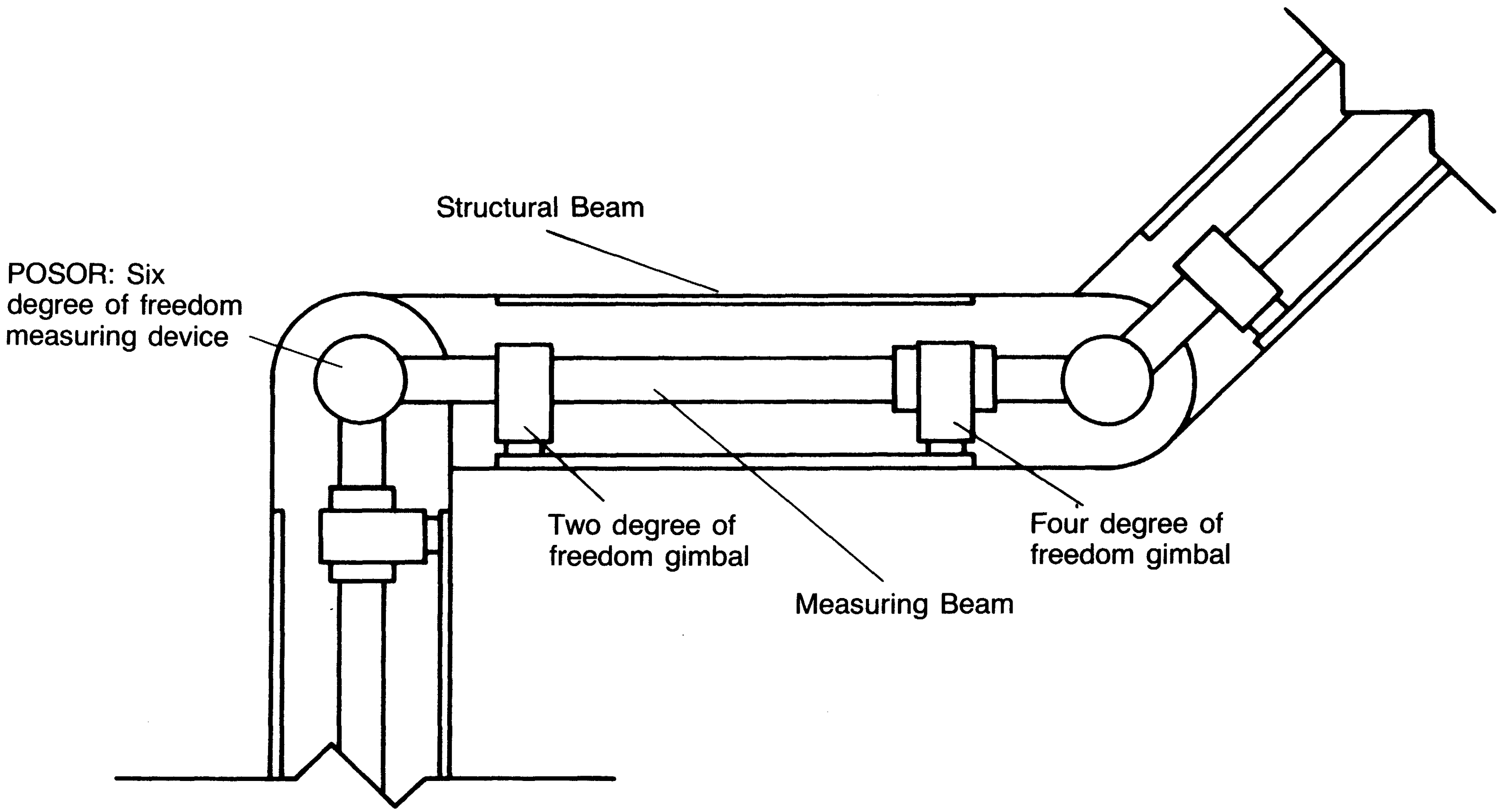

Figure 3.5 Schematic of measuring beam mounting inside structural beam

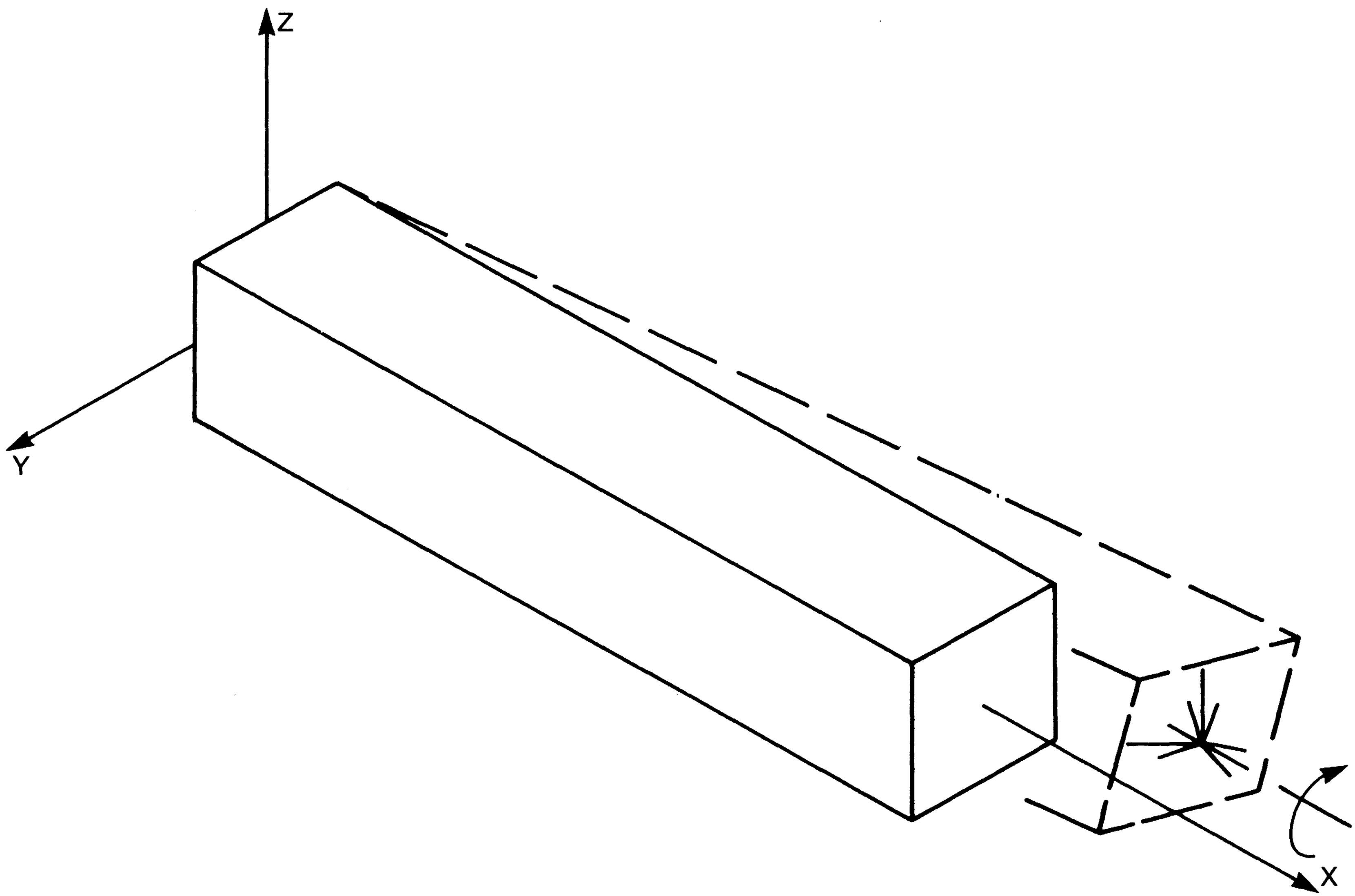

Figure 3.6 Relative elastic motions of a cantilever beam

The term gimbal does not necessarily imply the use of ball bearings because the required degrees of freedom are all small. Possible support schemes include magnetic levitation, air bearings, ball bearings, wire supports, or combinations thereof. In all cases, the lower the reaction torque and the higher the ratio of the beam moment of inertia to sensor system mass, the lower the induced error in the measuring beam system. In most cases, simplicity and reliability will be the chief design criteria, and direct mechanical support will be chosen. Note that the POSORs can sense bearing runout, so low friction and breakaway torque are more important than bearing accuracy. For detailed discussion of various types of gimbals, see section 6.2.3.

3.4 Conceptual High Accuracy Robot Designs

This section will discuss how the measuring beam system can be used in the design of high accuracy robots. For clarity extensive illustrations are provided but these are only conceptual designs and the backs of envelopes used to size components are not shown here.

Figure 3.7 shows two measuring beams supported by two and four degree-of-freedom gimbals (sans structural beams for clarity). The POSORs are of the Light Source - Lateral Effect Diode type. The plates at the ends of the measuring beams are identified as "transmitting planes" for the plates which contain the light sources, and as "receiving planes" for the plates which contain the lateral effect diodes and the impedance probes. Note that the design lends itself to a series of offset beams which makes the design of "double jointed" robots easy to accomplish.

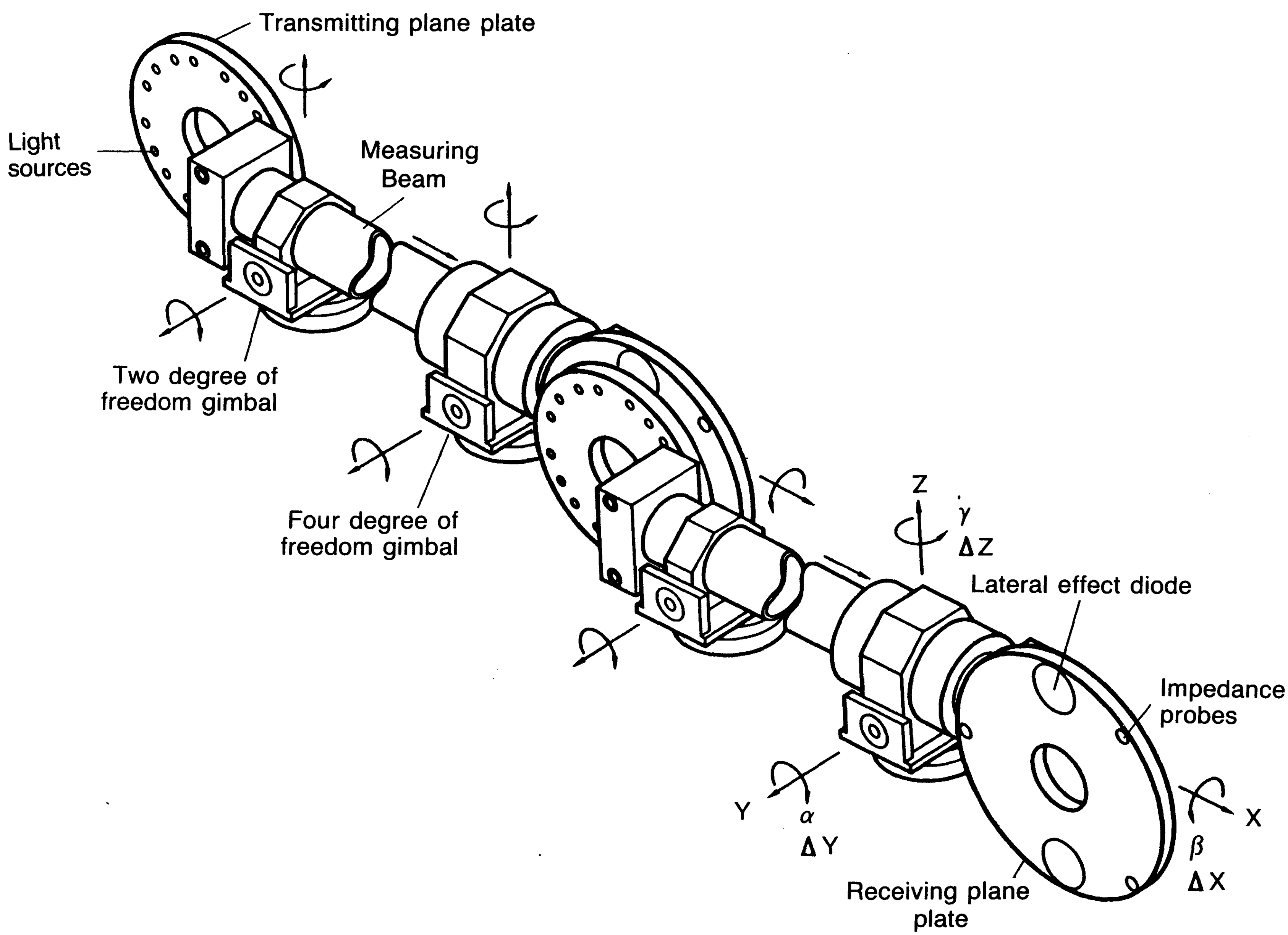

Figure 3.7 Measuring beams end to end, with lateral effect diode sensors (structural beams not shown)

Figures 3.8 through 3.11 show (overall view and details of joints) how a structural system and measuring system can be combined in a high accuracy five axis robot (for most high accuracy operations such as drilling, deburring, and cutting, a sixth axis is not needed). For these designs, a Bumpy Ring POSOR is used because ultimately it will replace the Lateral Effect Diode POSOR. Support wires are also used for gimbals (see section 6.2.3). The basic construction of the structural system consists of offset box beams joined by turntable (four point contact) bearings with integral gear teeth. This allows the drive motors (electric, pneumatic, or hydraulic) to drive the joints from the outside which prevents interference with the POSORs. Position control may be difficult due to gear backlash causing nonlinearities in the control system, but this can be overcome by using a micromanipulator (not shown here) as discussed in Chapter 1.

3.5 Remarks

To calibrate and operate a measuring system, its design and method of manufacture must also be considered. An error analysis can determine the effect of manufacturing tolerances and sensor accuracy on system performance and which quantities need to be calibrated. Thus calibration measurements can be traced to a standard reference which will help maintain inter system compatability. These calculations will also give insight needed for test equipment design.

To demonstrate the principle of the POSOR, that one large degree-of-freedom and five small degrees of freedom can be simultaneously

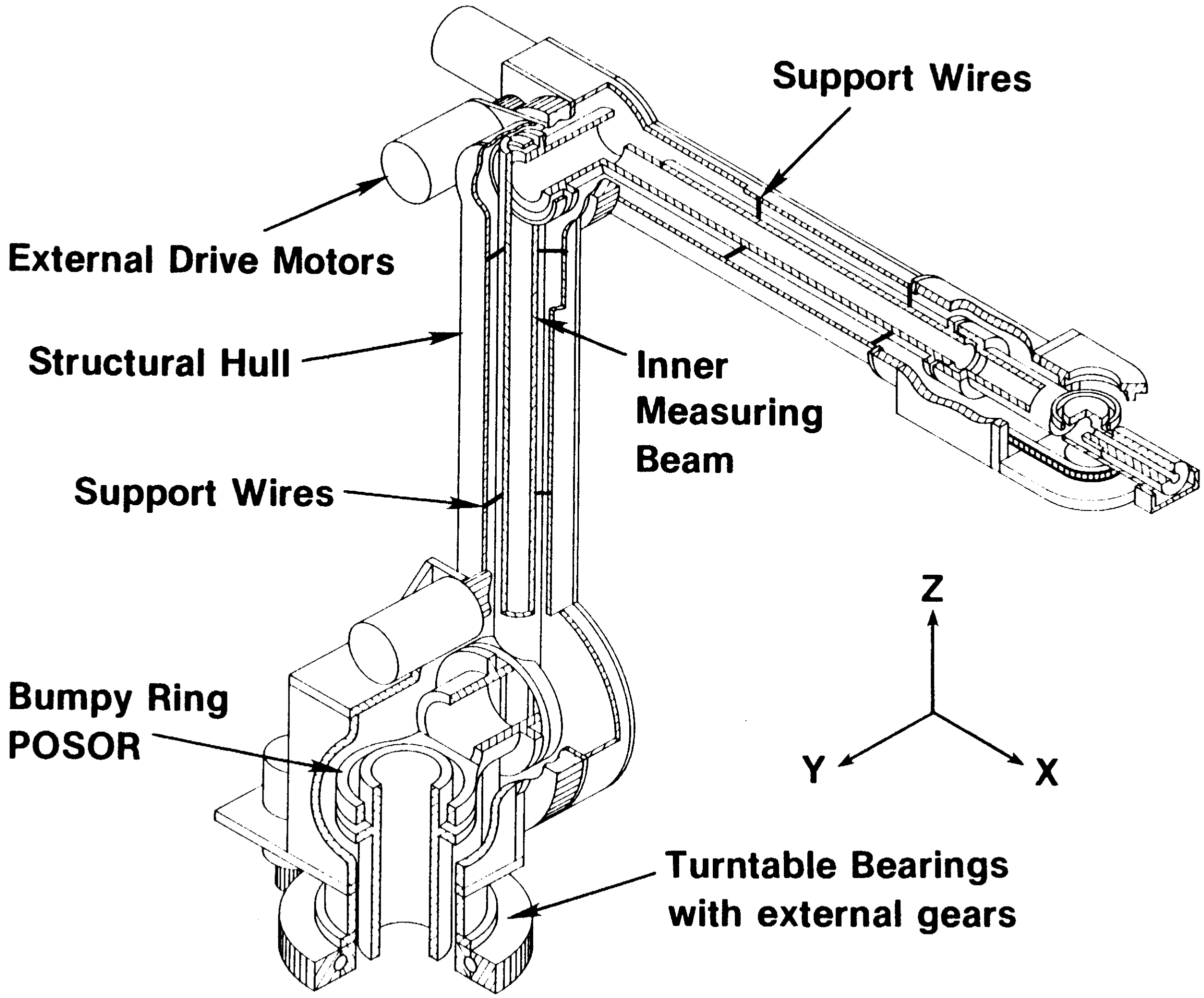

Figure 3.8 Conceptual design of a five degree of freedom, high payload, high accuracy robot. (impedance probes not shown here for clarity)

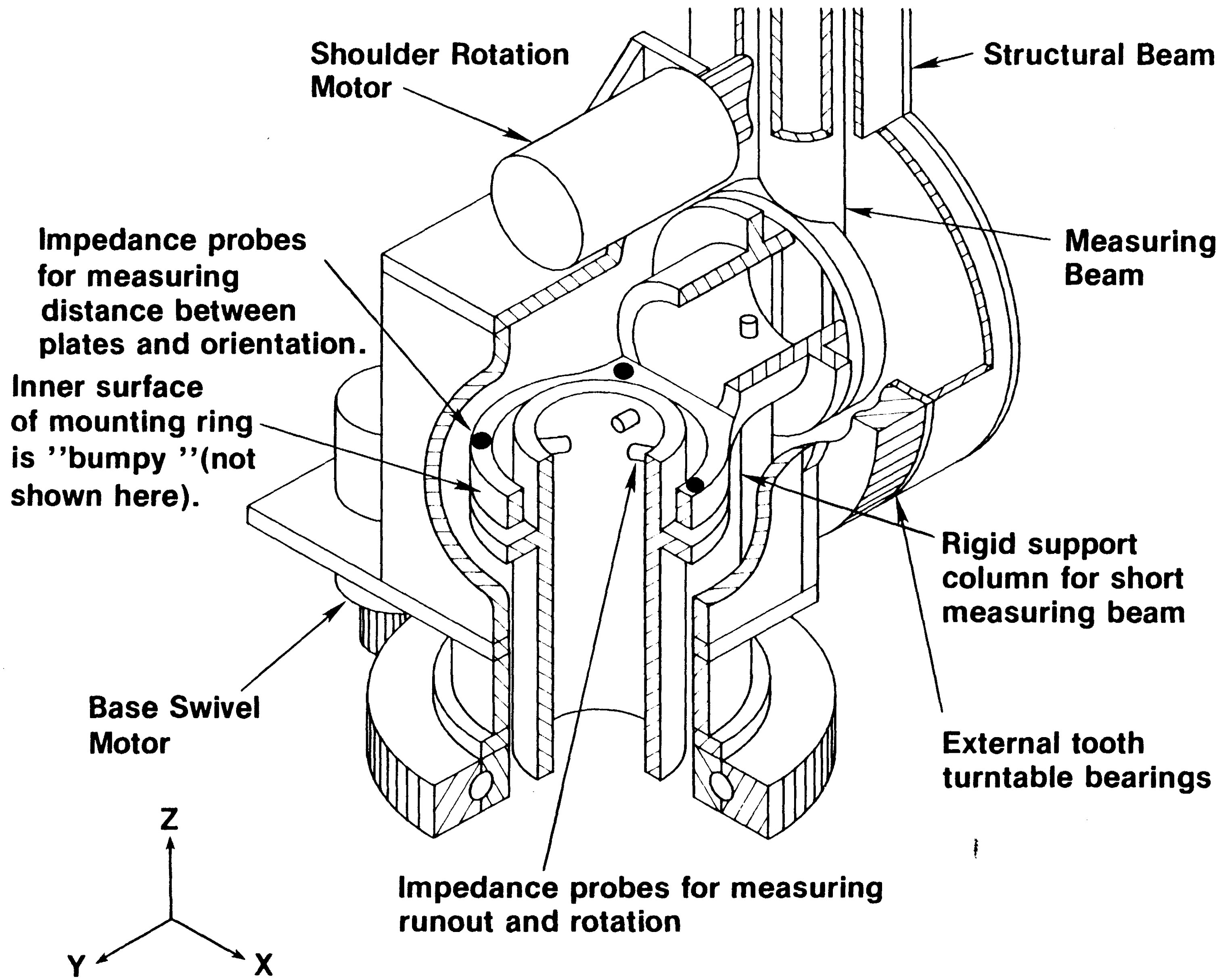

Figure 3.9 Detail of robot's base assembly

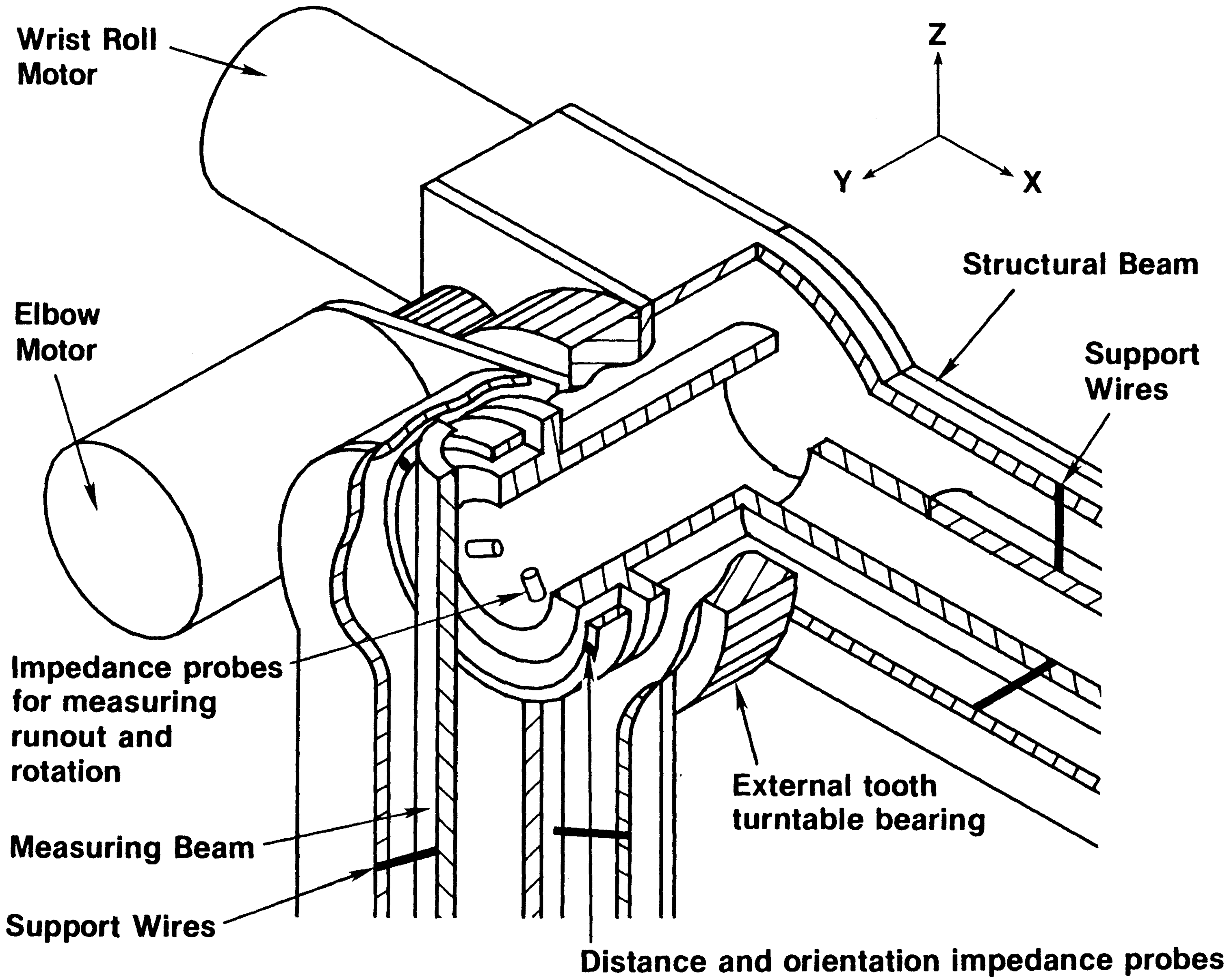

Figure 3.10 Detail of robot's elbow assembly

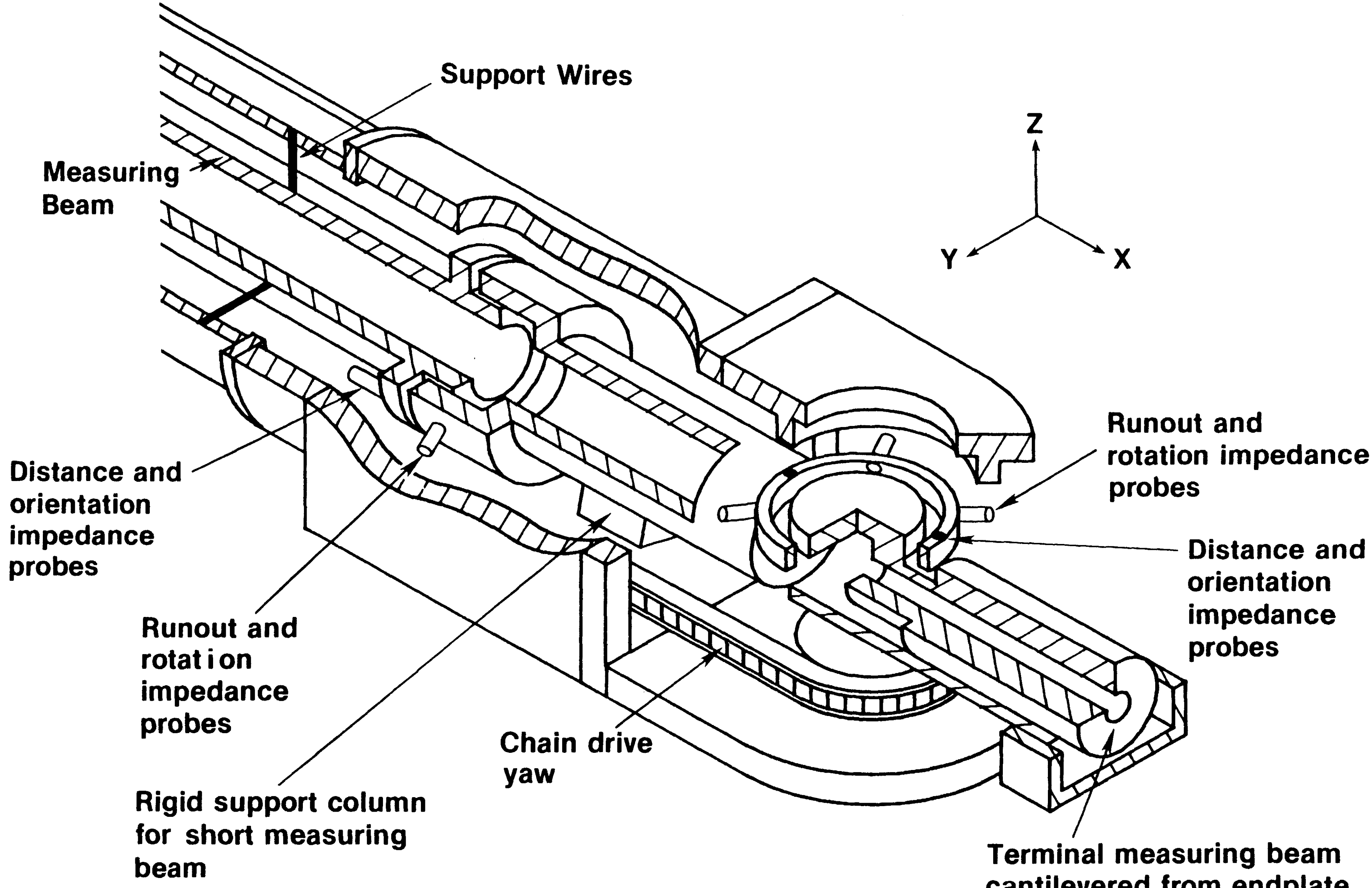

Figure 3.11 Detail of robot's wrist assembly

measured, a Lateral Effect Diode POSOR was designed built and tested. It was chosen because it was easier to build, and the algorithms to process the data are simpler than for the Bumpy Ring POSOR. For the Lateral Effect Diode POSOR, two sensor systems must be calibrated, the position sensing system (collimated light sources and lateral effect diodes), and the distance measuring system (impedance probes). Detailed calculations for their design and calibration are presented in Chapter 5. The experimental setup is described in Chapter 7, and Results and Conclusions are presented in Chapter 8.

3.6 Conclusions

This chapter has developed conceptual methods for uncoupling mechanical metrology errors from mechanical components (i.e. loading, wear, and age will not affect the system). Thus measurements can become as accurate as that of the sensors and initial calibration apparatus. The result is the development of a device that can measure one large degree of rotational freedom, two small rotational, and three small translational degrees of freedom. This device can be used with a goniometer type linkage to measure all the motions of an articulated structure regardless of its position or applied load.

References

[3.1] Hewlett Packard Co. 5528A Laser Measurement System User's Guide. October 1982.

[3.2] D. Whitehouse, 'Some Theoretical Aspects of Error Separation Techniques in Surface Metrology', J. Physics E: Sci. Instrum., vol. 9, 1976, pp 531-536

(this page left blank)

Chapter 4

Electromagnetic Sensors for Measuring Small Motions

4.1. Introduction

As pointed out in Chapter 1, any form of mechanical contact between surfaces whose relative position and orientation are to be measured, will introduce errors into the measurements. All surfaces which ride on bearings exhibit this behavior with the result that many small out of plane motions occur along with the intended motion. The purpose of this chapter is to discuss various forms of non-contact mechanical metrology sensors. The first section discusses distance measurements and the second section discusses lateral position measurements. Although it will not be used in a POSOR, interferometery will be necessary to calibrate POSORs, and thus will be discussed in some detail. The last section discusses methods for increasing accuracy of sensors.

Note that not only good sensors are required, they must be mounted correctly. Specifically, they should be rigidly mounted without stressing the sensor housing, and the axis of measurement should pass through the point on the body whose motion is of interest. Thus other small angular motions of the body cannot induce errors (by the lever arm whose length equals the distance from the measurement axis to the point). Errors of this type are called Abbe offset errors.

4.2 Distance Measurements

This section will describe various types of non contact distance measuring devices. Interferometery based distance measurements will not be discussed until Appendix 4A. Among the non-contact distance measuring devices available, are fiber optic levers, capacitance probes, and impedance probes.

4.2.1 Fiber Optic Levers

The distance of an object from a fiber optic "lever" can be determined based on the amount of reflected light that is sensed (an excellent overview of all types of fiber optic sensors is given by Giallorenzi et-al [4.1]). A sensor such as described by Kissinger [4.2] or Frank [4.3] uses transmitting and receiving fiber optic cables. A comprehensive analysis by Cook and Hamm [4.4] on a seven fiber bundle with one inner transmitting cable surrounded by six receiving cables provides an analytical model for evaluating fiber optic lever performance. The system is shown schematically in Figure 4.1. As the sensor moves away from the surface, the cross sectional area of the reflected light beam in the plane of the receiving fibers increases. Changes in the area of light falling onto the fibers as a function of change in distance will affect the measured intensity accordingly. Thus ideally the performance of the fiber optic lever is a function of the cross section geometry of the lever, the illumination exit angle, and the distance from the surface (the surface tilting or becoming contaminated can quickly lower resolution). For a seven fiber bundle,

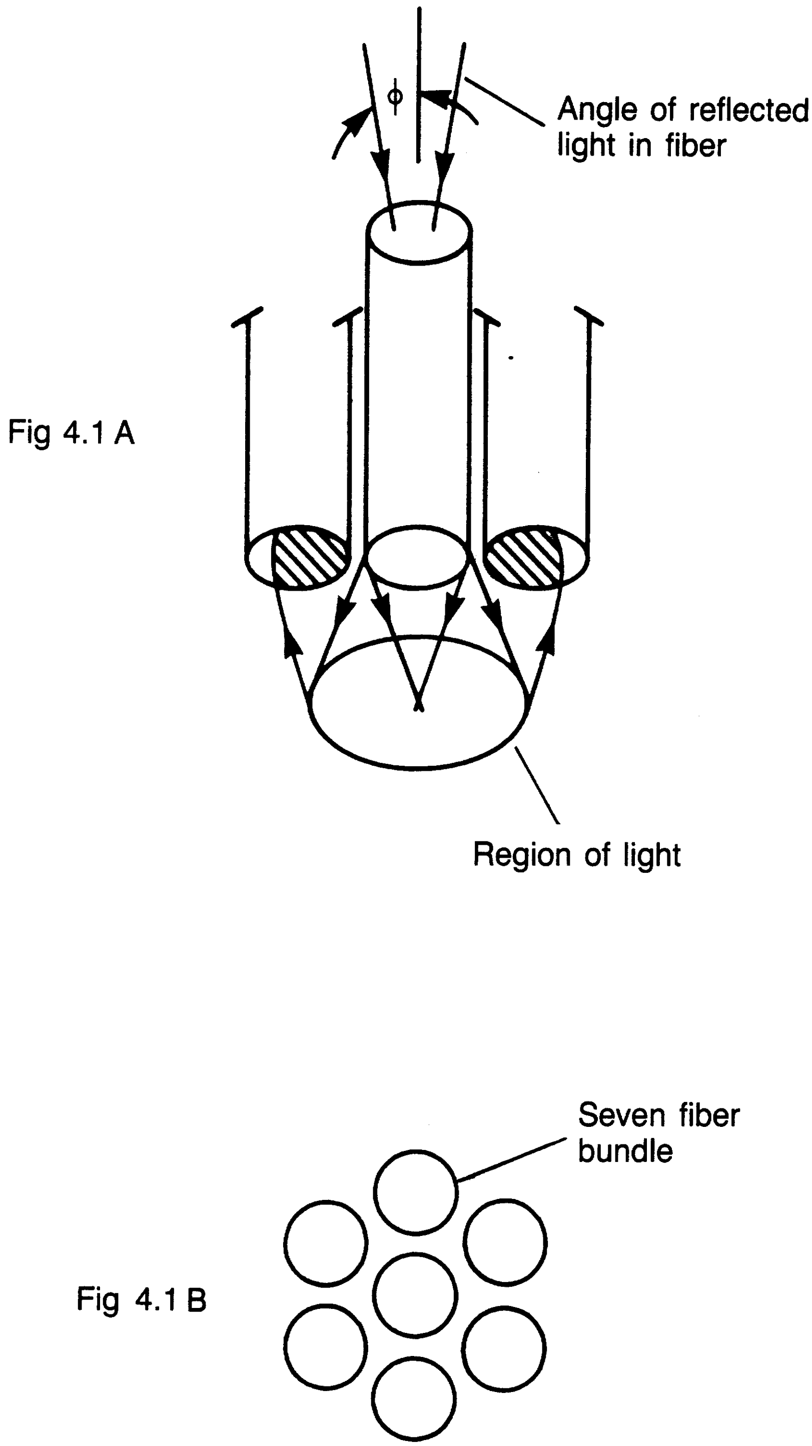

Figure 4.1 Fiber-Optic Lever construction

ranges of .025" are possible (note that .05" range will be required for the goniometer system described in Chapter 3). 12 bit accuracy is possible, however complex algorithms will be needed to determine the effect of the POSOR planes tilting on sensor readout. Also, surface finish becomes extremely critical. In view of these facts, fiber optic levers would not provide the necessary performance for a POSOR.

4.2.2 Capacitance Probes

Capacitance probes offer the best stability and highest accuracy of all distance measuring devices, other than interferometers. They are unaffected by the metallurgical properties of the target material (such as grain size), and have very low electrical noise levels due to their low circuit resistance. However, they are sensitive to things that can change the dielectric constant between them and the target surface. Earlier forms of probes, such as discussed by Lion [4.5] merely used one surface as one capacitor plate, and the other as the opposing plate. The distance between the plates is thus inversely proportional to the measured capacitance. Various signal processing techniques such as using a Van Zelst bridge (analogous to a wheatstone bridge circuit used in strain measurement) are then used to amplify the signal. The advantage of using a capacitance bridge (Van Zelst Bridge) is that it provides very high sensitivity with very low resistance; thus thermal noise, which is proportional to the square root of the system temperature, frequency, and resistance) is kept to a minimum [4.6]

Recently, a new type of capacitance probe has evolved [4.7], that does not need contacts connected to both surfaces. Instead, the effect of a surface on the field lines near a capacitor is measured. These probes can have very high resolutions (one part in one million) and can theoretically measure down to tens and hundreds of nanoinches. Unfortunately they are not yet widely available.

4.2.3 Impedance Probes

Eddy current or impedance probes use the principle of impedance variation which is caused by eddy currents induced in a conductive metal target. The coupling between a coil in a sensor and the target is dependent upon the distance between them. The electronics necessary to drive the system consists of an oscillator, linearization network, amplifiers, and a demodulator which provides an analog voltage proportional to distance between coil and target [4.5].

These probes are often used as limit switches to reset "home" positions on machine tools. Since they're output is not affected by the material that separates them from the target surface, they are also often used to sense the thickness of large sheets during manufacturing. This insensitivity to gunk (as long as the gunk contains no metallic particles) would make them valuable as POSOR sensors because temperature and humidity changes and various contaminants are bound to be present around a robot (unless its used in the electronics industry). Resolutions on the order of one part in 10^5 are obtainable from commercially available probes. When calibrated, accuracies of 5 μin (.13 μm) over a distance of .05" (1.3 mm) are possible. For extreme accuracy, a ferrous target should not be chosen, since variations in grain structure can affect the sensor output.

4.3 Lateral Position Measurements

This section discusses photodiode arrays and their application to measuring lateral displacements. These arrays have found broad use in video cameras, visual inspection stations, etc., as well as sensors to detect vibration and small angle changes (autocollimators). The types of photo detectors available include discrete array and monolithic diode devices. Their light wavelength sensitivity can range from infrared to ultra-violet [4.8].

Discrete arrays are one or two dimensional arrays of individual photodiodes with maximum two dimensional packing density currently on the order of 1024 by 1024 elements on a one half inch square surface [4.9]. Such arrays, or charge coupled devices, operate as follows. Each photodetector accumulates the light charge falling on its surface and the resultant charge is read by a shift register. The shift register scans all cells and outputs the light intensity profile. These detectors are very fast, and can be scanned at 10 - 100 MHz but are not very accurate.

A monolithic diode, or lateral effect diode is a continuous medium sensor so it can theoretically provide infinite resolution. The diode is arranged with a ground contact at its center, and four leads originating at 90° arranged around its circumference (lateral contacts). Position information about a light spot is determined by monitoring the photogenerated currents from each lateral contact.

When a light spot falls on a lateral effect diode, the current generated from each photon must travel to a lead. The resistance along the path to the lead determines the net contribution of each photons' energy to the current at each lateral contact. In this manner, the lateral effect diode acts as a light controlled variable resistor for measuring the position of the light spot on the X and Y axes of the detector. Linearity of the response is thus dependent on the uniformity of the resistance of the diode surface. Since no manufacturing process is perfect, the resistance will not be uniform and linearization of the diodes is mandatory if high accuracy is to be obtained. If lateral contacts A and C lie on the X axis, and pins B and D lie on the Y axis, then the X and Y position are given by:

$$X = \frac{A - C}{A + C} \qquad (4.1),$$

$$Y = \frac{B - D}{B + D} \qquad (4.2).$$

The responsitivity of the diode is the product of the accuracy and the scan frequency required. O'Kelly [4.10] gives the following for determining the responsitivity of the diode ΔR at a signal to noise ratio of one:

$$\Delta R = \frac{\left(4KT/R_s + E_n^2/R_s^2 + 2R_\lambda P_d q \right)^{1/2} \times L}{\sqrt{2}\ P_d R_\lambda} \qquad (4.3).$$

The variables and their values for a 1.25" square diode are given by the manufacturer (United Detector Technology, Hawthorne Ca.):

K = Boltzman's constant = 1.38×10^{-23} joules/K,

T = temperature = 300 K

R_s = Resistance between back contacts = 1000 Ω,

E_n = Amplifier input noise voltage = 10×10^{-9} volts/$\sqrt{\mathrm{Hz}}$,

P_d = monochromatic incident power = .001 watts,

R_λ = detector responsitivity = .25 amp/watt,

q = electron charge = 1.60×10^{-19} coulomb,

L = distance between back contacts = 1.25".

Substituting the above into (4.3), the sensitivity is $\Delta R = 5\times10^{-8}$ in/$\sqrt{\mathrm{Hz}}$. Typical rise time for the diode is given as 5 μsec, so with light spot oscillation period of 400 μsec will give a resolution of 2.5 μin. These values are acceptable for use in the system described in Chapter 3, and detailed requirements are given in Chapter 5.

4.4 Methods of Increasing Sensor Accuracy and Resolution

To overcome the problem of electrical noise inherent in all circuits, averaging techniques are used to increase resolution by the square root of the number of averages taken [4.11]. To allow a large number of data points to be taken, once the rise time of the sensor is reached, readings can be collected at the speed of the analog to digital converter. Note that the conversion in an analog to digital converter is a deterministic event; thus averaging will not increase its accuracy. A 16 bit accuracy analog to digital converter (analog to digital converter76) is available from Burr-Brown of Arizona which has a unit price of $225 (for quantities of 1-25 units) and a conversion time of 17 μsec. Allowing 25 μsec per data point, 400 samples could be taken in 10 msec which would allow a servo update time of 20 msec.

The above will increase the resolution of a sensor, the accuracy can be improved only by comparing the sensors output to that of a standard reference. Laser interferometery provides the best reference, and the technique for deriving a best statistical fit polynomial to describe the sensor output is called linearization [4.12]. As long as the sensor's output is repeatable, the accuracy can be made as good as the statistical curve fitting process used.

4.5 Remarks

A more comprehensive overview of 'robotic' sensors is given in a report by Hall [4.13] which updates Lion's book [4.5]. However it only describes sensing methods in general and does not quote accuracy or resolution limits. Once the specific need for the POSOR sensors is made known, experts in the field will be no doubt find better ways to make the required measurements.

REFERENCES

[4.1] T.G. Giallorenzi et al, 'Optical Fiber Sensor Technology', IEEE Jou. Of Quantum Electronics, Vol. QE-18, No. 4. April 1982 pp 626-665

[4.2] C.D. Kissinger, 'Fiber Optic Proximity Probe', U.S. Patent #3,327,584, Sept. 1967

[4.3] W.E. Frank, 'Detection and Measurement Device having a Small Flexible Fiber Transmission Line', U.S. Patent #3,273,447, Sept. 1966

[4.4] R.O. Cook, C.W. Hamm, 'Fiber Optic Lever Displacement Transducer', Applied Optics, Vol. 18, No. 19, Oct. 1979, pp3230-3241

[4.5] K.S. Lion, Instrumentation in Scientific Research, McGraw-Hill N.Y. 1959, pp62-72

[4.6] Opstelton, Warmoltz, Van Zeltz, 'Device for Measuring Low Pressures', U.S. Patent 3.066,535, Dec. 4, 1962

[4.7] B. Foulon, 'A New Method of Roundness Measurement by Capacitive Detectors', European Space Agency Technical Translation No. 1979-9, Oct. 1980

[4.8] A. Tebo, 'IR Detector Technology Part II: Arrays', Laser Focus/Electro-optics, July 1984 pp 68-82

[4.9] P.W. Fry, 'Silicon Photodiode Arrays', Jou. of Physics E, Vol. 8, No. 5, may 1978 pp337-349

[4.10] B. O'Kelly, 'Lateral-Effect Photodiodes', Laser Focus/Electro-optics March 1976 pp 38-40

[4.11] I.S. Sokolnikoff, R.M. Redheffer, Mathematics of Physics and Modern Engineering, McGraw Hill, Second Edition, pp 642-645

[4.12] J.V. Moskaitis, D.S. Blomquist, 'A Microprocessor Based Technique for Transducer Linearization', Presicion Engineering, Jan. 1983, Vol. 5 No. 1, pp 5-8

[4.13] D.J. Hall Robotic Sensing Devices CMU technical report CMU-RI-TR-84-3

[4.14] Hewlett Packard Corp., 5528A Laser Measurement System User's Guide, 1982.

APPENDIX 4A

Mechanical Motion Measurement by Laser Interferometery

Laser Interferometers can be used to measure virtually any physical event that can cause a phase shift in a laser. This section, however, will only discuss methods used for measuring distance, angles, and straightness. Using three basic optics devices, an interferometer, retroreflector, and a reflector, virtually any motion can be detected. Combinations of these optics are discussed below.

Interferometeric measurement begins with a stable coherent light source (Helium-Neon gas laser) and a cylindrical permanent magnet which causes the laser to oscillate at two slightly different frequencies (Zeeman splitting) which have opposite circular polarizations. The two beams f_1 and f_2 pass through optical glass quarter and half-wave plates which change the circular polarizations of f_1 and f_2 to linear perpendicular polarizations. The beam is then expanded through a collimating telescope and projected through a 45° beam splitter which sends most of the beam out of the laser head to the measurement optics. A portion of the beam is sampled to determine the difference in the frequencies $f_1 - f_2$, and to control the tuning of the laser (maintain output frequency constant).

During measurement, the beam passes through special optics (discussed below) which return a portion of the original output beam

(f_1-f_2) and a Doppler shifted frequency component Δf if a change in the quantity to be measured has occurred. A demodulating polarizer makes their polarizations equal which then allows the Doppler shifted beams to form interference fringes. The returned component $f_1-f_2+\Delta f$ pulses are counted. Counts from the f_1-f_2 sampled beam (taken before beam left the laser head) are also made and subtracted from the Δf count beam to correct for any drift between the two beams' frequencies. The above described process is illustrated in block diagram form in Figure 4A.1.

The optics involved are:

Linear Retroreflector: (Figure 4A.2) an optically ground and polished three surface prism (trihedral prism, often referred to as a corner cube) that reflects an incoming laser back parallel to itself and at a separation distance twice that of the incoming beams' distance from the corner apex.

Linear Interferometer: This optic is shown in Figure 4A.2 with the diagonal line representing a polarized beam splitter which reflects the f_1 component up to a retroreflector back to the beam splitter which sends it back to the laser head's receiving port (because it is still 90° to the direction the beam splitter lets light pass through). The other component f_2 passes through the beam splitter and is reflected back by the retroreflector through the interferometer and into the receiving port for comparison with the f_1 component.

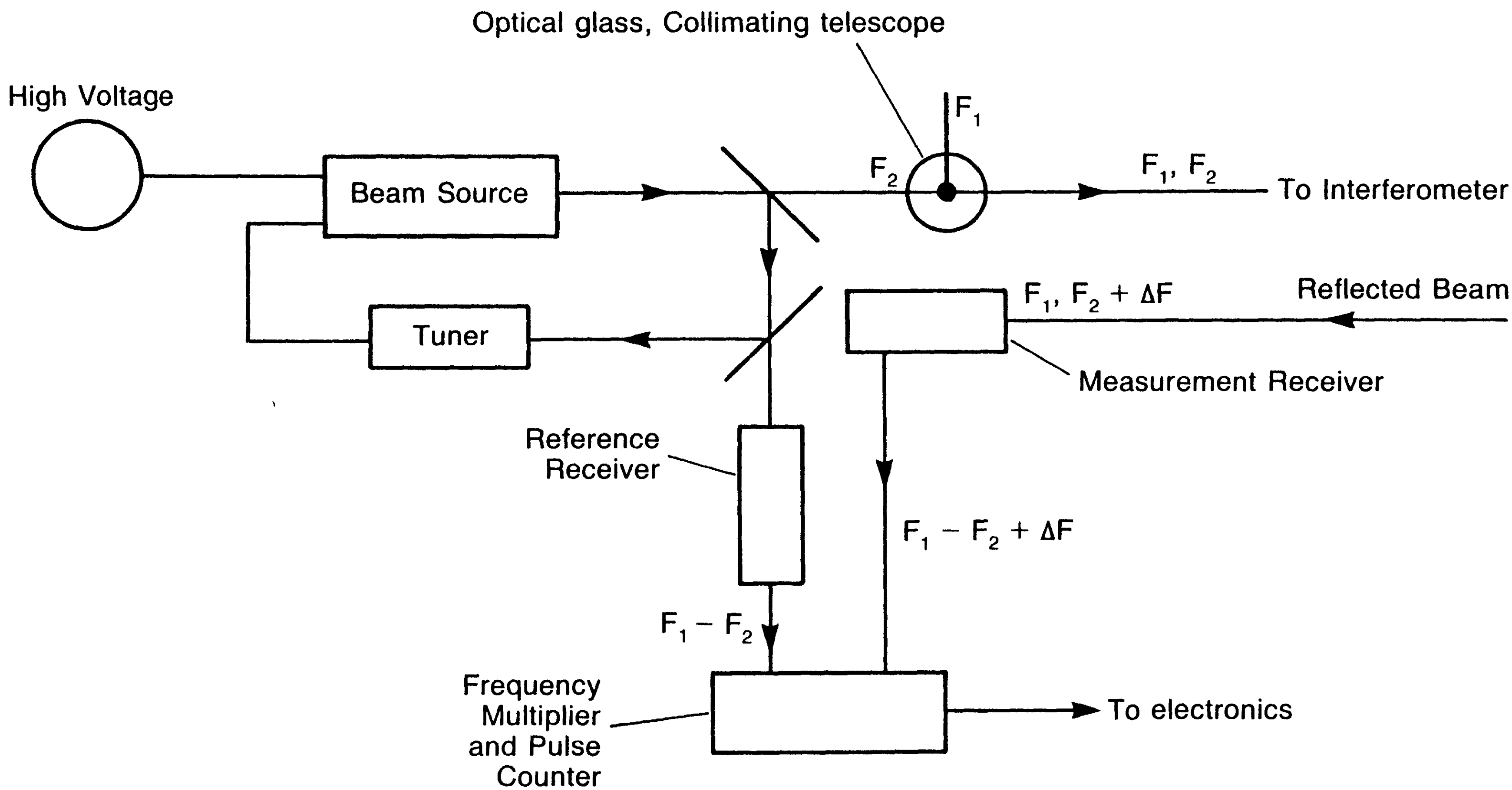

Figure 4A.1 Block diagram of Laser Interferometer's optical system

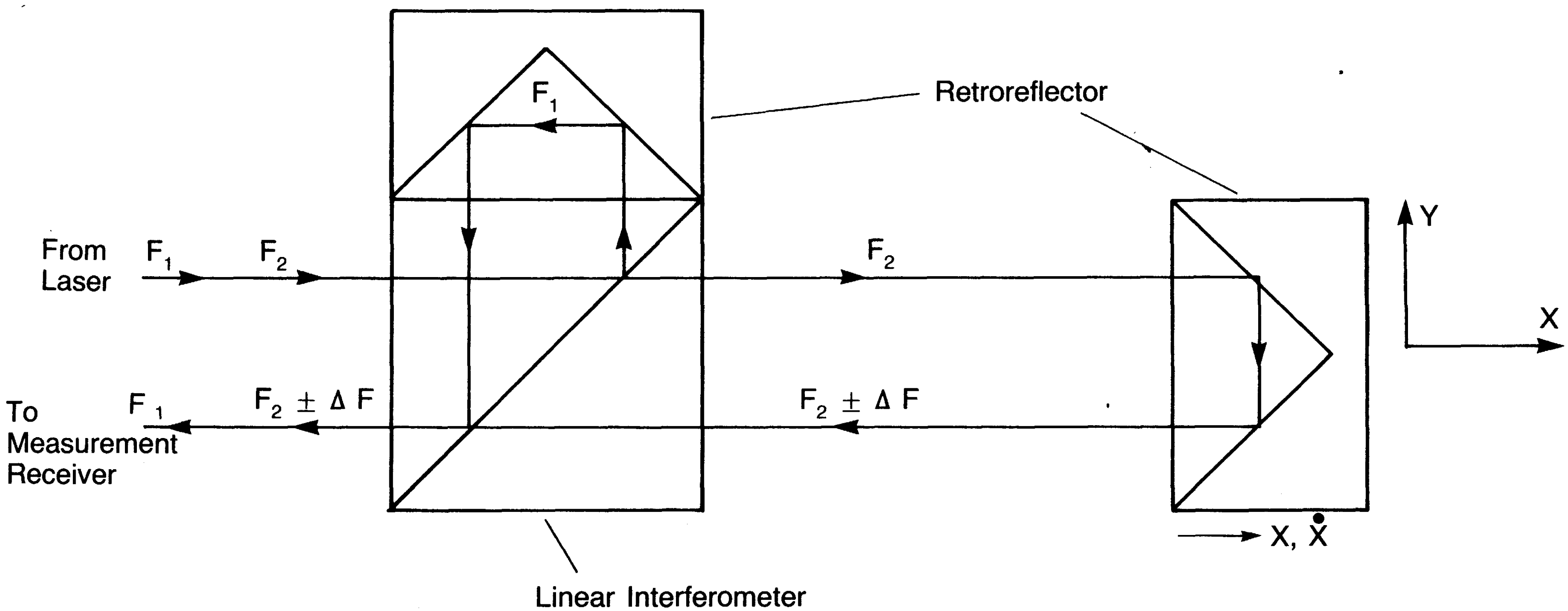

Figure 4A.2 Linear Interferometer and Retroreflector arranged for distance and velocity measurements

Angular Interferometer: This optic is basically a linear interferometer with a beam bender located above it as shown in Figure 4A.3. It is used in angular and flatness measurements.

Angular Reflector: This optic contains two retroreflectors which are spaced at a precisely known distance apart. It is shown in Figure 4A.3.

Straightness Interferometer and Reflector: These optics must be used as a matched pair so the reflector will return the two frequency components directly back to the interferometer (Figure 4A.4). The interferometer contains a Wollaston Prism (it has a different index of refraction for each of the two perpendicular polarity components of the laser beam) which splits the two component beam from the laser head into two components which travel to the reflector along precisely controlled paths. The orientation of the plane of the two exit paths is adjusted by turning the interferometer so vertical and horizontal straightness can be measured. The reflector contains two plane mirrors which reflect the beam components back along their respective paths to the interferometer.

These optics are combined as follows to perform distance and velocity measurements, angular measurements, flatness measurements, and straightness measurements.

Distance Measurement: Figure 4A.2 shows a linear interferometer and a retroreflector used for distance or velocity measurements. Note that the incoming beams can be directed around corners, etc., with appropriate beam bending optics. The interferometer splits the f_1 and f_2

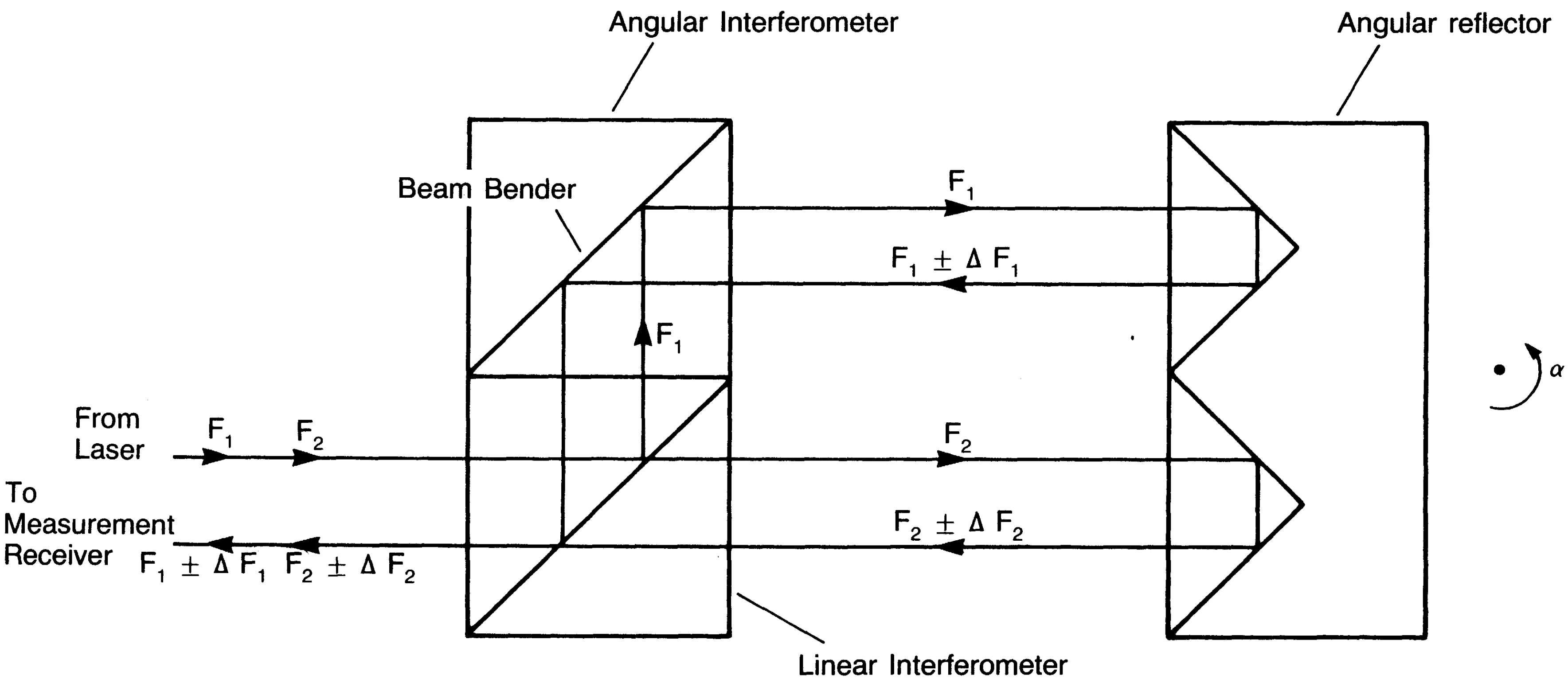

Figure 4A.3 Angular Interferometer and Reflector arranged for angular measurements

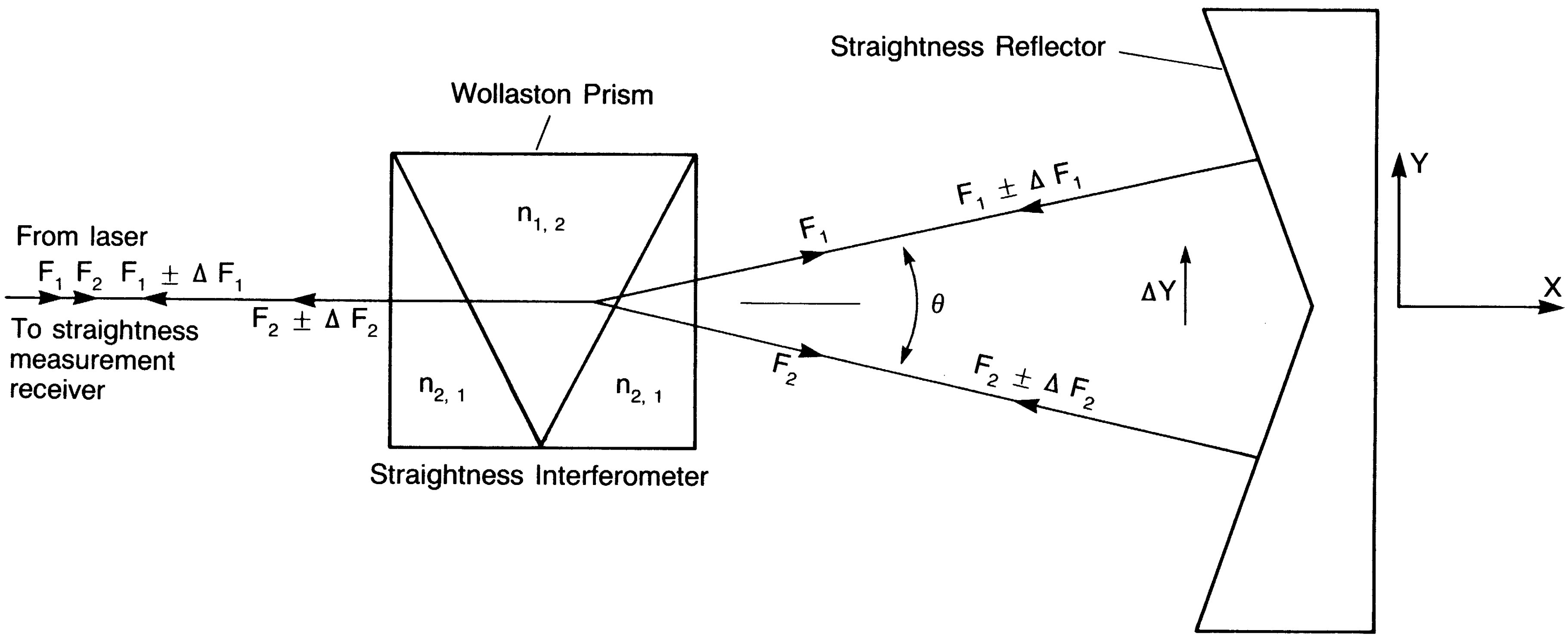

Figure 4A.4 Straightness Interferometer and Reflector arranged for straightness measurements

components, sends the f_2 component to the reflector which returns it to the interferometer with a Doppler shift component Δf_2. Both beams return to the laser head, which operates as described previously. The difference Δf_2 is then related electronically to distance and velocity.

Angular Measurements: Angular measurements are made from a sine measurement, the optics are arranged as shown in Figure 4A.3. These optics create two parallel beam paths between the interferometer and reflector at frequency f_1 and f_2. Precision optics allow the distance between the paths to be precisely known (factory calibration traceable to the National Bureau of Standards). Any rotation of the optics in the plane of the beam paths will cause a Doppler shift. The changes in the lengths of the two beam paths divided by the distance between the paths is the sine of the angle.

Flatness Measurements: Flatness is determined by integrating a series of angular measurements. It requires that the reflector be moved an equal distance each time.

Staightness Measurements. The optics are shown in Figure 4A.4. Initially the two beam paths have the same relative length, but any Y direction motion will cause the path lengths to differ which indicates a ΔY motion of

$$\Delta Y = 2\Delta \ell \sin(\theta/2) \qquad (4A.1).$$

An initial error in alignment will seem to cause a ΔY motion as the optics are moved along the X axis but this is easily subtracted off using a first order curve fit routine. Variations in the optics setup can be used to measure squareness and parallelism.

Environmental error is introduced only into distance and velocity measurements. The errors are: velocity of light compensation, deadpath error, material temperature, and beam misalignment (cosine error).

The velocity of light through air is dependent upon temperature, humidity, and pressure. The absolute accuracy of the measurement will be affected by one part per million for any one of: air temperature change of 1 ^{o}C, air pressure change of .1" (2.5 mm) Hg, or humidity change of 30%.

A deadpath error is a complication of the velocity of light error. It is the error associated with the entire path length that the laser travels through and between the error (the linear scaler multiplier of the V.O.L. term, where the V.O.L. term is analogous to the strain and the total displacement is strain times distance).

If the material temperature changes, then depending on the laser head position and that of the optics, the measured motion will be that of the occurring process plus that due to thermal growth. The required temperature control can be easily calculated for each specific setup using Hooke's Law.

If the axis of the laser is not coincident with the axis of motion, then a cosine error will result. This misalignment is removed during initial setup of the optics by moving the axis back and forth and looking for a change in the return beams path. A variation on the cosine error is called Abbe's offset error which basically says that when making any measurement, the axis of the measuring device should be as coincident as possible with the axis to be measured.

For more detailed discussions and methods for setting up the optics, see the Hewlett Packard Laser Measurement System User's Guide [4.14].

(this page left blank)

Chapter 5

Analysis of Statistical Error in a Six Degree-of-Freedom Measuring Device

5.1 Introduction

This chapter will describe methods for determining the statistical error in a POSOR (six degree-of-freedom POSition-ORientation sensing device as described in Chapter 3) although the methodology can be applied to any system. The first step in determining total system error is to formulate a "Resolution Error Budget", which assumes everything is perfect except for the sensors whose errors are characterized by standard deviations from best fit linearization curves (as discussed in 4.5). The next step is to formulate an "Alignment Error Budget" which assumes that the sensors are perfect, but there are variations in the sensors' assumed position and orientation. Calculations are all based on idealized parameters and deviations from them, and the total system error (the "Total Error Budget") is found from a propagation of errors approach. To illustrate the concepts, they are applied to two specific systems of a POSOR (as described in Chapter 5): the Impedance probe system, and the Light Source-Lateral Effect Diode System.

5.2 Error Analysis of Mechanical Metrology Systems

In performing an error analysis of a mechanical metrology system, it is important to draw an "Error Body Diagram" of the system which shows the geometry of the system and the local sensor coordinate systems about which errors could exist. The next step is to derive the system equations and to study the affect that system parameter perturbations have on system output. The method is analogous to drawing Free Body Diagrams for mechanics problems: Once the system is modeled answers to problems are obtained by systematic straightforward analysis. In the following discussions, all errors are meant to be standard deviations and physical quantities are assumed to be uncoupled so properties of random error analysis apply. Thus errors can be combined by assuming propagation of errors (total deviation is equal to the square root of the sum of the squares of the individual errors) as described by Ku [5.1, 5.2]].

The error analysis is critical to the initial design of a mechanical metrology system because it will tell approximately how accurate the sensors and physical dimensions must be in order to achieve a required accuracy. For the initial design stage, it is reasonable to assume that all the parameters of a certain type have the same deviation so the effect on total system error can be determined. Then a limit to errors of this type can be set. Examples of this methodology will be given below for the light source-lateral effect diode system of a POSOR and for the impedance probe system of a POSOR.

5.2.1 Formulating the Sensor Resolution Error Budget

For this discussion it is assumed that all high resolution sensors are based on linear measurements (encoder to shaft misalignments, etc., prevent use of rotation sensors as shown in Chapter 1). The first step in forming the sensor resolution error budget is to draw the "Error Body Diagram" for the case of "everything perfect except sensor accuracy" as shown in Figure 5.1. In defining the coordinate system of the sensor (see Figure 5.1) it will also be assumed that the Z axes are colinear with the axes of the sensors. For linear measurements of changes in the distance between the sensor and the target the measurement will be as accurate as the sensor. On the other hand, angular measurements are always made using two sensors spaced a known distance (a+b) apart, so the error in the angle σ_α due to variations in sensor readings σ_{ℓ_2} and σ_{ℓ_3} is:

$$\sigma_\alpha = \frac{\left(\sigma_{\ell_2}^2 + \sigma_{\ell_3}^2 \right)^{1/2}}{a + b} \qquad (5.1)$$

For a multi-sensor system, each degree-of-freedom must have its error due to sensor resolution determined. For an articulated structure that uses POSORs, the effect of sensor resolution at each joint should be represented by the translational and orientation error that it will produce at the structure's endpoint. The net effect of all errors is then determined by propagation of errors.

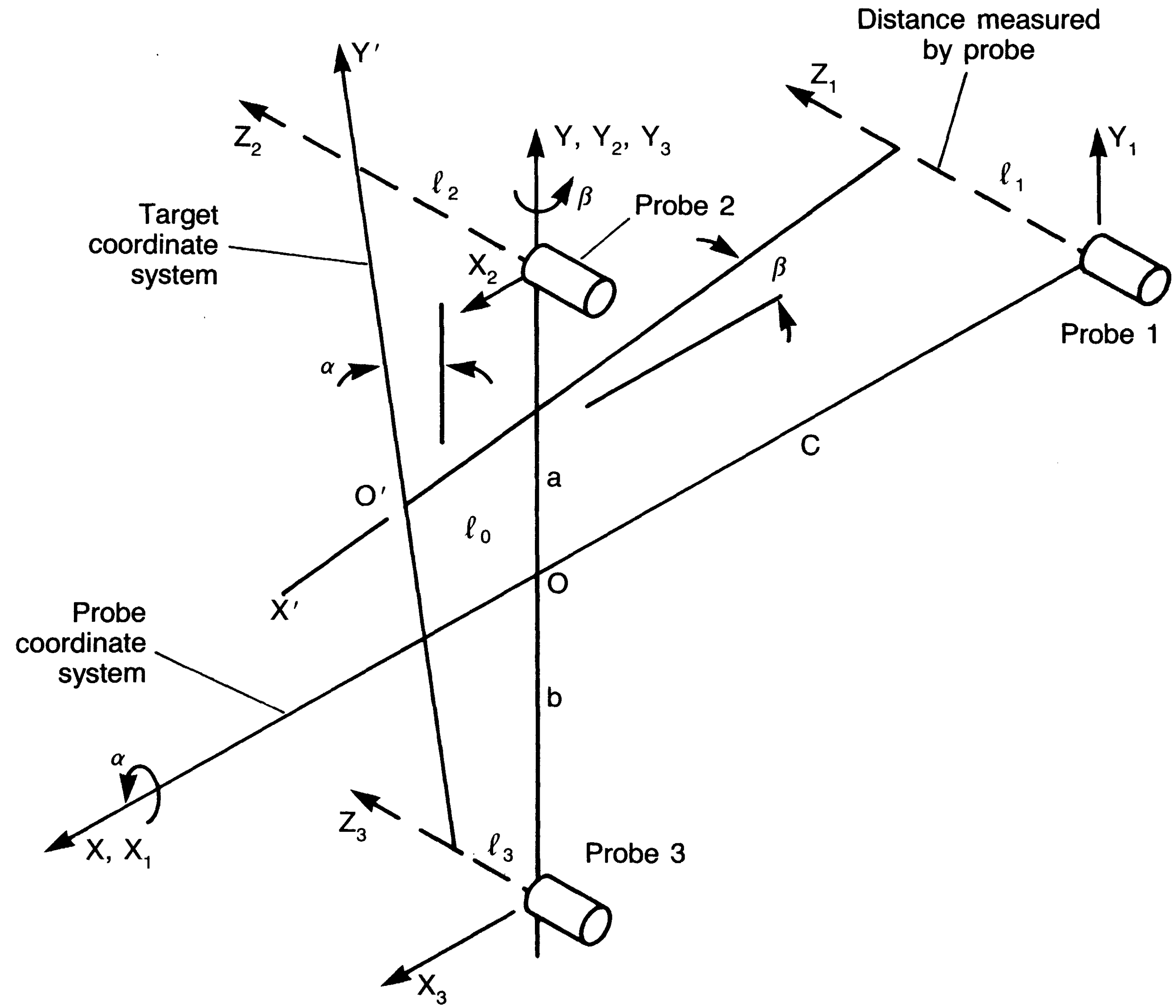

Figure 5.1 Sensor resolution error body diagram for triad of distance measuring sensors

5.2.2 Formulating the Sensor Alignment Error Budget

Formulating the Sensor Alignment Error Budget requires the careful drawing of an Error Body Diagram. Some effects such as the surface inclination to the sensor require experimental verification to show that, for example, the target motion is equal to the motion along the sensor axis [5.3] (even though the sensors' electromagnetic field fans out). The effect of sensor alignment errors on the system are determined by introducing variations one at a time into all six degrees of freedom that characterize the sensors position and orientation.

In the most general sense, assume that a degree-of-freedom ξ is determined by a function that relates the system geometry and the sensor output. A deviation σ_ζ in each degree-of-freedom ζ that describes the sensors location must be introduced to determine the error σ_ξ it produces in the desired measurement:

$$\sigma_\xi = f(\zeta) - f(\zeta + \sigma_\zeta) \qquad (5.2).$$

For consistency, it is best first to determine the effects of linear perturbations in the X, Y, and Z coordinate locations of the sensors, followed by angular perturbations α_X, α_Y, and α_Z of the sensors orientations about the X, Y, and Z axes respectively.

To illustrate these concepts, the impedance probe system and the light source-lateral effect diode system of a POSOR are studied in detail below.

5.3 Analysis of Impedance Probe System

5.3.1 Impedance Probe System Sensor Resolution Error Budget

The impedance probe system is used in a POSOR for determining two small angular and one small translational degree-of-freedom and is shown schematically in Figure 5.1. For illustrative purposes, the dimensions a, b, and c will be assumed to be equal to 1.5", 1.5", and 3" (38, and 76 mm) respectively (the spacing for the Impedance Probe System to be used in the experimental POSOR described in Chapters 3 and 6). The general system equations describing the degrees of freedom ℓ_{XY} (Z motion), α, and β assume that the angles are not Euler angles, but are rotations of the target plane (X'Y' plane) about the X and Y axes respectively in the sensor coordinate plane:

$$\ell_{XY} = \ell_3 + (b + Y)\sin\alpha - X\sin\beta \qquad (5.3),$$

$$\alpha = \tan^{-1}\left(\frac{\ell_2 - \ell_3}{a + b}\right) \qquad (5.4),$$

$$\beta = \tan^{-1}\left(\frac{\ell_1 - (\ell_2 b + \ell_3 a)/(a + b)}{c}\right) \qquad (5.5).$$

All error calculations are based on very small perturbations, so small angle assumptions are valid (i.e. $\tan^{-1} f(\xi) = f(\xi)$). When applied to (5.4) and (5.5) and substituted into (5.3):

$$\ell_{XY} = \frac{-X\ell_1}{c} + \frac{\ell_2}{a+b}\left(b + Y + \frac{Xb}{c}\right) + \ell_3\left(1 - \frac{b + Y - Xa/c}{a+b}\right) \quad (5.6).$$

To determine the possible error in the calculation of the distance between planes at any point, $\sigma_{\ell XY\ell i}$, due to an error $\sigma_{\ell i}$ in probe #i's reading, ℓ_i and $\sigma_{\ell i}$ are inserted into (5.2) with $f(\xi)$ given by (5.6):

$$\sigma_{\ell XY\ell_1} = -\sigma_{\ell_1} X/c \quad (5.7),$$

$$\sigma_{\ell XY\ell_2} = \frac{b + Y + Xb/c}{a+b}\,\sigma_{\ell_2} \quad (5.8),$$

$$\sigma_{\ell XY\ell_3} = \left(1 - \frac{b + Y - Xa/c}{a+b}\right)\sigma_{\ell_3} \quad (5.9).$$

With the assumption that all $\sigma_{\ell i}$ are equal, the total error $\sigma_{\ell XY\ell}$ is the square root of the sum of the individual errors squared (propagation of errors [5.1]):

$$\sigma_{\ell XY\ell} = \sigma_\ell\left(\frac{X^2}{c^2} + \frac{(b+Y+Xb/c)^2}{(a+b)^2} + \left[1 - \frac{(b+Y-Xa/c)}{(a+b)}\right]^2\right)^{1/2} \quad (5.10).$$

Substituting the given values for a, b, and c with X = Y = 0, $\sigma_{\ell XY\ell} = .71\sigma_\ell$. If X = -1" (25mm), and Y = 1.5" (38mm) (to be the location of the center of the lateral effect diodes), then $\sigma_{\ell XY\ell} = .78\sigma_\ell$. Note that if all the errors where assumed to be equal and to occur simultaneously, then $\sigma_{\ell XY\ell} = \sigma_\ell$. Thus the propagation of errors is saying that all the errors are not likely to occur at once and thus the expected error within the region of the probes is less than for any one probe as the distance from a probe is increased. Note that if the individual probe coordinates are substituted into (5.7) then $\sigma_{\ell XY\ell} = \sigma_\ell$ always.

The angular error $\sigma_{\alpha\ell i}$ due to an error in the probe reading $\sigma_{\ell i}$ is determined by applying the principle of (5.2) to the linearized Equation 5.4 with the following results:

$$\sigma_{\alpha\ell_2} = \frac{\sigma_{\ell_2}}{a + b} \qquad (5.11),$$

$$\sigma_{\alpha\ell_3} = \frac{-\sigma_{\ell_3}}{a + b} \qquad (5.12).$$

The net error $\sigma_{\alpha\ell}$ assuming that all the probe errors σ_ℓ are equal is found by the propagation of errors to be:

$$\sigma_{\alpha\ell} = \frac{\sigma_\ell\sqrt{2}}{a + b} \qquad (5.13).$$

With the given values of "a" and "b", the net error is $.47\sigma_\ell$/in ($.0186\sigma_\ell$/mm).

Similarly, the angular error σ_β is determined by applying the principle of (5.2) to the linearized Equation 5.5 with the following results:

$$\sigma_{\beta\ell_1} = \frac{\sigma_{\ell_1}}{c} \qquad (5.14),$$

$$\sigma_{\beta\ell_2} = \frac{-\sigma_{\ell_2} b}{c(a + b)} \qquad (5.15),$$

$$\sigma_{\beta\ell_3} = \frac{-\sigma_{\ell_3} a}{c(a + b)} \qquad (5.16).$$

The net error $\sigma_{\beta\ell}$ assuming that all the probe errors σ_ℓ are equal is found by the propagation of errors to be:

$$\sigma_\beta = \frac{\sigma_\ell}{c(a + b)} \left(2(a^2 + ab + b^2) \right)^{1/2} \qquad (5.17).$$

With the given values of "a" and "b", the net error is $\sigma_\beta = .82\sigma_\ell$/in (.0321 σ_ℓ/mm).

The next step in determining the total system error is to determine the effect of errors in the known positions and orientations of the sensors on the system error. Then the total error budget can be found.

5.3.2 Impedance Probe System Sensor Alignment Error Budget

This section will formulate the impedance probe sensor alignment error budget by determining the effect of an error in each sensor's position and orientation coordinate on the linear and angular error of the impedance probe system. The best method for doing this is to determine the effects of varying the characteristic physical quantities a, b, c, ℓ_1, ℓ_2, and ℓ_3 (shown in Figure 5.1) in the describing equations 5.4, 5.5, and 5.6. Then a table is made which lists all the variations in the sensor coordinates (6 degrees of freedom) and how they affect the characteristic physical quantities. By this method, much repetition of algebraic manipulation is avoided. The effects of errors in the sensor readings ℓ_i were found above, so only the effects of variations in distance between the sensors needs to be determined.

The linear distance between the two plates of the POSOR at any point X, Y is determined by the sensor measurements and the spacing between the sensors as given by (5.6). Inserting "a" and σ_a into (5.2) with $f(\xi)$ given by (5.6) gives the following expression for the error $\sigma_{\ell XY}$ in the calculated distance ℓ_{XY} between the plates at any XY coordinate:

$$\sigma_{\ell XYa} = \frac{\sigma_a(b + Y + Xb/c)(\ell_2 - \ell_3)}{(a + b)(a + b + \sigma_a)} \qquad (5.18).$$

Similarly, an error σ_b causes an error $\sigma_{\ell XYb}$ of:

$$\sigma_{\ell XYb} = \frac{\sigma_b(Y - a - Xa/c)(\ell_2 - \ell_3)}{(a + b)(a + b + \sigma_b)} \qquad (5.19),$$

and an error σ_c causes an error $\sigma_{\ell XYc}$ of:

$$\sigma_{\ell XYc} = \frac{X\sigma_c}{c(c + \sigma_c)} \left(\ell_1 - \frac{\ell_2 b + \ell_3 a}{a + b} \right) \qquad (5.20).$$

When evaluating the order of magnitude values given by Equations 5.18, 5.19, and 5.20, the sigma in the denominator is considered small with respect to a, b, and c and the sensor reading differences are assumed to be maximum (on the order of .05" (1.27 mm) for most types of POSORs). With the previous values of a, b, and c, at the origin (X, Y = 0) the errors are: $\sigma_{\ell XYa} = .0083\sigma_a$, $\sigma_{\ell XYb} = -.0083\sigma_b$, and $\sigma_{\ell XYc} = 0.0$. At the coordinates of the center of a lateral effect diode (X = -1", Y = 1.5" (-25, and 38mm) the errors are: $\sigma_{\ell XYa} = .0139\sigma_a$, $\sigma_{\ell XYb} = 0.0$, and $\sigma_{\ell XYc} = .0028\sigma_c$. From these results, the largest error even at a large error in position of .001" (.0254mm) results in an error of only 14 μin (.35 μm).

The last step is to determine the effect on the calculation of the angles α and β from variations in the sensor spacing σ_a, σ_b, and σ_c. Proceeding as before with Equation 5.2 using (5.4) and then (5.5) for f(ξ), the following relations are found (assumes a >> σ_a and b >> σ_b):

$$\sigma_{\alpha a} \approx \frac{(\ell_2 - \ell_3)\sigma_a}{(a + b)^2} \tag{5.21}$$,

$$\sigma_{\alpha b} \approx \frac{(\ell_2 - \ell_3)\sigma_b}{(a + b)^2} \tag{5.22}$$,

$$\sigma_{\beta a} \approx \frac{(\ell_3 - \ell_2)b\sigma_a}{c(a + b)^2} \tag{5.23}$$,

$$\sigma_{\beta b} \approx \frac{(\ell_2 - \ell_3)a\sigma_b}{c(a + b)^2} \tag{5.24}$$,

$$\sigma_{\beta c} \approx \left(\frac{\ell_1 - (\ell_2 b + \ell_3 a)/(a + b)}{c^2}\right)\sigma_c \qquad (5.25).$$

With the above basic equations, the effect of any system perturbation on the calculated physical quantities ℓ_{XY}, α, and β can be determined. For linear motion perturbations, Figure 5.2 shows the correlation between sensor XY position errors and errors in the relative distances between the sensors a, b, and c. Table 5.1 lists various errors in sensor position and the equivalent σ_a, σ_b, and/or σ_c error which is to be used in equations 5.18, 5.19, or 5.20 respectively. Note that the Z position of a sensor is not critical, since the sensors would have to be calibrated once they are fixed in place (see Chapter 7 for experimental procedure) and any "error" would be accounted for in the sensor linearization curve (see Chapter 4).

For angular perturbations (sensor orientation errors), Figure 5.3 shows the general situation for a sensor that has errors in orthogonality to the XY plane it is mounted in of $\sigma_{\varepsilon Xi}$ and $\sigma_{\varepsilon Yi}$ about the X_i and Y_i axes respectively (subscript i refers to sensor number). Since the target planes' rotation is defined by rotations α and β about the X and Y axes respectively, the equivalent errors in the distance measurement ℓ_i caused by errors $\sigma_{\varepsilon Xi}$ and $\sigma_{\varepsilon Yi}$ are found from the law of sines and small angle approximations to be:

$$\sigma_{\ell i} = \frac{\ell_i \sigma_{\varepsilon Xi}(\sigma_{\varepsilon Xi} - 2\alpha)}{2} \qquad (5.26),$$

$$\sigma_{\ell i} = \frac{\ell_i \sigma_{\varepsilon Yi}(\sigma_{\varepsilon Yi} - 2\beta)}{2} \qquad (5.27).$$

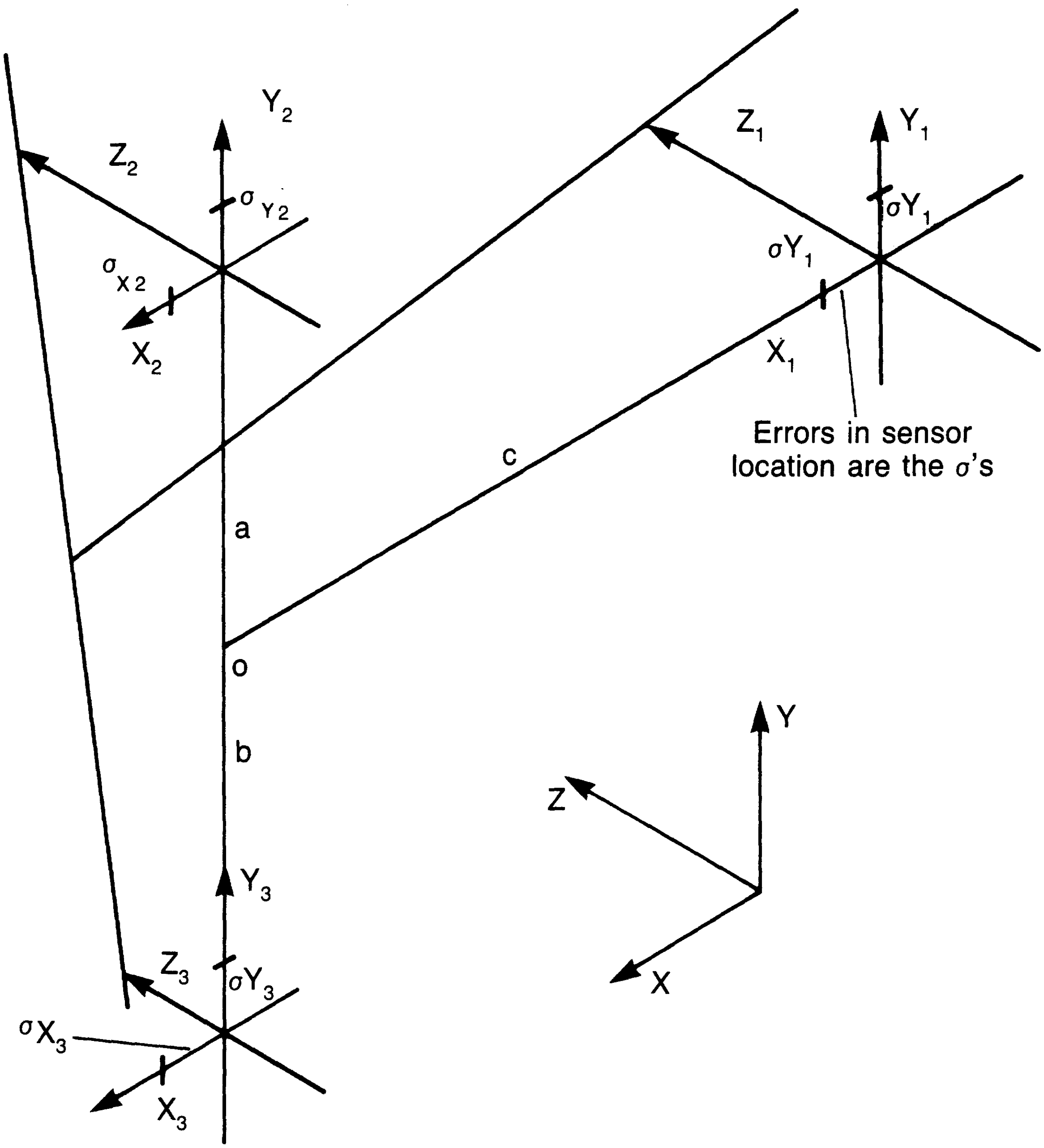

Figure 5.2 Correlation between sensor XY position errors and errors in a, b, and c

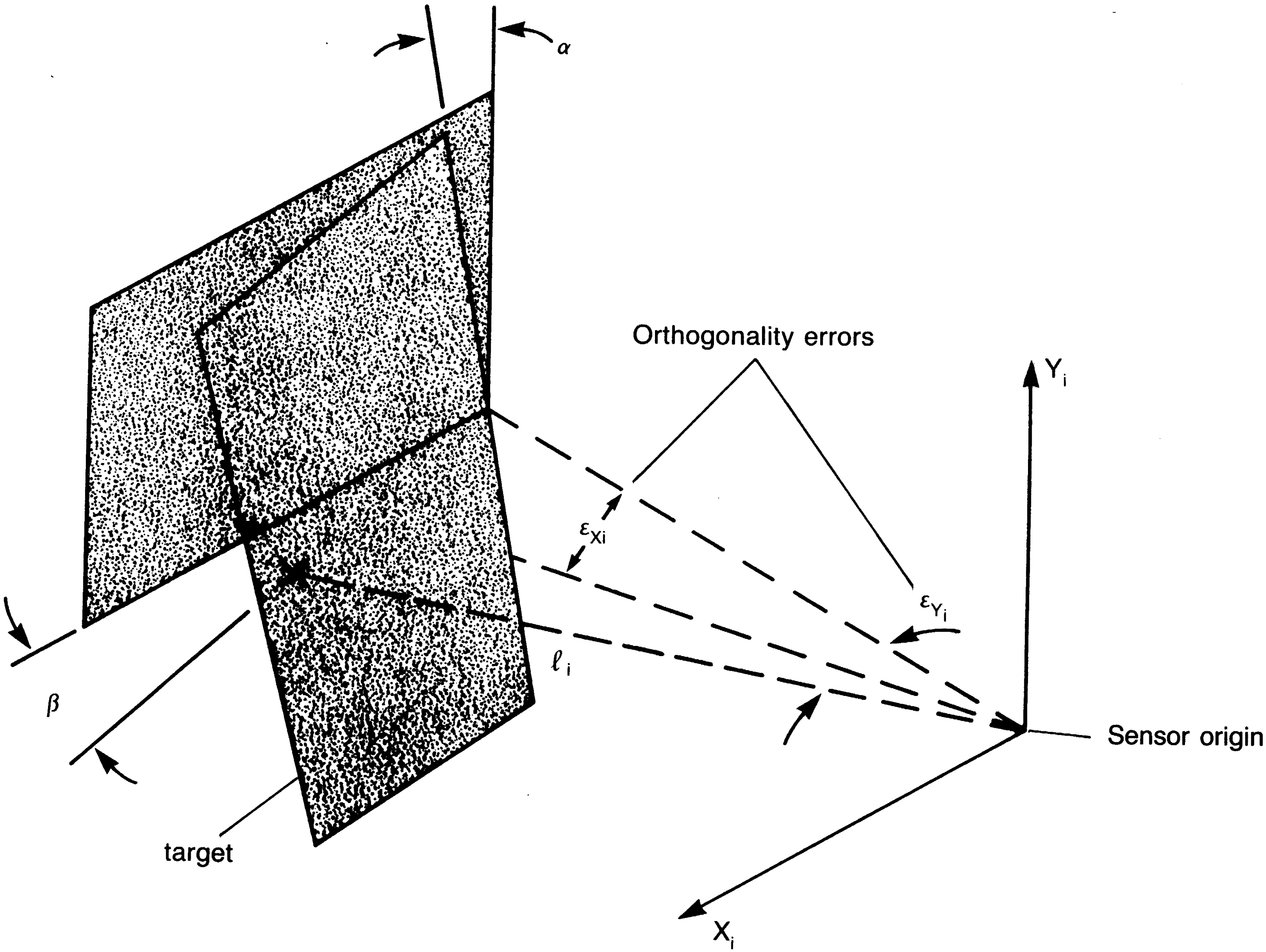

Figure 5.3 Effect of error in sensor orthogonality to mounting surface on measured distance between sensor and target

Table 5.1 Correlation Between Impedance Probe XY Position Errors and Errors in Probe Spacing a, b, and c

Sensor Position Error	Equivalent σ_a	Equivalent σ_b	Equivalent σ_c
σ_{X_1}	0.	0.	$-\sigma_{X_1}$
σ_{Y_1}	$-\sigma_{Y_1}$	σ_{Y_1}	0.
σ_{X_2}	$\approx 0.$	$\approx 0.$	$\approx \frac{\sigma_{X_2} b}{a + b}$
σ_{Y_2}	σ_{Y_2}	0.	0.
σ_{X_3}	$\approx 0.$	$\approx 0.$	$\approx \frac{\sigma_{X_3} a}{a + b}$
σ_{Y_3}	0.	$-\sigma_{Y_3}$	0.

These values are used on Equations 5.11, 5.12, 5.14, 5.15, and 5.16 to determine the error that they cause in the calculation of the angles α and β.

5.3.3 Formulating the Impedance Probe System Total Error Budget

This section will summarize the effects of system errors on the calculated values of the desired quantities ℓ_{XY}, α and β. Following each type of error equation found above were characteristic values for the errors assuming given values of the sensor spacing a, b, and c and "worst case conditions". Using these values and those found in Table 5.1, the total error budget for the impedance probe system of the test POSOR (described in Chapters 3 and 7) is presented in Table 5.2. Because no obvious problems occur (such as trying to measure an angle from a long leg rather than from the short leg of a triangle), substitution of representative values for the sigmas is not done until Chapter 7 where experimental data is obtained.

5.4 Analysis of Light-Source-Lateral Effect Diode System

5.4.1 Light Source-Lateral Effect Diode Sensor Resolution Error Budget

This section will apply the error budget principles of section 5.2 to arrive at the sensor resolution error budget for the Light Source - lateral effect diode sensor system used in a POSOR to determine one large rotational and two small translational degrees of freedom. As was done for the impedance probe system, the first step is do write the

Table 5.2 Total Error Budget for Impedance Probe System for Test POSOR

Perturbation Error	Induced Error ($\sigma_{\ell 0,0}$)	Induced Error ($\sigma_{\ell -1,1.5}$)	Induced Error (σ_{α}-in)	Induced Error (σ_{β}-in)
σ_{ℓ}	$.71\sigma_{\ell}$	$.78\sigma_{\ell}$	$.47\sigma_{\ell}$	$.82\sigma_{\ell}$
σ_{a}	$.0083\sigma_{a}$	$.0139\sigma_{a}$	$.0056\sigma_{a}$	$.0028\sigma_{a}$
σ_{b}	$-.0083\sigma_{b}$	0.	$.0056\sigma_{b}$	$.0028\sigma_{b}$
σ_{c}	0.	$.0028\sigma_{c}$	0.	$.0056\sigma_{b}$
$\sigma_{\varepsilon X}$	$.0178\sigma^2_{\varepsilon X}$	$.0195\sigma^2_{\varepsilon X}$	$.0118\sigma^2_{\varepsilon X}$	$.0103\sigma^2_{\varepsilon X}$
$\sigma_{\varepsilon Y}$	$.0178\sigma^2_{\varepsilon Y}$	$.0195\sigma^2_{\varepsilon Y}$	$.0118\sigma^2_{\varepsilon Y}$	$.0103\sigma^2_{\varepsilon Y}$

system characteristic equations which relate the desired quantities to the physical constants and measured variables of the system.

Figure 5.4 shows the idealized system with the lateral effect diodes located at X, Y coordinates h_i, g_i in the impedance probe coordinate system XYZ, and the light sources located at X', Y', coordinates $h_{\ell i}$, $g_{\ell i}$ in the light source coordinate system X'Y'Z' (the lateral effect diodes' coordinate systems are oriented 180° to the XY coordinate system only so as to match the experimental setup). As derived in section 5.3, the X'Y'Z' coordinate system is tilted by the non-Euler angles α and β. The rotation angle Θ of the X'Y'Z' coordinate system is defined about the Z' axis. This allows Θ to rotate without changing α or β and vice versa. The desired quantities are the projected XY coordinates (along a line parallel to the Z axis) of the X'Y'Z' origin, and the angle Θ.

In determining the system characteristic equations, the first step is to determine the projected coordinates of the light source onto the lateral effect diode (hereafter referred to as "diode"). Since the angles α and β are independent, then the offsets associated with the light beam being tilted by α and β will also be independent. The distance $\ell_{XY\ell i}$ from the light spot to the light source plane is found by substituting the light spot coordinates X_{di} and Y_{di} into (5.6). From Figure 5.5, the projected coordinates are found to be:

$$X_{\ell pi} = h_i - X_{di} + \ell_{XY\ell i}\cos\alpha \, \frac{\sin 2\beta}{2} \qquad (5.28),$$

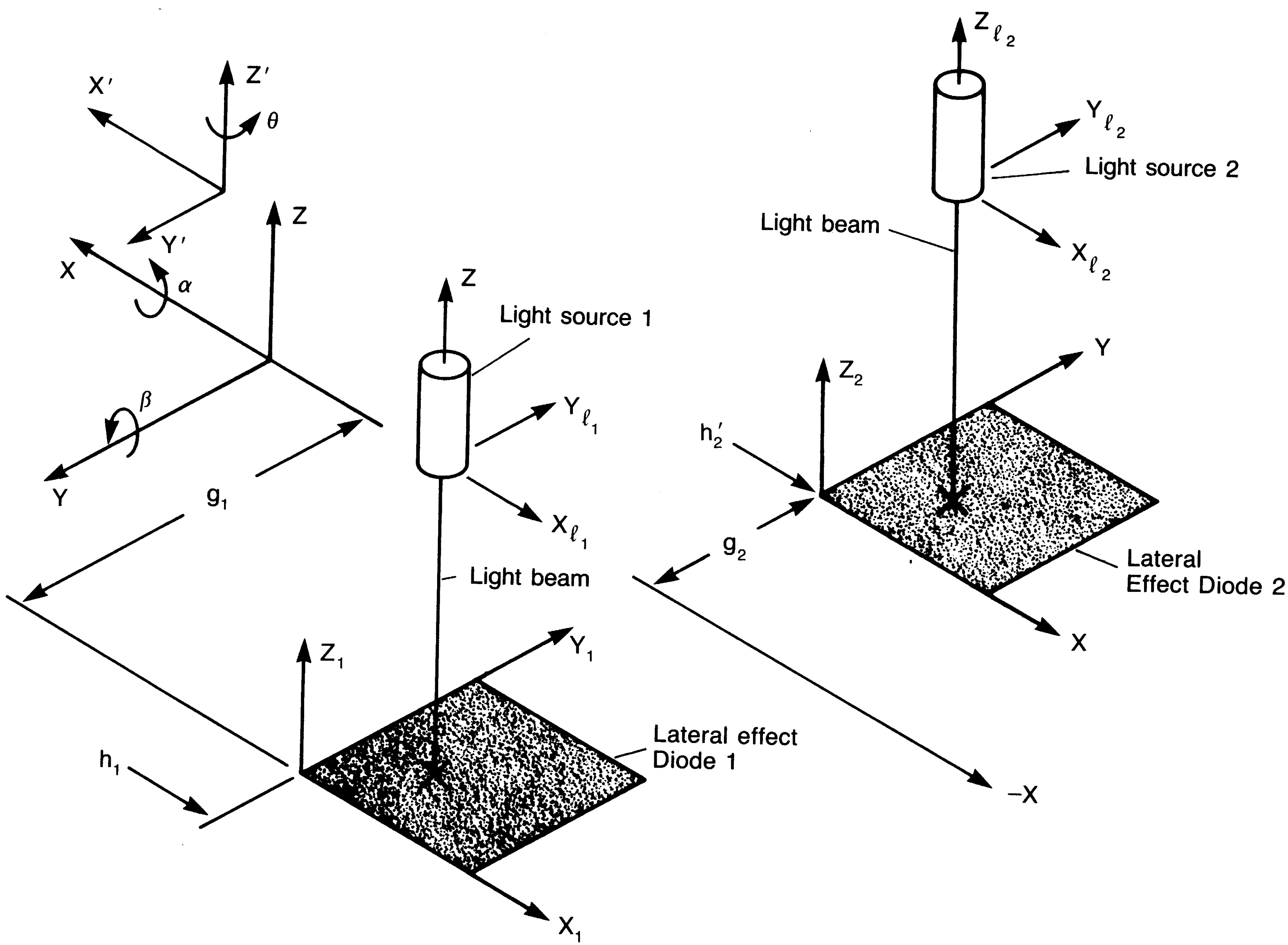

Figure 5.4 Sensor resolution error body diagram for light source lateral effect diode system

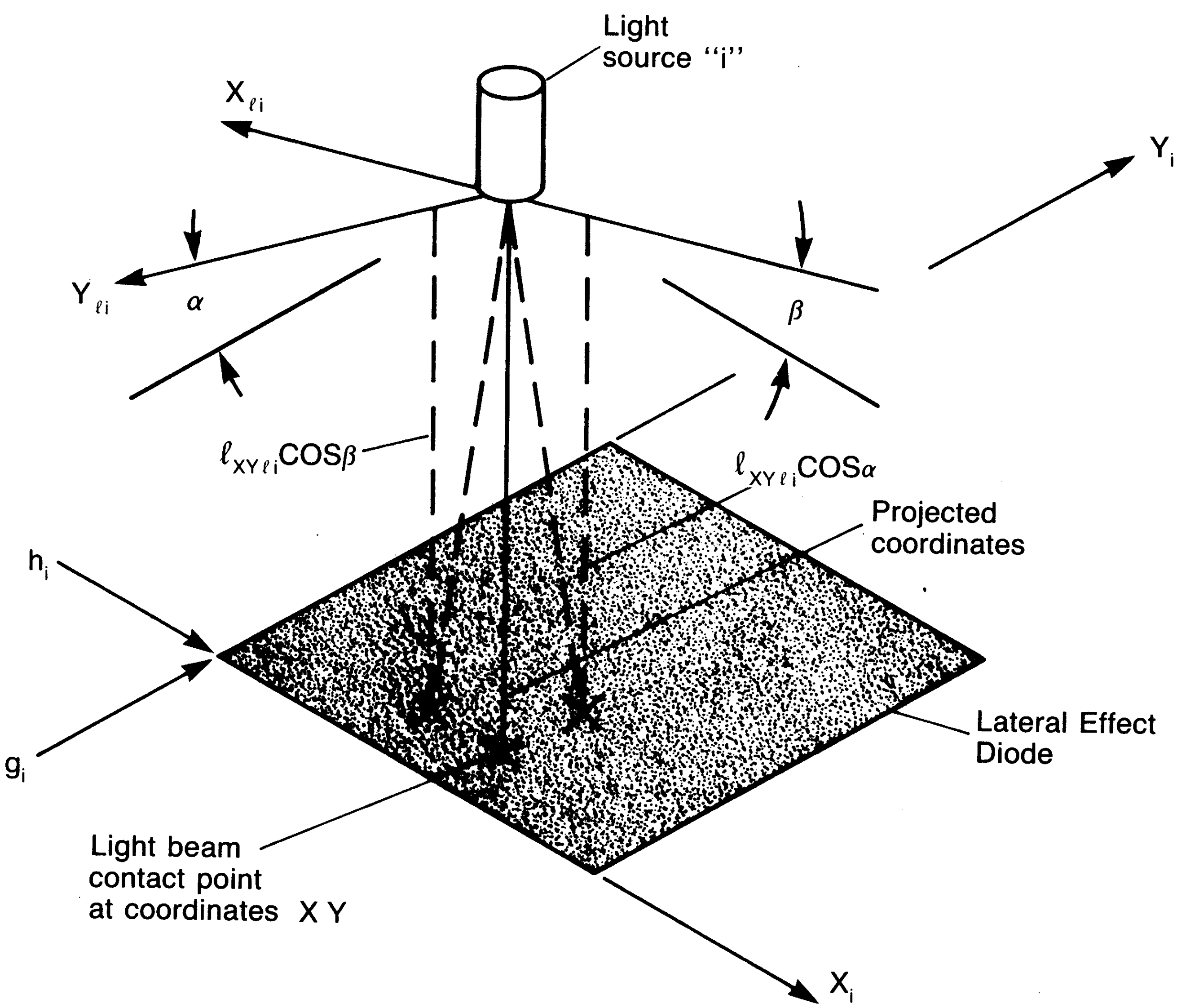

Figure 5.5 **Geometry to determine projected coordinates of light source in XYZ coordinate system**

$$Y_{\ell pi} = g_i - Y_{di} - \ell_{XY\ell i}\cos\beta\,\frac{\sin 2\alpha}{2} \qquad (5.29).$$

To determine the projected coordinates X_0 Y_0 of the X'Y'Z' origin, the projected distances of the light sources coordinates must be subtracted from (5.28) and (5.29):

$$X_0 = h_i - X_{di} + \ell_{XY\ell i}\cos\alpha\,\frac{\sin 2\beta}{2} - h_{\ell i}\cos\beta \qquad (5.30),$$

$$Y_0 = g_i - Y_{di} - \ell_{XY\ell i}\cos\beta\,\frac{\sin 2\alpha}{2} - g_{\ell i}\cos\alpha \qquad (5.31).$$

The angle Θ of rotation of the X'Y'Z' coordinate system about its Z' axis is found from the weighted difference of the Y_{di} and X_{di} coordinates of the light spots. The weighting (by $\cos\alpha$ and $\cos\beta$ respectively) is necessary to prevent a rotation α (or β) from changing one leg of the slope triangle. The angle Θ is thus:

$$\Theta = \tan^{-1}\left(\frac{(-Y_{d_1} + g_1 + Y_{d_2} - g_2)\cos\alpha}{(-X_{d_1} + h_1 + X_{d_2} - h_2)\cos\beta}\right) \qquad (5.32).$$

To prevent numerical errors in the calculation of Θ, it might be useful to use the arc-sine function when near a multiple of $\pi/2$.

The error in the X'Y'Z' origin location (ignoring second order effects from calculation of $\ell_{XY\ell}$) is directly proportional to the errors in the diode and light source location coordinates, the diode accuracy, and to a lesser extent the angles α and β, as can be seen from Equations 5.30, and 5.31. Errors in the calculation of α and β will have to be small (on the order of micro radians) for the impedance probe system to be satisfactory, so the effects of σ_a and σ_b can be ignored here.

In order to find the error in the rotation angle Θ, it would be desirable to linearize (5.32) based on: (assumes that Θ is less than about 10°):

$$\tan^{-1}(f(\zeta)) - \tan^{-1}(f(\zeta + \partial\zeta)) = (f(\zeta)) - (f(\zeta + \partial\zeta)) \quad (5.33).$$

However, as shown in Figure 5.4, the angle is nearer 90°. In order to allow the use of the same notation, we will look at the arc-cotangent which has a linearization form similar to (5.33) except that it is valid near $\Theta = 90°$. Also, since errors in α and β will be on the order of microradians, the cosines of these errors will be negligible, even when amplified by the length of a robot arm. Thus errors in Θ can be calculated using Equation 5.2 with $f(\zeta)$ given by:

$$f(\zeta) = \frac{- X_{d_1} + h_1 + X_{d_2} - h_2}{- Y_{d_1} + g_1 + Y_{d_2} - g_2} \quad (5.34).$$

This assumption will in effect cause a phase shift of 90°, so the σ_X is really the σ_Y and vice versa.

To determine the effect of errors σ_X and σ_Y on the X_0, Y_0 and Θ quantities, Equation 5.2 is used with $f(\xi)$ given by Equations 5.30, 5.31, and 5.34:

$$\sigma_{XO} = \sigma_X \tag{5.35}$$

$$\sigma_{YO} = \sigma_Y \tag{5.36}$$

$$\sigma_{\Theta X} \approx \frac{- X_{d_1} + h_1 + X_{d_2} - h_2}{[- Y_{d_1} + g_1 + Y_{d_2} - g_2]^2} \sigma_X \tag{5.37}$$

$$\sigma_{\Theta Y} = \frac{\sigma_Y}{- Y_{d_1} + g_1 + Y_{d_2} - g_2} \tag{5.38}$$

For illustrative purposes, assume that the diode readings are: $X_{d_1} = 0$, $Y_{d_1} = 0$, $X_{d_2} = .5"$ (12.7 mm), and $Y_{d_2} = 0$. Also assume that the origin coordinates are: $h_1 = h_2 = -1"$ (25.4 mm), $g_1 = 1.5"$ (38.1 mm), and $g_2 = -1.5"$. Thus typical system angular errors are $\sigma_{\Theta X} = .0555\sigma_X$ and $\sigma_{\Theta Y} = .333\sigma_Y$. The basic effect is that the distance between the light spots (ΔX) is like a cosine error and is negligible compared to the side to side motion (ΔY) which causes a direct effect. The next section will investigate the effects of position and orientation errors in the light source and diode locations.

5.4.2 Light Source-Lateral Effect Diode Sensor Alignment Error Budget

The effect of X or Y position errors in the light source and diode locations can be obtained from Equations 5.20 and 5.21 respectively. The effect of Z position errors will not affect relative accuracy. The orientation errors are:

1) Parallelism error between diode axes $\sigma_{Z\Theta}$,

2) Non-orthogonality of axes $\sigma_{Zi\gamma}$

3) Relative flatness of diodes $\sigma_{Xi\alpha}$ and $\sigma_{Yi\beta}$

4) Light source orientation errors $\sigma_{X\ell i\alpha}$ and $\sigma_{Y\ell i\beta}$.

An angular error peculiar to the linearization process is the deviation in orthogonality $\sigma_{Zi\gamma}$ of the sensor axes relative to each other. For this system, orientation errors will be converted into equivalent translational errors (as was done for the impedance probes). These equivalent translational errors for orientation errors in the light source and diode locations are obtained from the geometry shown in Figure 5.5 and are listed in Table 5.3.

5.4.3 Formulating the Light Source-Lateral Effect Diode Total Error Budget

This section will summarize the effects of system errors on the calculated values of the desired quantities X_0, Y_0, and Θ. Following each type of error equation found above were characteristic values for the errors assuming given values of the diode and light source spacing and "worst case conditions". Using these values and those found in Table 5.3, the total error budget for the light source-lateral effect diode system of the test POSOR (described in Chapters 3 and 7) is presented in Table 5.4. Because no obvious problems occur (such as trying to measure an angle from a long leg rather than from the short leg of a triangle), substitution of representative values for the sigmas is not done until Chapter 7 where calibration data is presented.

Table 5.3 Correlation Between Light Source and Diode Orientation Errors and Errors in Translation

Orientation Error	Equivalent σ_X	Equivalent σ_Y
For Diode i:		
$\sigma_{Xi\alpha}$	0.	$\frac{X_{di}\sigma^2_{Xi\alpha}}{2}$
$\sigma_{Yi\beta}$	$\frac{Y_{di}\sigma^2_{Yi\beta}}{2}$	0.
$\sigma_{Z\Theta}$	$\frac{X_{di}\sigma^2_{Z\theta}}{2}$	$\frac{Y_{di}\sigma^2_{Z\theta}}{2}$
$\sigma_{Zi\gamma}$	$\frac{X_{di}\sigma^2_{Zi\gamma}}{2}$	$\frac{Y_{di}\sigma^2_{Zi\gamma}}{2}$
For Light Source i:		
$\sigma_{X\ell i\alpha}$	$\ell_{XY\ell i}\sigma_{X\ell i\alpha}$	0.
$\sigma_{Y\ell i\beta}$	0.	$\ell_{XY\ell i}\sigma_{X\ell i\alpha}$

Table 5.4 Total Error Budget for Light Source-Lateral Effect Diode System for Test POSOR

Perturbation Error	Equivalent Error (σ_X)	Equivalent Error (σ_Y)	Induced Error ($\sigma_{\theta X}$)	Induced Error ($\sigma_{\theta Y}$)
σ_X	σ_X	0.	$.0555\sigma_X$	0.
σ_Y	0.	σ_Y	0.	$.3333_Y$
$\sigma_{X\alpha}$	0.	$.25\sigma^2_{X\alpha}$	0.	$.0833\sigma^2_{X\alpha}$
$\sigma_{Y\beta}$	$.25\sigma^2_{Y\beta}$	0.	$.0139\sigma^2_{Y\beta}$	0.
$\sigma_{Z\Theta}$	$.25\sigma^2_{Z\Theta}$	$-.25\sigma^2_{Z\Theta}$	$.0139\sigma^2_{Z\Theta}$	$-.0833\sigma^2_{Z\Theta}$
$\sigma_{Z\gamma}$	$.25\sigma^2_{Z\gamma}$	$.25\sigma^2_{Z\gamma}$	$.0098\sigma^2_{Z\gamma}$	$.0833\sigma^2_{Z\gamma}$
$\sigma_{X\ell\alpha}$	$.05\sigma_{X\ell\alpha}$	0.	$.0028\sigma_{X\ell\alpha}$	0.
$\sigma_{Y\ell\beta}$	0.	$.05\sigma_{Y\ell\beta}$	0.	$.0167\sigma_{Y\ell\beta}$

Note that the values presented above use the values from Table 5.3 and Equations 5.34 - 5.37.

5.5 Conclusions

The analysis presented above was based on the assumption that random errors were introduced to the system. The effects of these errors on the desired system quantity were found by the use of a difference equation (5.2). Note that many of the random errors that can effect system accuracy are errors in fixed quantities, which came about due to uncertainty in determining these quantities (such as distance between sensors).

Hence the only error of a random nature that should appear in the operation of a POSOR would be due to electronic noise. Errors in placement of the sensors, for instance, will not appear as random errors (because the sensors are "rigidly" held in place), but will manifest themselves as steadily increasing errors. The meaning of the "predicted standard deviation of the error" is that the value used to predict the expected steadily increasing error in the system could itself have an error in it. The one exception is the error in calibration of the diodes which will rise and fall as the diode is traversed.

This chapter has presented a general method for formulating sensor resolution and sensor alignment error budgets. In formulating the error budget, the dominant errors are identified which allows attention to be focussed in the areas of greatest potential benefit. Similar error budgets will be required when determining the relative positions of

POSORs that are attached to a common measuring beam, but are not necessary for the testing of a single POSOR. Recent work by Vaishnav and Magrab [5.4] offers the option of determining the relative position of the POSORS in-situ. The abstract from their paper titled "A General Procedure to Evaluate Robot Positioning Errors" is quoted below:

"A new approach to characterize the errors that result from lateral and angular misalignments of the geometric axes of an industrial robot from their assumed positions and orientations is presented. The formulation does not use the usual Deavit-Hartenberg approach. First, a general kinematic formulation for an ideal robot with an arbitrary number of links is developed. The geometric errors in axes locations and orientations are then shown to be skew coordinate transformations with origin translations, and are incorporated into the analysis using general tensor algebra. The final forms of forward and backward transformations contain up to 9(N+2) error parameters for a robot with N physical links. Physical meaning of the error parameters as well as a procedure to calculate these parameters using multiple linear regression analysis are demonstrated".

References

[5.1] H.H. Ku, 'Statistical Concepts in Metrology', Handbook of Industrial Metrology American Society of Tool and Manufacturing Engineers, Prentice Hall New York 1967, pp 20-50

[5.2] H.H. Ku 'Notes on the Use of Propagation of Error Formulas', Journal of Research of the National Bureau of Standards-C Engineering and Instrumentation, Vol 70C, No 4, 1966

[5.3] D. Daubman, Kaman Instr. Corp., personal communication.

[5.4] Vaishnav, Magrab "A General Procedure to Evaluate Robot Positioning Errors" to be published in International Journal of Robotics

(this page left blank)

Chapter 6

Analysis and Design of Metrology Frame Components for Articulated Structures

6.1 Introduction

This chapter will formulate the analytical tools necessary for designing metrology frame structural components (for articulated structures) as described in Chapter 3. The system building blocks consist of a measuring beam, support gimbals, and a six degree-of-freedom POSitioning and ORientation sensing device (POSOR). The first section describes the overall test system configuration (scale model of a "real" system). Detailed static and dynamic analysis of measuring beams is then presented. Various types of gimbals are then investigated in detail. Design algorithms are described in detail to aid in making judgement about possible system performance.

6.2. Test System Configuration

The metrology frame design presented here is a possible full scale model of the system which could be used in the main arms of a 60" (1.5m) reach robot. In order to test the concept of a POSOR (that one large degree of rotational freedom and two small rotational and three small translational degrees of freedom can be simultaneously measured) the test system is designed to simulate limited motions of a structural beam. The large degree-of-freedom, however, is limited to about five angular degrees to prevent having to use more than two lasers (a larger degree-of-freedom would require more lasers which only serves to test how well lasers can be pulsed which is not the subject of the test).

The test system is shown in Figure 6.1, and consists of a POSOR and a measuring beam that is supported by two gimbals. The gimbals provide two and four degrees of freedom of motion respectively. The end of the measuring beam near the two degree-of-freedom gimbal has the POSOR's sensor plane (this plane contains the impedance probes and lateral effect diodes) attached to it. The other end of the measuring beam has an angle plate attached, from which measurements will be made to determine the accuracy of the POSOR. The four degree-of-freedom gimbal is mounted to a two axis linear stage which is used to simulate the bending motion of a structural beam. The two degree-of-freedom gimbal can rotate about the X axis to simulate twist of the structural beam. A coordinate measuring machine is used to measure the motions of the angle plate as the structural beam is moved (gimbals).

6.2.1 Static Analysis of Measuring Beam

This section will discuss the choice of the measuring beam cross section and placement of the gimbals. The measuring beam contributes to the weight of the metrology frame and is responsible for its primary stiffness. Static deflections of the measuring beam, caused by the accelerated mass of the components supported, are predictable and can be compensated for with a software correction. Alternatively, the cross

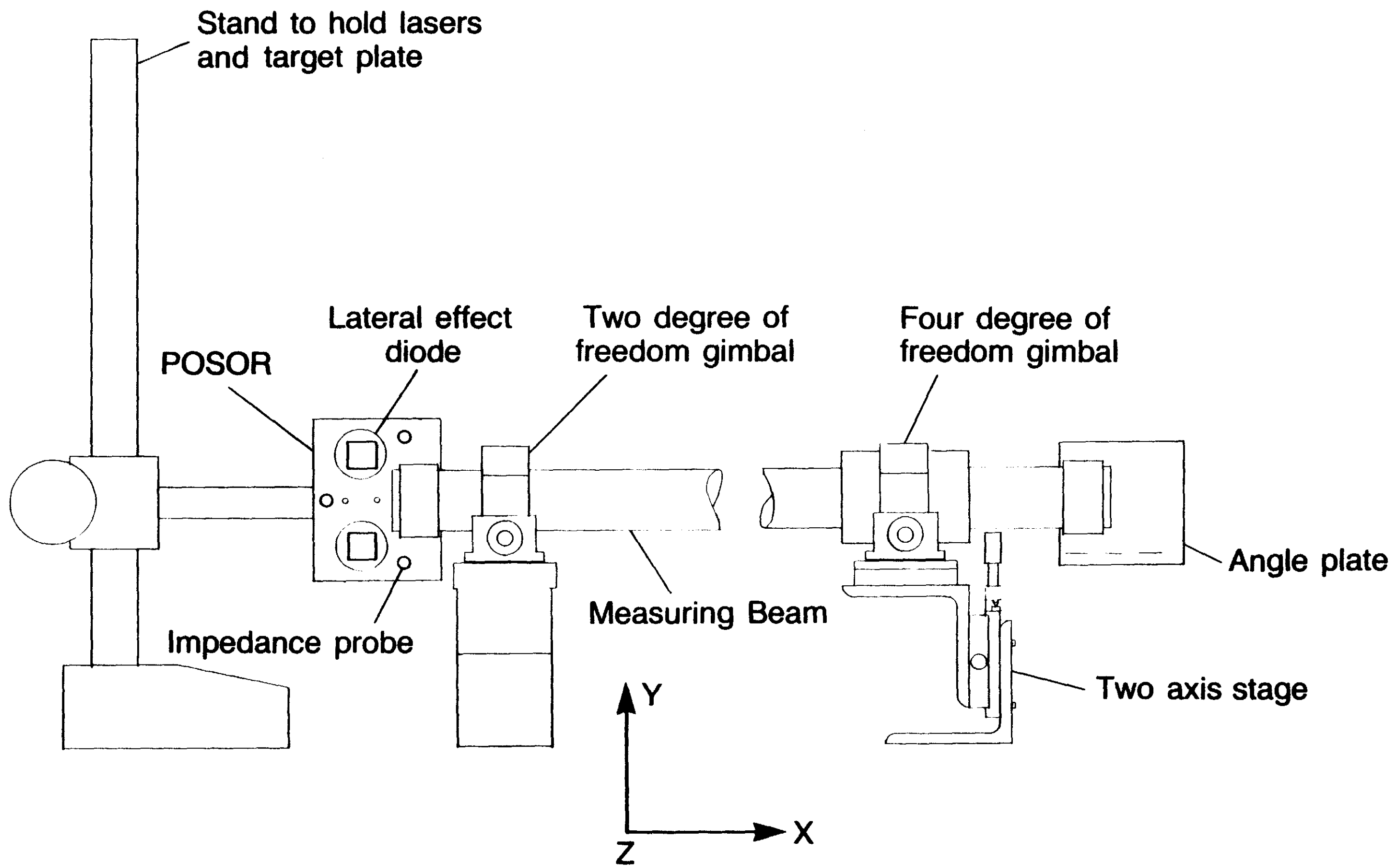

Figure 6.1 Schematic of measuring beam POSOR test assembly

section of the beam can be chosen such that the slope due to elastic deflections is below a set threshold (e.g. angular resolution of the POSERS).

The loading of a measuring beam is shown schematically in Figure 6.2. The following analysis assumes that linear elastic materials are used. For special applications, where high stiffness and low thermal growth are desired, composite materials could be used. The bending moment can be shown to be:

$$\begin{aligned} M(x) = {} & -W_1\langle x\rangle + [W_1(a/b + 1) - W_2c/b]\langle x - a\rangle + [W_2(c/b + 1) - \\ & W_1a/b]\langle x - a - b\rangle - W_2\langle x - a - b - c\rangle + -\frac{W}{2}\langle x\rangle^2 + \\ & -\frac{W}{2b}[(b + a)^2 - c^2]\langle x - a\rangle^2 + \\ & -\frac{W}{2b}[(b + c)^2 - a^2]\langle x - a - b\rangle^2 \end{aligned} \qquad (6.1).$$

The slope at any point on the beam is:

$$\begin{aligned} \alpha(x) = {} & \frac{1}{EI}\Big(-W_1\langle x\rangle^2/2 + [W_1(a/b + 1) - W_2c/b]\langle x - a\rangle^2/2 + [W_2(c/b + 1) \\ & - W_1a/b]\langle x - a - b\rangle^2/2 - W_2\langle x - a - b - c\rangle^2/2 + -\frac{W}{6}\langle x\rangle^3 + \\ & -\frac{W}{6b}[(b + a)^2 - c^2]\langle x - a\rangle^3 + \\ & -\frac{W}{6b}[(b + c)^2 - a^2]\langle x - a - b\rangle^3 + C_1\Big) \end{aligned} \qquad (6.2).$$

The constant C_1 is evaluated at the point where the bending moment is a maximum (slope = 0), and the maximum slope occurs where the bending moment is a minimum. The optimum placement of the supports would not necessarily be to minimize (6.2); dynamic considerations, resistance to bearing reaction torques, and minimizing relative motion between the

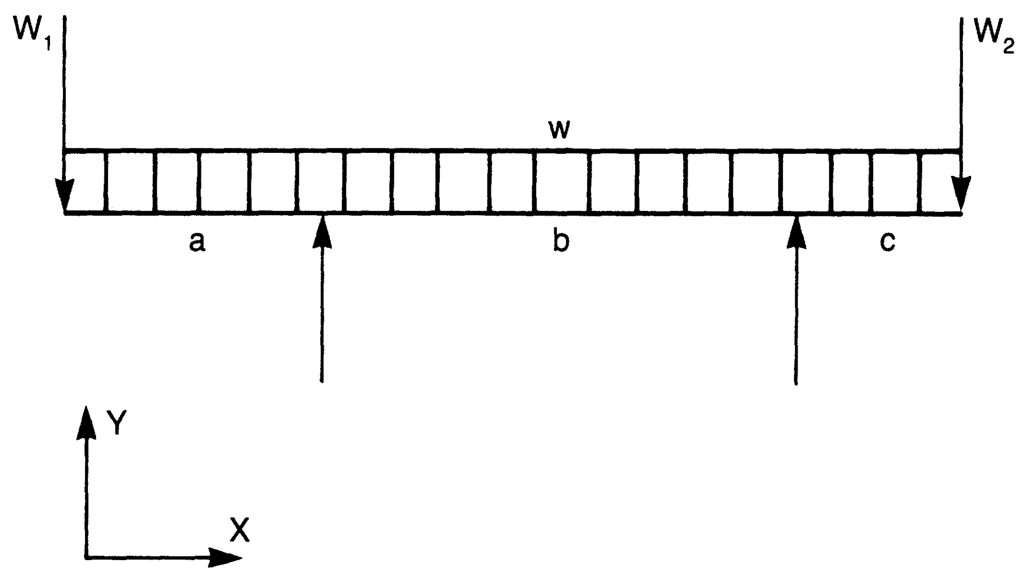

Figure 6.2 Measuring beam loading diagram

POSOR disks must be considered. Also, the moment of inertia I must also be sufficient to resist bearing reaction torques and to provide sufficient dynamic response.

The static deflection of the measuring beam, which can be compensated for by a software correction, does not have to be considered in the present tests since the gravity vector will not be changing position any appreciable amount.

6.2.2 Dynamic Analysis of Measuring Beam Performance

This section will compare the natural frequencies of measuring beams and structural beams. It is important that the dynamic performance of the measuring beam system not restrict the performance of the structural system. The measuring frame to be modeled is shown in Figure 6.3. Because the inertia of the POSOR plates needs to be considered, finite element analysis will be used to determine system natural frequencies and modes. As an example, the dynamic performance of a measuring beam system for a two link robot arm will be evaluated and compared to the robot arm.

The requirement for dynamic performance of the measuring beam system is to have the natural frequencies of a single measuring beam be higher than those of the entire structure. For this example, an aluminum measuring beam length of 30" (.76 m), OD = 2" (50.8 mm), ID = 1.75" (44.5 mm), with 10" (254 mm) diameter $^1/_2$" (12.7 mm) thick aluminum POSORs at each end and gimbles located 6" (152.4 mm) from each

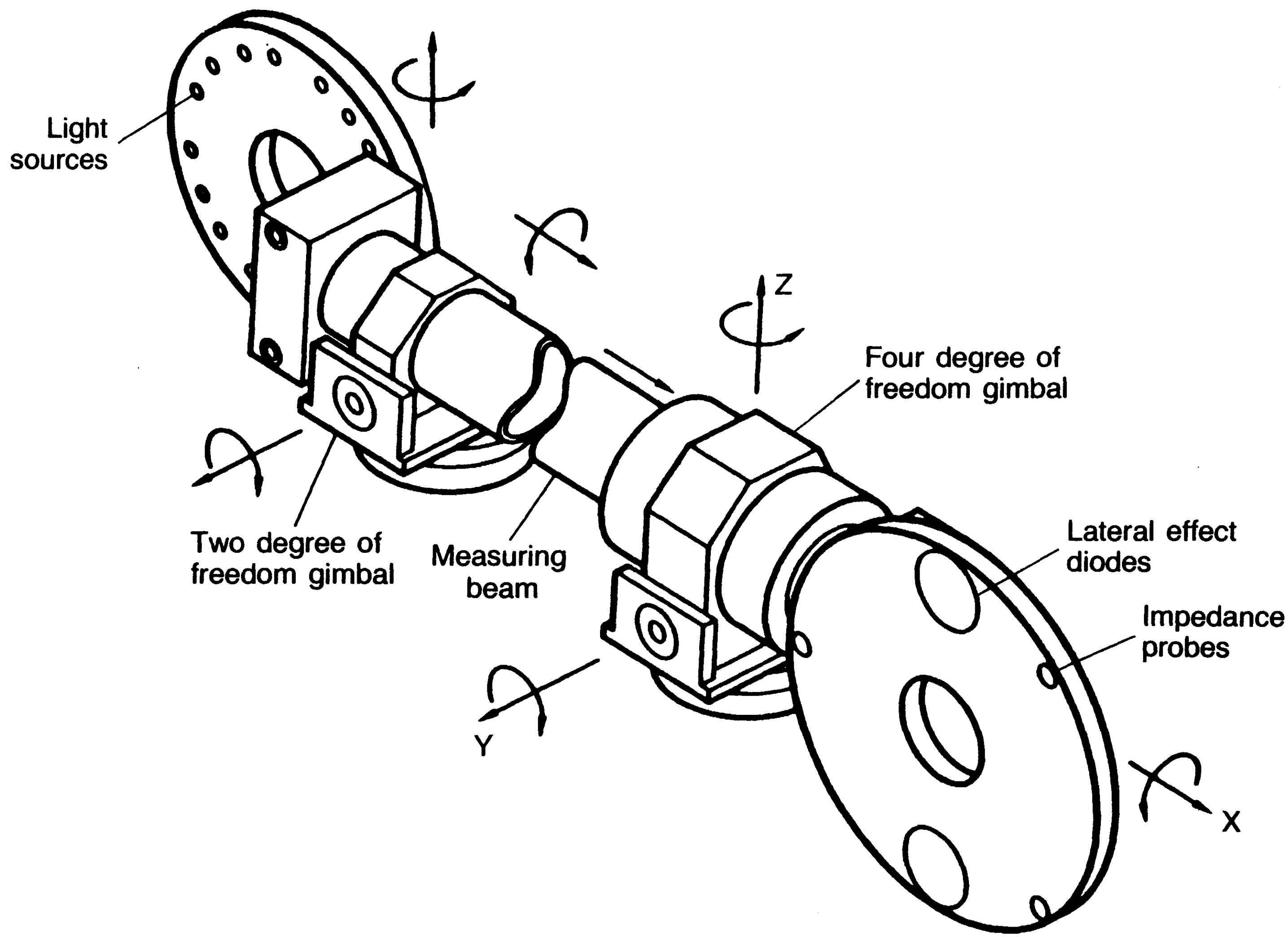

Figure 6.3 Measuring beam assembly for dynamic performance model

end will be modeled. At least two such measuring beams would run along the first and second main structural links of an articulating robot. The robot joint is assumed rigid, so the two links are modeled as an aluminum structural box beam with length of 60" (1.52 m), and cross section 6"×4"×$^1/_8$" (152×102×3 mm). The beam is assumed to be loaded uniformly by its own weight times a factor of two (this will account for the weight of the measuring beam, cables, etc., a factor of five or so is necessary if the actuators are to be considered but they are ignored here).

The first three structural beam natural frequencies (in one plane) are easily found in closed form (see for example Meirovitch, <u>Elements of Vibration Analysis</u> [1.28]) to be (rad/sec): ω_1 = 318, ω_2 = 1994, ω_3 = 5583. The first three structural beam natural frequencies in a plane orthogonal to that above (beam bending sideways) are: ω_1 = 235, ω_2 = 1475, ω_3 = 4131. The measuring beam mode shapes were determined by finite element analysis and the results are given in Appendix 6A. The corresponding natural frequencies are for the plane of vertical bending: ω_1 = 817, ω_2 = 1156, ω_3 = 1332, and in the plane of sideways bending: ω_1 = 886, ω_2 = 1263, ω_3 = 1332. The first harmonic of the measuring beam is thus three times that of the structural beam for both planes of bending.

The above example shows that it is relatively simple to choose a measuring beam geometry whose first mode is several times higher than the articulated structure within which it is made to fit. This ratio will have to be determined by control engineers who will design the controller, but it is important to know that the ratio can be altered. Thus measuring beam dynamics should not be a problem with respect to measuring beam system performance.

6.2.3 Analysis of Gimbal Designs

This section will discuss various gimbal designs. The gimbals are critical elements in the measuring beam system because deflections of the measuring beam caused by gimbal reaction torques are not predictable (breakaway torques are not repeatable). Consequently, it is important to design the system so the effects of the latter are below a desired threshold. As shown below, the magnitude of the degrees of freedom that the gimbals must provide are small, so it will be easy to establish and maintain a suitable reaction torque threshold. Note that since the POSORs measure all motions of the measuring beam, the gimbals do not have to be accurate, but they must have a low reaction torque.

The required amount of angular freedom α_g that the gimbals must provide is equal to the structural beam deflection δ divided by the beam length ℓ. For the following examples, the range of motion is based on that encountered in a 30" (.76 m) long rectangular cross section box beam loaded by a 1000 lb (454 kg) end force (with a design stress of 5000 psi (34.9 MPa)). This beam would have rotations on the order of .0020 radians, and an axial length change of .001" (.0254 mm).

In a two major link structure (total reach = 2ℓ), each end of the measuring beam (length ℓ) can be at the slope imposed by the bearing reaction torques. The endpoint error is thus made up of components from the error at the far end (distance ℓ_1) and the near end (distance ℓ_2). Thus the allowable bending reaction torque Γ to keep the endpoint error below a threshold $\Delta\xi$ is:

$$\Gamma = \frac{2EI\Delta\xi}{\ell(\ell_1 + \ell_2)} \tag{6.3}$$

For a total endpoint error of $\Delta\xi$ = 50 μin (.0125 mm), E = 10×10^6 psi (70 GPa), measuring beam OD = 2" (50.8 mm), ID = 1.75" (44.5 mm), and $\ell = \ell_1 = \ell_2$ = 30" (.76 m), the maximum allowable gimbal reaction torque is Γ = .3529 in-lbs (39.9 N-mm).

For the twisting error about the measuring beam's length, assume that the error amplification is equal to the length of one measuring beam. For this case, the allowable torsion is:

$$\Gamma = \frac{GI_p\Gamma\xi}{\ell^2} \tag{6.4}$$

Using the previous values, the allowable torsion Γ = .2100 in-lbs (23.73 N-mm). Based on these values and a measuring beam assembly weight of W_m = 12 lbs (5.5 kg), wire support, air bearing, and ball bearing gimbals are analyzed below.

6.2.3.1 Wire Support Gimbal Design

Wire support gimbals are very simple structures which would require the least amount of maintenance, and require the least amount of space. This would allow the measuring beam size to approach the structural beam size, which would increase static and dynamic performance. Figures 6.4 and 6.5 show four degree-of-freedom (motions Θ_Y, Θ_Z, Θ_X, and ΔX) and two degree-of-freedom (motions Θ_Y and Θ_Z) wire support gimbals respectively. They are similar except that the diagonal wires shown in Figure 6.5 provide stiffness along and about the X axis. The gimbal reaction torques are calculated below based on the assumption that the wires do not have bending or torsional stiffness (e.g. cables). The initial wire tensions are assumed equal to the measuring beam assembly weight which is on the order of 12 pounds (5.44 kg). With the 12 lb (5.44 kg) measuring beam, a steel wire diameter D of .020" (1.27 mm) will have a design stress of 22.3 ksi (155 kPa).

For the four degree-of-freedom gimbal, shown in Figure 6.4, the reaction torque about the Y axis due to a motion Θ_Y is caused by the two Z axis wires being displaced in the X directions. The X axis displacement causes the wires to move through an angle ε:

$$\varepsilon \approx \frac{\Theta_Y D}{2\ell_W} \qquad (6.5),$$

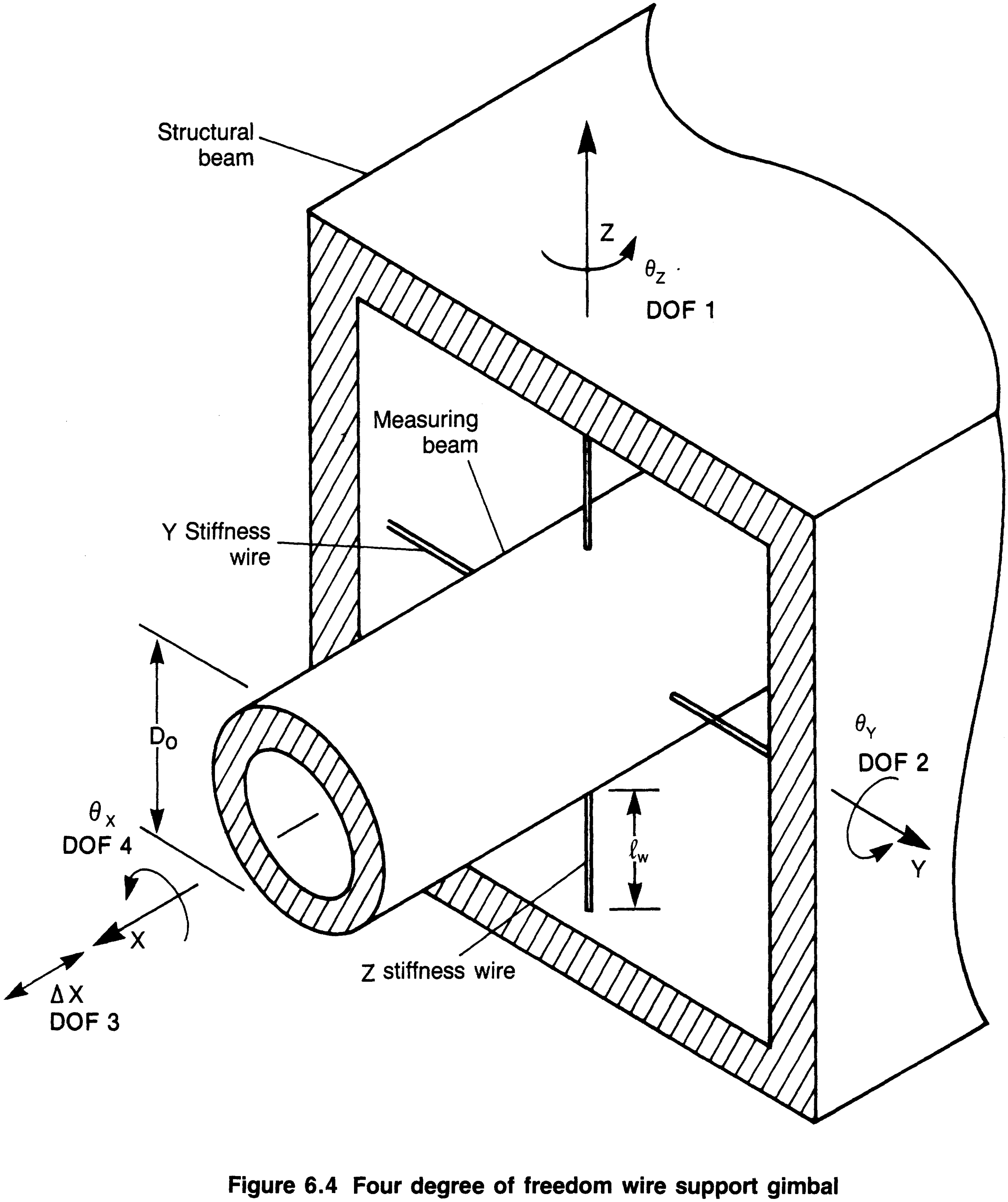

Figure 6.4 Four degree of freedom wire support gimbal

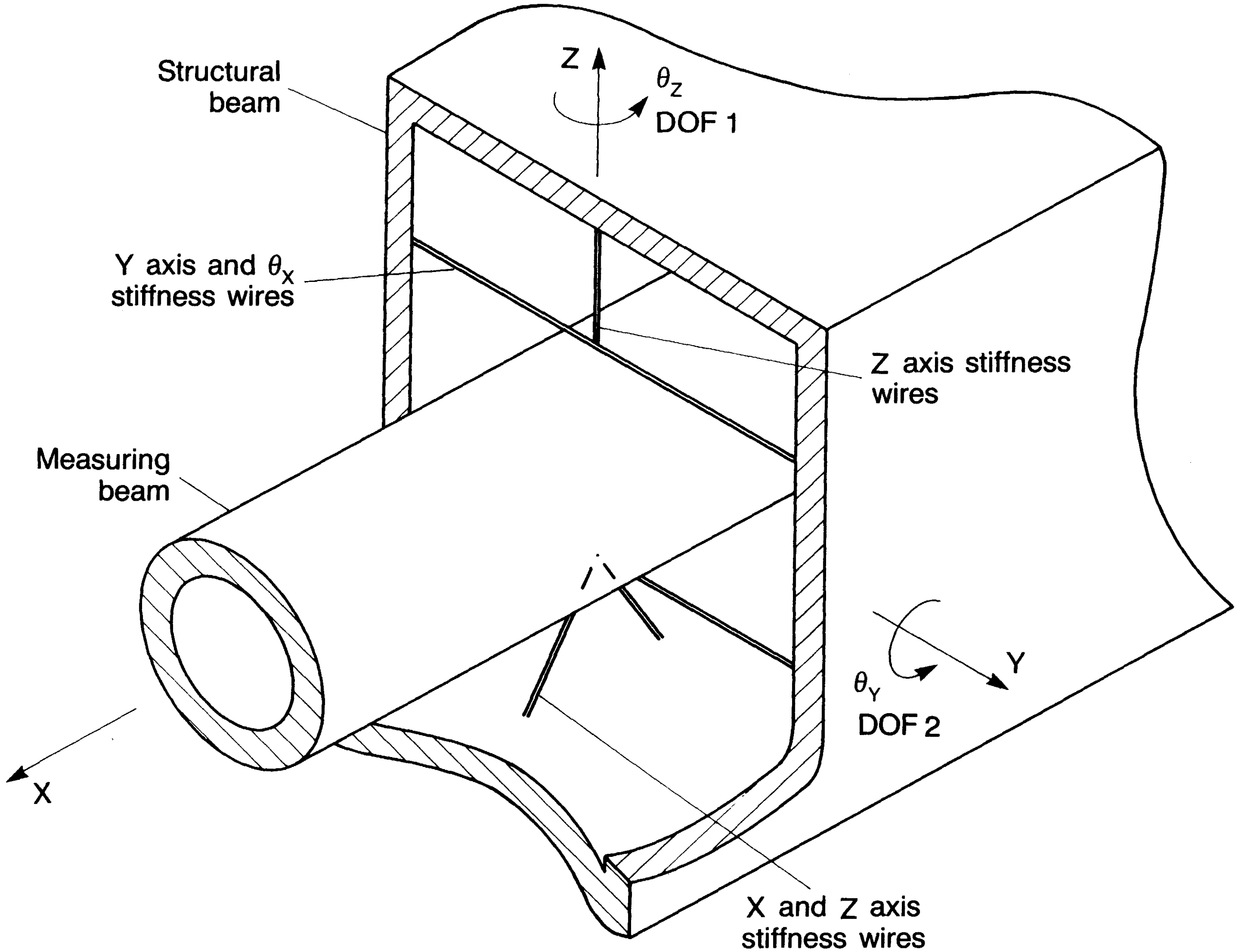

Figure 6.5 Two degree of freedom wire support gimbal

This causes the two wires to stretch, increase in tension, and impose a tangential force at the OD of the tube producing a reaction torque Γ_Y:

$$\Gamma_Y \approx (AE\varepsilon^2 + 2W_M)D\varepsilon/2 \qquad (6.6).$$

With the previous values, the minimum required wire length would be ℓ_W = .145" (3.68 mm). The wire stress due to the length change is on the order of 2850 psi (20 MPa). This shows that for the small required motions, the wire length can be very small. The same values are obtained for the wires which provide the Θ_Z degree-of-freedom. For the Θ_X degree-of-freedom, the same analysis holds except that there are four wires instead of 2 and typically the amount of error amplification is less than half the measuring beam length. Thus approximately the same value is obtained for the required wire lengths. The ΔX requirements are even less.

For the two degree-of-freedom gimbal, there are four wires which act to restrain the Θ_Y motion; hence, the required wire length is .271" (6.88 mm). These wires will actually have to be longer in order to clear the measuring beam diameter. For the Θ_Z motion, the measuring beam pivots about the bottom wires. For this case, the angle ε is:

$$\varepsilon \approx \frac{\Theta_Y D}{\ell_W} \qquad (6.7).$$

This causes the three wires to stretch, increase in tension, and impose a tangential force at the OD of the tube producing a reaction torque Γ_Y:

$$\Gamma_Y \approx 3\varepsilon D\left(AE\varepsilon^2/2 + W_M\right) \qquad (6.8).$$

The required wire length is found to be .813" (20.7 mm). Two of these wires will actually have to be longer in order to clear the measuring beam diameter.

The other degrees of freedom are restrained by wires which are directly in tension. The first mode of the gimbal supported system can be estimated by assuming that one wire supports half of the measuring beam mass, and that the motions are uncoupled, so only translational motions occur:

$$\omega_n = [2AE/\ell_w M_s]^{1/2} \qquad (6.9).$$

With the previous values, and ℓ_w = .8" (20.4 mm), ω_n = 868 rad/sec which is on the order of the first mode frequencies found for the example in section 6.3.2.

This section provided the basic formulas for determining the minimum required wire lengths for wire support gimbals. Representative values were found, and it was shown that wire support gimbals could easily be made to meet most performance specifications. The main advantage of wire support gimbals are low maintenance requirements; however, they may be difficult to install (setting wire tension, and aligning POSOR disks, for instance, may be difficult).

6.2.3.2 Yoke Type Gimbals

The other major type of gimbals use bearings to support a load, usually through many degrees of motion. They are considered here because they are the stiffest type of gimbal that can be constructed, and are the easiest to install (but they are the most difficult to construct). Two types of yoke gimbals will be considered here, aerostatic bearing support, and ball bearing support. A yoke gimbal that uses only aerostatic bearings would provide the lowest reaction torques (almost un-measurable). The use of ball bearings would lessen manufacturing and maintenance costs, but the reaction torque would be much higher, and fretting corrosion problems could occur. Note that for both types of gimbals accuracy is not a concern because the POSORs can sense all motions of the measuring beam.

A two degree-of-freedom gimbal design that uses only aerostatic bearings is shown in cross section in Figure 6.6. The design is rather complex; however, it does not require the microinch tolerances normally associated with aerostatic bearings, since they are designed for low friction not high accuracy. Analysis of reaction torques is not necessary, because if the bearings have not grounded out, there will be no reaction torques. The four degree-of-freedom air bearing gimbal would float the measuring beam in the collar. These designs are too complex for the simple system required to test the principles of this thesis and will not be discussed further although methods for designing aerostatic bearings are discussed in section 6.2.3.5.

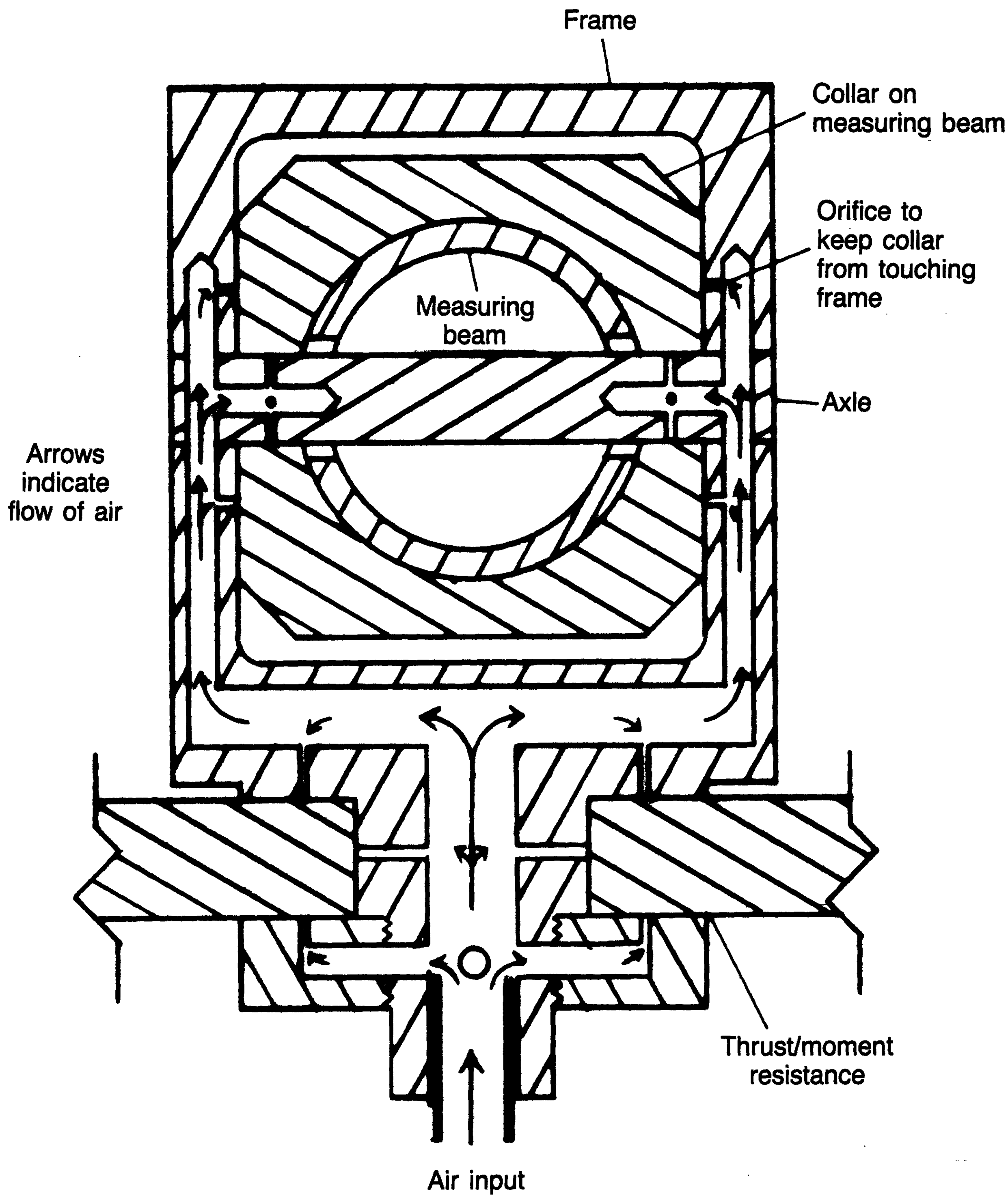

Figure 6.6 Schematic of two degree of freedom aerostatic bearing gimbal

Two and four degree-of-freedom ball bearing gimbals are shown in Figures 6.7 and 6.8 respectively. For the ball bearing gimbals, each gimbal has a turntable bearing and a pair of yoke bearings; in addition, the four degree-of-freedom gimbal has an aerostatic bearing assembly. The aerostatic bearing provides the degrees of freedom along and about the X axis more efficiently than could a ball bearing assembly. Before discussing these designs in detail, the expected loads are computed.

In order to evaluate required bearing performance, each set of bearings is assumed loaded by a force equal to one half the mass of the system accelerated at the current system value G and produces a reaction torque caused by the load times the coefficient of friction μ acting at a radius r_b. The system's mass is composed principally of a measuring beam, a receiving plane, a transmitting plane, two holding blocks, the air bearing assembly, and two yokes; their sum total mass is M_s. The distance between the yokes is ℓ_y, and the length of the measuring beam is ℓ_m. The maximum angle of deflection of the round measuring beam caused by the bearing reaction torque is ε_m:

$$\varepsilon_m = \frac{\left(M_s + \pi\rho(r_o^2 - r_i^2)\ell_m\right)\mu r_b G \ell_y}{E\pi(r_o^4 - r_i^4)/4} \qquad (6.10).$$

The worst effect of this angular error will be to produce an error in the angles α, β, and ω which are measured by each POSOR. For the gross errors of a system with two long main measuring beams, the first POSOR will measure an angle α that is off by $+\varepsilon_m$ and this error acts over the distance $2\ell_m$. At the next joint, an error $+\varepsilon_m$ is contributed

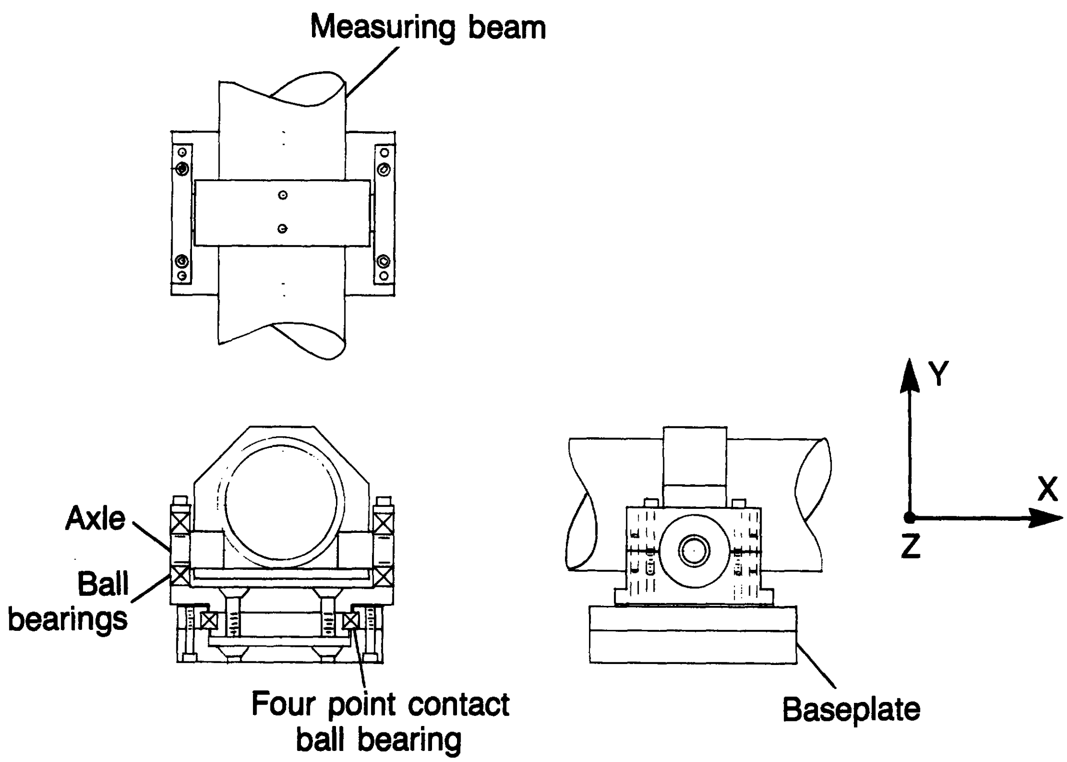

Figure 6.7 Two degree of freedom ball bearing gimbal assembly

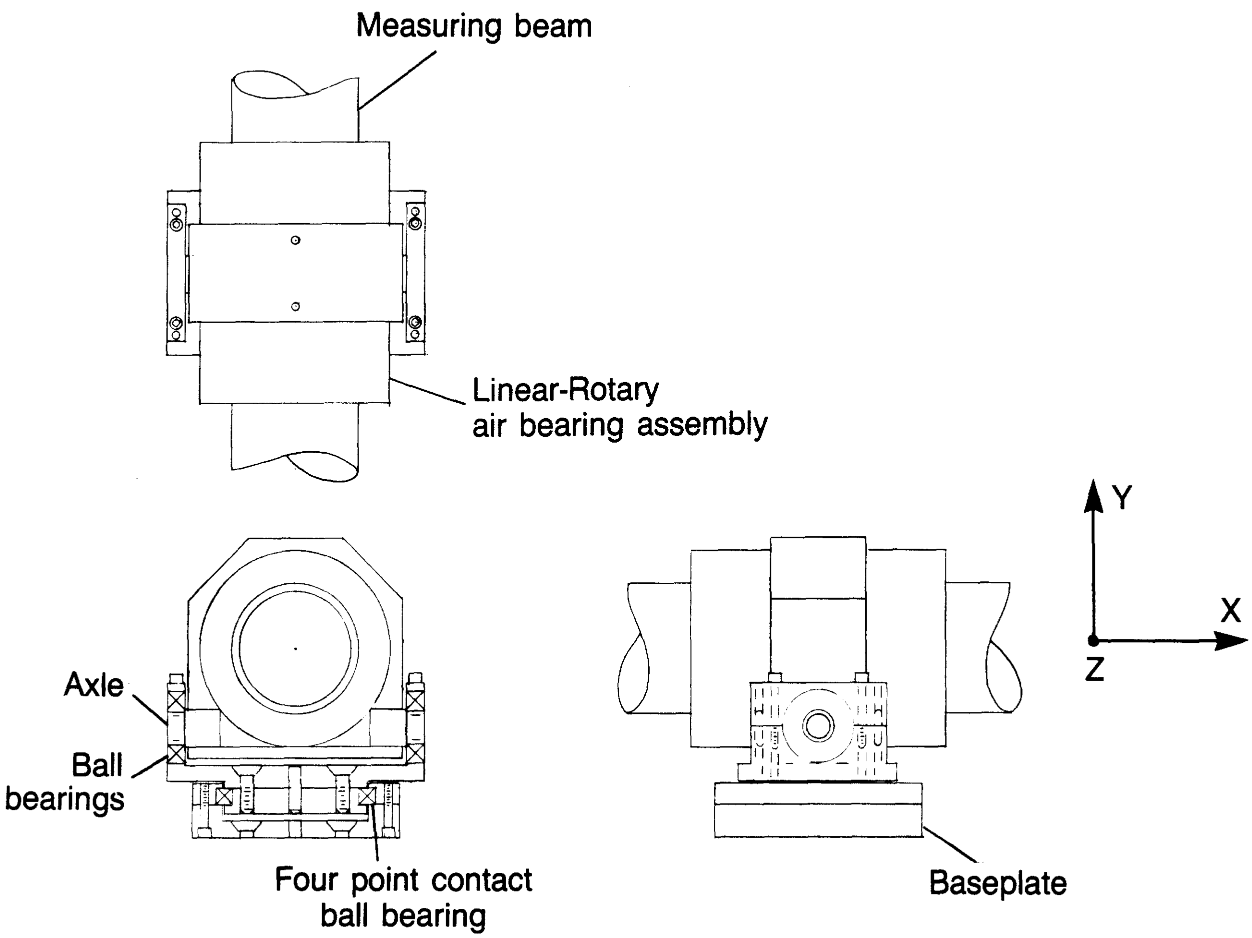

Figure 6.8 Four degree of freedom gimbal assembly

by each measuring beam and acts over the length ℓ_m. Thus the endpoint error is $4\epsilon_m\ell_m$. If the allowable endpoint error associated with this particular source is $\Delta\xi$, then substituting the above into (6.10) and solving for the maximum allowable value μr_b:

$$\mu r_b = \frac{\Delta\xi E\pi(r_o^4 - r_i^4)}{16[M_s + \pi\rho(r_o^2 - r_i^2)\ell_m]G\ell_y\ell_m} \tag{6.11}$$

Note that very fine positioning accuracy is only required for the final position adjustment; thus the major acceleration will be that of gravity plus a small dither component (the dither would be the final homing in on the desired position). If the robot dithers sinusoidally across an amplitude of .010" with a period of .030 seconds (≈ 3 controller time constants) then the acceleration in addition to gravity is 1g. Some typical values are (assume acceleration of 2g): r_o = 1.0" (25.4 mm), r_i = .875" (22 mm), E = 10^7 psi (70 GPa), M_s = 12 lbs (5.5 kg), $\delta\xi$ = .0005" (.0013 mm), ρ = .2 lbs/in^3 (5286 kg/m^3), ℓ_m = 30" (.76 m), and ℓ = 18" (.46 m). The allowable value for μr_b is thus .0082" (.208 mm). This is not necessarily too restrictive a value to obtain.

Instrument bearings typically have coefficients of friction of .001, and the radius for the yoke would only be on the order of .3" (7.6 mm) (for a .375" (9.5 mm) shaft). The turntable bearing could possibly be of the type used in the test model, for although the large radius (1" (25.4 mm)) resists moment loads well, its coefficient of friction is of the order of .007 (value given by Kaydon Corp.). Note that for the size of the components used in the test, the error due to the larger bearings

μr_b value will be negligible. For industrial implementation, each application would have to carefully consider these design values. For this thesis, the ball bearing design will be used because it is much simpler to assemble and modify if needed. Chapter 7 describes tests performed to determine μr_b for the bearings used. With these values in mind, the gimbals of Figures 6.7 and 6.8 are discussed in greater detail below.

The two degree-of-freedom gimbal is shown in Figure 6.7. The design goals are to make it as reaction torque free and as small as possible. To meet the design criteria, the design uses a yoke on a turntable approach. A collar is fixed to the measuring beam by set screws and epoxy. The base of the collar has a line bored hole in which an axle is located. The axle is supported by a pair of bearings which are in turn held in the yoke by a split housing arrangement. This design allows very delicate preloading of the system so high starting torques will not be induced. The yoke's base is turned and fits into the ID of a large diameter KAYDON "Reali-Slim" four point contact bearing. This bearing is a four point contact bearing which can resist forces and moments in any direction. By using this one large diameter bearing the need for a second yoke to straddle the first is avoided.

The four degree-of-freedom gimbal is shown in Figure 6.8, and is identical to the two degree-of-freedom gimbal except that the collar which holds the measuring beam is designed as an aerostatic bearing. This aerostatic bearing will allow the measuring beam to slide and rotate within the collar. Rolling element bearings were considered, but their size and weight prevented their use. For example, a Thompson ball bushing bearing for a 2" (50.8 mm) diameter shaft weighs 10 pounds (4.5 kg). Also, the use of ball bushings would require a hard wear resistant surface. The algorithm used to design the aerostatic bearing is discussed in the next section.

6.2.3.3 Ball Bearing Yoke Design to Resist Fretting Corrosion

The ball bearings used in the gimbals will not see more than one-half degree or so of rotation; thus the possibility exists for the breakdown of the lubricant film and for fretting fatigue to occur if metallic bearings are used. Note that glass ball bearings with polyacetal races are available (Jilson Corp 201-488-4646) and can meet the friction criteria.

Fretting fatigue is caused by repeated alternating sliding contact of two adjacent surfaces. As noted by O'Connor [6.1], damage can occur with slip amplitude as small as 40 microinches (1 μm) and Tomlinson et al. [6.2] puts the figure at values as low as one microinch (.025 μm) . The action of fretting tends to increase the coefficient of friction until stresses high enough to initiate a fatigue crack form; however, we are more concerned about metal to metal contact resulting in higher coefficients of friction. This occurs when metal to metal contact causes local cold welds between asperites which are then torn apart. The newly exposed fresh metal surface quickly oxidizes and the process repeats. Thus fretting fatigue is often referred to as fretting corrosion.

For the combined loads placed on the gimbals of 6.2 pounds/gimbal (2.8 kg) @ 2g's acceleration, the bearing stresses are very high. The compressive stresses for the bearings were determined from a series of equations initially derived by Hertz and referenced here from Timoshenko [6.3]. A program CONTACT.FOR, which is given in Appendix 6B, is used to analyze bearing contact stresses. The equations have complicated functions of the radii of curvature of the surface, but the stress varies as the cube root of the load. Thus even small loads produce very large stresses which is why fretting fatigue can so easily occur.

For a 3/8" (9.5 mm) bore 7/8" (22 mm) OD bearing with seven 5/32" (4 mm) diameter balls, it can be assumed in the worst case only two balls bear the load. For the yoke bearings this means each ball is at most loaded by 2.2 pounds (9.8 N). However, the resulting compressive stresses are 123 ksi (859 kPa). Note that Waterhouse [6.4] suggests that for hardened steel the applied compressive stress should be 1/5th to 1/10th of the maximum allowable in order to provide for 10^7 cycles of life. Thus fretting fatigue would soon become a problem unless forced lubrication methods were employed.

The large 2" (50.8 mm) diameter bearing is rated for radial, thrust, and moment loads. The groove is arch shaped to allow this sort of loading but it complicates the analysis. Thus to enable an estimate of the compressive stresses, the applied loads are normalized by the maximum allowable static loads. The cube root of this ratio times the maximum allowable compressive stress will thus approximate the maximum stress imposed by the present loading [6.3]. The combined load of 6.2

pounds (27 N) thrust and 16 in-pounds (1.8 N-m) moment is equivalent to a 36.8 pound (164 N) radial load. The maximum radial load the bearing will support is 683 pounds (3038 N) which generates a 400 ksi (2.8 GPa) compressive stress (bearing values courtesy of Mike Purchase at Kaydon Corp.). From the above, the compressive stress for the present case is found to be 154 ksi (1.1 GPa) . Thus the Kaydon bearing could also experience problems with fretting fatigue.

There are several possible methods by which fretting corrosion can be avoided: 1) force lubrication between balls and races with pressurized lubricant, 2) use special greases for oscillating conditions such as Nye Co.'s RHEOLUBE-951, 3) coat the bearing surface to prevent metal to metal contact or to provide noncorrosive surfaces, 4) make the bearings from dissimilar materials. The first solution would be messy and may contaminate the POSORs' surfaces. The second solution will require periodic changing of the grease and still has the potential for failure. The third solution is viable and is currently available from Fafnir Co. Fafnir's plating process ("Fafcote-TDC") applies a thin hard (RC-70) chrome plating to the bearing components. The coated "Fafcote" bearing is not yet in production, so it will be some time before fatigue data is gathered. Note that the chrome surface will form a hard tough oxide layer which at least will not corrode. The last option, however, may also be promising as is discussed below.

Since the loads are so low, the potential exists for using a plastic such as Teflon or Delrin for the races with glass, steel or aluminum balls. Note that the plastic has a much lower modulus of elasticity than steel so the footprint areas would increase which would lower the contact stress. If Delrin is used (modulus of elasticity = 450 ksi (3.1 GPa)) and we assume that it is a linear elastic material, then the maximum compressive stress is found to be 12 ksi (8.4 GPa). Delrin has a 1% yield strength of 5.2 ksi (36 MPa), and a 10% yield strength of 18 ksi (69 MPa). The use of soft metals such as brass results in compressive stresses of 78 ksi (537 MPa) which precludes their use. Thus it is apparent that more research must be done in this area if ball bearing gimbals are to be used in commercial metrology frames.

6.2.3.4 Principles of Aerostatic Bearing Design

Air bearings are normally associated with ultra-precision spindles that are only moderately loaded but may operate at very high RPM's. Most low speed ultra low friction applications use oil fluid bearings because of their greater load carrying capability, and they have less stringent manufacturing tolerances. Also fluid viscosity terms are minor at low velocities. However, hydrostatic, as opposed to aerostatic, bearings are messy and would quickly contaminate the POSORs' surfaces. Thus aerostatic bearings are the only type of fluid-static bearings that are applicable for use in measuring beam systems.

Aerostatic bearings do not depend on shaft rotation to generate lift. Instead, high pressure air is forced through capillaries or orifices into the region between a shaft and a housing. These flow restrictors prevent the air from selecting an unrestricted exit path.

The main disadvantage in using air is that it is compressible which for some designs can lead to instability problems. The designs which are prone to instabilities are pointed out in the following general description of air bearing design.

A typical aerostatic bearing is shown in cross section in Figure 6.9. Air is forced into a number of pockets which surround a shaft. The pressure inside the pocket is nearly uniform and drops linearly across the lands to the atmosphere. As the shaft is displaced, the land's gap in the displaced direction decreases causing a pressure rise. The opposing land's gap increases causing a pressure drop; thus an equilibrium shaft eccentricity is reached. It is possible to eliminate the lands and have the air flow just between the shaft and the housing, but then the large region of constant pressure would not be present and the load rating drops.

If the pockets are too big, then aerostatic instability, or "pneumatic hammer", as described by Modjarrad [6.5] may occur. This type of instability occurs because as the bearing surfaces approach, air will be compressed in some pockets instead of flowing out the bearing. On the other hand, the opposing pocket will take a finite time to fill. Thus there is a time lag between the required balancing pressure and the applied load, and the shaft will oscillate. If the damping effect provided by the lands is not carefully chosen, then this instability can occur.

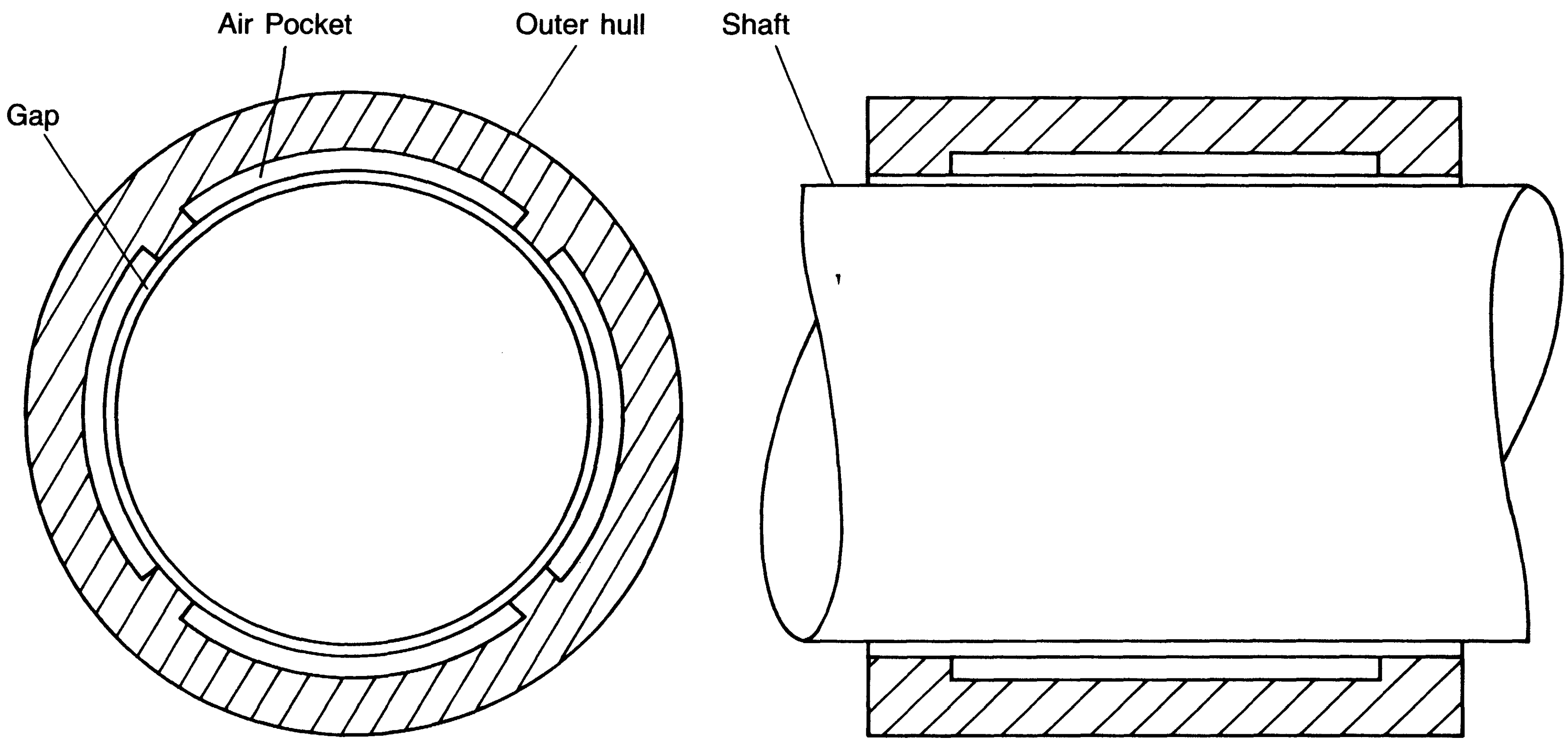

Figure 6.9 Schematic of aerostatic bearing cross sections

Various theoretical methods have been used to model pneumatic hammer. Sun [6.6] describes the phenomenon occurring not only in pocketed bearings, but in porous surface bearings as well. Pinkus [6.7] gives a well presented description of the effect, and derives the critical relationship between pocket and land size. For the present design application, however, ample performance can be obtained from a non-pocketed bearing.

Pneumatic hammer can be avoided by not using pockets, which reduces the load capacity of the bearing but decreases machining costs. It can also be avoided by using groove compensated bearings, as patented by Arneson [6.8], which also have a very high load capacity. This latter type of bearing has shallow longitudinal grooves machined into the shaft which are calibrated to have a precise flow resistance relative to the ungrooved portions in such a way as to give the added lift affect of having pockets without as great a chance of an instability occurring.

The type of bearing design used in the present application will thus depend on the type of robot that is to be built. For the present case of a test system, the theory of operation of a "plain" bearing will be used to design a plain aerostatic bearing. If after testing, its performance is not satisfactory, it can be modified to be of the grooved design.

6.2.3.5 Development of Aerostatic Bearing Design Algorithm

This section will formulate the equations for fluid flow necessary to predict performance of aerostatic bearings. Various authors provide charts and graphs to assist in air bearing design, but they do not give the designer a feel for what is going on. Thus the equations derived below will be included in a FORTRAN program that will allow the effects of the various parameters to be plotted and tabulated. The goal is to develop a design which has very forgiving dimensional tolerances. Such a design would thus be economical to implement and should be more trouble-free.

For plain journal aerostatic bearings, the load capacity is a function of the bearing geometry and the method used to introduce the flow. The geometry is changed by altering the length to diameter ratio and the radial clearance. The method of introducing the flow can be controlled by varying the inlet orifice size. The net radial restoring force provided by the bearing can be determined from the Navier-Stokes equations. The following symbols are defined for this section only:

C inside radius of housing minus outside radius of shaft

C_d orifice discharge coefficient

D shaft diameter

L bearing length

R bearing radius

W load

a orifice radius

e_c eccentricity

h film thickness

m number of orifices

p pressure

u, v, w linear velocity components

x, y, z cartesian coordinates

ε eccentricity ratio e_c/C

μ absolute viscosity

ρ density

The assumptions made in applying the NS equations are:

1) The height of the film, which separates the surfaces, is very small compared to the radial and longitudinal distances; thus the curvature of the bearing can be ignored, and a cartesian reference frame used.

2) There is no variation of pressure across the film; thus $\frac{\partial P}{\partial y} = 0$.

3) The flow is laminar.

4) There are no external forces on the fluid film (ignore gravity).

5) Fluid inertia forces are small compared to viscous shear forces: thus $\frac{Du}{Dt} = \frac{Dv}{Dt} = \frac{Dw}{Dt} = 0$.

6) No slip condition at fluid/surface interfaces.

7) Since the y dimension is so small compared to the others, only the higher order derivatives of y are retained.

These assumptions reduce the Navier-Stokes equations to:

$$\frac{1}{\mu}\frac{\partial p}{\partial x} = \frac{\partial^2 y}{\partial y^2} \qquad (6.12),$$

$$\frac{1}{\mu}\frac{\partial p}{\partial x} = \frac{\partial^2 y}{\partial y^2} \qquad (6.13).$$

The dimension X is along the circumference of the bearing and Z is along the longitudinal direction. For the static case, the surface velocity is zero, and integrating the above yield:

$$u = -\frac{1}{2\mu}\frac{\partial p}{\partial x}\, y(y - h) \qquad (6.14),$$

$$w = -\frac{1}{2\mu}\frac{\partial p}{\partial z}\, y(y - h) \qquad (6.15).$$

There will be cross flow from the higher pressure regions to the lower pressure regions which is accounted for by the continuity equation:

$$\frac{\partial}{\partial x}(\rho u) + \frac{\partial}{\partial y}(\rho v) + \frac{\partial}{\partial z}(\rho w) = 0 \qquad (6.16).$$

Substituting (6.14) and (6.15) into (6.16) and integrating before differentiating yields the Reynolds equation for the zero surface velocity case:

$$0 = \frac{\partial}{\partial x}\left(\frac{\rho h^3}{\mu}\frac{\partial p}{\partial x}\right) + \frac{\partial}{\partial z}\left(\frac{\rho h^3}{\mu}\frac{\partial p}{\partial z}\right) \qquad (6.17).$$

Pinkus and Sternlight [6.7] solved (6.17) for a compressible and incompressible flow with laminar or turbulent feeding. They assumed that a ring of m orifices are equally spaced about the circumference of a housing in the center of it. Their results for the compressible fluid bearing case with orifice inlets are presented below.

The parameters Λ_t and λ_t are used to describe flow into the bearing gap through orifices:

$$\Lambda_t = \frac{2.25 \times C_d^2 a^4 L^2 \mu^2 m}{C^6 \rho (p_s - p_a)} \qquad (6.18),$$

$$\lambda_t = \Lambda_t \left(1 + (1 + 2/\Lambda_t)^{1/2} \right) \qquad (6.19).$$

The parameter Y is defined as:

$$Y = \left(\frac{(L/D)(1 + \lambda_t)}{\lambda_t (p_s^2/p_a^2 - 1)} \right)^{1/2} \qquad (6.20).$$

The error function and Dawson's function are denoted by Φ and Ψ respectively. The load which the bearing will support is given by:

$$W = \frac{3\pi\varepsilon L D p_a}{4Y} \left\{ \frac{e^{-Y^2}\left(\Psi(\sqrt{Y^2 + L/D}) - \Psi(Y)\right) - (\sqrt{\pi}/2)e^{Y^2}\left(\Phi(\sqrt{Y^2 + L/D}) - \Phi(Y)\right)}{(L/D)\cosh(L/D) + \lambda_t \sinh(L/D)} \right\} \qquad (6.21).$$

The above equations are assembled in a program AIR.FOR which is presented in Appendix 8A.

6.2.3.6 Digital Analysis of Bearing Performance

The measuring beam's diameter is chosen based on a deflection criteria as given previously. Thus a logical choice is to design the aerostatic bearing for the four degree-of-freedom gimbal based on the same diameter. This allows the bearing length and orifice size to be chosen. It is assumed that 80 psi (551 kPa) shop air will be used as an air supply. The largest loads that the air bearing must resist will be those caused by robot accelerations. These are generally set by the robot controller as part of a detailed path plan.

The bearing for the testing unit will be designed for a load of 4g's. Note that the aerostatic bearing must resist the reaction torque of the yoke bearings about an axis parallel to a radius. Thus two rows of orifices are arranged around the housing, and are spaced such that the distance between rows is equal to one half the length of the bearing housing. A series of holes is drilled in the circumference of the shaft at the point where they will lie midway between the rows of orifices; thus the single housing will act as two adjacent bearings and will be able to resist a moment. This design method is described by Wilcock and Booser [6.9]. The loads are thus 16.2 pounds (73 N) radial and 32 in-lb (3.62 N-m) moment.

The input parameters of interest, which can be varied in the design, are the length L, the radial clearance C, the orifice radius a, and to a lesser extent the orifice coefficient C_d. The obtainable surface finish for the bearing surfaces must also be an order of magnitude finer than the minimum surface gap. The parameter which is most difficult to control, however, is the orifice discharge coefficient. Each of these parameters will be varied and their effect on the bearings performance. Then the optimum choice will be made to yield a manufacturable bearing.

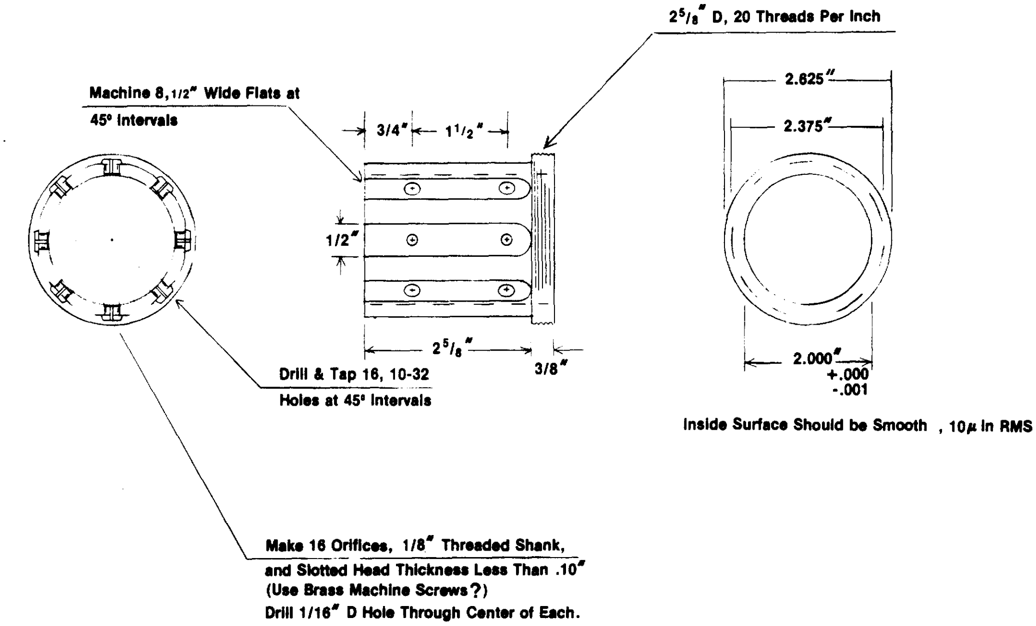

Figure 6.10 Aerostatic bearing core

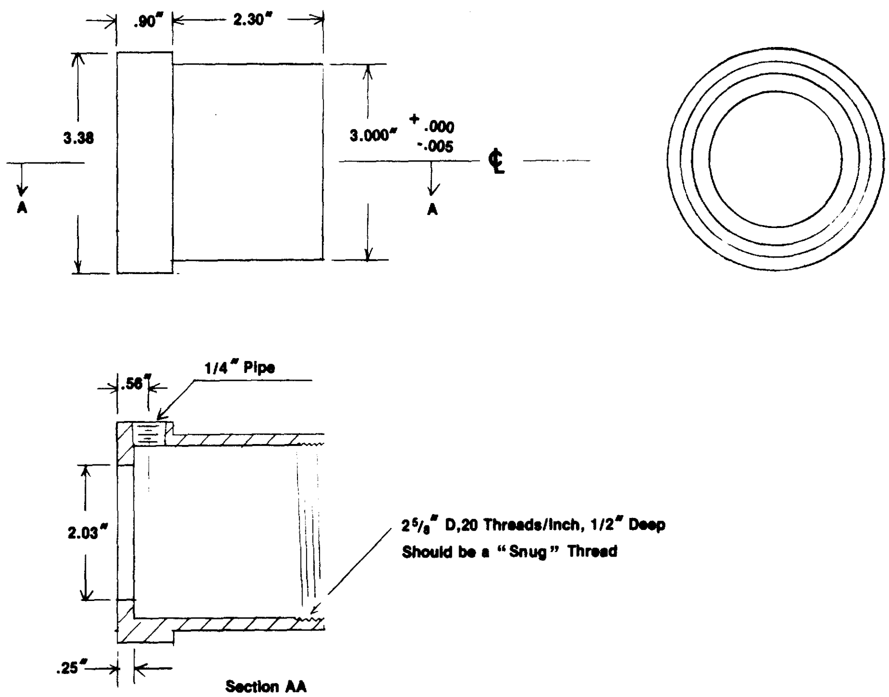

Figure 6.11 Aerostatic bearing hull

Orifices have had extensive use as flow metering devices in many fields and the amount of literature dedicated to their study is voluminous. Theoretical studies by Rivas and Shapiro [6.10] for rounded entrance non-contracting orifices indicate that C_d varies with the Reynolds number in a fairly predictable manner. Other researchers such as Tsai [6.11], and Perry [6.12] confirm this. The problem is that it is difficult to determine the Reynolds number for aerostatic bearing orifices since the flow rate cannot be determined until C_d is known. Rather than go through an elaborate iterative program, which may yield a value which is not easily controllable, the effect of a broad range of orifice coefficients is studied.

The program AIR.FOR was modified to allow the L/D ratio to be input along with a starting value for the orifice coefficient. The program then looped over the orifice coefficients incrementing the bearing gap clearance through a cycle each loop. Data was gathered with the other parameters set at reasonable values as indicated on the plots. The results are presented in Figures 6.12 and 6.13. As would be expected from (6.19), the discharge coefficient, which is raised to a lower power than the other functions, does not effect the load capacity of the bearing very much. However it is interesting to note that with an orifice radius of .030" (.762 mm), the load capacity goes down with increasing discharge coefficients, while the opposite is true for an orifice radius of .015" (.381 mm). Evidently, the effect of larger C_d values is to let too much air into the bearing which does not allow as large a pressure differential to build up. Of course not letting enough air in would lead to bearing gaps which would be too small. Since the

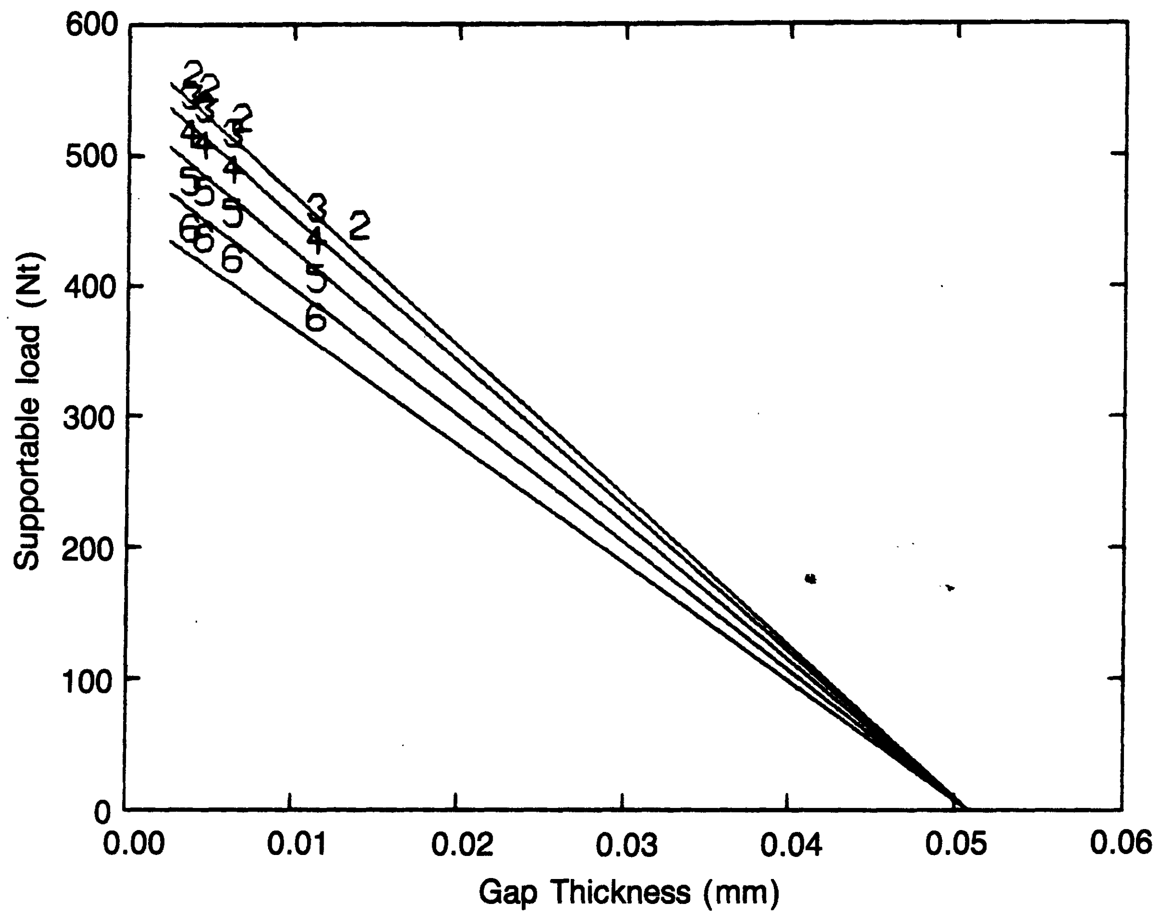

Figure 6.12 Aerostatic bearing performance with Cd = .4 – .8, a = .030″, C = .002″, L/D = 1, p = 80 psi

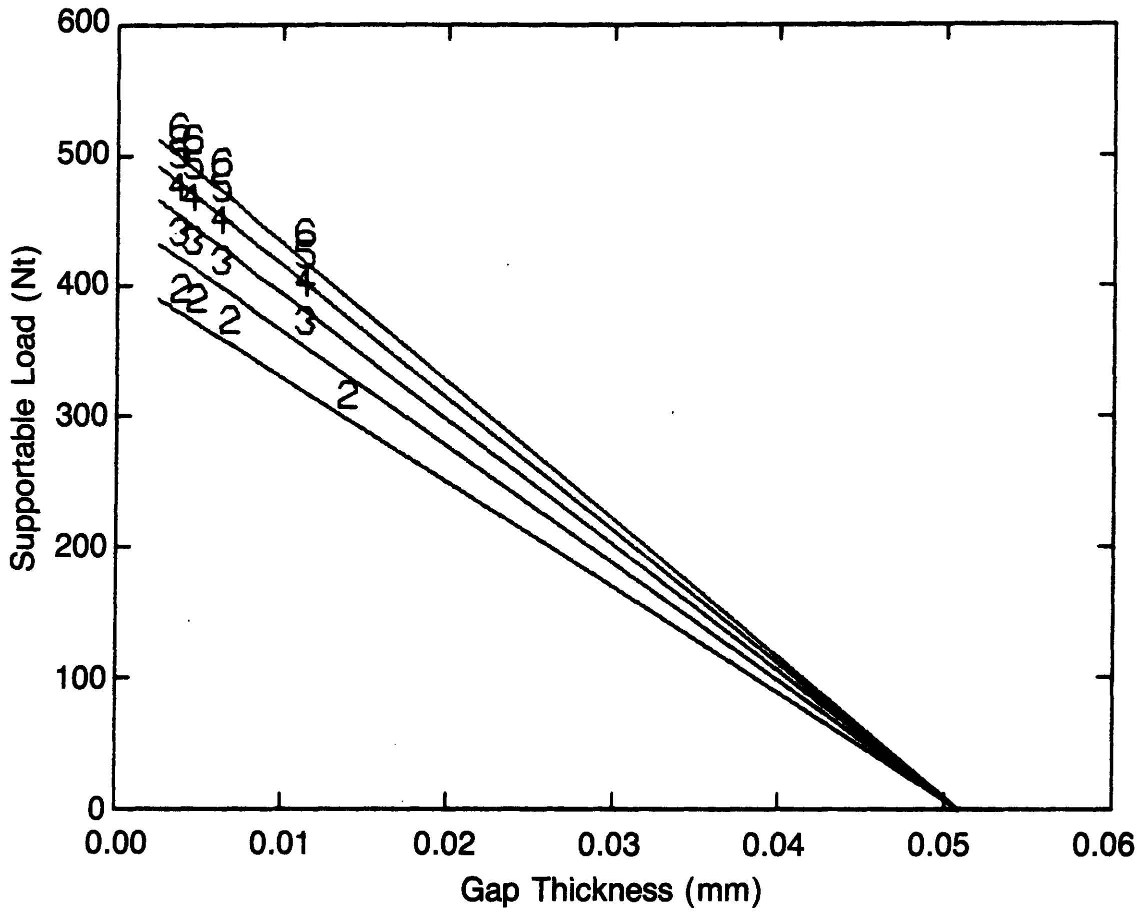

Figure 6.13 Aerostatic bearing performance with Cd = .4 − .8, a = .015″, C = .002″, L/D = 1, p = 80 psi

orifices used are to have a rather shallow throat length, a midrange value of .6 will be assumed and an orifice radius of .030" (.762 mm) will be used.

The effect of the other parameters was then studied using AIR.FOR. Figures 6.14 through 6.16 show the effect of varying the radial clearance on the load supporting capability. As shown in Figure 6.14 with a radial clearance of .001" (.025 mm), as the L/D ratio increases the load capability decreases because too much air is flowing so there is not a large pressure differential. As shown in Figure 6.15 with a radial clearance of .002" (.051 mm) the load capability rises then falls, with the maximum being at an L/D ratio of 1.5. Even at an L/D ratio of 1, when the radial gap is .0015" (.038 mm), the bearing will support 22 pounds (100 N). As shown in Figure 6.16, with a radial clearance of .004" (.102 mm), the performance begins to decrease.

Thus it seems that a workable aerostatic bearing that will run off of shop air can be obtained if the orifice diameter is .060" (1.52 mm), the L/D ratio is 1, the maximum radial clearance is .002" (.051 mm), and two such bearings are placed back to back which will enable moment loads to be resisted.

6.3 Conclusions

This chapter presented algorithms for designing measuring beam system components. The static performance of measuring beams subject to supporting gimbal reaction torques was found and a typical size system

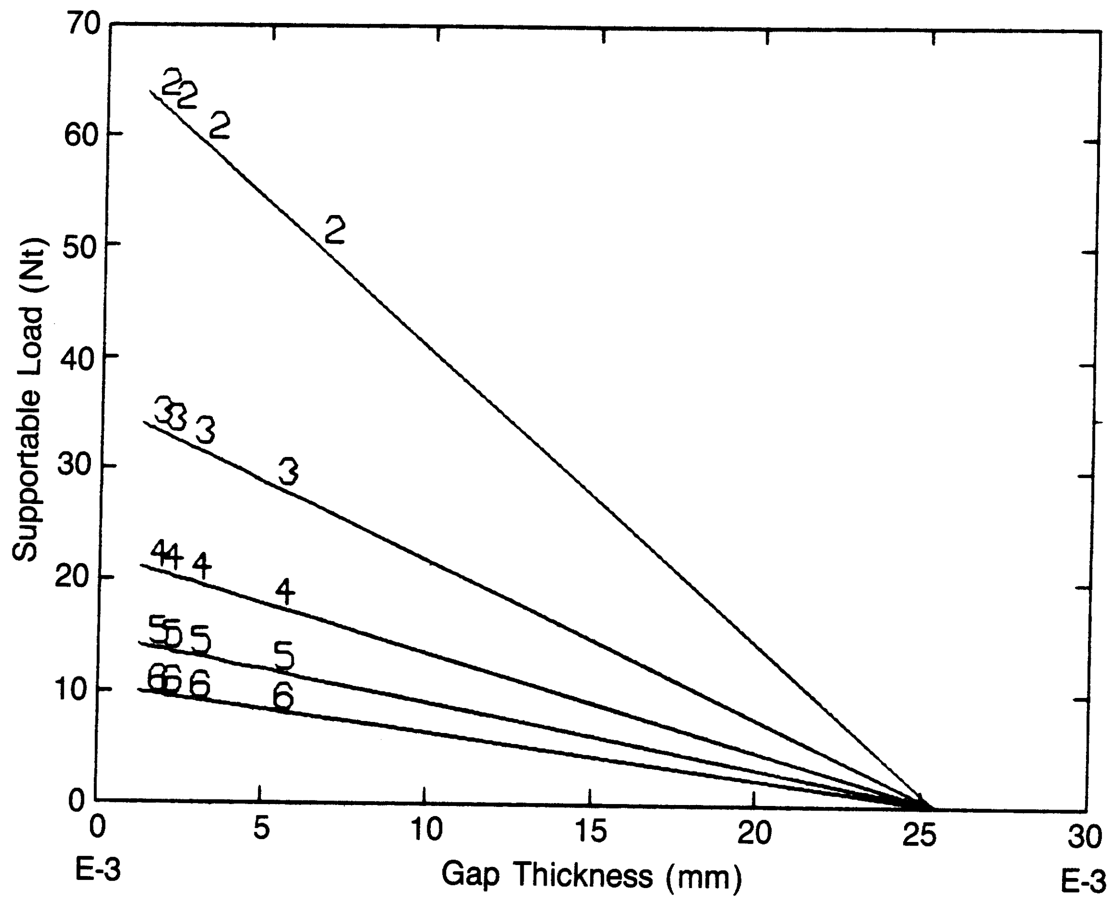

Figure 6.14 Aerostatic bearing performance with Cd = .6, a = .030″, C = .001″, L/D = .5 – 2.5, p = 80 psi

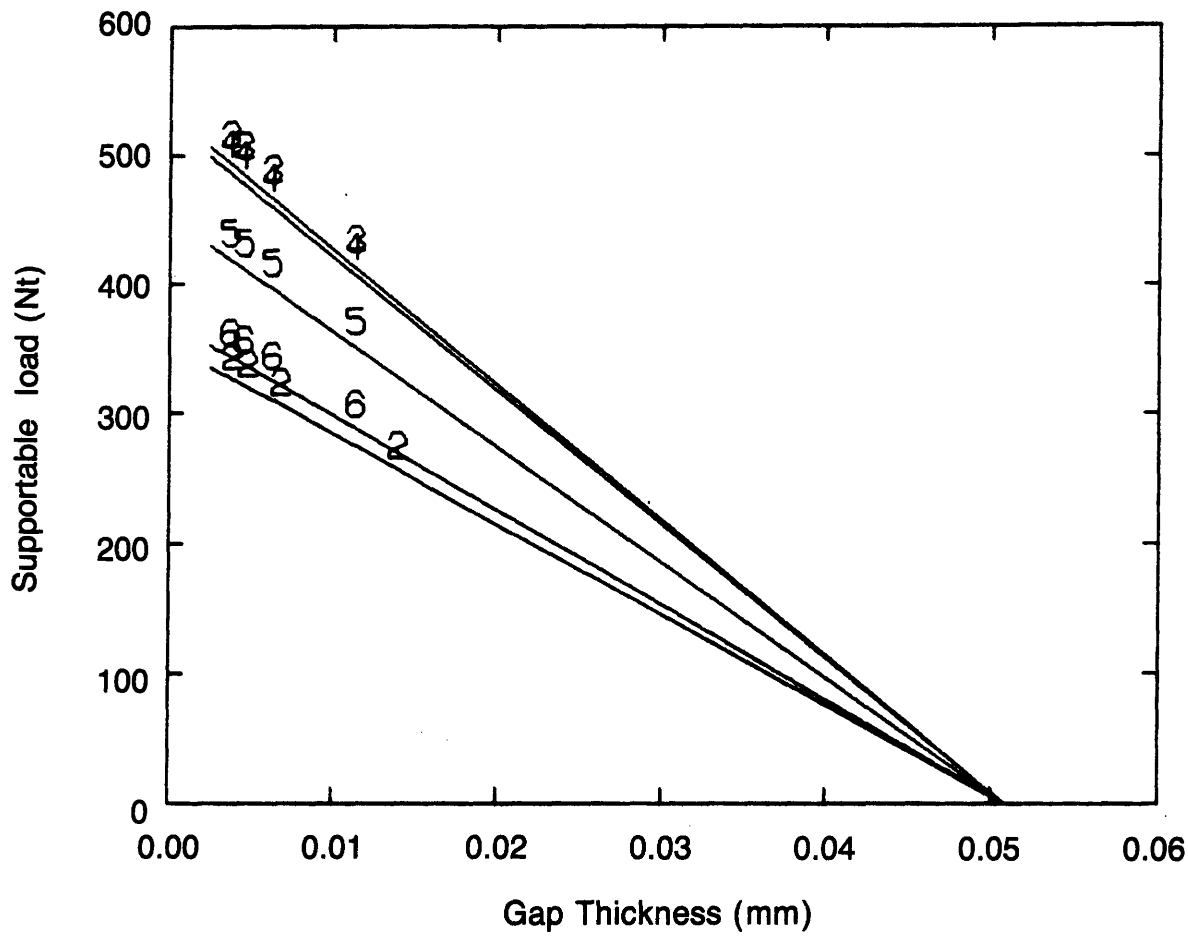

Figure 6.15 Aerostatic bearing performance with Cd = .6, a = .030, c = .002″, L/D = .5 − 2.5, p = 80 psi

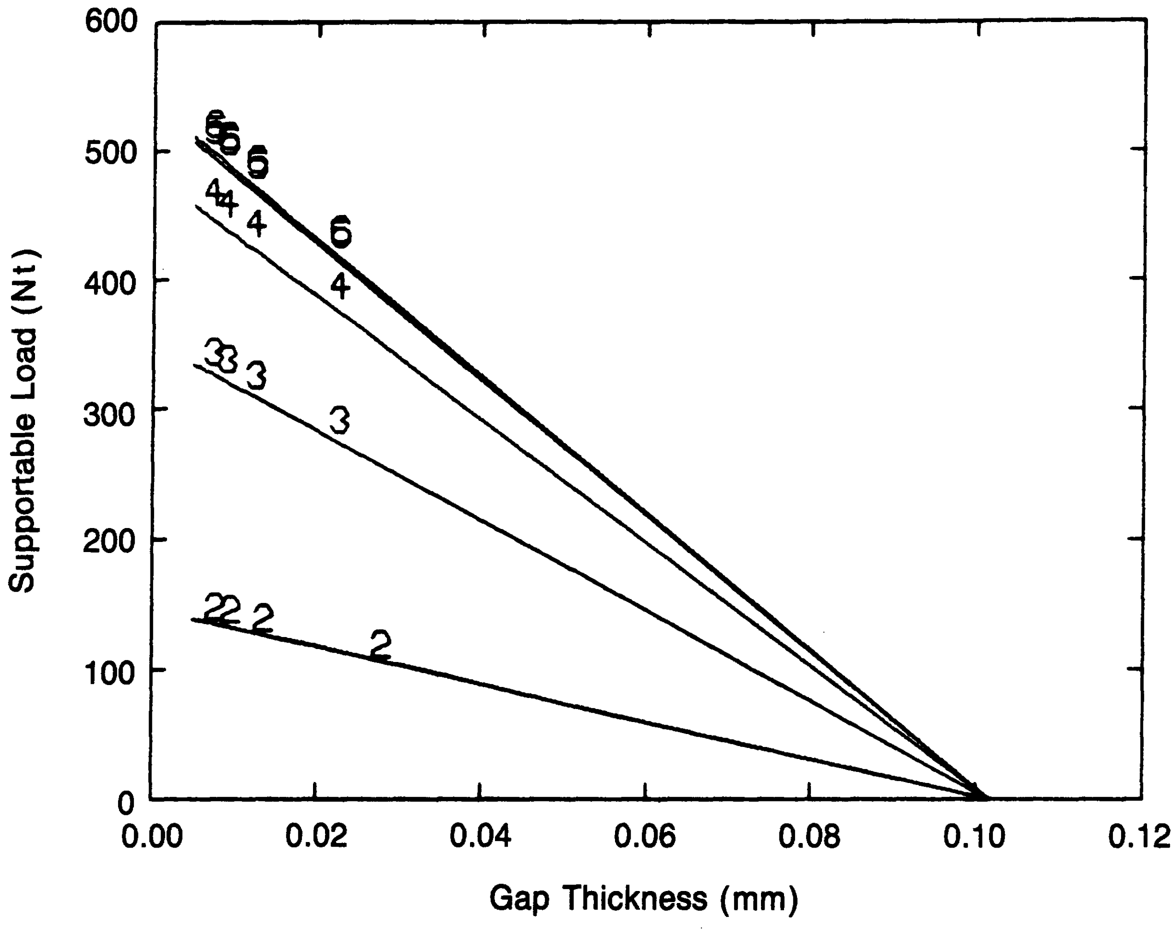

Figure 6.16 Aerostatic bearing performance with Cd = .6, a = .030″, C = .004″, L/D = .5 − 2.5, p = 80 psi

was designed. Similarly, the dynamic performance of a measuring beam system was compared to the dynamic performance of a typical two link articulated structure and a typical measuring beam first mode was found to be twice that of the structure. Various types of supporting gimbals, air, ball bearing, and aerostatic, were all found to be able to provide the desired performance. For the test system, a combination air/ball bearing gimbal system was chosen. Subsequently, a detailed algorithm was developed to aid in the design of low friction, large bearing gap aerostatic bearings (very economical to produce).

References

[6.1] J.J. O'Connor, 'The Role Of Elastic Stress Analysis in the Interpretation of Fretting Fatigue Failures' Fretting Fatigue, edited by Waterhouse, Applied Science Publishers London, 1981, pp23

[6.2] G.A. Tomlinson et al, Proceedings Institute of Mechanical Engineers, vol 141, 1939 p 223.

[6.3] S. Timoshenko, Theory of Elasticity McGraw Hill First Edition 1934, pp 339-350

[6.4] R.B. Waterhouse, 'Avoidance of Fretting Failures', Fretting Fatigue, edited by Waterhouse, Applied Science Publishers London, 1981, pp238

[6.5] A. Modjarrad, 'Ultra Precision Spindle Design', undated manuscript from Cranfield Unit for Precision Engineering, Cranfield, Bedford, UK.

[6.6] D. Sun 'Stability of Gas Lubricated, Externally Pressurized Porous Journal Bearings', Trans ASME Jou. Lub. Tech. July 1975, pp494

[6.7] O. Pinkus, B. Sternlight, Theory of Hydrodynamic Lubrication, Mcgraw-Hill NY, 1962, pp179-193

[6.8] H.E.G. Arneson 'Hydrostatic Bearing Structure', U.S. Patent #3,305,282, Feb. 21, 1967

[6.9] D.F. Wilcock, E.R. Booser, Bearing Design And Application, Mcgraw-Hill NY, 1957, pp355-365

[6.10] M.A. Rivas, A.H. Shapiro, 'On the Theory of Discharge Coefficients for Rounded-Entrance Flowmeters and Venturis', Trans ASME vol. 78, 1956, pp489-497

[6.11] D.H. Tsai, M.M. Slawsky, 'Determination and Correlation of Flow Capacities of Pneumatic Components', National Bureau of Standards Circular 588, Oct. 1957

[6.12] J.A. Perry, 'Critical Flow Through Sharp-edged Orifices', Trans ASME vol 71, 1949, pp757

APPENDIX 6A

Results of Finite Element Analysis of

Measuring Beam Dynamics

***** EIGENVALUE (NATURAL FREQUENCY) SOLUTION *****

MODE	FREQUENCY (CYCLES/TIME)
1	129.798310
2	140.721214
3	183.779175
4	201.010994
5	211.716768
6	426.793661

***** EIGENVECTOR (MODE SHAPE) SOLUTION *****

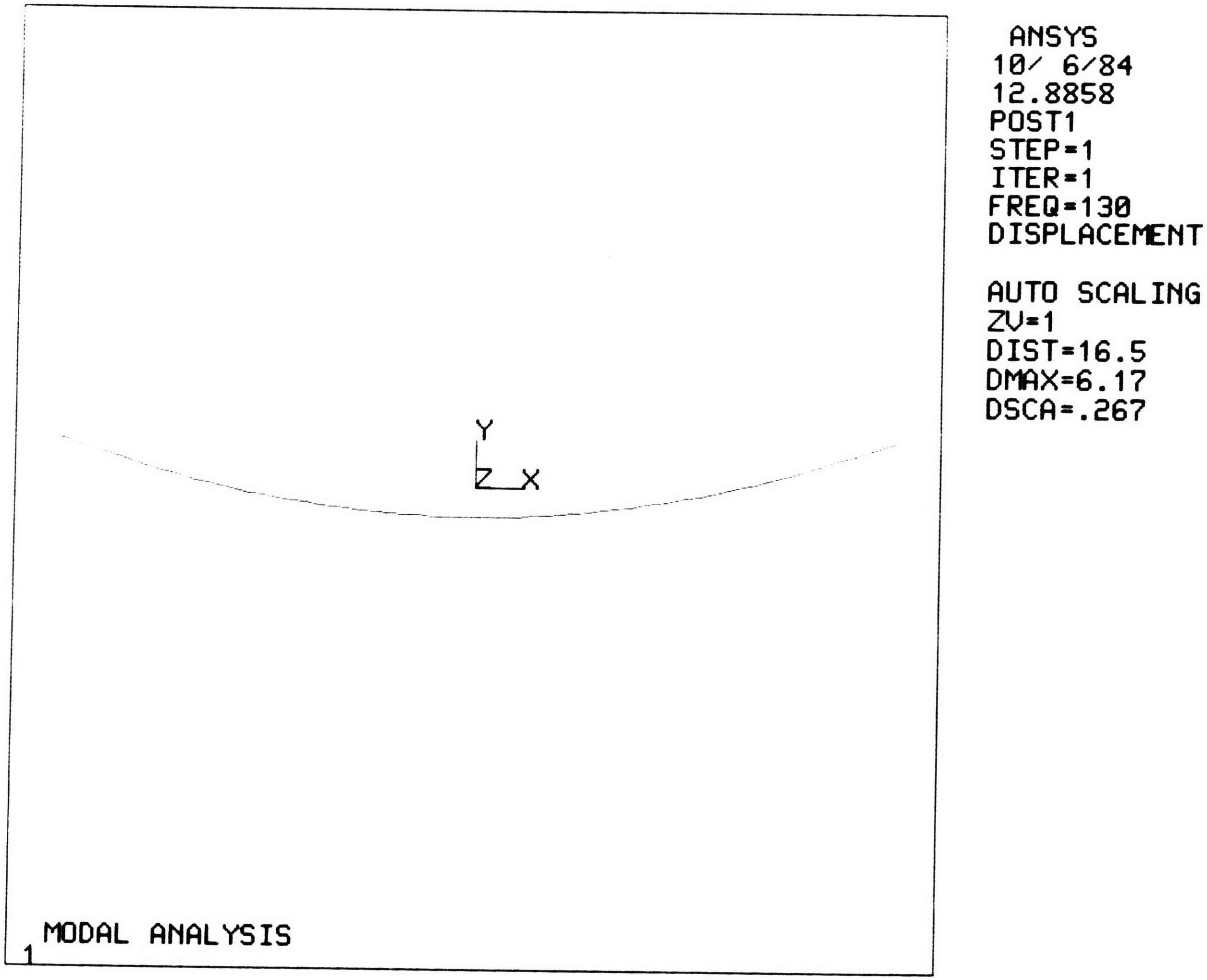
ANSYS
10/ 6/84
12.8858
POST1
STEP=1
ITER=1
FREQ=130
DISPLACEMENT
AUTO SCALING
ZV=1
DIST=16.5
DMAX=6.17
DSCA=.267
Y
Z X
1
MODAL ANALYSIS

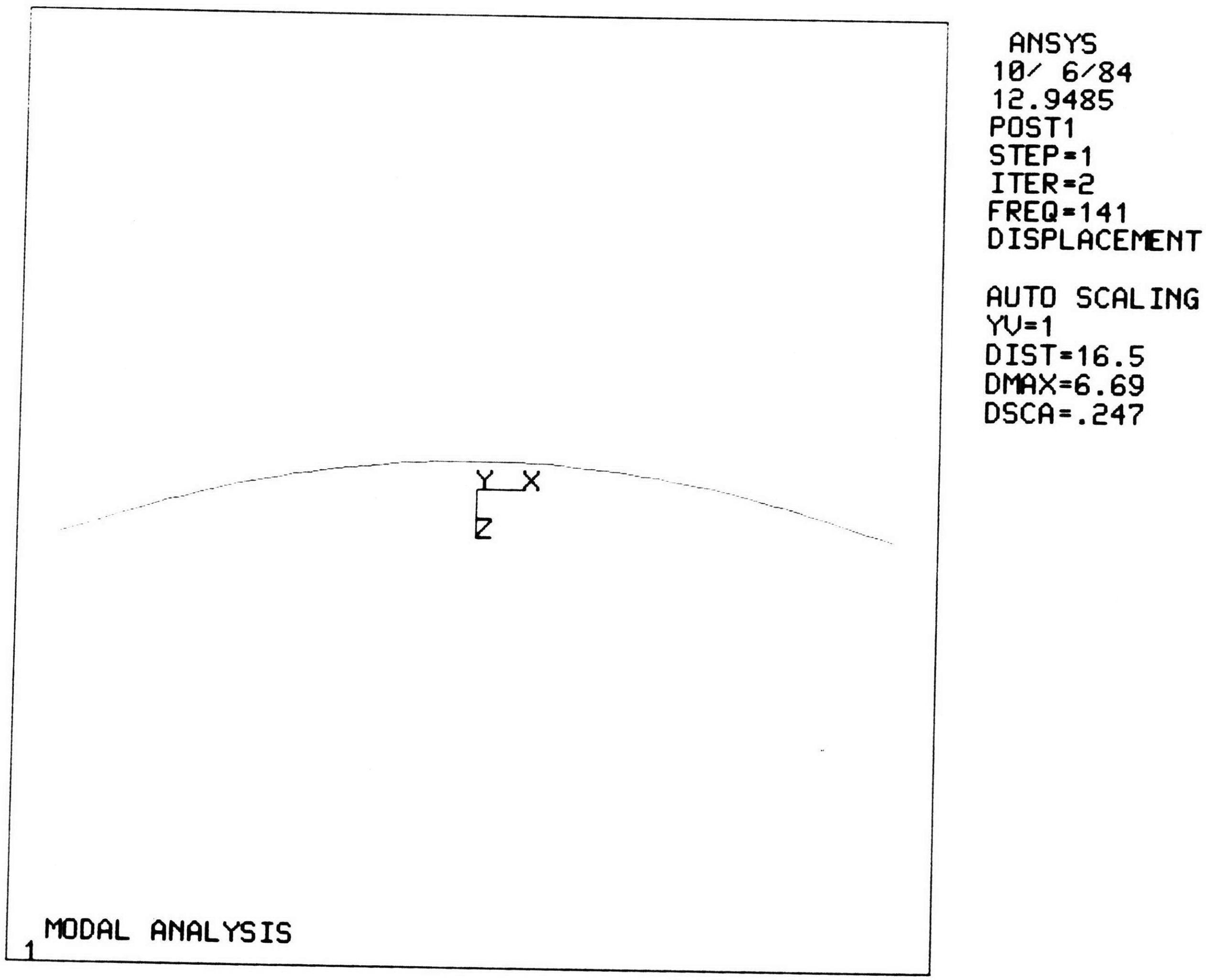
ANSYS
10/ 6/84
12.9485
POST1
STEP=1
ITER=2
FREQ=141
DISPLACEMENT
AUTO SCALING
YV=1
DIST=16.5
DMAX=6.69
DSCA=.247
Y
X
Z
1
MODAL ANALYSIS

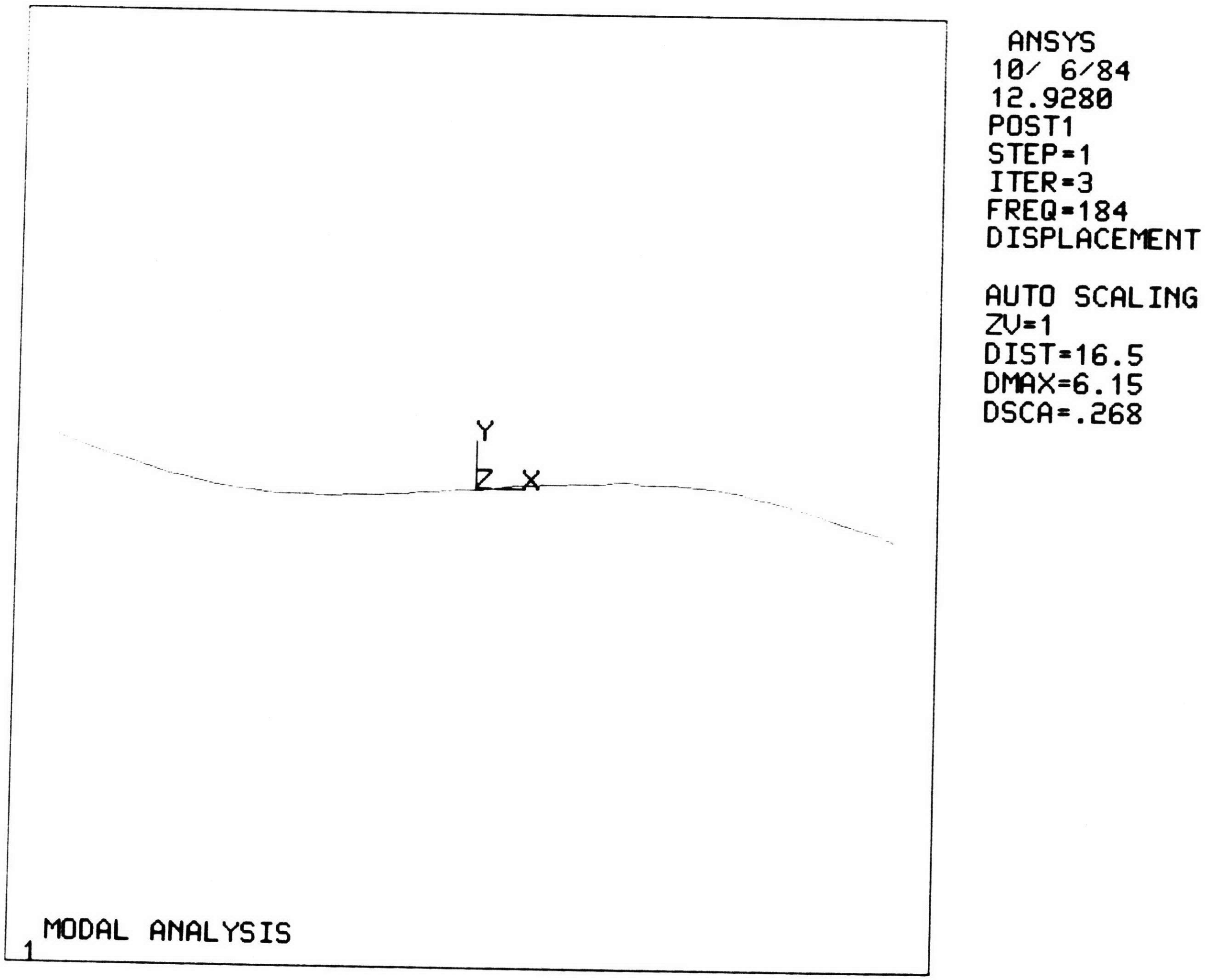
ANSYS
10/ 6/84
12.9280
POST1
STEP=1
ITER=3
FREQ=184
DISPLACEMENT
AUTO SCALING
ZV=1
DIST=16.5
DMAX=6.15
DSCA=.268
Y
Z X
1
MODAL ANALYSIS

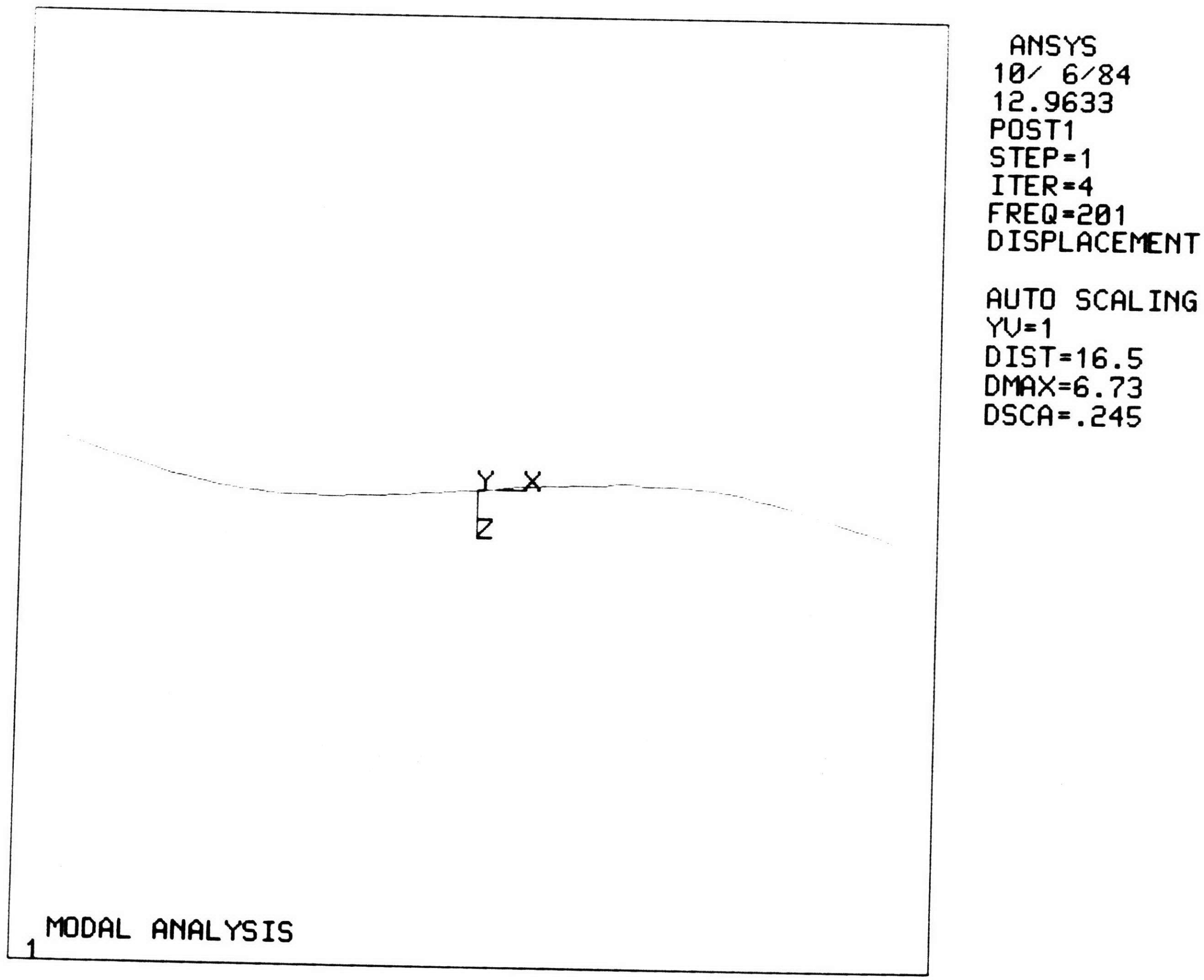
ANSYS
10/ 6/84
12.9633
POST1
STEP=1
ITER=4
FREQ=201
DISPLACEMENT
AUTO SCALING
YV=1
DIST=16.5
DMAX=6.73
DSCA=.245
Y
X
Z
1
MODAL ANALYSIS

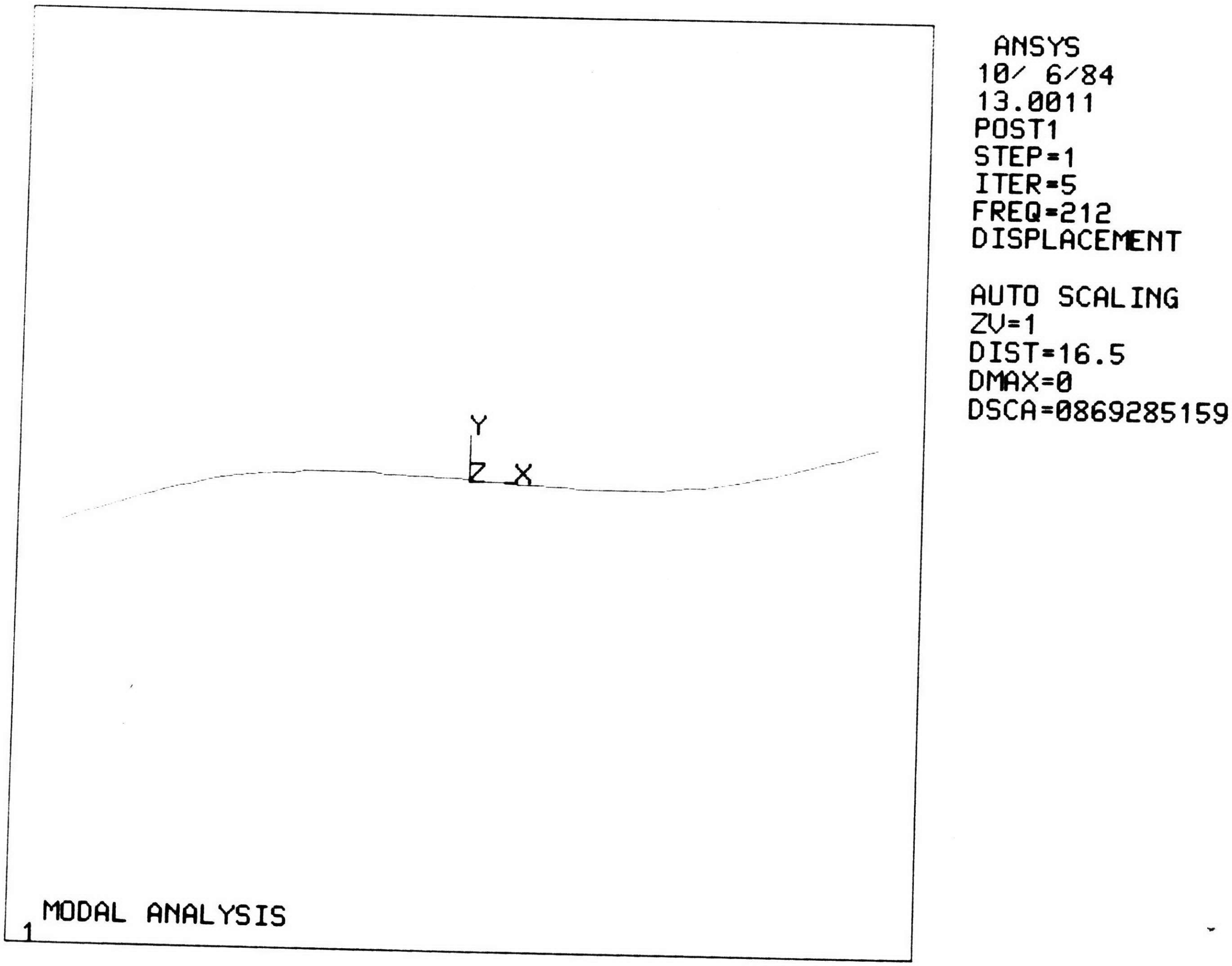
ANSYS
10/ 6/84
13.0011
POST1
STEP=1
ITER=5
FREQ=212
DISPLACEMENT
AUTO SCALING
ZV=1
DIST=16.5
DMAX=0
DSCA=0869285159
Y
Z X
1
MODAL ANALYSIS

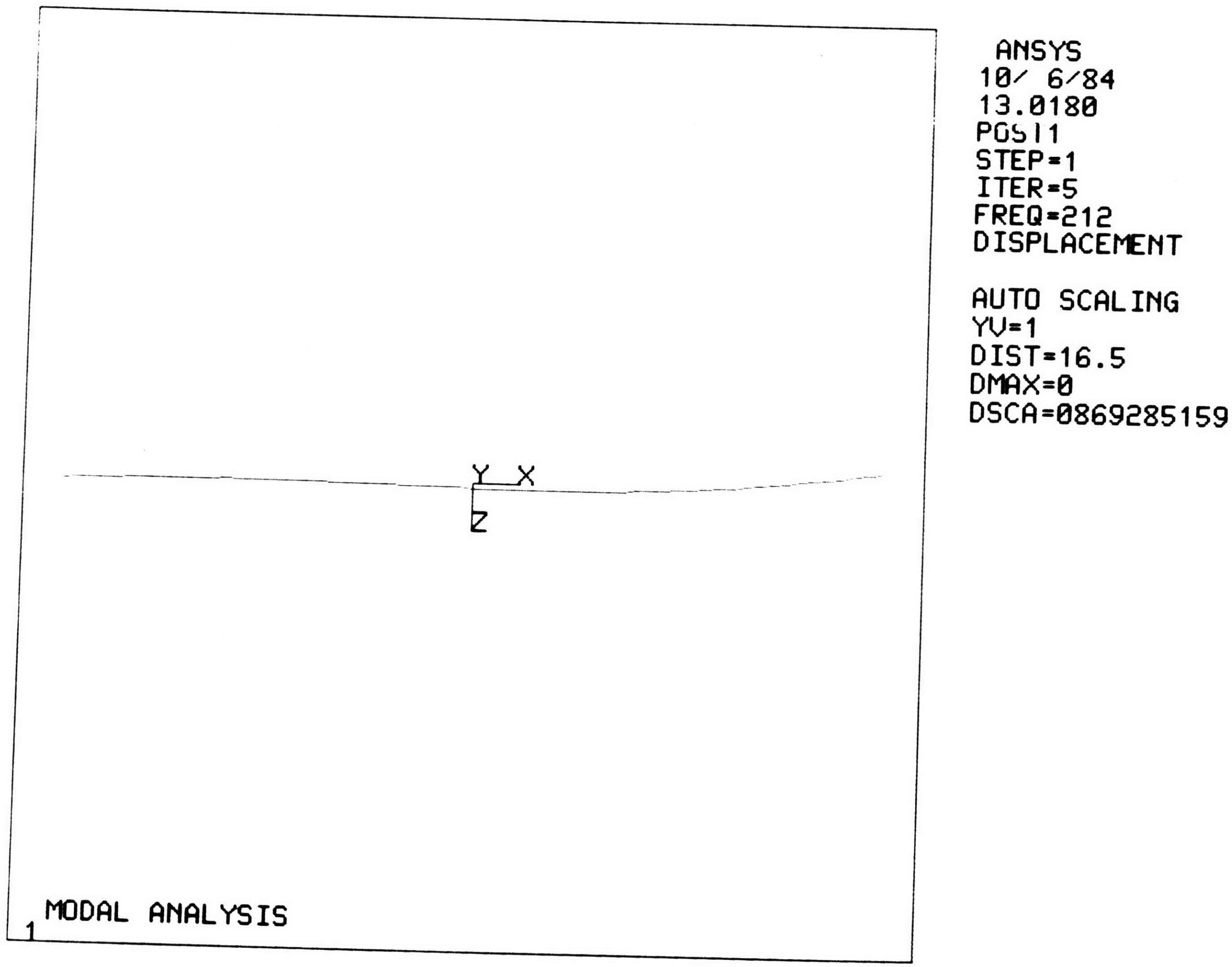
ANSYS
10/ 6/84
13.0180
POST1
STEP=1
ITER=5
FREQ=212
DISPLACEMENT
AUTO SCALING
YV=1
DIST=16.5
DMAX=0
DSCA=0869285159
Y
X
Z
1
MODAL ANALYSIS

APPENDIX 6B

FORTRAN Analysis Programs

```
        2        + 1.005 E-2*THETA +.2366
        C
                EM = 1.155 E-7*THETA**4 -3.466 E-5*THETA**3
        2        + .004062*THETA**2 - .2353*THETA + 6.9756
        C
        C
                A = EM*(.75*P*(AETA1 + AETA2)/BPA)**.333
        C
                B = EN*(.75*P*(AETA1 + AETA2)/BPA)**.333
        C
                SIGMAC = 1.5*P/(3.14*A*B)
        C
        C
                TAUMAX = .3*SIGMAC
        C
                PRINT*, 'A = ',A
                PRINT*, 'B = ',B
        C
                PRINT*,  'THE MAX. COMPRESSIVE STRESS IS: ',SIGMAC,' PSI'
                PRINT*, ' '
                PRINT*, 'THE MAX. SHEAR STRESS IS: ',TAUMAX,' PSI'
        C
                END
```

```
PROGRAM SECTIONS

    Name                                        Bytes   Attributes

  0 $CODE                                        1290   PIC CON REL LCL   SHR    EXE    R
D NOWRT LONG
  1 $PDATA                                        521   PIC CON REL LCL   SHR  NOEXE    R
D NOWRT LONG
  2 $LOCAL                                        244   PIC CON REL LCL NOSHR  NOEXE    R
D   WRT LONG

    Total Space Allocated                        2055

ENTRY POINTS

    Address   Type  Name

  0-00000000        CONTACT

VARIABLES

    Address   Type  Name                  Address   Type  Name                 Address  T
ype  Name               Address   Type  Name

  2-00000044  R*4  A                   2-00000014  R*4  AETA1                2-00000018
R*4  AETA2               2-00000048  R*4  B
  2-00000034  R*4  BMA                 2-00000030  R*4  BPA                  2-00000000
R*4  E1                  2-00000004  R*4  E2
  2-00000040  R*4  EM                  2-0000003C  R*4  EN                   2-00000010
R*4  P                   2-00000008  R*4  PNU1
```

```

      PROGRAM CONTACT
C
C     CALCULATES MAX COMPRESSIVE AND MAX SHEAR STRESSES
C     OF TWO SURFACES IN CONTACT.
C
      PRINT*, 'YOUNGS MODULUS OF MATERIAL 1? (PSI)'
      ACCEPT*,  E1
      PRINT*, 'YOUNGS MODULUS OF MATERIAL 2? (PSI)'
      ACCEPT*, E2
      PRINT*, 'POISONS RATIO OF MATERIAL 1?'
      ACCEPT*, PNU1
      PRINT*, 'POISONS RATIO OF MATERIAL 2?'
      ACCEPT*, PNU2
      PRINT*, 'APPLIED LOAD? (LBS)'
      ACCEPT*, P
C
      AETA1 = (1-PNU1**2)/E1
      AETA2 = (1-PNU2**2)/E2
C
      PRINT*, 'IF OBJECT 1 IS INSIDE OBJECT 2 THEN OBJECT 2'
      PRINT*, 'HAS NEGATIVE RADII, AND VISA-VERSA.'
      PRINT*, ' '
      PRINT*, 'IF ANY OF THE FOLLOWING ARE INFINITE, ENTER ZERO'
C
      PRINT*, 'MIN. RADIUS OF OBJECT 1? (IN)'
      ACCEPT*, R1
      PRINT*, 'MAX. RADIUS OF OBJECT 1? (IN)'
      ACCEPT*, R11
      PRINT*, 'MIN. RADIUS OF OBJECT 2? (IN)'
      ACCEPT*, R2
      PRINT*, 'MAX. RADIUS OF OBJECT 2? (IN)'
      ACCEPT*, R22
C
      PRINT*, 'ANGLE, IN DEG., BETWEEN THE PLANES WITH THE'
      PRINT*, 'MIN. OR MAX. RADII?'
      ACCEPT*, PSI
C
      PSI = (3.14*PSI)/180
C
      IF (R1 .EQ. 0.)  GOTO 100
         R1 = 1/R1
  100 IF (R11 .EQ. 0.) GOTO 200
         R11 = 1/R11
  200 IF (R2 .EQ. 0.)  GOTO 300
         R2 = 1/R2
  300 IF (R22 .EQ. 0.) GOTO 400
         R22 = 1/R22
C
C
  400 BPA = .5 *(R1 + R11 + R2 + R22)
      BMA = .5*((R1-R11)**2 + (R2-R22)**2 + 2*(R1-R11)*
     1     (R2-R22) * COS(2*PSI))**.5
C
      THETA = 180/3.14 * ACOS(BMA/BPA)
C
      EN = 5.454 E-7 *THETA**3 -6.659 E-5*THETA**2
```

```
DATA FOR AIR BEARING DESIGN. enter dimensions in required units!!!
Enter bearing radius R (mm)
25.4
Enter radial clearance C (mm)
.1016
Enter supply pressure (Pascals)
551584.0
Enter ambient pressure (Pascals)
101353.6
Enter viscosity of air (Kg/m-s)
1.853E-05
Enter density of air (lbm/in**3)
1.183
Enter orifice radius (mm)
.8
Enter discharge coeff.
.6
Enter number of orifices
8.
CHARACTER DATA
Enter 40 character x label for load vs gap thickness
Gap Thickness (mm)
Enter 40 character y label for load
Supportable load (Nt)

end of data input
```

```
CCCCCCCCCCCCCCCCCCCCCCCCCCCCCCCCCCCCCCCCCCCCCCCCCCCCCCCCCCCCCCCCCCC
C
C      AIR.FOR by Alex Slocum, Sept. 10, 1984, to analyze performance
C      capabilities of air bearings
C
CCCCCCCCCCCCCCCCCCCCCCCCCCCCCCCCCCCCCCCCCCCCCCCCCCCCCCCCCCCCCCCCCC
       REAL LOAD(6,20)
       REAL mu, L, Lt, m, K, LD
       CHARACTER*40, XLABL, YLABL
       OPEN(UNIT = 4, NAME = 'AIR.INP', STATUS = 'OLD')
       OPEN(UNIT = 7, NAME = 'AIR.OUT', STATUS = 'NEW')
       READ(4,10) R, C, ps, pa, mu, rho, a, Cd, m
10     FORMAT( //9(G12.4//) )
       READ(4,11) XLABL, YLABL
11     FORMAT( 2( A40// ) )
       R = R/1000.  !CONVERT mm to m
       C = C/1000.
       A = A/1000.
       print*,  R, C, ps, pa, mu, rho, a, Cd, m,
      1     XLABL, YLABL, XLABS, YLABS
       DO 20 I = 1, 20
          LOAD(1,I) = 1000.*C/REAL(I)  ! surface gap mm
20     CONTINUE
       D = 2.*R
CCCCCCCCCCCCCCCCCCCCCCCCCCCCCCCCCCCCCCCCCCCC
CCCC LOOP OVER L/D RATIOS
CCCCCCCCCCCCCCCCCCCCCCC
       DO 100 I = 1, 5
          L = REAL(I)*R
          LD = L/D
          WRITE(6,12) LD, Cd, 2000.*a
          WRITE(7,12) LD, Cd, 2000.*a
12        FORMAT(//10X,'L/D = ',G12.4,5X,'Cd = ',G12.4,5X,
      1      'Nozzle D (mm) = ',G12.4/10X,
      1      'BEARING GAP',5X,'SUPPORTABLE LOAD',5X,' STIFFNESS',5X,
      1      'ECCENTRICITY'/10X,'     mm     ',5x,'       Nt        ',5x,
      1      '    Nt/mm ',5X,'     MM' /)
          DO 200 J = 1, 20  ! LOOP OVER ECCENTRICITY RATIOS
             e = 1. - 1./REAL(J)   ! ecentricity ratio
             AA = (2.25*Cd*Cd*L*L*mu*mu*m*a**4)/(R*R*rho*(ps-pa)*C**6)
             Lt = AA*( 1. + SQRT(1. + 2./AA) )
             Y = SQRT( ( LD*(1. + Lt) )/( Lt*((ps/pa)**2 - 1. )) )
             Ys = Y*Y
             fY = SQRT( Ys + LD )
             psi1 = DAWS(fy)/EXP(-fY*fY)
             psi2 = DAWS(Y)/EXP(-Y*Y)
             FYLD = 2.3562*( EXP(-Ys)*( psi1 - psi2 )
      1             - .8862*EXP(Ys)*(ERF(fY) - ERF(Y) ) )
             W = L*D*pa*e*FYLD/( ( LD*COSH(LD) + Lt*SINH(LD) )*Y )
             EE = 1000.*C*E
             K = W/(EE + 1.E-08)
             LOAD( I+1, J) = W
             WRITE(7,201) LOAD(1,J), W, K, E
201          FORMAT(9X,G12.4, 7X, G12.4, 4X, G12.4, 5X, G12.4)
200       CONTINUE
             WRITE(6,201) LOAD(1,J), W, K, E
100    CONTINUE
```

```
0058          CALL QPICTR( LOAD, 6, 20, QY(2,3,4,5,6), QX(1), QXLAB(XLABL),
0059        1              QYLAB(YLABL), QLABEL(4) )
0060          STOP
0061          END
```

PROGRAM SECTIONS

```
    Name                                    Bytes   Attributes

  0 $CODE                                    1243   PIC CON REL LCL   SHR    EXE    R
D NOWRT LONG
  1 $PDATA                                    267   PIC CON REL LCL   SHR NOEXE    R
D NOWRT LONG
  2 $LOCAL                                    904   PIC CON REL LCL NOSHR NOEXE    R
D   WRT LONG

    Total Space Allocated                    2414
```

ENTRY POINTS

```
    Address    Type  Name

  0-00000000         AIR$MAIN
```

VARIABLES

```
    Address    Type  Name             Address    Type  Name                    Address    T
ype  Name              Address    Type  Name

  2-0000025C  R*4   A             2-0000027C  R*4   AA                  2-0000024C
R*4  C              2-00000260  R*4  CD
  2-00000270  R*4   D             2-00000278  R*4   E                   2-0000029C
R*4  EE             2-00000288  R*4  FY
  2-00000294  R*4   FYLD          2-0000026C  I*4   I                   2-00000274
I*4  J              2-00000240  R*4  K
  2-00000234  R*4   L             2-00000244  R*4   LD                  2-00000238
R*4  LT             2-0000023C  R*4  M
  2-00000230  R*4   MU            2-00000254  R*4   PA                  2-00000250
R*4  PS             2-0000028C  R*4  PSI1
  2-00000290  R*4   PSI2          2-00000248  R*4   R                   2-00000258
R*4  RHO            2-00000298  R*4  W
  2-000001E0  CHAR XLABL          2-00000264  R*4   XLABS               2-00000280
R*4  Y              2-00000208  CHAR YLABL
  2-00000268  R*4   YLABS         2-00000284  R*4   YS
```

ARRAYS

```
    Address    Type  Name                   Bytes  Dimensions

  2-00000000  R*4   LOAD                     480   (6, 20)
```

(this page left blank)

Chapter 7

Methods and Results of Calibration and Testing Procedures of a Measuring Beam System for Articulated Structures

7.1 Introduction

Chapter 3 described the necessary components for a goniometer to measure robot motion using non-contact sensing motions. Chapter 5 derived the error budgets necessary to determine how accurate such a system could be and Chapter 6 formulated general design algorithms and presented a specific test design for a measuring beam system (goniometer) to determine position and orientation of articulated structures. This chapter will focus on the procedures for calibration and testing of the measuring beam system as they were performed. Actual results will be reported along with their effect on the final measurements (using equations derived in Chapter 5). The final test results for the assembled POSOR are presented with conclusions in Chapter 8.

The first section of this chapter will discuss the general experimental setup used in calibrating measuring beam system components. It will also discuss errors in the calibration tests caused by environmental effects and physical misalignments in the system. The individual calibration experiments and their results are then discussed in detail. From the results of the calibrations, the achievable error for the POSOR is predicted using the system error budgets formulated in Chapter 5.

The first experiment will be to gather data on the gimbal bearing coefficients of friction, to ensure that the maximum allowable coefficient of friction (Equation 6.11) is not exceeded. Also the air bearing performance will be tested to determine its maximum load capability. The next set of experiments entail calibrating the light source lateral effect diode system which includes: determining stability and repeatability of the lateral effect diodes, linearization of the lateral effect diodes, determining the X and Y axes offsets of the diodes, and determination of the light source inclination angles. The last set of experiments entail calibrating the impedance probe system which includes tests for: linearization, stability and repeatability, and probe spacing.

7.2 General Experimental Environment During Calibration of POSOR Components

All the experiments were performed in a room which was temperature and access controlled. The general setup is shown in Figure 7.1 which shows the electronics bench, laser interferometers, and the CNC vertical machining center used as a stage (these components are discussed in greater detail in following sections). All critical measurements were performed with stationary components clamped and epoxied in place, and all setups were stress relieved with a calibration hammer (a good solid blow to the vertical machining center table).

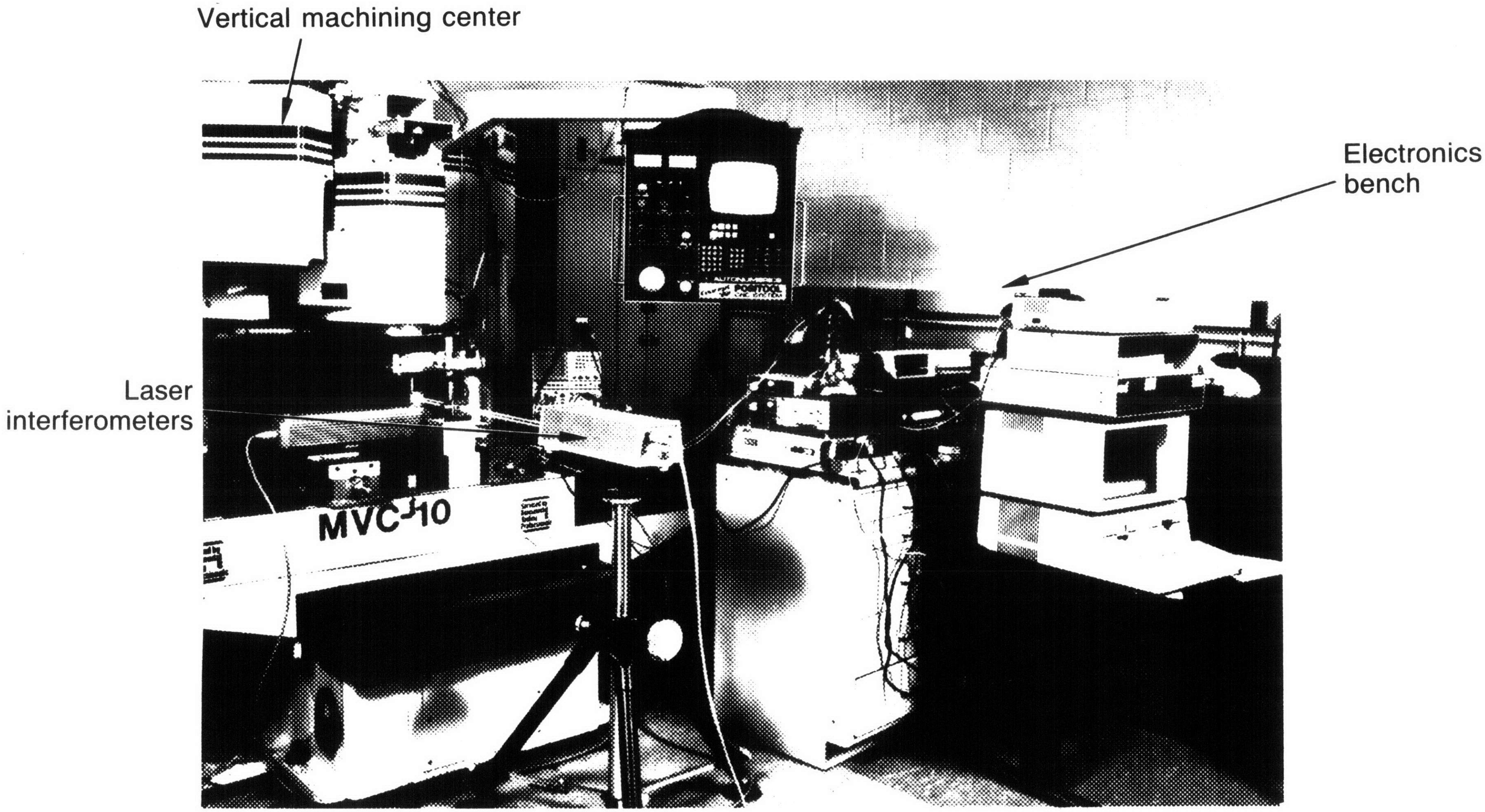

Figure 7.1 General experimental setup for calibration of POSOR components

The critical factors in a calibration experiment for a mechanical metrology system are: temperature control, accuracy of measuring instruments, alignment (of sensor axis, measurement axis, and motion control axis), accuracy of motion control system, and accuracy of electronics. Before testing the components, however, the system itself must be tested to determine accuracy, stability, and repeatability. This is done by using devices such as laser interferometers and standard reference voltage supplies. These tests are discussed in detail below.

Environment: The atmospheric environment of the room in which the calibration measurements were made can affect them by way of thermal expansion, varying the velocity of light, and causing drift in the electronics. During the entire experiment, the temperature in the room never varied more than .1° F (.06° C). By keeping the distance between the laser optics less than .5", 2" and 10" (12.7, 50.8, 254 mm) for the impedance probes and the lateral effect diode Y and X axis measurements respectively, the thermal growth error due to the cast iron stage would be at most .3 μin, 1.2 μin and 6.0 μin (.01, .03, and .15 μm) respectively. The principal error in the laser interferometer measurements occurred from the changing barometer readings which affect the velocity of light compensation factor [7.1]. For 24 hour runs, the worst case error was (.9997300 - .9997350) = 5 μin/inch distance between the interferometer and the retroreflector. For any one calibration run (less than 12 hours) the error was (.9997300 - .9997310) = 1 μin/inch. In general, tests were not run when a changing weather system was predicted (changing barometric pressure affects the velocity of light in air). The electronics were not affected by the small variations in air properties as was shown by testing with a standard reference voltage supply.

Mechanical Systems: Calibration measurements are made by varying a quantity a known amount and comparing it to the sensor reading which requires careful alignment of the components. For the distance measurements made, the alignment of the axes of the laser interferometer, the actuation stage, and the sensor was done using a dial gauge set in the spindle of the vertical machining center. The maximum alignment error was at most .002 inch per inch which results in a cosine error of 4 μin per inch of travel. Alignment of angular motion axes is discussed in the section on determining distance between the impedance probes.

Accuracy and repeatability of the motion control system axes is important in keeping Abbe's offset error (see section 4.1) at a minimum. Specifically, yaw, pitch, roll, and straightness of the axes need to be measured. For the Auto Numerics MVC-10 CNC vertical machining center used as a stage, the angular motions about the X and Y axes were all about 1 arc second per inch of travel, and the straightness was on the order of 5 μinch per inch (.13 μm/m) of travel. The biggest source of error was a computer controlled stepper motor driven stage as discussed in detail below.

For reasons discussed in Section 7.4.1 (calibration of the lateral effect diodes), it was necessary to use a computer controlled stepper motor driven stage. The accuracy and repeatability characteristics of the stage (which were not good) are discussed below, their effect on the calibration of sensors is discussed in the specific description of the experiment.

The straightness, yaw, and pitch of a Klinger computer controlled stepper motor driven ball slide stage with .75" of travel were measured using interferometery techniques described in Chapter 4. These motions about the stage axis of motion are shown schematically in Figure 7.2. The straightness is shown in Figure 7.3. The curve is at an incline because of a misalignment between the laser axis and the stage motion. Extreme care was not taken during alignment of the straightness optics because some incline is always present and it is easier to remove the incline with a software correction. As shown in Table 7.1, 6 runs were made with a mean variation in straightness of of .000408" (10 μm). The repeatability, however is only on the order of .001" (.0254 mm). The yaw is shown in Figure 7.4 and shows a repeatability of about 5 arc seconds. The pitch is shown in Figure 7.5 and shows a repeatability of about 2 arc seconds with the exception of a bump of about 10 arc seconds at an X position of .3" (7.6 mm).

Electronics: All calibration data was acquired digitally. The data aquisition system and Klinger stage were controlled by an HP 9836 microcomputer. Motions of the machine tool had to be controlled manually using the machine tool controller. To digitize the sensor signals, a Hewlett Packard Corp. 3421A Data Aquisition/Control Unit was used.

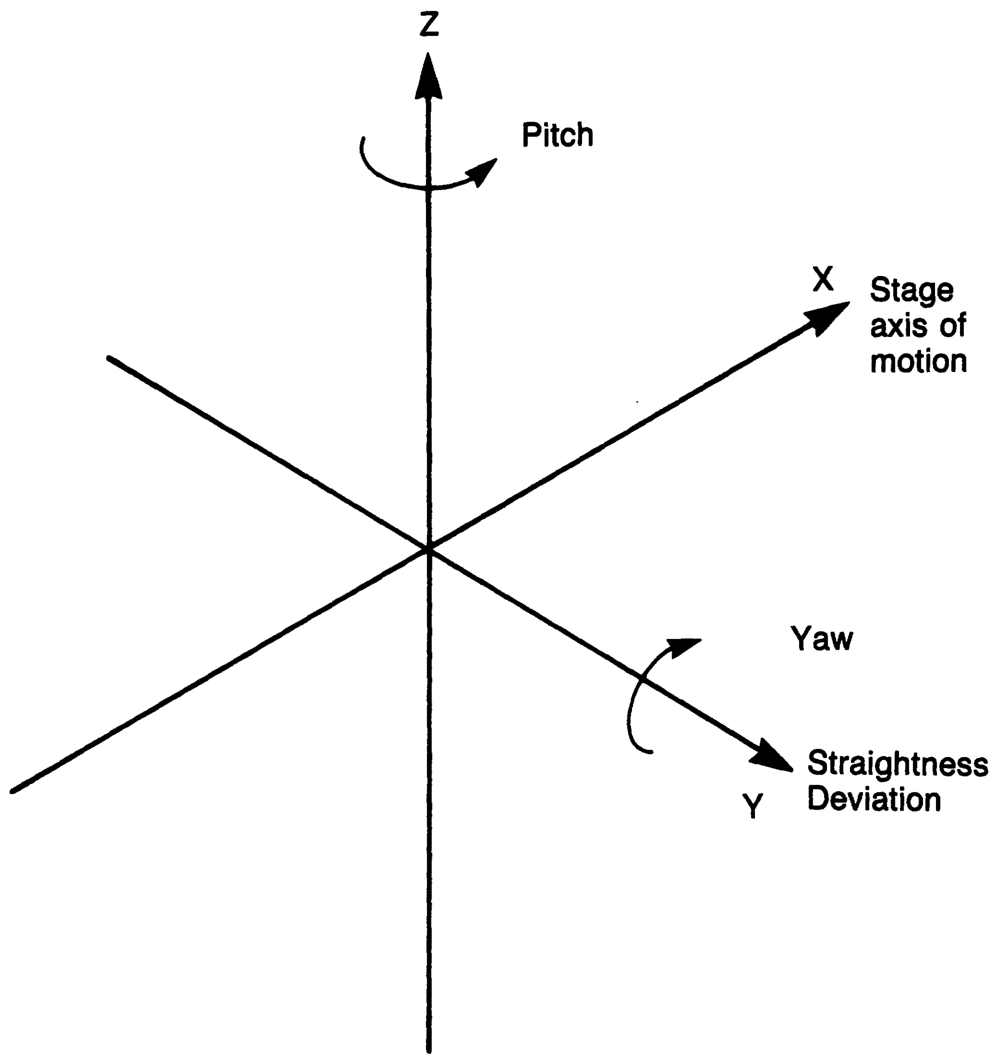

Figure 7.2 Measured errors in Klinger stage motion

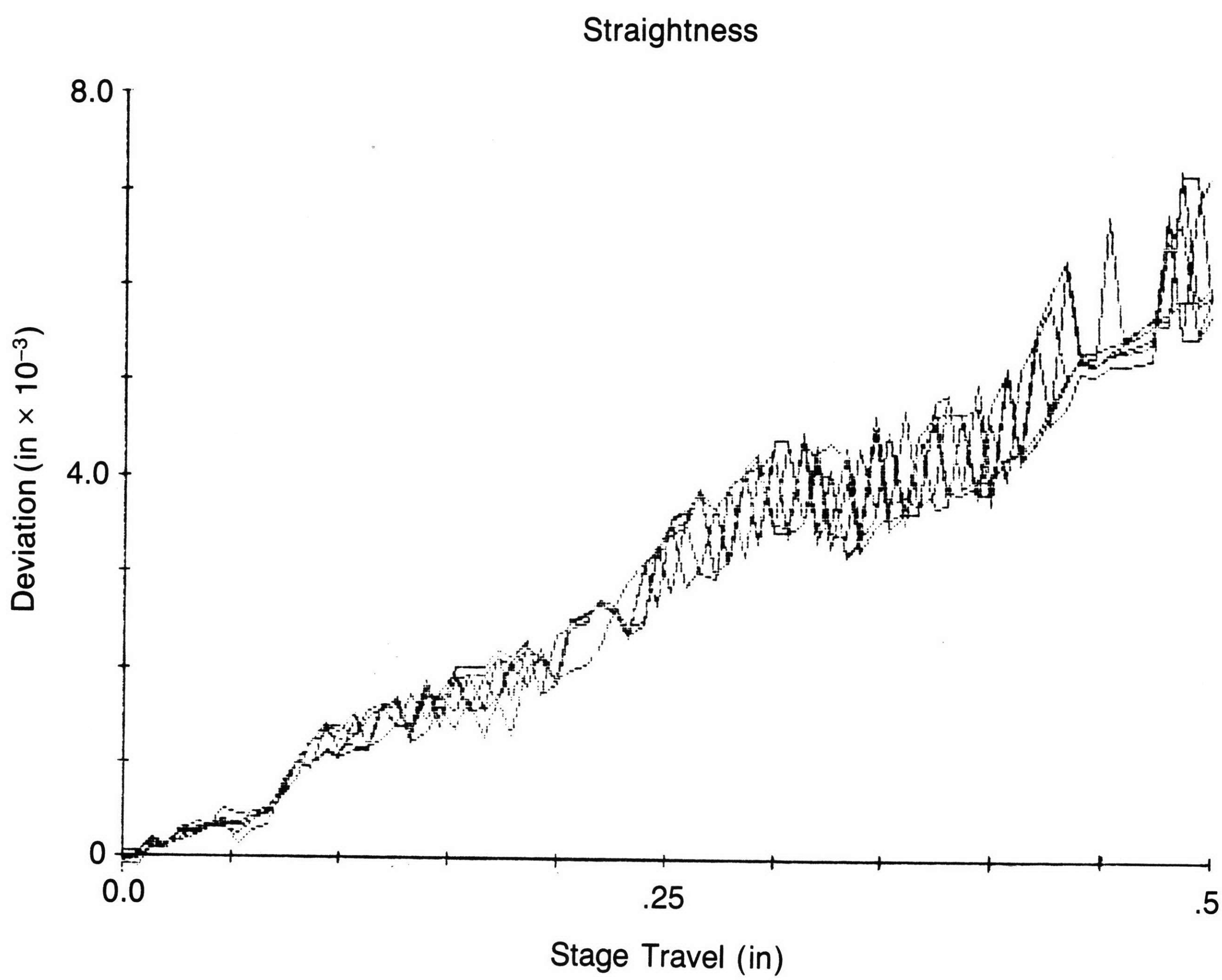

Figure 7.3 Straightness of Klinger computer controlled stage

Table 7.1 Straightness of Klinger Computer Controlled Stage

Run	b^* (in)	m^*	Deviation (in)
1	-.000322	.012730	.000410
2	-.000213	.012335	.000416
3	-.000193	.012382	.000396
4	-.000131	.011912	.000399
5	-.000111	.011923	.000404
6	-.000086	.012072	.000422

* These are the coefficients to a linear curve fit of individual runs all shown in Figure 7.3 (i.e $y = mx + b$)

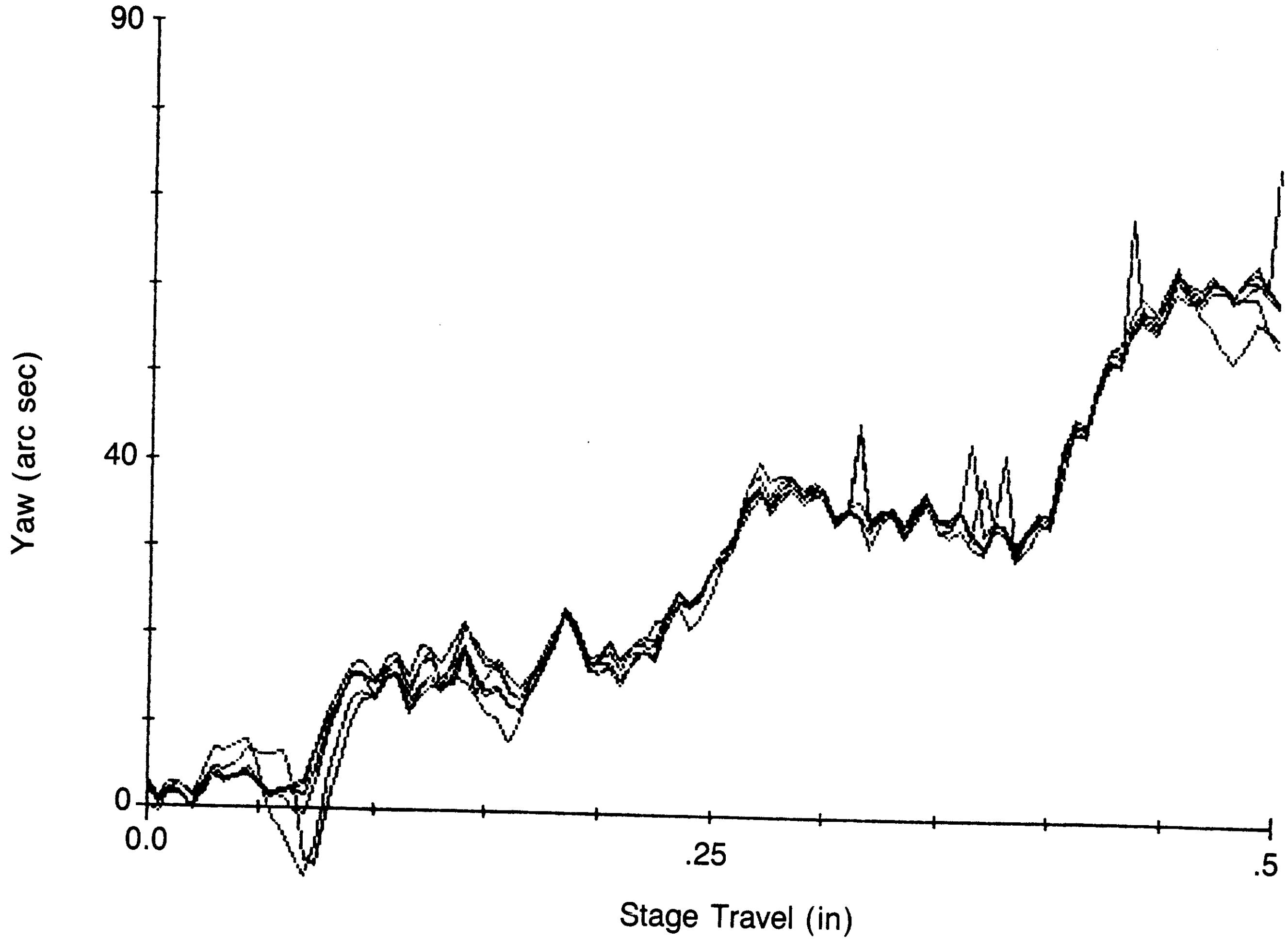

Figure 7.4 Yaw of Klinger computer controlled stage

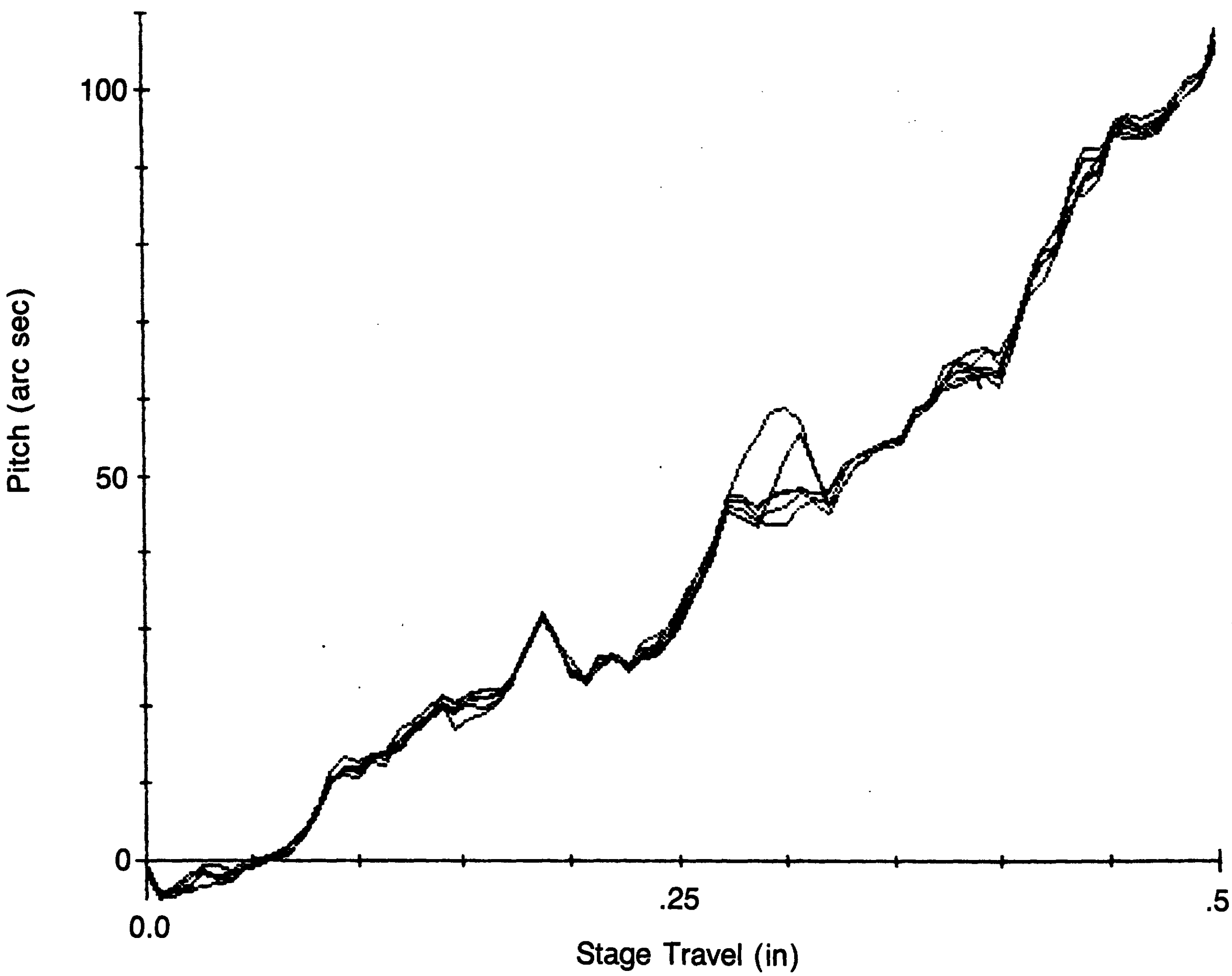

Figure 7.5 Pitch of Klinger computer controlled stage

The analog to digital converters in the data aquisition unit are of the dual slope type so most noise is integrated out. Depending on the sampling time, different bit accuracies can be obtained. For this experiment (performed in the static mode), the sampling time was not important compared to accuracy, so the maximum resolution range (which allows 10 readings per second from all channels to be taken) on the data acquisition unit was chosen. In this mode, the 60 cycle noise rejection is 80 dB. It was found that the best performance was obtained from taking five readings and discarding the outlying point. This allowed for filtering of random spikes that seemed to occur once every day or so.

The accuracy of the data aquisition system was tested (using a standard reference voltage supply), and was found to meet the manufacturer's specifications [7.2]. For example, when operating in the $5^1/_2$ digit range with input range of ± 1 volt, accuracy of ± 65 μV can be obtained (1 part in 15,385 or 14 bits). This would correspond to .625"/15385 = 41 μin (1 μm) on the diode and .05"/15385 = 3 μin (.08 μm) for the impedance probes. Note that the unit had an "auto ranging" feature which allowed 14 bit accuracy for different maximum voltage levels.

Similarly, to test the stability of the wire wrapped circuit board used for processing the diode output, a standard reference voltage supply was used as an input (to simulate the output from the diodes) to the board and the output was read with the analog to digital converter. The accuracy of the system was found to be equal to that of the analog to digital converter, so for all intents and purposes, the board was "perfect". Similarly, the combination of the board and the "regular" voltage supply were found to be stable to the amount that could be read by the analog to digital converter.

7.3 Determination of Bearing Coefficients of Friction

This section describes tests on the candidate bearings for use on the four and two degree-of-freedom gimbals described in 6.4.3.1. These tests are necessary to determine if bearings designed to resist fretting corrosion also have low enough coefficients of friction to prevent distortions of measuring beam components.

The maximum load the aerostatic bearing could support without any high spots dragging was determined by holding the 2 degree-of-freedom gimbal while loading weights on top of the bearing. This value was found to be 20 - 25 pounds. For the back to back bearing construction shown in Figures 6.10 and 6.11, there is no vent between the rings of orifices, so the unit was probably acting as a single bearing with an L/D ratio of 2. The measured radial gap was .0025" with an uncertainty of about .0002" (.0635 mm, and .0051 mm). With the stall load of 100 N, Figure 6.15 indicates that this would correspond to a bearing gap of .0017" (.042 mm). It is not known if the bearing grounded out on a high spot or if the model is not accurate for the system. In either case, the bearing was good enough for the POSOR design for which it was intended.

For purposes of determining suitability of various ball bearings for measuring beam gimbal designs, the breakaway coefficients of friction of various bearings were found using the apparatus shown in Figure 7.6. The outer race was supported, and a thrust load F was applied to the inner race. From a point coincident with the axis of rotation of the bearing, a piece of ground shim stock (tolerances of +/- .0001") was attached and extended radially outward. A deflection was imposed on the end of the shim stock by a precision linear stage. When the bearing started to rotate, a reading was made, and then the stage was backed off until it was no longer touching the shim stock. The bearing radius times the coefficient of friction is thus:

$$\mu r_b = \frac{\delta 3EI}{F\ell^2} \qquad (7.1).$$

As discussed in Chapter 6, fretting corrosion is a concern with limited degree-of-freedom ball bearing gimbal applications. Thus it was desired to test instrument bearings (tolerance class ABEC 9) as well as "regular" grade (ABEC 3) bearings that had a hard chrome plating on all surfaces. The large turntable bearing (tolerance class ABEC 1) used for the base of the gimbal was only available without chrome plate but a better grade could probably be obtained with a hard chrome plate. Note that the irregularities in the chrome plate limit the tolerance class achievable to ABEC 3. Lubricants used were a light machine oil (MIL-L-6085) and a fretting corrosion inhibiting grease (Anderol 794). The bearings tested are shown in Figures 7.7, 7.8, 7.9, and 7.10.

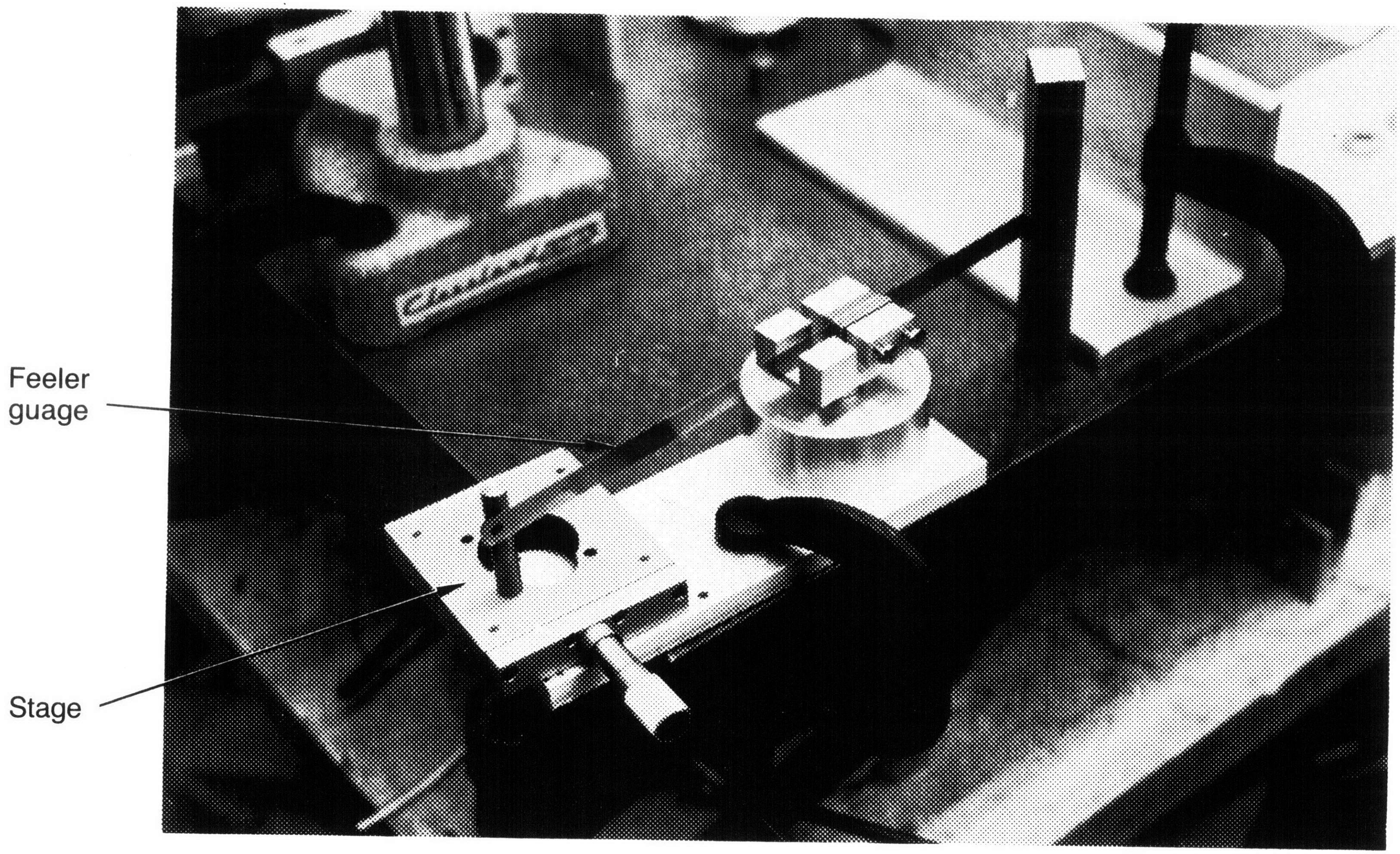

Figure 7.6 Apparatus for determining bearing breakaway coefficient of friction

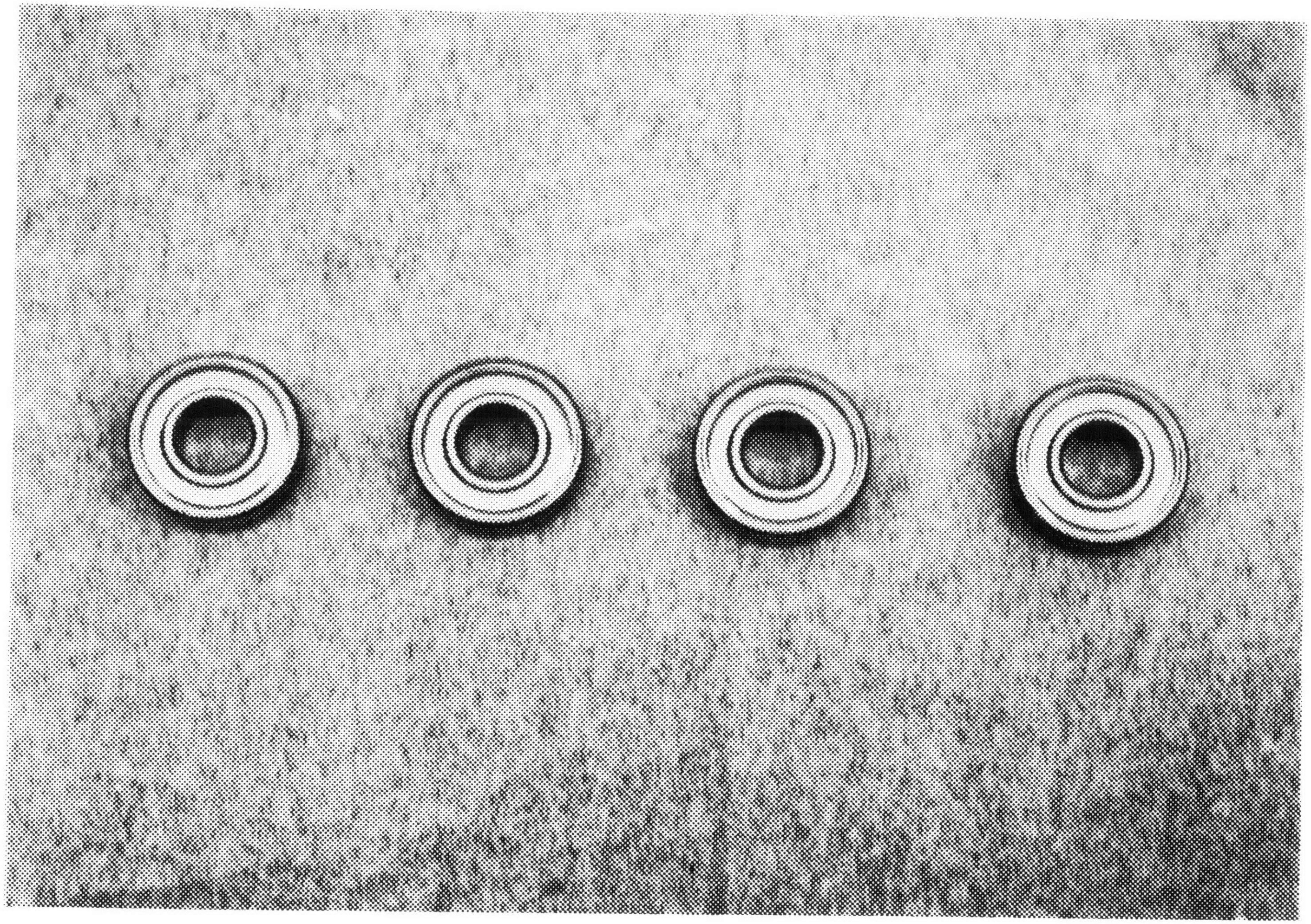

Figure 7.7 NHBB 3/8″ instrument bearings lubricated with MIL-L-6085 oil

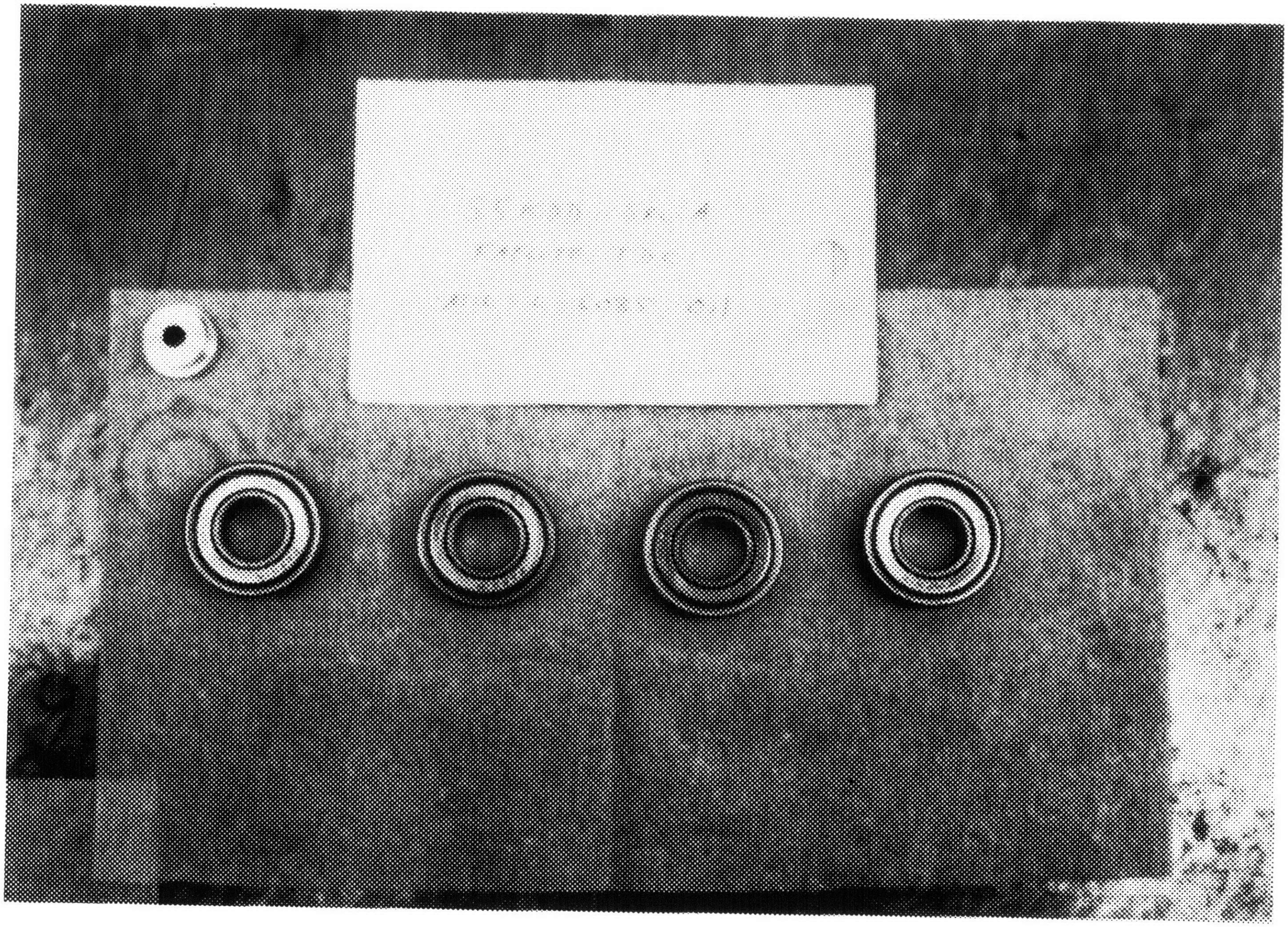

Figure 7.8 **Fafnir "Fafcote" 1/2" bearings lubricated with MIL-L-6085 oil**

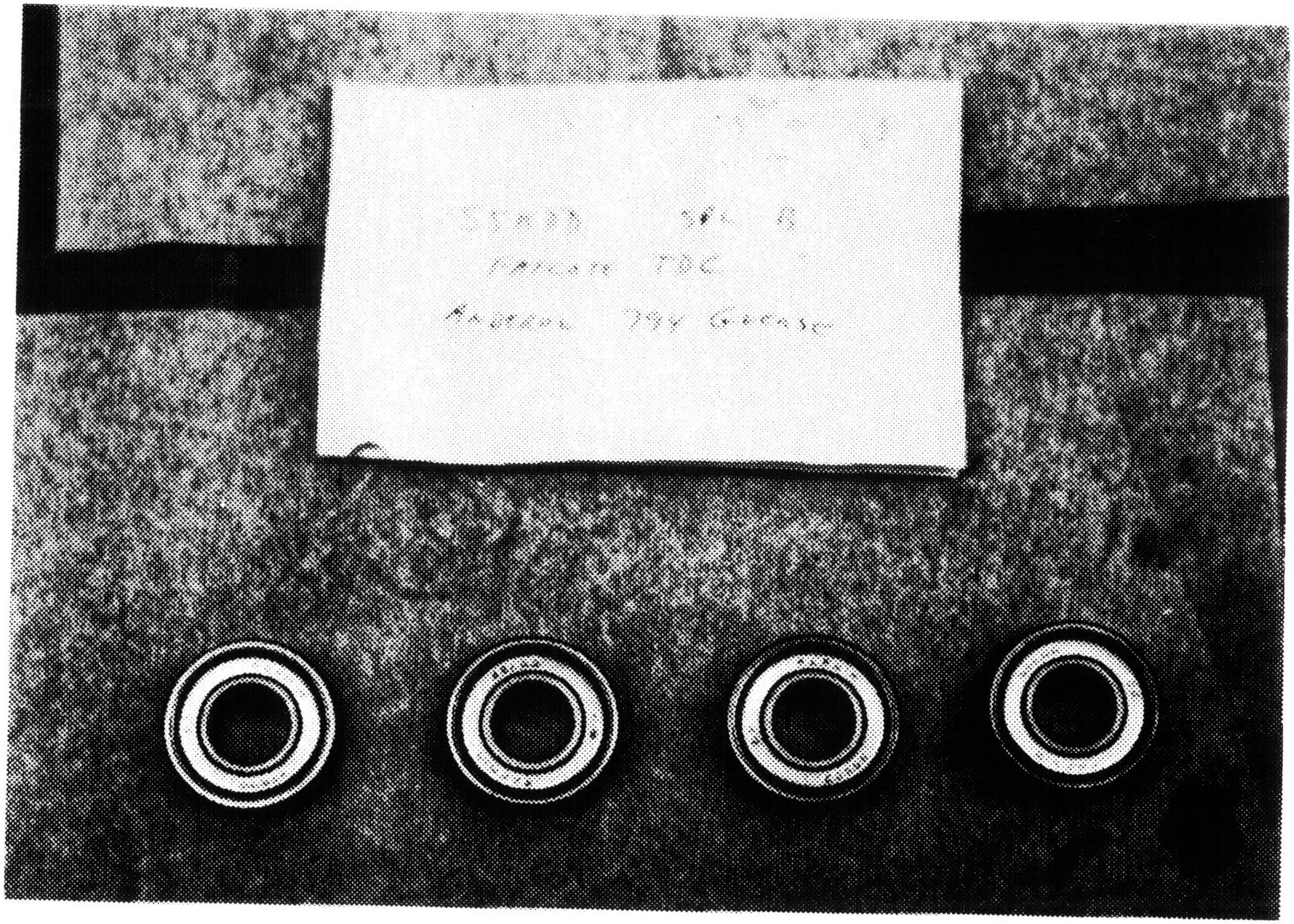

Figure 7.9 **Fafnir "Fafcote" bearings lubricated with Anderol 794 grease**

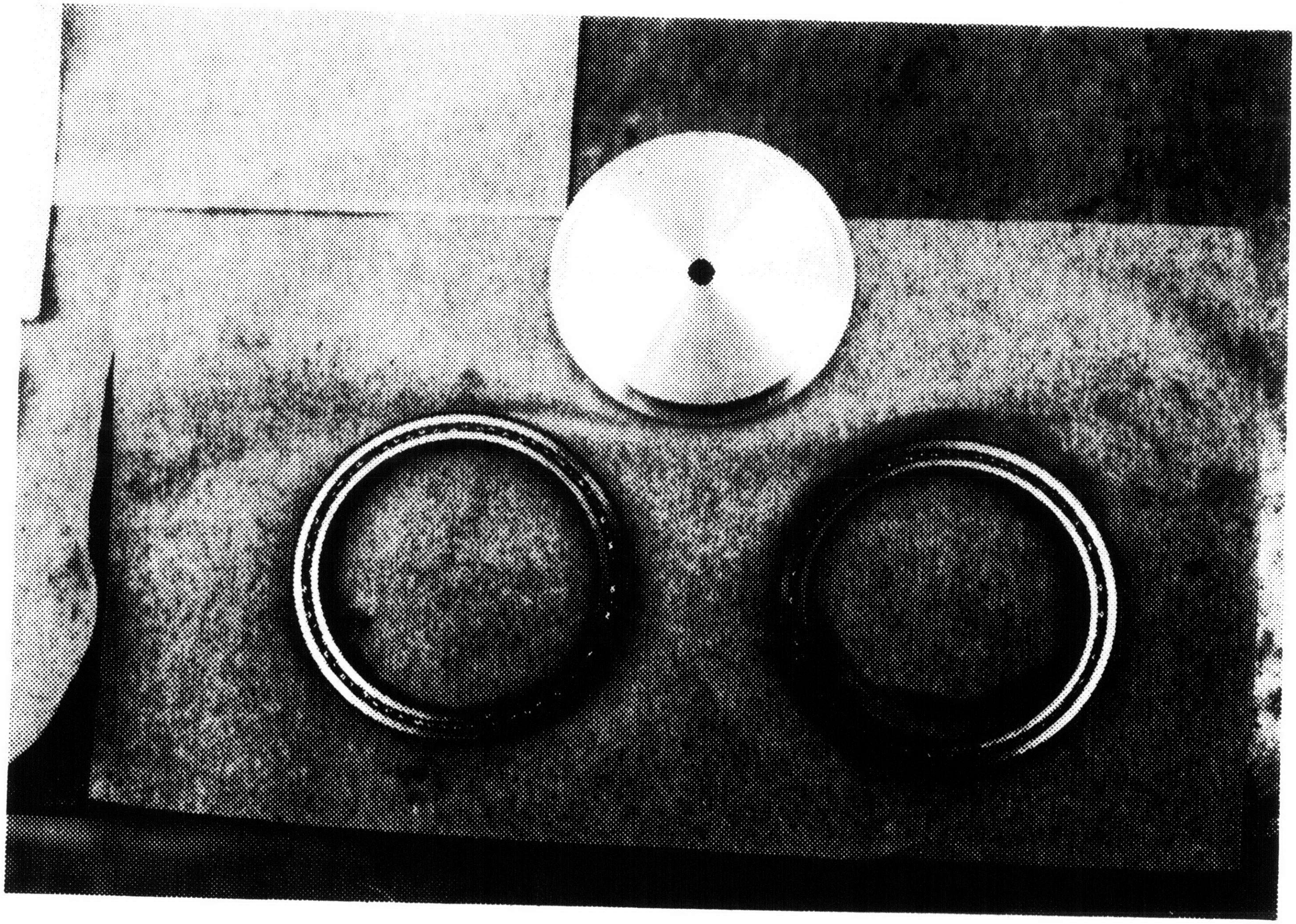

Figure 7.10 Kaydon ''Reali-Slim'' 2″ bearings lubricated with MIL-L-6085 oil

For the gimbal yoke bearings, four readings were taken for each of four bearings of three types of bearings. For the turntable bearing, only two bearings of the same type were tested. The results are given in Table 7.2. All the bearings tested satisfied the criteria of Eq. 6.11 with the exception of those lubricated with the grease. Thus the fretting corrosion problem could be avoided without exceeding the threshold breakaway coefficient of friction by the use of the "Fafcote" bearings.

7.4 Calibration of the Light Source-Lateral Effect Diode System Components

This section will discuss the various tests done on the Light Source-Lateral Effect Diode system that included: stability, linearization, axes offsets, repeatability, and light source inclination angles. All the tests were made using a test configuration the same as or similar to the one described below. Following subsections describe each of the calibration tests in detail, and results are presented. The total system accuracy is discussed in the summary for this section.

Photographs of the calibration apparatus are shown in Figures 7.11, 7.12, and 7.13. The lateral effect diodes were epoxied to an aluminum strip with their axes roughly parallel. The flatness to which the diodes were held to the strip was .005"/inch which yields orientation errors $\sigma_{X\alpha}$ and $\sigma_{Y\beta}$ of .005 radians each (based on measurements on the glass covering the diodes). The aluminum strip was then mounted to a block on the stage. The geometry of the system required that the diode

Table 7.2 Results of Bearing Coefficient of Friction Tests

Bearing	lube	$\overline{\mu r_b}$*	$\bar{\sigma}$
NHBB 3/8"	MIL-L-6085	.000308	.000069
FAFNIR 55KDDSPCB FAFCOTE TDC	Anderol 794	.011096	.002708
FAFNIR 55KDDSPCA FAFCOTE TDC	MIL-L-6085	.001033	.000470
KAYDON KA020XPO	MIL-L-6085	.002431	.000711

*All dimensions are in inches.

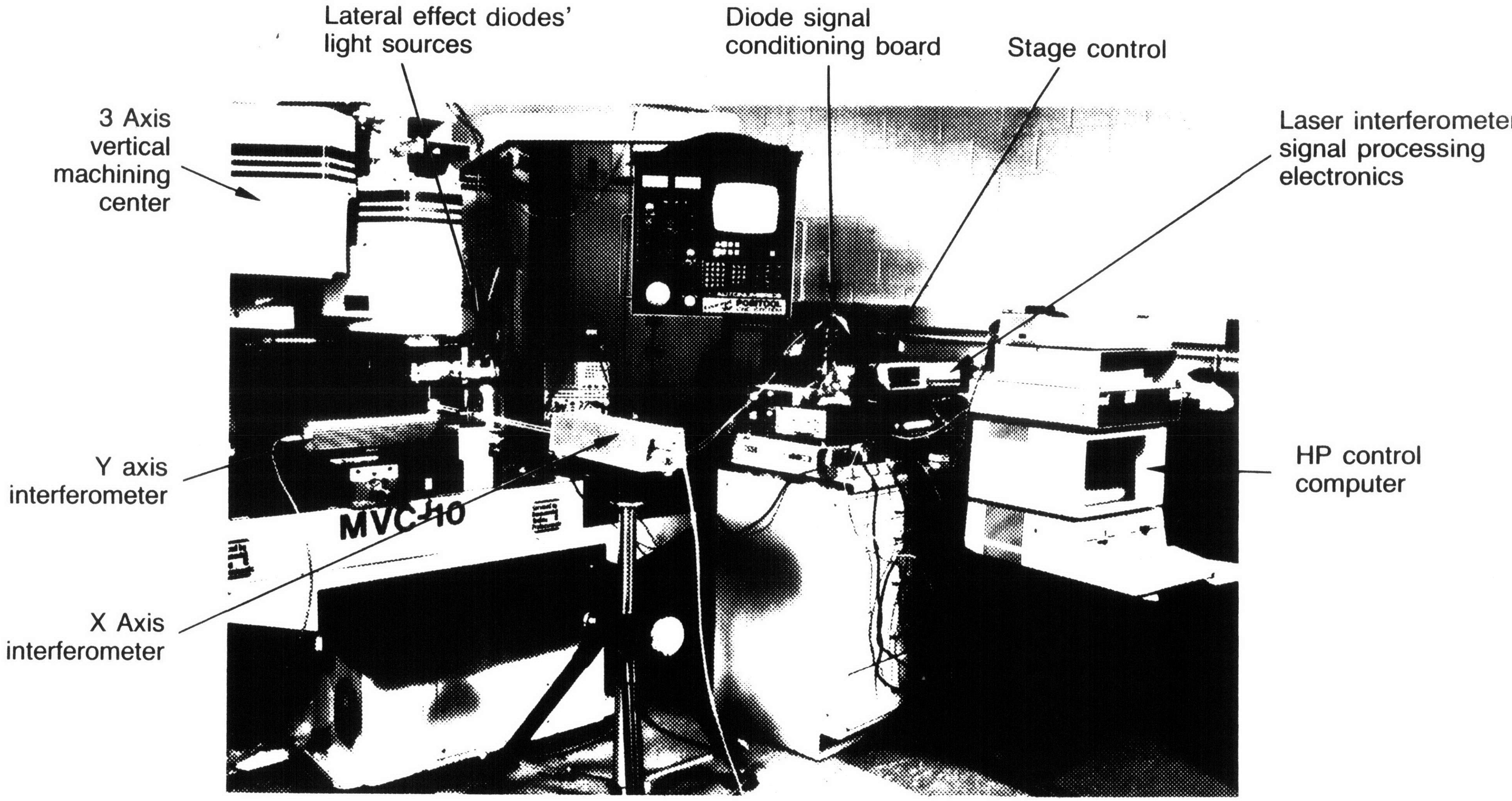

Figure 7.11 Overall view of light source-lateral effect diode system calibration test setup

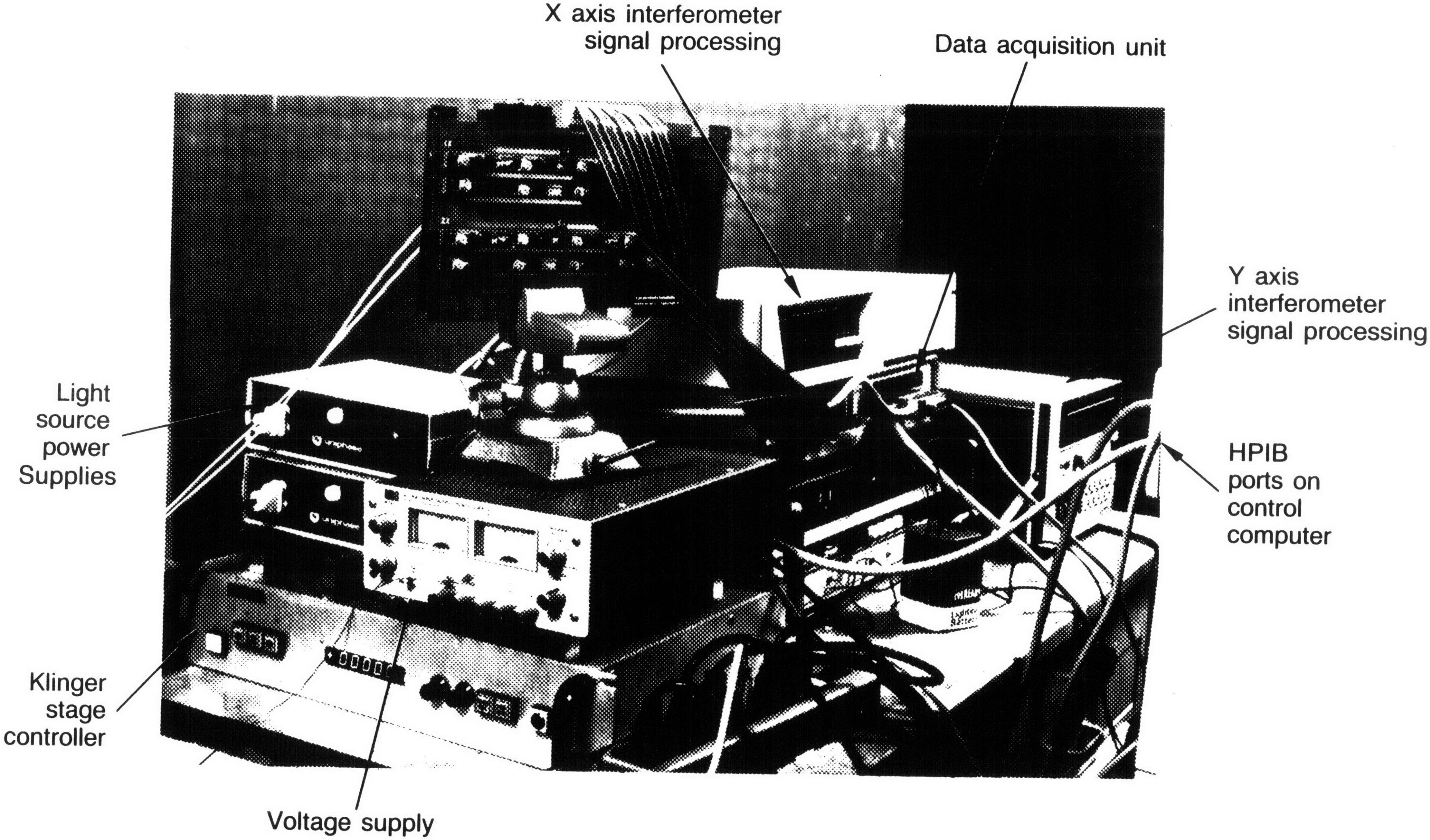

Figure 7.12 Electronics for light source-lateral effect diode system calibration experiments

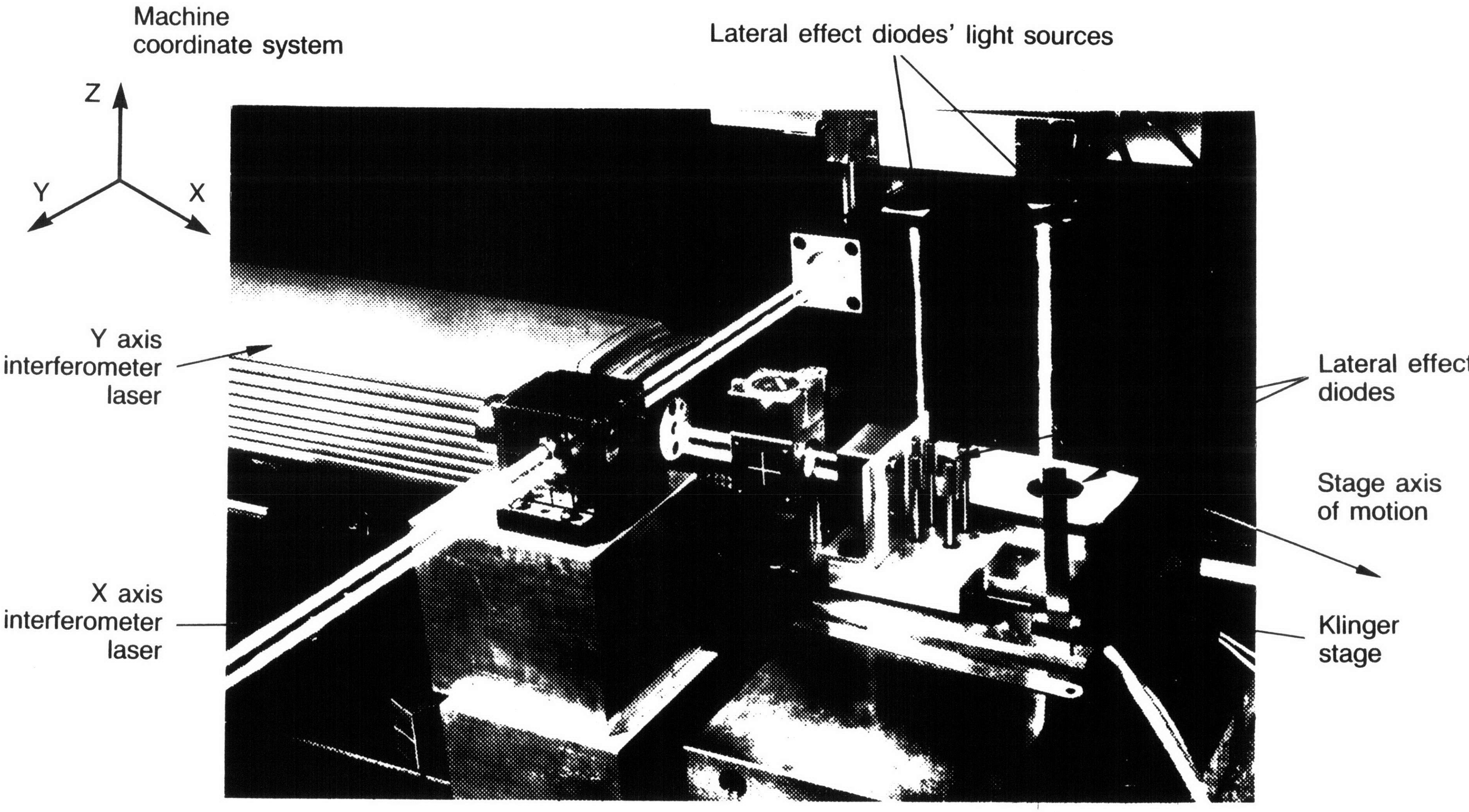

Figure 7.13 Close up of light source-lateral effect diode system XY calibration setup

Y_d axes (diode axes have the subscript "d") were along the machine tool X axis and it is regretted if this causes any confusion in the discussion that follows.

The system was aligned with respect to the machine tool coordinate system using a dial gauge (with .0005" per division, resolution to .00025" (6.4 μm)) held in the spindle. When aligning the stage, it was shimmed so its axis of motion was parallel to the machine tool X axis within .001"/inch of travel, and the glass surfaces of the diodes were brought to within .005"/inch (.0127 mm) perpendicularity with the machine tool Z axis. The interferometer optics were mounted within .002"/inch parallelism with the machine tool axes. Thus the angular error associated with the measurements along the diode X_d and Y_d axes (Y and X axes of the machine tool) was $\sqrt{.001^2 + .002^2 + .005^2} = .0055$ radians. Thus the cosine error (between what a perfect diode would read and the laser interferometer) over .625" of stage travel would be at most 9 μin (.23 μm). The error in orthogonality σ_{ZY} between the linearized X_d and Y_d diode axes would be equal to that between the laser interferometers which was $\sqrt{.002^2 + .002^2} = .0028$ radians.

By using a light sources over each diode, two diodes could be calibrated at once. This also forced the X_d and Y_d axes to be parallel. Since the lasers became warm to the touch after operating for ten minutes, the entire system was always allowed to soak overnight prior to a test. Following subsections will describe the results of tests for stability, linearization, axes offset, repeatability, and light source inclination angle.

7.4.1 Determination of Light Source-Lateral Effect Diode System Stability

The first test was to determine the stability of the system which did not require the use of the laser interferometer. Note that "system stability" implies the stability of the diode and the laser. For this test, the diode behavior was assumed to be linear with .625"/10 volts and the stability error was the voltage drift times the gain. Diode stability was tested by taking 3000 samples at a single point near the edge of the diode over a 12 hour period. During this time, the room temperature varied by .15°. The lasers were anchored in a large aluminum block with the distance from the anchor point to the first laser about 5" (127 mm) and the distance to the second laser about 8" (203 mm). Thus the error due to thermal growth could be $.15° \times 7 \mu s \times 5" =$ 5.3 μin (1.4 μm). There is no more error for the second laser because the diodes were also mounted on an aluminum strip, so the net growth between the lasers and the diodes would be the same.

The errors in stability were random and thus not caused by thermal growth. The standard deviation of the stability error for the X_d and Y_d axes of diodes 1 and 2 respectively were 89, 101, 41, and 62 μin (2.23, 2.52, 1.03, and 1.55 μm) (Note that the equivalent resolution of the analog to digital converter was shown to be 41 μinches). The source of the ≈50 μin (1.3 μm) stability error in diode 1 could be due to the diodes or to the laser. In either case, the system was judged stable enough to proceed. Tests using an LED and fiber optic cable with a collimating index rod had a system stability only of .0005", so beam stability is a critical factor.

7.4.2 Linearization of Light Source-Lateral Effect Diode System

This section will discuss the linearization of the lateral effect diodes. Note that not only the diodes but the entire system associated with determining the position of the light spots was in effect linearized, because all the signal processing electronics were used to gather the data which was compared to the laser readings.

In order to linearize the diodes, the Y axis of the machine had to be held steady while the X axis (stage) was moved forward, then returned to the home position. Then the Y axis of the machine tool bed was incremented and locked. The process was repeated until the entire surface of the diode was covered. Because the analog to digital converter was so slow, and to allow for settling time between motions, it took two minutes to read the nine channels of data (8 channels of diode and one thermister).

Thus for any reasonably thorough mapping of the diodes (on the order of 15×15 points), the duration of the experiment required it to be at least semi-automated to prevent human error from ruining the experiment.

The ideal test condition for mapping the surface of the diodes would have the multiple Y_d passes stop at the same point each time throughout the test (multiple Y_d passes and single step increments of the X_d axis sweep out the diode). To check how good the position repeatability was, 10 runs back and forth along the diode Y_d axis were made with 15 stage stops per run and the standard deviation from the mean (repeatability of stops) was 55 μin. Experience with precision ball screws has shown that they can be repeatable to 10 microinches (.25 - .50 μm) [1.7]. The rotational error of the stepper could be at most .25 steps and the stage has 5 μin/step resolution, so about 15 μin of error can be accounted for. Since the laser interferometer beam was about 2" (50.8 mm) from the stage axis and the stage yaw repeatability was 5 arc seconds, the rest of the error was probably due to Abbe's offset error (2"×25 μrad = 50 μin (1.3 μm)). As will be seen below, the diode X_d axis curve fit polynomials varied little with the Y_d position, so the stage positioning was judged adequate.

During testing, the room had to be kept dark (the diodes detect 60 Hz flourescent lights beautifully). Most, if not all, the noise would be filtered out by the dual slope analog to digital converter in the data aquisition module, but it was thought best to eliminate as many potential errors as possible. Reflections from the laser bouncing off the protective glass cover of the diode, to the half silvered lasing cavity mirror and back to the diode presented the biggest "ambient" light problem. This was overcome by tilting the lasers and covering the ends with dark felt. Cleanliness was also a concern, so before each run, the surface of each diode was cleaned with very pure acetone.

Before mapping the entire diode, trial runs were made along one edge to determine the number of points needed and the order of curve fit required. Runs with forty points were made, and curve fits greater than ninth order were no better than ninth order curves. It was also determined that 15 points was the minimum number that was needed for a ninth order fit to prevent the curve from just following individual points.

Note that there is no basic reason of physics that would account for this high order; however, the wavyness of the silicon (due to manufacturing process) or the curve merely tracking the poor performance of the stage could be reasons why a high order fit was required. To determine if it were the latter, a trial run was made using the machine tool bed as the stage and a ninth order curve still gave the best fit; thus even though the stage motion may be causing ripples in the data, the manufacturing process for the diodes also causes ripples with the net effect of requiring a high order polynomial to linearize the diodes.

The requirement for a high order linearization curve (on the order of nine) meant that a 15×15 grid of points had to be mapped. The "raw" data from the diode linearization experiments is shown in Figures 7.14 - 7.17. It shows the processed diode output (ratio of differences between back contact voltages) as a function of the (laser interferometer measured) relative position between the light spots and the diodes. The diode response is not only non-linear along a particular path, the curves vary from side to side of the diode. The various curves were fitted using a "canned" least squares routine with curve order ranging from third to ninth. The standard deviations of the data from each of

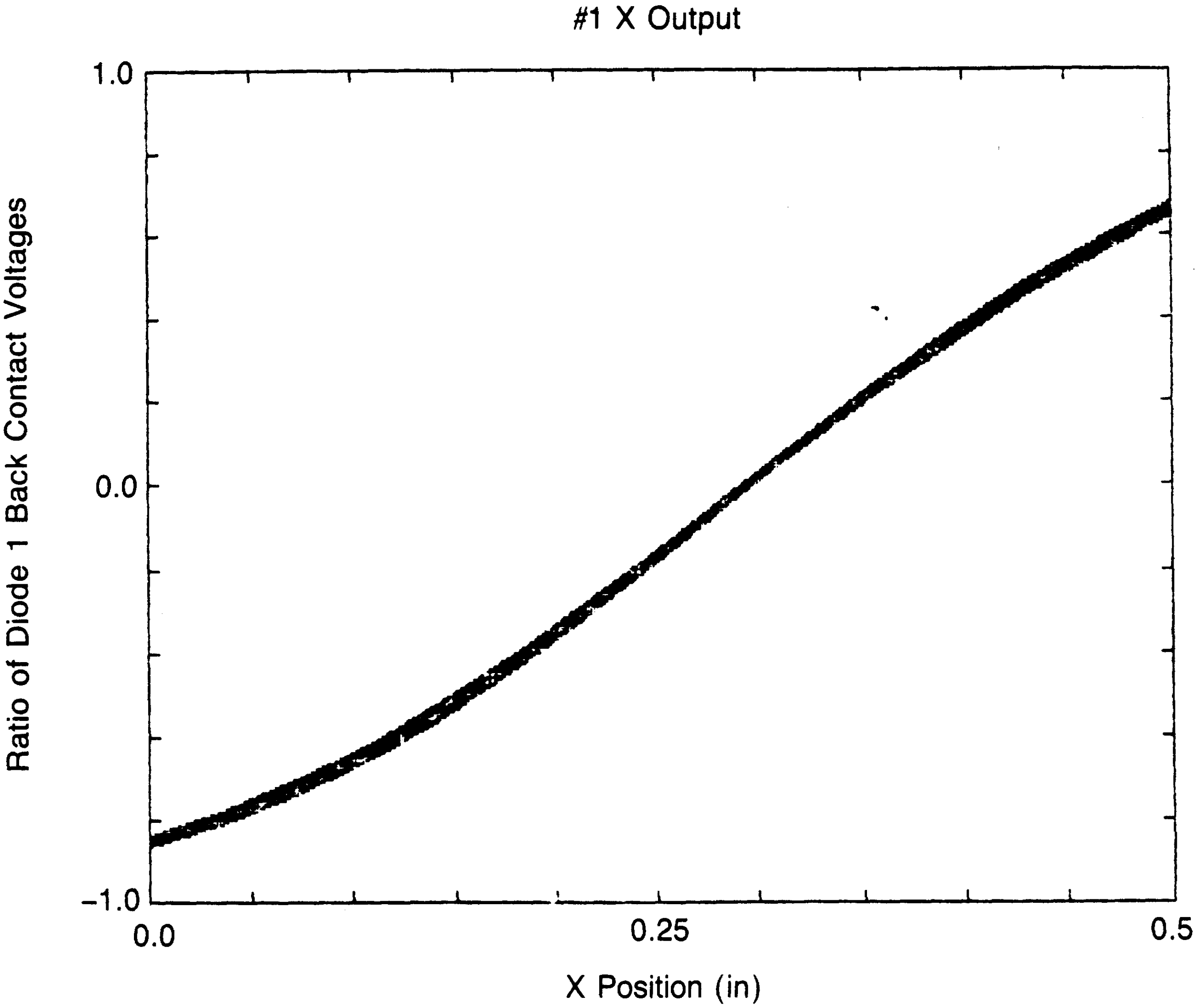

Figure 7.14 Position of light spot on diode 1 measured by a laser interferometer, verses diode output

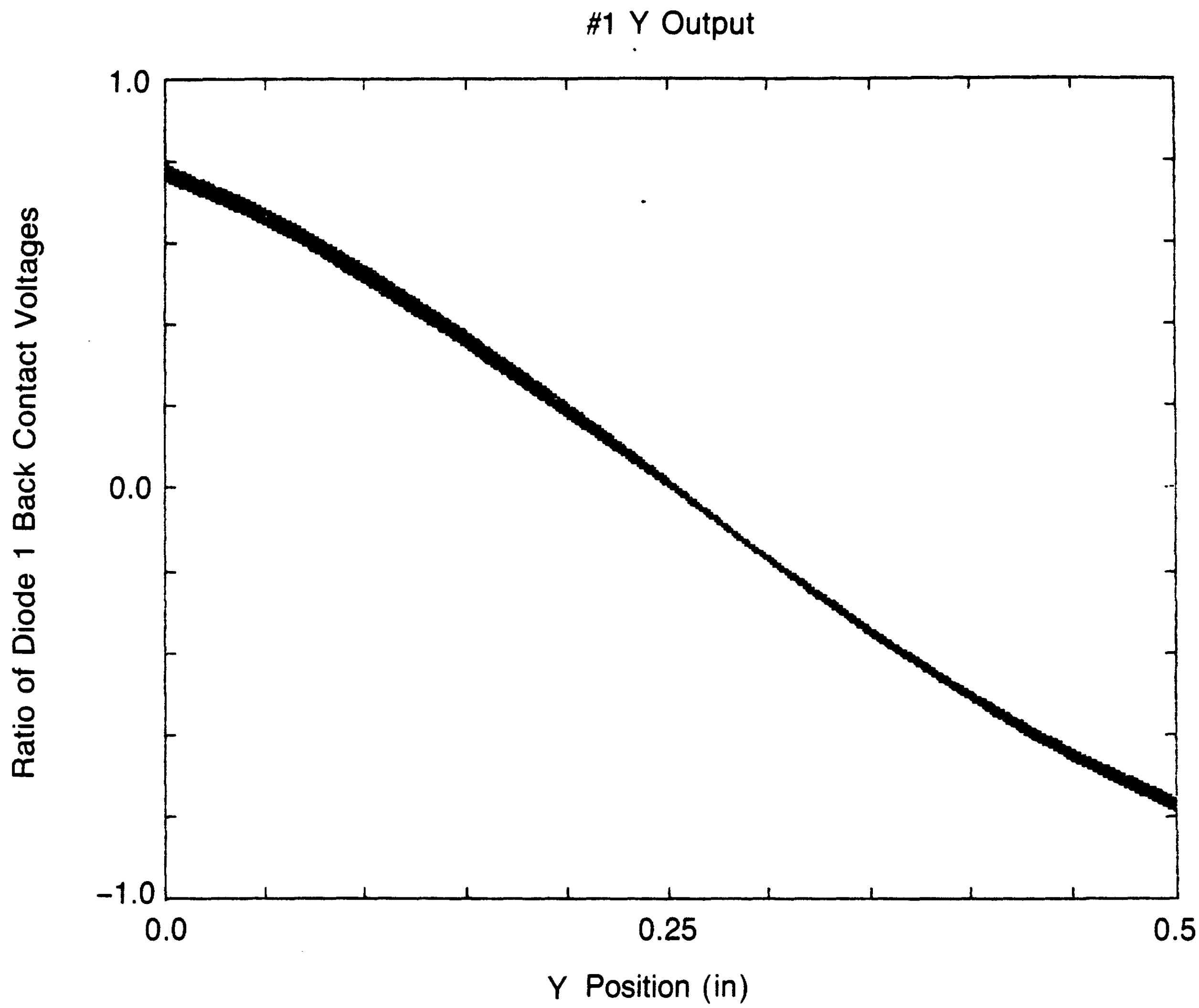

Figure 7.15 Y position of light spot on diode 1 measured by a laser interferometer, verses diode output

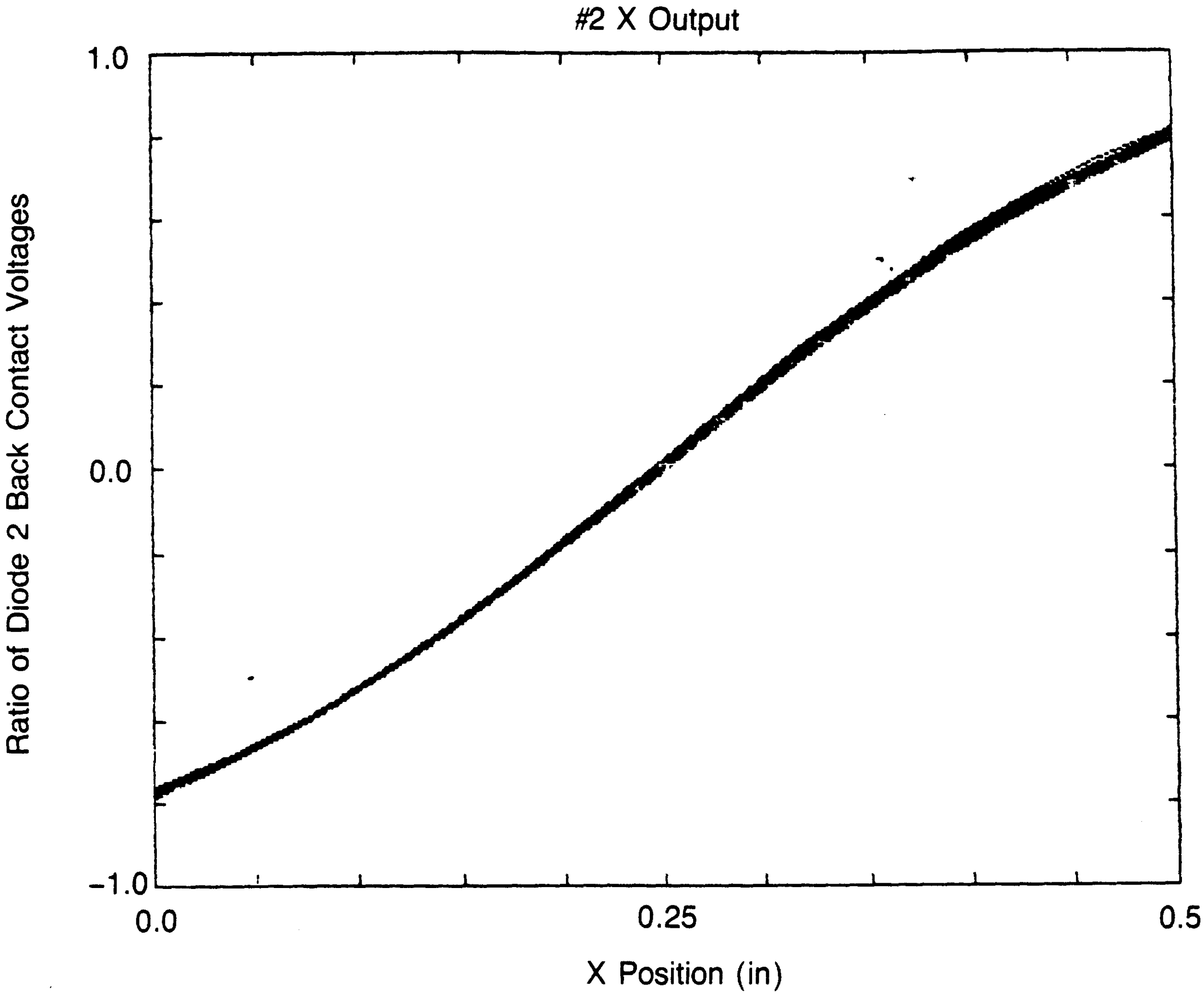

Figure 7.16 X position of light spot on diode 2 measured by a laser interferometer, verses diode output

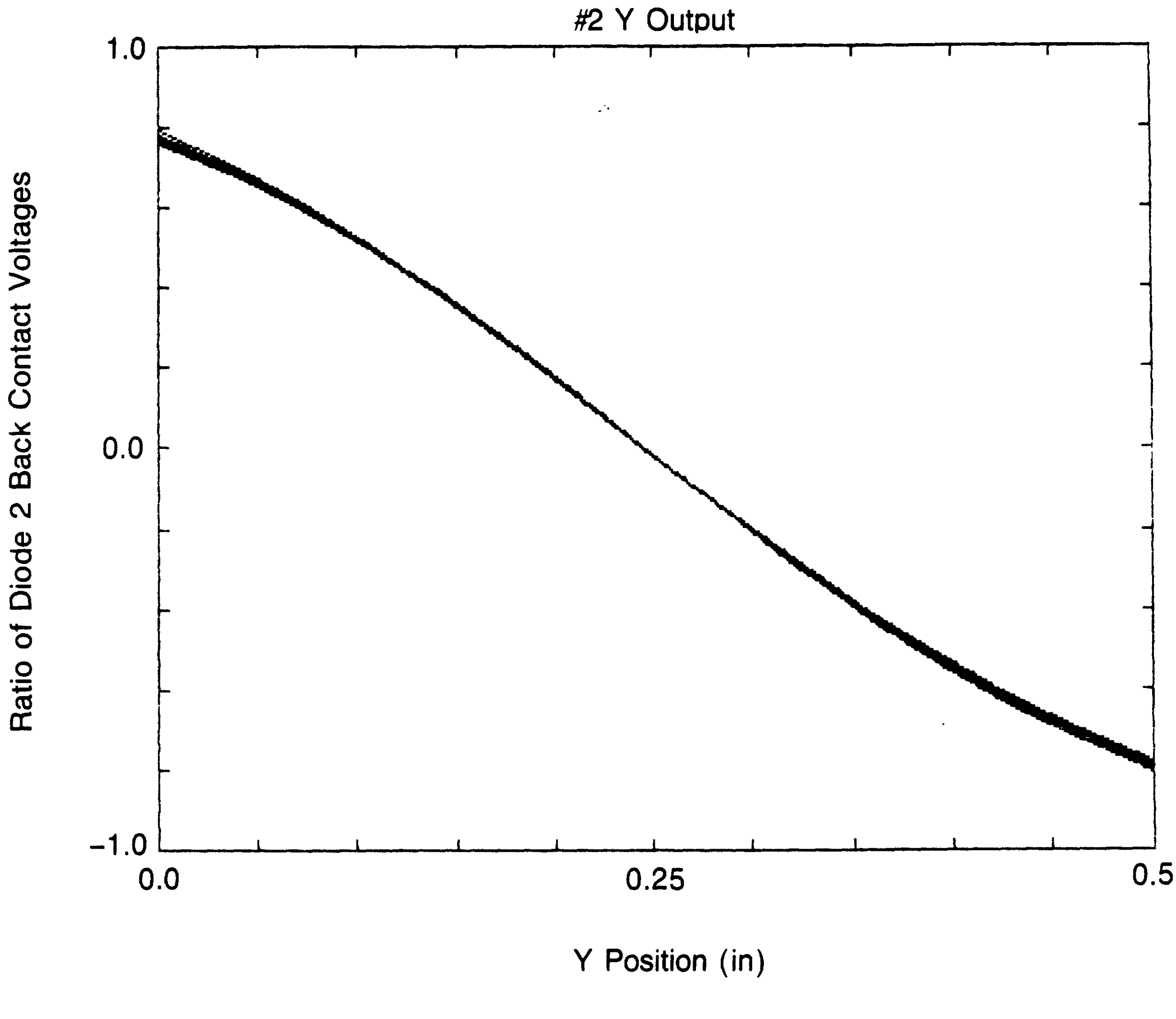

Figure 7.17 Y position of light spot on diode 2 measured by a laser interferometer, verses diode output

the 15 X_d and 15 Y_d curves are listed in Tables 7.3 - 7.6. These tables show that at least a 7th order curve is needed. For each of the diodes' X_d and Y_d axes, the standard deviations of the data from the curves (for orders 7, 8, and 9) are plotted in Figures 7.18 - 7.21. Table 7.7 lists the average deviation for all the curves on a particular axis, and the maximum and minimum deviations. Based on this data, the curves that seemed to provide the best fit were the ninth order ones (for programming purposes it was desirable that the same order curves were chosen for both diodes).

The accuracy (standard deviation) of the diodes are thus given by the $\bar{\sigma}_9$ row in Table 7.7. It should have been possible to linearize the diodes with an error on the order of the stability of the diodes. Whether the large errors were caused by manufacturing processes or large Abbe's offset error (a result of the stage yaw, pitch and straightness) is not known. But based on the performance of the diodes when tested on the machine tool bed (see next section) it is probably the latter. These errors and their effects on total system accuracy will be discussed along with other system errors in the summary section on the Light Source-Lateral Effect Diode System. The coefficients for the X_d and Y_d curves for the two diodes are listed in Appendix 8A along with all the software developed to analyze the sensory output.

The algorithm for obtaining a linearized value when the light spot fell between mapped points is discussed in Chapter 8 along with the other data processing algorithms. It needs to be noted here, that errors associated with the algorithm were: σ_{X_1} = 35 µin, σ_{X_2} = 25 µin,

Table 7.3 Standard Deviations of Diode 1 X Data from Nth Order Linearization Curves

Order of Curve Fit:

Y Position	3rd	4th	5th	6th	7th	8th	9th
	Standard Deviations (μ in)						
1	3324	1427	502	368	183	192	198
2	3218	1336	221	209	109	106	112
3	3177	1361	150	157	165	165	173
4	3107	1484	183	177	154	164	179
5	3085	1599	281	176	147	141	154
6	2969	1639	271	172	184	155	162
7	2819	1560	265	188	195	191	203
8	2601	1404	324	283	298	279	295
9	2408	1315	240	194	206	202	211
10	2335	1223	402	297	315	287	292
11	2232	1218	422	292	290	216	212
12	2162	1032	416	267	283	300	267
13	1979	969	341	230	241	235	225
14	2143	899	451	232	204	221	241
15	2429	1258	628	343	348	272	214

Table 7.4 Standard Deviations of Diode 1 Y Data from Nth Order Linearization Curves

Order of Curve Fit:

X Position	3rd	4th	5th	6th	7th	8th	9th
	Standard Deviations (μ in)						
1	1442	1502	239	226	122	53	58
2	1219	1278	273	253	133	142	118
3	1332	1397	310	119	125	131	136
4	1339	1404	179	170	179	117	122
5	1559	1635	208	162	73	70	63
6	1424	1490	160	159	159	97	85
7	1546	1608	370	372	284	151	97
8	1532	1581	265	226	108	114	105
9	1565	1623	341	330	205	211	159
10	1511	1570	143	126	130	138	133
11	1432	1476	157	161	165	176	192
12	1361	1412	227	232	214	202	188
13	1201	1232	234	232	208	223	229
14	1141	1190	240	254	211	157	148
15	1100	1153	211	209	192	206	218

Table 7.5 Standard Deviations of Diode 2 X Data from Nth Order Linearization Curves

Y Position	3rd	4th	5th	6th	7th	8th	9th
	Order of Curve Fit: Standard Deviations (μ in)						
1	1393	1357	340	356	262	227	247
2	1165	1144	396	398	356	262	287
3	917	955	342	362	320	296	302
4	889	929	163	168	176	182	194
5	941	952	171	167	177	189	140
6	1138	1156	264	207	221	222	199
7	1434	1477	352	219	233	231	213
8	1633	1699	357	221	233	246	243
9	1738	1821	334	195	206	215	229
10	1783	1870	340	193	206	206	225
11	1667	1740	264	171	180	176	192
12	1519	1585	173	156	154	158	159
13	1349	1408	192	196	152	161	174
14	1275	1334	319	309	136	106	111
15	1423	1478	371	349	164	175	172

Table 7.6 Standard Deviations of Diode 2 Y Data from Nth Order Linearization Curves

Order of Curve Fit:

X Position	3rd	4th	5th	6th	7th	8th	9th
	Standard Deviations (μ in)						
1	1514	1360	142	74	55	54	54
2	1214	1054	115	44	39	41	39
3	1106	980	211	172	164	109	107
4	1014	992	192	90	96	87	61
5	1074	1125	255	147	157	163	109
6	1245	1284	281	123	130	124	53
7	1369	1357	266	139	141	146	82
8	1400	1419	306	118	125	96	62
9	1413	1474	341	281	269	83	81
10	1314	1377	340	265	277	270	266
11	1270	1325	247	176	185	62	57
12	1268	1316	138	100	107	72	62
13	1302	1360	101	104	74	79	78
14	1447	1516	148	157	63	67	62
15	1674	1723	268	277	125	94	102

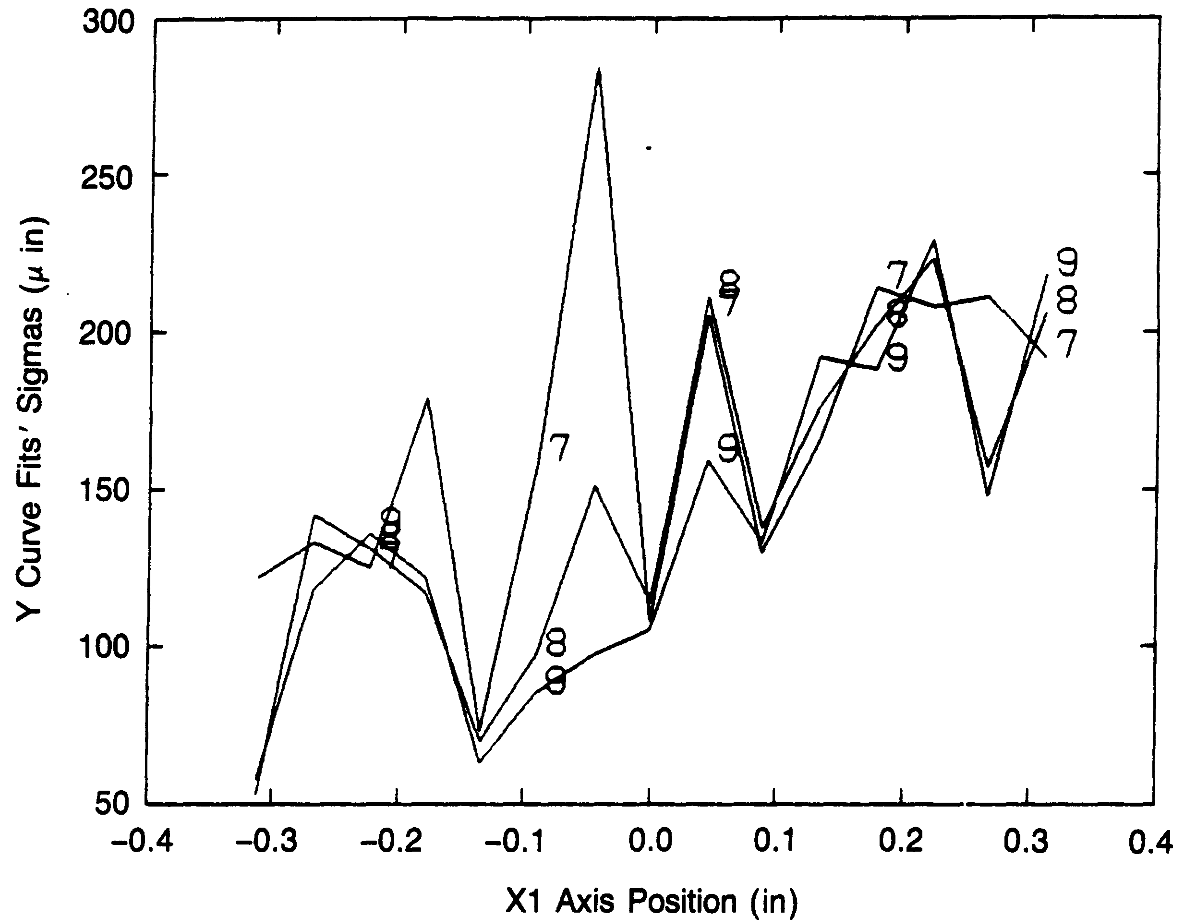

Figure 7.18 Standard deviations of diode 1 X axis data from least squares fitted curves (7th, 8th, 9th order)

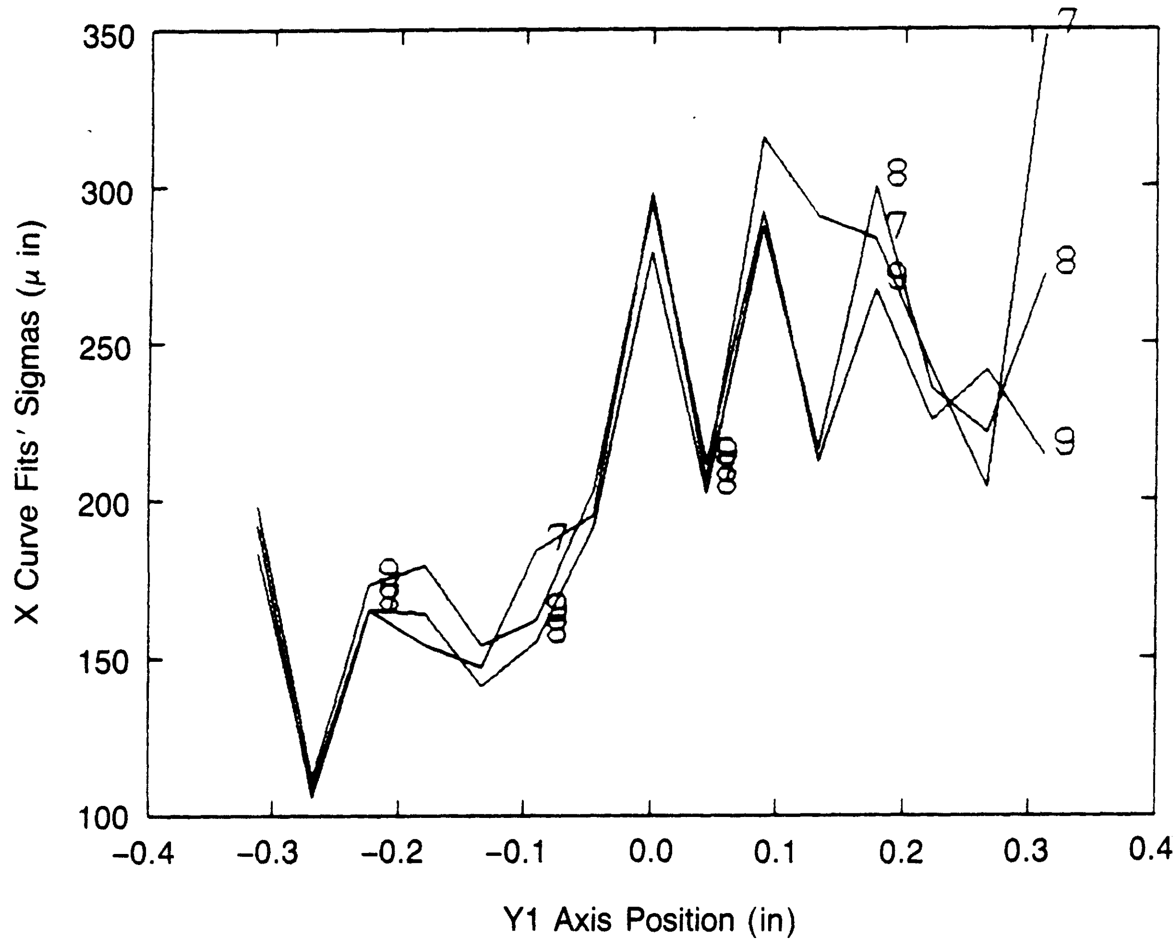

Figure 7.19 Standard deviations of diode 1 Y axis data from least squares fitted curves (7th, 8th, 9th order)

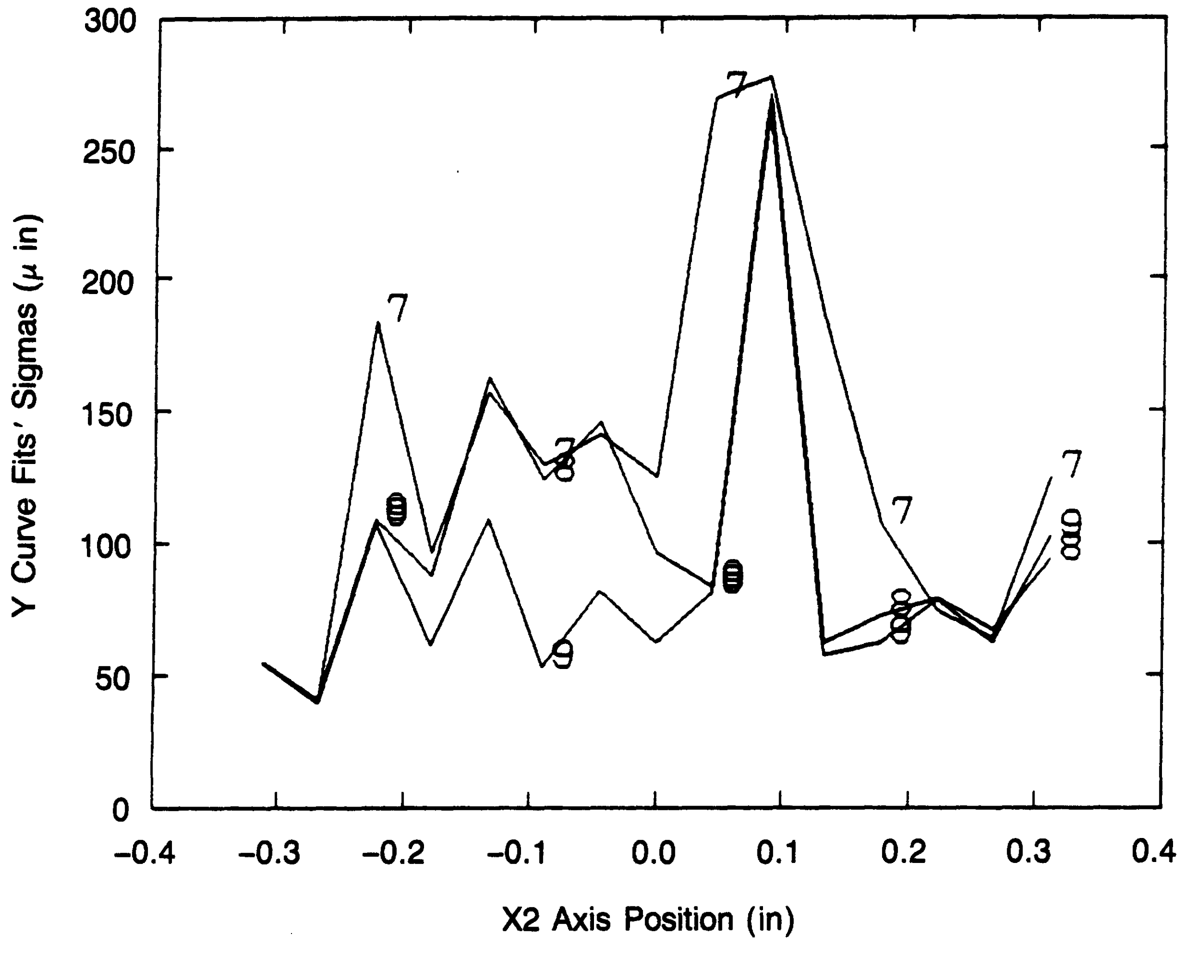

Figure 7.20 Standard deviations of diode 2 X axis data from least squares fitted curves (7th, 8th, 9th order)

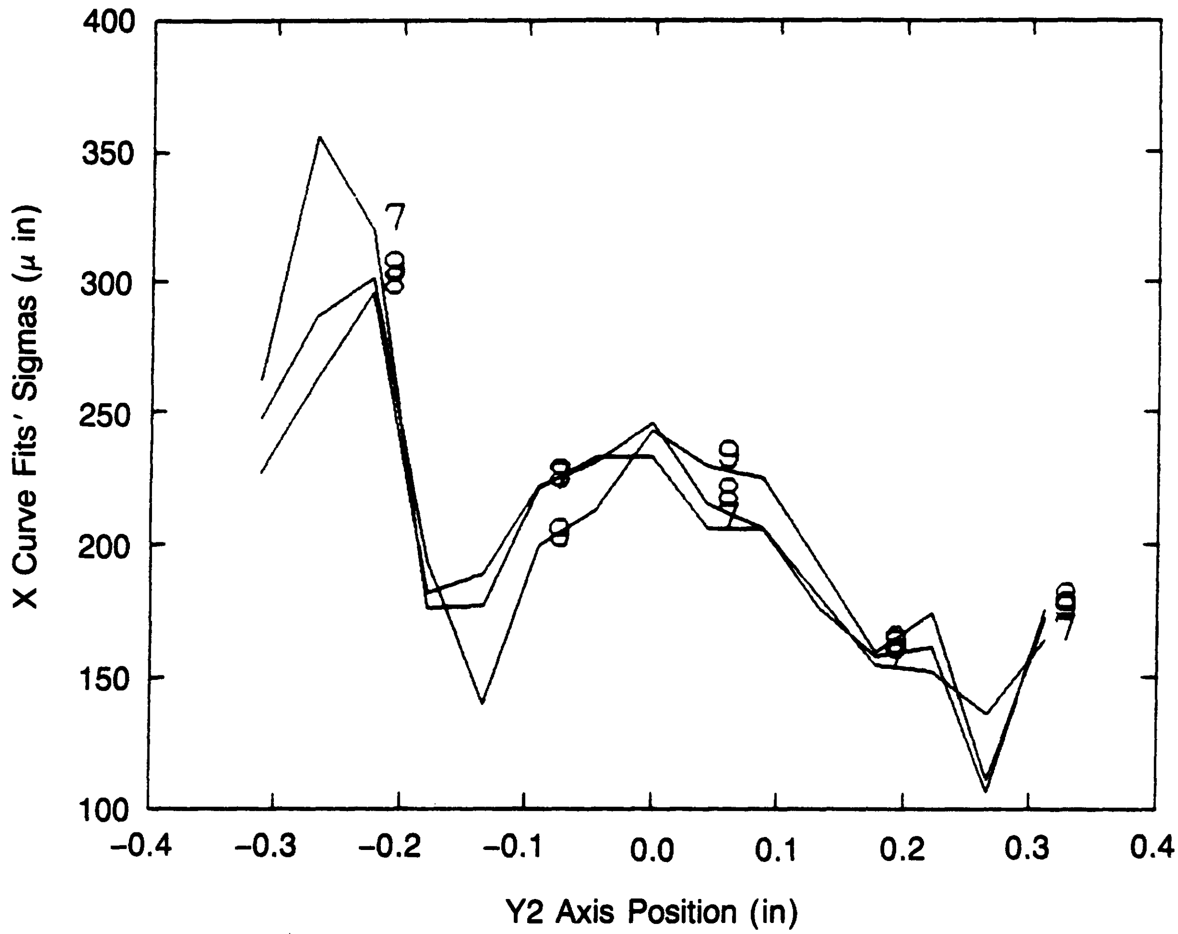

Figure 7.21 Standard deviations of diode 2 Y axis data from least squares fitted curves (7th, 8th, 9th order)

Table 7.7 Averages of Deviations from Data for 7th, 8th, and 9th Order Diode Linearization Curves

	Diode Number and Axis			
	1 X	1 Y	2 X	2 Y
	Deviation (μ in)			
$\bar{\sigma}_7$	221	167	212	135
$\bar{\sigma}_8$	208	146	203	103
$\bar{\sigma}_9$	209	137	206	85
σ_{7high}	348	284	356	277
σ_{8high}	300	223	296	270
σ_{9high}	295	229	302	266
σ_{7low}	109	73	136	55
σ_{8low}	141	53	106	41
σ_{9low}	112	58	111	39

σ_{Y_1} = 25 μin, and σ_{Y_2} = 30 μin (.9, .6, .6, and .8 μm). These values were obtained by assuming a grid size equal to four times as coarse as used to map the diodes, and then interpolating to the "known" center point of the coarse grid. The error for the fine grid was then assumed to be one fourth that for the coarse grid.

7.4.3 Determination of Light Source-Lateral Effect Diode System Repeatability

Three types of tests were done to determine repeatability of the Light Source-Lateral Effect Diode system: back and forth tests on the Klinger stage, back and forth tests on the machine tool bed, and repeatability of calculations of the diodes' axes offsets. All tests, with the exception of the latter, were done toward the edge of the diodes, and the X_d axis position on the diode was held constant.

The first set of tests were run using the Klinger stage. These tests were run by computer control and were allowed to run overnight. A ninth order curve was fitted to each run of the test, and the curves were compared digitally by subtracting the first run's curve from all subsequent runs. The results of this test are shown plotted in Figures 7.22 and 7.23. The snape of the curves are all similar owing to the curve fit; however, their deviation from the first curve is random. For both diodes, the standard deviation of the repeatability is on the order of 150 μin (3.75 μm).

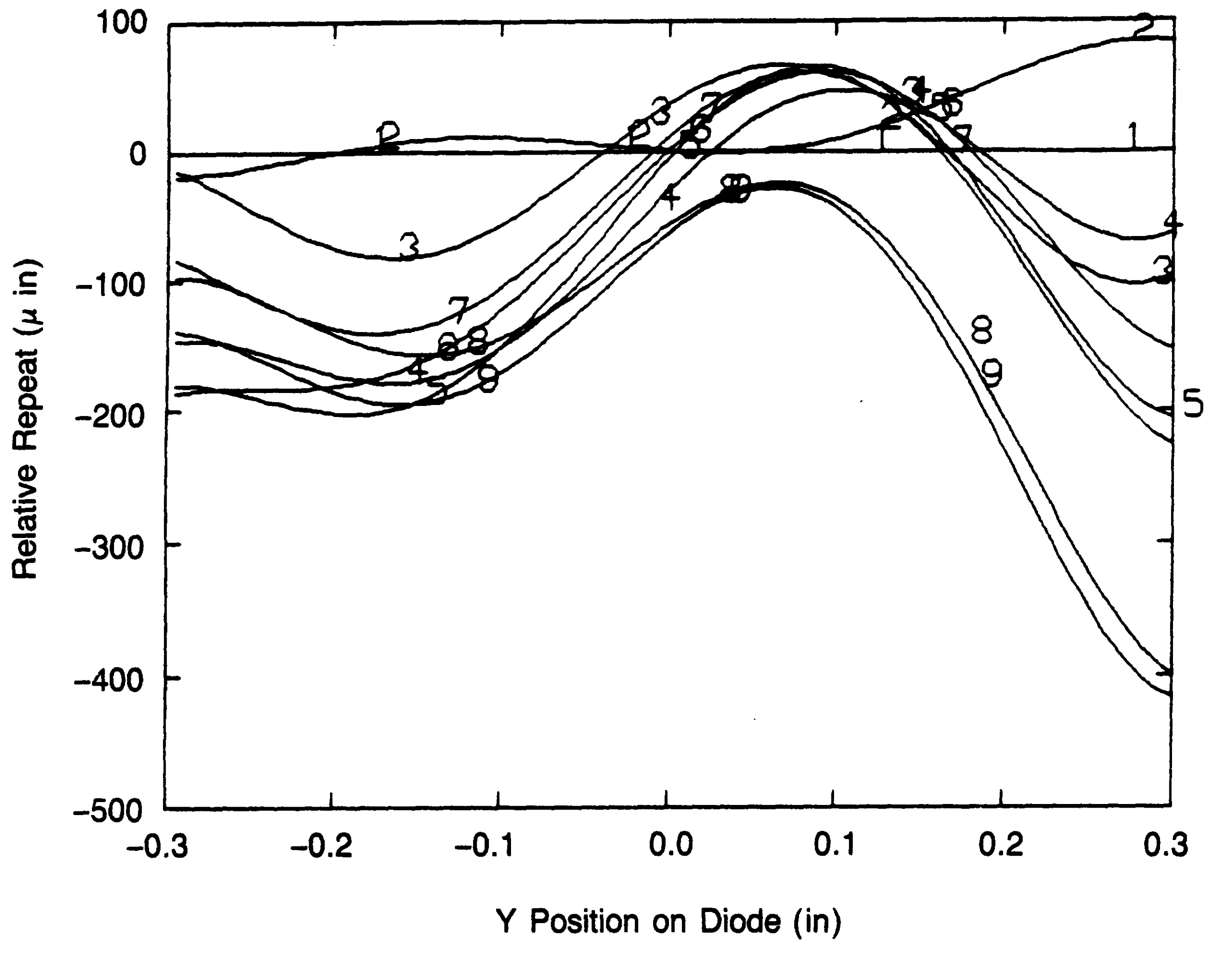

Figure 7.22 Repeatability of diode 1, measured by subtracting linearized results of first pass from all subsequent passes (stage used was Klinger)

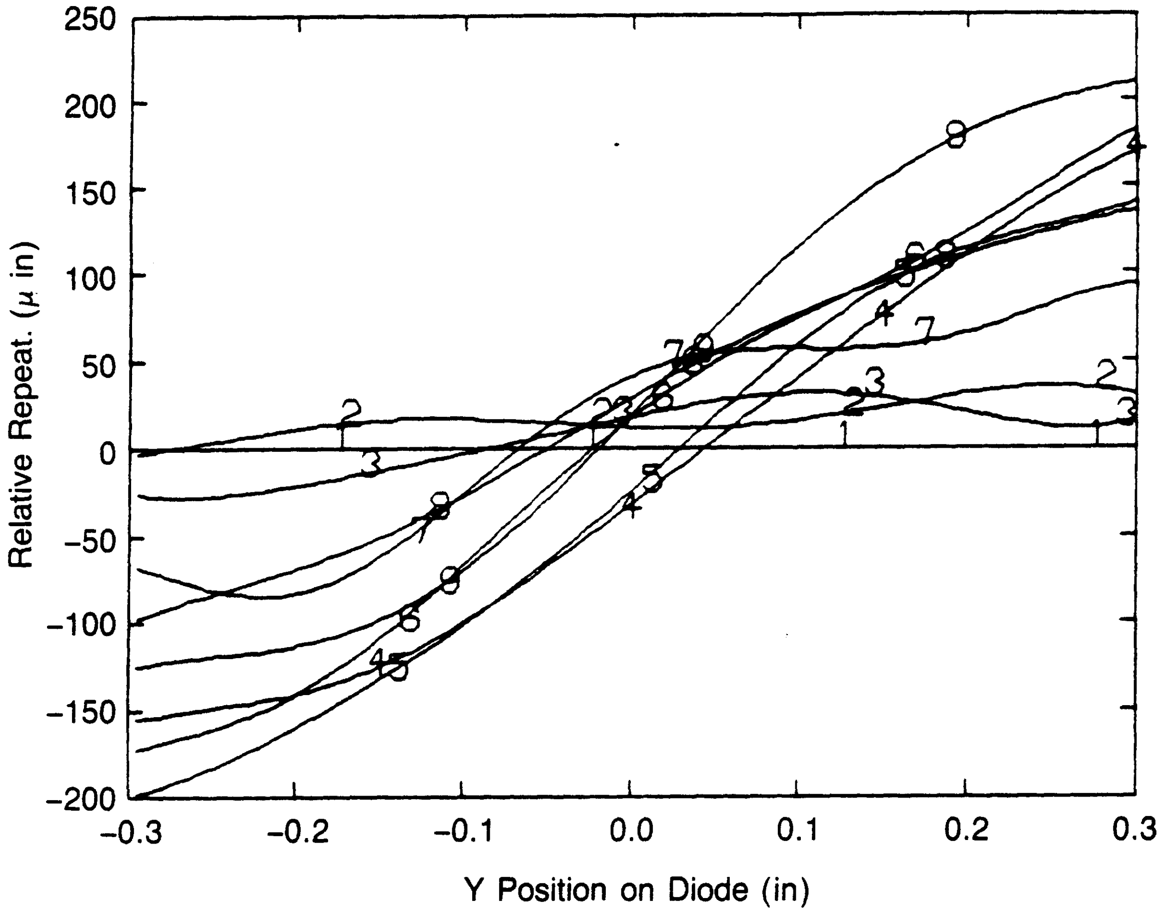

Figure 7.23 Repeatability of diode 2, measured by subtracting linearized results of first pass from all subsequent passes (stage used was Klinger)

Since the Klinger stage was known to have poor performance, these values were questionable, so a similar test was run using the vertical machining center bed. Figures 7.24 and 7.25 show the results of repeatability tests on the diodes (made using the machining center as a stage). The repeatability for diode 1 is on the order of 80 μin (2 μm) and that for diode 2 is on the order of 40 μin (1 μm). These are equal to the stability values for the two diodes as discussed in Section 7.4.2.

The effect of the Klinger stage performance on the tests shows up most noticeably in the X_d axis linearizations. With the optics available, it was not possible to mount the X_d motion optics on the stage. Thus only the Y axis motion of the vertical machining center (X_d diode axis) was measured by the laser and none of the straightness error in the stage. The pitch and yaw errors in the stage showed up as Abbe offset errors on the order of 20 μin (.5 μm).

The next set of tests were indirect measurements of the diodes' repeatability. The diode axes' offsets had to be found and multiple runs were made. Thus the variation of calculated axes offsets are also an indication of diode repeatability.

7.4.4 Determination of Lateral Effect Diodes' Axes Offsets

As calibrated, the diodes' X_d and Y_d axes were forced to parallel to within the limit of the orthogonality of the laser interferometers (found to be .0028 radians). However, it was not possible to determine

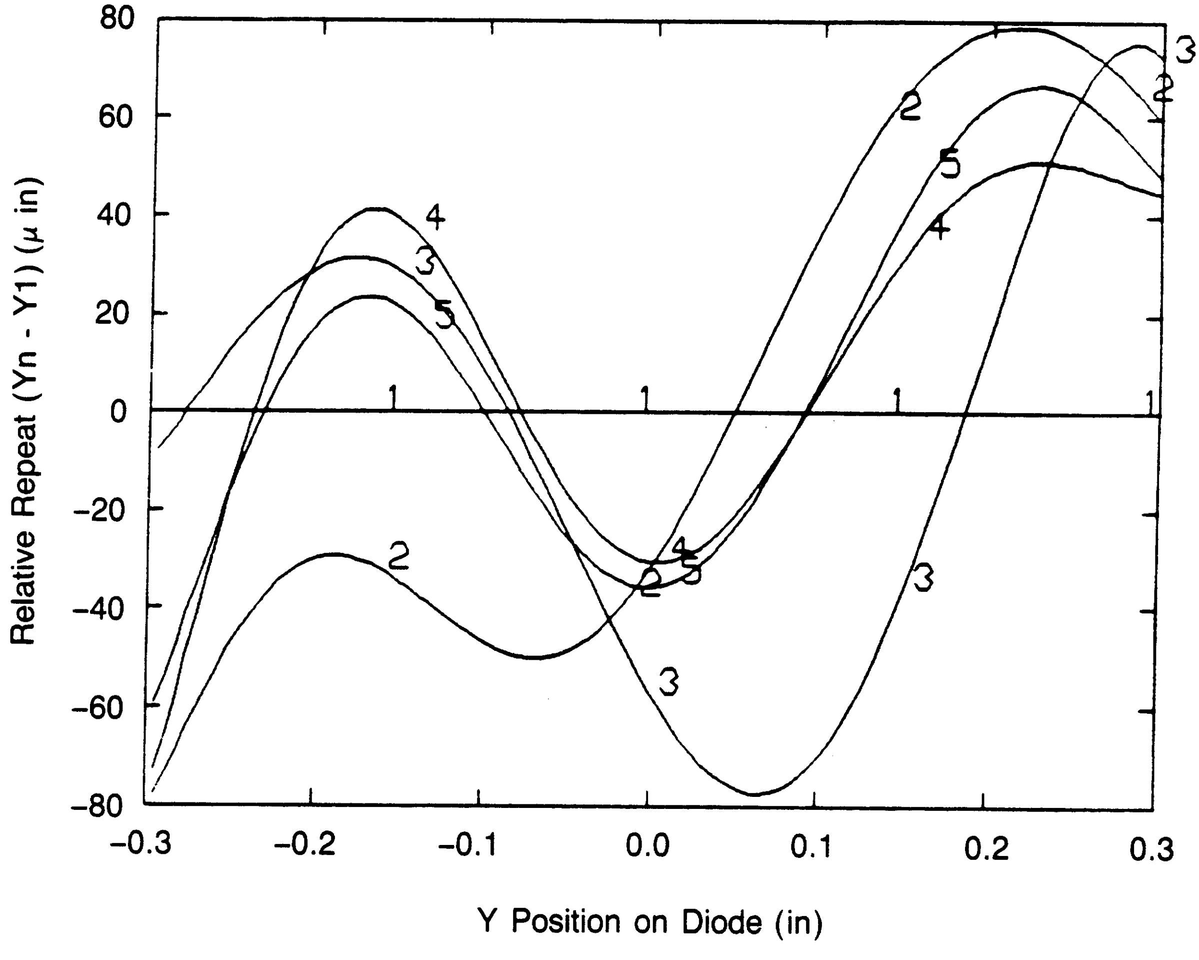

Figure 7.24 **Repeatability of diode 1, measured by subtracting linearized results of first pass from all subsequent passes (stage used was machining center)**

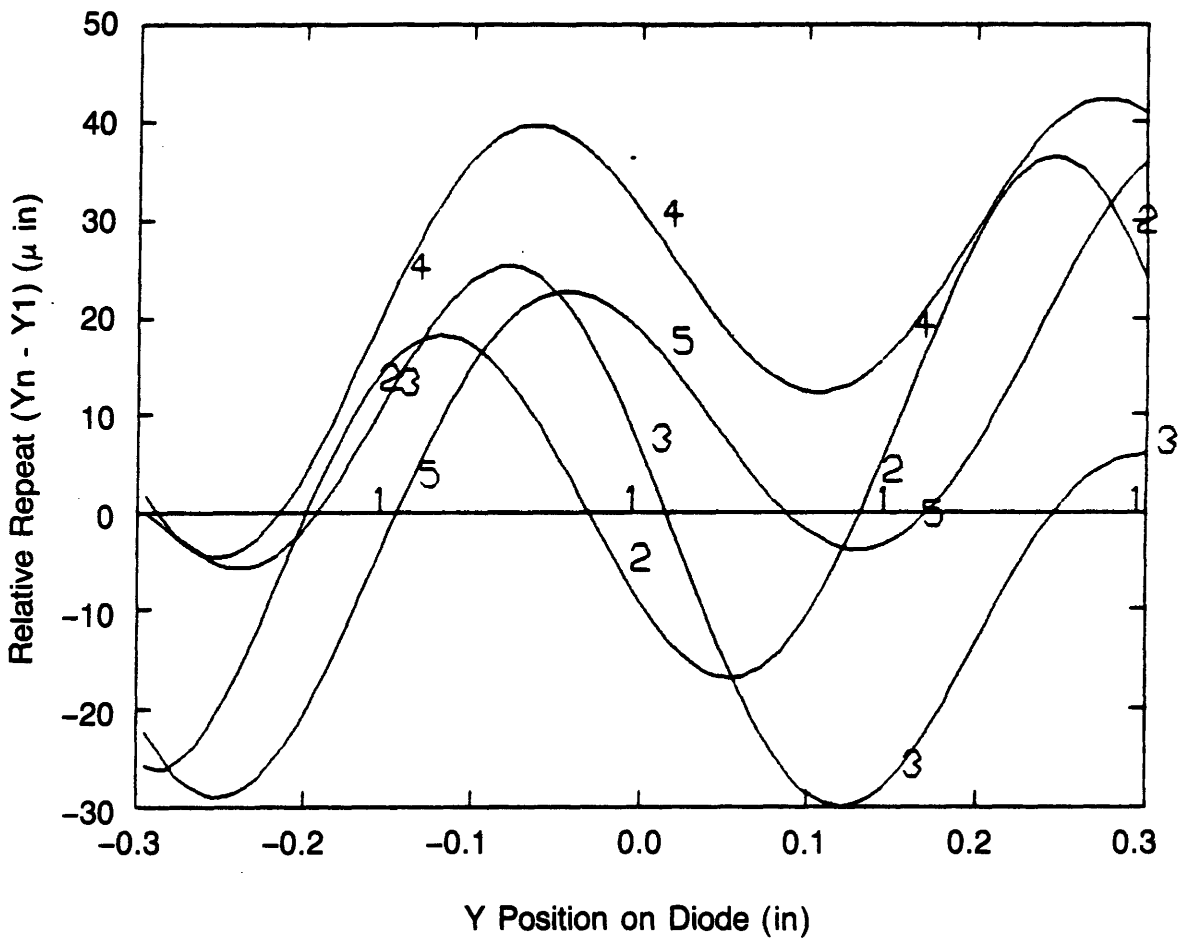

Figure 7.25 Repeatability of diode 2, measured by subtracting linearized results of first pass from all subsequent passes (stage used was machining center)

where the center of the light sources were, so they could not both be made to lie on the stage X axis; thus there would be an offset in the X_d and Y_d axes of the two diodes. To determine the resultant offsets A and B in the diodes' X_d and Y_d axes respectively (as shown in Figure 7.26) a light source was spotted on diode 1, and then moved a known distance ℓ (measured by laser interferometer) until it spotted diode 2. Unfortunately, the setup did not ensure that the path of the light spot was parallel to the linearized Y_d axes of the diodes, thus the following algorithm was developed.

As shown in Figure 7.26, multiple runs were made corresponding to starting at the bottom of diode 1 and ending on the bottom of diode 2 (also middle, and top were made). The distances (ℓ) between groups of points were measured with a laser interferometer. Since the machine tool bed was used as the stage for the 3" (76 mm), the multiple runs will all lie on the same line to within 3 arc seconds (machine tool bed is good to 1 arc second per inch as discussed in the opening section of this chapter). Thus the angle Φ can be easily found from differences in readings on the same diode. The A and B offsets are thus found from:

$$\Phi = \tan^{-1}\left(\frac{Y_{2run1} - Y_{2run3}}{X_{2run1} - X_{2run3}}\right) \tag{7.2}$$,

$$A = \ell\cos\Phi + X_2 - X_1 \tag{7.3}$$,

$$B = \ell\sin\Phi + Y_2 - Y_1 \tag{7.4}$$.

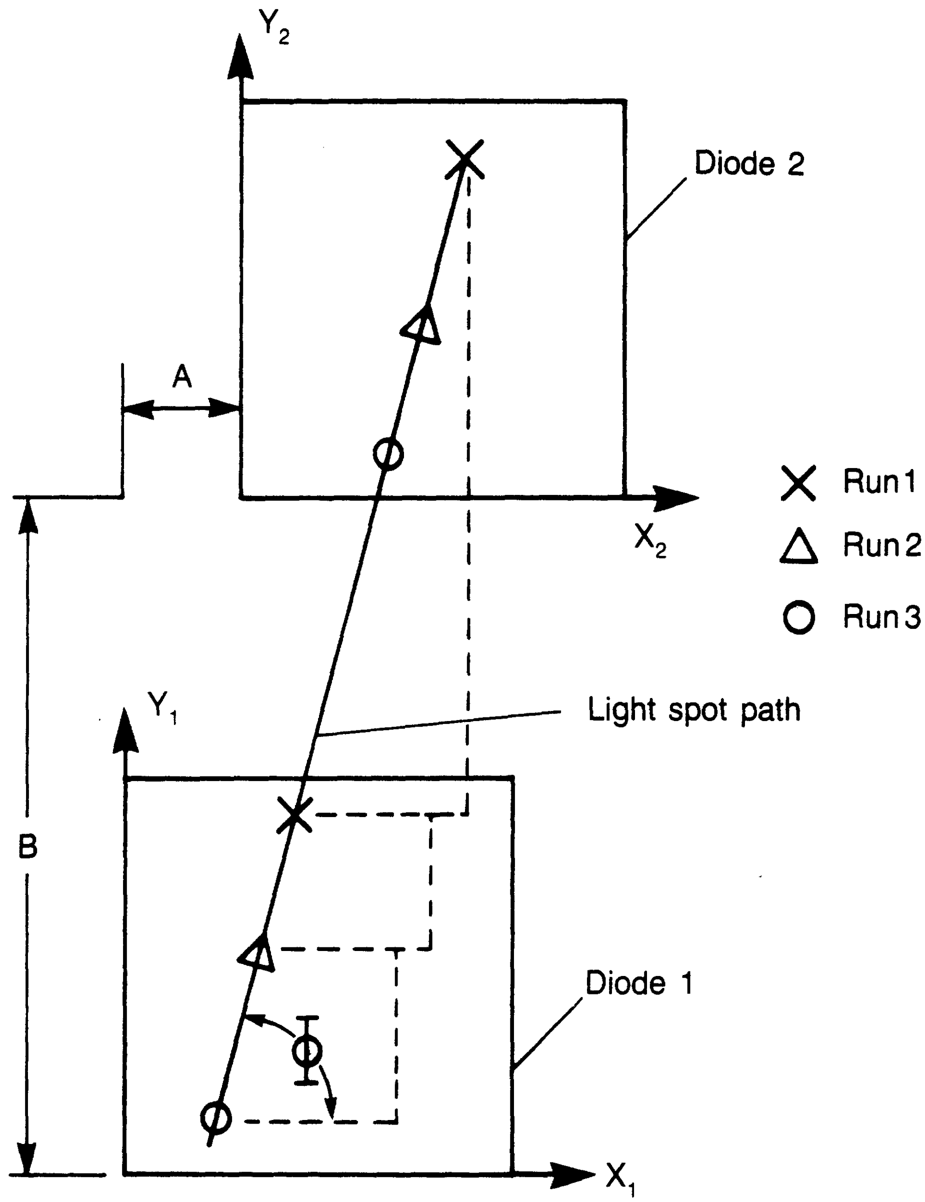

Figure 7.26 Schematic representation of test to determine diode axes' offsets

Ten runs were made to obtain the angle and distance values. The angle Φ was determined from the readings from diodes 1 and 2, and the values were $\Phi_1 = 89.436235°$, $\sigma_{\Phi_1} = .004666°$, $\Phi_2 = 89.570242°$, $\sigma_{\Phi_2} = .004264°$. When the results from the two diodes were combined, the values were $\Phi = 89.503239°$, and $\sigma_\Phi = .029424°$. The source of this error (systematic versus random error) cannot be explained at this time; therefore the average value will be used to find the offsets A and B. The results of this portion of the test, however, were very good: A = .051780, σ_A = .000012", B = 3.012019", and σ_B = .000035" (1.3152, .0003, 76.5053, and .0009 mm). These results also show very good repeatability for the system. When the effect of the angular error is incorporated into (7.3) and (7.4) using Equation 5.2, the errors are σ_A = .001541" and σ_B = .000037" (.0391, and .0009 mm).

The "proper way" to do the test would have been to use the same setup as was used to linearize the diodes which would have eliminated the error in Φ. Initially this was done, but the data taken was from an area of the diode that was not linearized. The data could not be analyzed until the curve fitting interpolation routines were developed (see Chapter 8) and another user was waiting for the vertical machining center, thus in the hurry to collect all the data needed for the rest of the experiment, this mistake was made. When the machine became free again, the above test and analysis were made.

7.4.5 Determination of Light Source Inclination Angles

This section will describe the tests and algorithms used to determine the angles of inclination of the light sources, whose effect on system accuracy are discussed in 5.4.2. For purposes of analyzing the data, the light source orientation angles are defined as the Euler angles ϕ and ψ as shown in Figure 7.27 (compare to the α and β notation shown in Figure 5.5).

To determine the angles ϕ_i and ψ_i for the two diodes, a Z axis motion must be added to the existing test setup (the vertical machining center conveniently provided this motion). As the light sources are moved away (along the Z axis) from the diodes, if they are not orthogonal to the diodes, then the light spots will appear to drift across the diodes as shown in Figure 7.27. The effect of the light sources' plane not being parallel to the diode plane as the two are moved apart is overcome by taking one set of readings, and then rotating the light sources 180° and redoing the tests. The average of angles ψ_1 and ψ_2 will then cancel this effect as well as the effect of the Z axis not being orthogonal to the XY plane. Note that the angle ϕ is not affected by the possible slight misalignment between the planes. For the actual test, motions along the Z axis were done in steps, and the output from the diodes was linearized and stored. With a total of I X_d, Y_d, and Z measurements taken as described above, the angles averaged respectively to yield: (where Z_{ij} is the net motion along the Z axis and subscript i

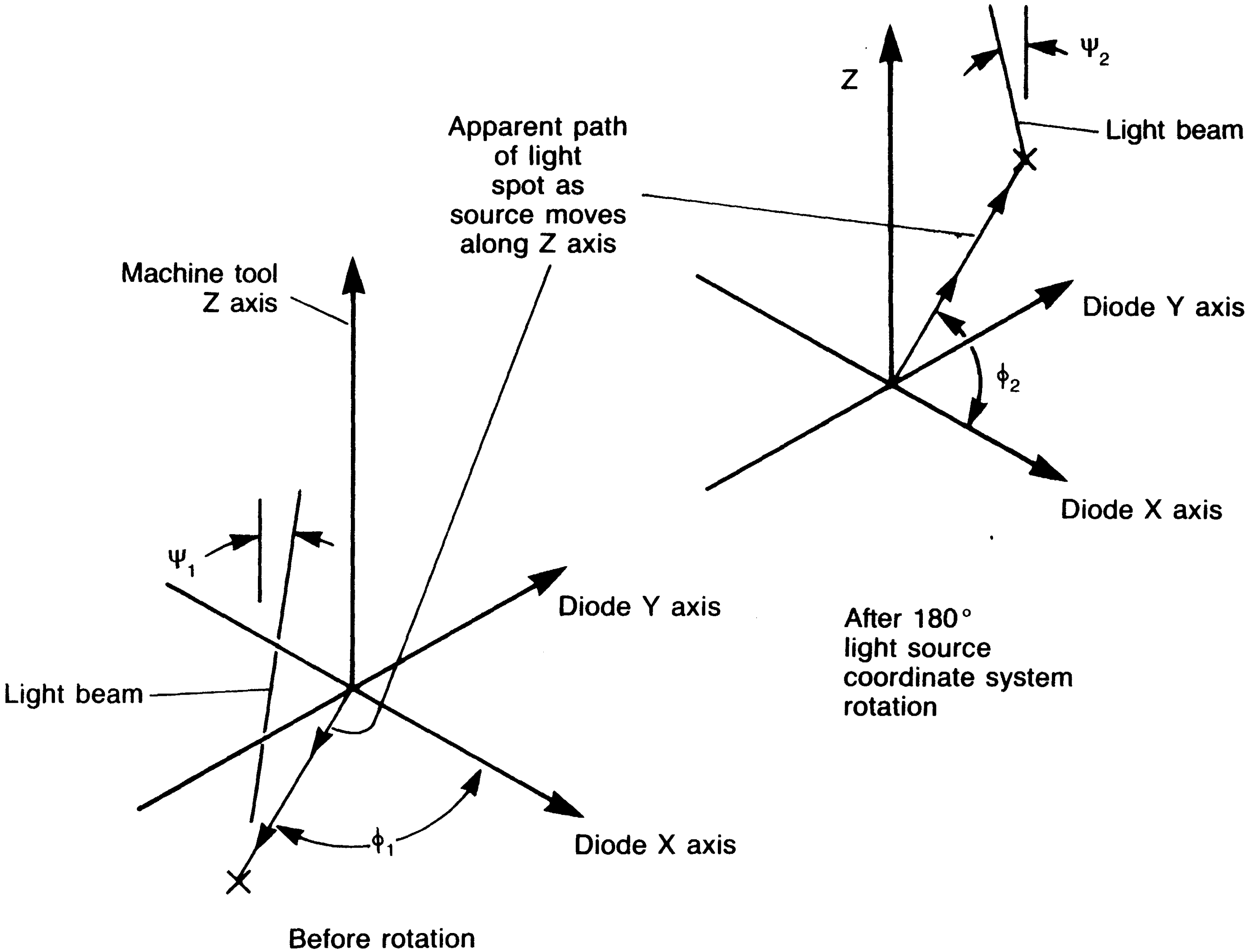

Figure 7.27 Schematic representation of test to determine light source orientation angles.

is the diode/light source number, and subscript j is the increment number):

$$\phi_i = \frac{\sum_{j=1}^{I} \tan^{-1}(Y_{ij}/X_{ij})}{I} \qquad (7.5),$$

$$\psi_i = \frac{\sum_{i=1}^{I} \tan^{-1}\left(\frac{(X_{id}^2 + Y_{id}^2)^{1/2}}{Z_i}\right)}{I} \qquad (7.6).$$

Note that after the light sources were rotated 180°, the ϕ and ψ for a particular light source will be obtained from data from the other diode.

The angles $\alpha_{X\ell i}$ and $\beta_{Y\ell i}$ of the two light sources (as shown in Figure 5.5) are found from the angles ϕ and ψ by:

$$\alpha_{X\ell i} = \psi \sin\phi \qquad (7.7),$$

$$\beta_{Y\ell i} = -\psi \cos\phi \qquad (7.8).$$

An error in ψ is directly proportional to the errors $\sigma_{X\ell i\alpha}$ and $\sigma_{Y\ell i\beta}$, while an error in φ must be evaluated using Equation 5.2:

$$\sigma_{X\ell i\alpha} = \psi\left(\sin\phi - \sin(\phi + \sigma_\phi)\right) \qquad (7.9),$$

$$\sigma_{Y\ell i\beta} = \psi\left(\cos\phi - \cos(\varphi + \sigma_\varphi)\right) \qquad (7.10).$$

The results of the experiment and the subsequent data analysis are given in Table 7.8.

7.4.6 Summary of Physical Characteristics of the Calibrated Light Source-Lateral Effect Diode System

The net effect of all the "errors" (system limits) are listed in Table 7.9. The worst errors were due to the stage and to the error in diode axes X offset. The root mean square of the errors indicates that the Light Source-Lateral Effect Diode system will have errors of: σ_X = 1572 μin (39 μm), σ_Y = 207 μin (5 μm), and σ_Θ = 111 μradians. The meaning of these values with respect to the final system tests will be discussed in Chapter 8.

7.5 Calibration of the Impedance Probe System

This section will describe the tests performed on the impedance probe system for: linearization, probe spacing, and stability and repeatability. First the system electronics are discussed. The individual test setups are then described in each subsection and results from the tests are also presented. The summary will evaluate the total impedance system performance based on the methods developed in Chapter 5.

The electronics supplied with the probes were suspicious in that screws were used to adjust gain, zero, and linearity. That in itself is not so bad, but every now and then the readings would change by a couple

Table 7.8 Results of Light Source Orientation Tests

All Angles in Radians

Angle	Light Source 1	Light Source 2
ϕ	-.746148	.748083
σ_ϕ	.0908	.0866
ψ	.003996	.002762
σ_ψ^*	.000638	.000707
$\alpha_{X\ell i}$	-.002713	.001879
$\alpha_{X\ell i\alpha}$	.000514	.000509
$\beta_{Y\ell i}$	-.003996	-.002762
$\sigma_{Y\ell i\beta}$	.001045	.000933

*These $\sigma_{\psi i}$'s are the sum of the $\sigma_{\psi i}$ and the corresponding values from (7.20) and (7.21)

Table 7.9 Results of Light Source-Lateral Effect Diode System Calibration: The Total System Error Budget

Perturbation Error	Value	Induced σ_X (μin)	Induced σ_Y (μin)	Induced σ_Θ (μrads)
Axes offset errors:	(μin)			
σ_X	1541	1542	0.	85.5
σ_Y	37	0.	35	11.7
Linearization errors:				
σ_{X_1}	209	209	0.	11.6
σ_{Y_1}	137	0.	137	45.6
σ_{X_2}	206	206	0.	11.4
σ_{Y_2}	85	0.	85	28.3
Repeatability:				
σ_{X_1}	80	80	0.	4.4
σ_{Y_1}	80	0.	80	26.7
σ_{X_2}	50	50	0.	2.8
σ_{Y_2}	50	0.	50	16.7
Interpolation error:				
σ_{X_1}	35	35	0.	1.9
σ_{Y_1}	25	0.	25	8.3
σ_{X_2}	25	25	0.	1.4
σ_{Y_2}	30	0.	30	10.0

Table 7.9 Continued

Perturbation Error	Value	Induced σ_X (μin)	Induced σ_Y (μin)	Induced σ_Θ (μrads)
Angular errors:	(μrads)			
Diode flatness:				
$\sigma_{X\alpha_1}$	5000	0.	6.3	.3
$\sigma_{Y\beta_1}$	5000	6.3	0.	2.1
$\sigma_{X\alpha_2}$	5000	0.	6.3	.3
$\sigma_{Y\beta_2}$	5000	6.3	0.	2.1
Diode axes orthogonality error:				
$\sigma_{Z\Theta}$	2800	2	2	.7
$\sigma_{Z_1\gamma}$	2800	2	2	.7
$\sigma_{Z_2\gamma}$	2800	2	2	.7
Light source orientation errors:				
$\sigma_{X\ell_1\alpha}$	514	25.7	0.	1.4
$\sigma_{Y\ell_1\beta}$	1045	0.	52.3	17.5
$\sigma_{X\ell_2\alpha}$	509	25.5	0.	1.4
$\sigma_{Y\ell_2\beta}$	933	0.	46.7	15.6
Root mean square errors:				
		1572	207	111

tenths of a volt. Also it was discovered that if the oscillator-demodulater box was wapped with the tip of the small adjustment screwdriver, the readings would shift by many volts. Thus a dedicated system (robot) would require the use of electrical components whose properties are fixed and stable.

7.5.1 Linearization of Impedance Probes

The impedance probes had to be linearized in the as mounted position on the POSOR plate; thus to avoid large Abbe's offset error, the vertical machining center bed was used as a stage and the interferometer was positioned at a point roughly coincident with the centroid of the triangle formed by the probes. The target was the other POSOR plane. The setup is similar to the one shown in Figure 7.30, except that a distance interferometer was used. The oscillator - demodulator boxes supplied with the probes were adjusted so the zeros between the probes were offset by about .1 volt, and the gain was set to about .05"/volt (1.27mm/volt). The "linearity" was also set to make the response as "linear" as possible.

The linearization curve should not include data beyond the range of probe stability and repeatability. As shown in Figure 7.28, the probes are only good out to about .05" (1.27 mm). This however is sufficient for most POSOR designs (larger diameter probes are available with longer ranges). The linearization test was conducted by manually controlling the vertical machining center bed, and signalling the analog to digital converter when it should read the probe and interferometer channels.

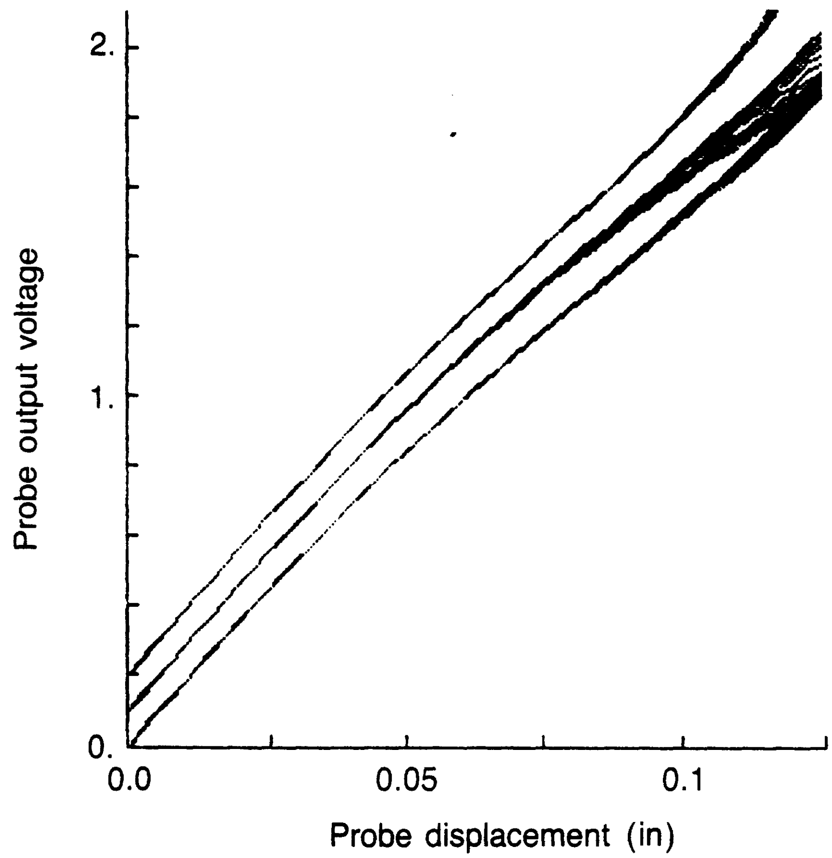

Figure 7.28 Impedance Probe output voltage and repeatability as a function of displacement over long distances

Twenty one points along the path were taken, and various order curves were tried to determine the most appropriate to fit the data. A fourth order curve was found to be the best, with deviations on the order of 5 μin (.13 μm). The resulting linearization polynomials' coefficients are given in Table 7.10. The accuracy of the linearization is discussed in Section 7.5.4 along with probe stability and repeatability.

There is no easy method for determining the error in orthogonality between the probes and the plate which they are mounted in. Most of the effect of such an error, however, can be "calibrated out" by making sure that the orientation between the plate that holds the probes and the target plate does not change as they are moved apart. The orientation angle errors $\sigma_{\varepsilon Xi}$ and $\sigma_{\varepsilon Xi}$ (discussed in 5.3.2) will thus be equal to the change in the orientation of the plates as they are moved away from each other. The equivalent sensor accuracy error is due to the rotation of the machine tool bed times the distance from the machine ways to the test. (a form of Abbe offset error). This value is on the order of $.05'' \times 5\mu rad \times 15'' = 3.8$ μin (.1 μm).

7.5.2 Determination of Relative Position of the Impedance Probes

In order to determine the probe spacings a, b, and c as shown in Figure 7.28 (and in Figure 5.1), known angles α and β must be introduced to the target plane coordinate system and a, b, and c must be calculated from Equations 5.4 and 5.5. Since two sets of angular interferometer optics were not available, the angles were introduced and measured

Table 7.10 Impedance Probe Linearization Coefficients

$$\text{Displacement} = A_0 + A_1X + A_2X^2 + A_3X^3 + A_4X^4$$

	Probe 1	Probe 2	Probe 3
A_0	-.0061186	.0096695	.0173366
A_1	-.0537874	-.0569624	-.0588981
A_2	-.0013568	.0034440	.0103716
A_3	-.0125008	-.0102412	-.0180598
A_4	.0040221	.0008111	.0054609

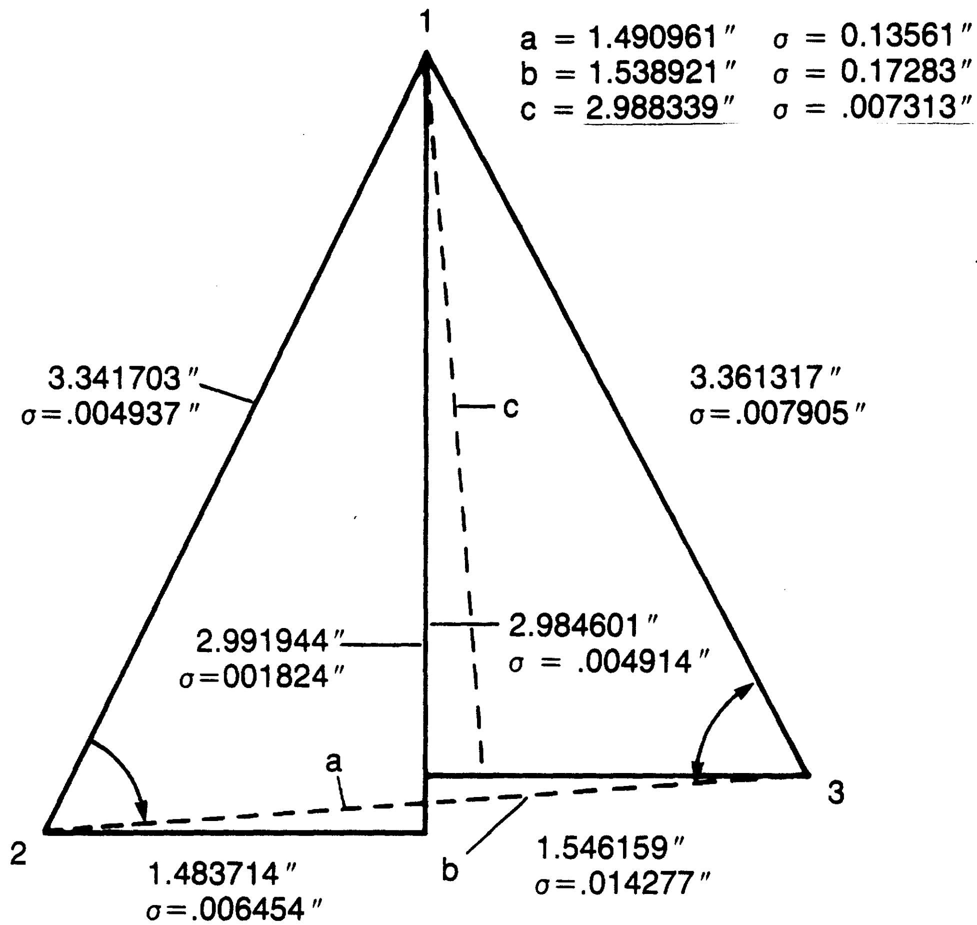

Figure 7.29 Measured distances between probes, and geometry for calculating a, b, and c

separately, and the relative distances between the probes were calculated as described below (rather than in the probe coordinate system which may not be aligned perfectly with the coordinate system α and β are to be made in). The distance a, b, and c were then found from these values.

To introduce the angles α and β individually, the apparatus shown in Figures 7.30 and 7.31 was used. The probes were mounted to a plate which was held to a ground shaft (axle) which was held to the bed of the machine tool. A dial indicator in the spindle was used to indicate the axle in to be perpendicular to the spindle to within .0005"/5" (to account for axle straightness, a measurement was made and the reading was ≈ .0003'/5", the axle was rotated and the measurement made again and was on the order of ≈ .0002"/5" but in different directions). The spindle thus formed one axis of motion and the axle the other axis of motion. Moving the spindle a finite amount was tricky because of stick slip. The axle was moved by shimming up the rear end of the plate. Each run was done separately and the angles were measured with an angular interferometer as shown in Figures 7.30 and 7.31.

The distances between probes 2 and 1, and 2 and 3 were determined from changes in the angle α and changes in the probe readings ℓ by:

$$D_{2i} = \frac{(\ell_2 - \ell_i)}{\tan\alpha} \qquad (7.11).$$

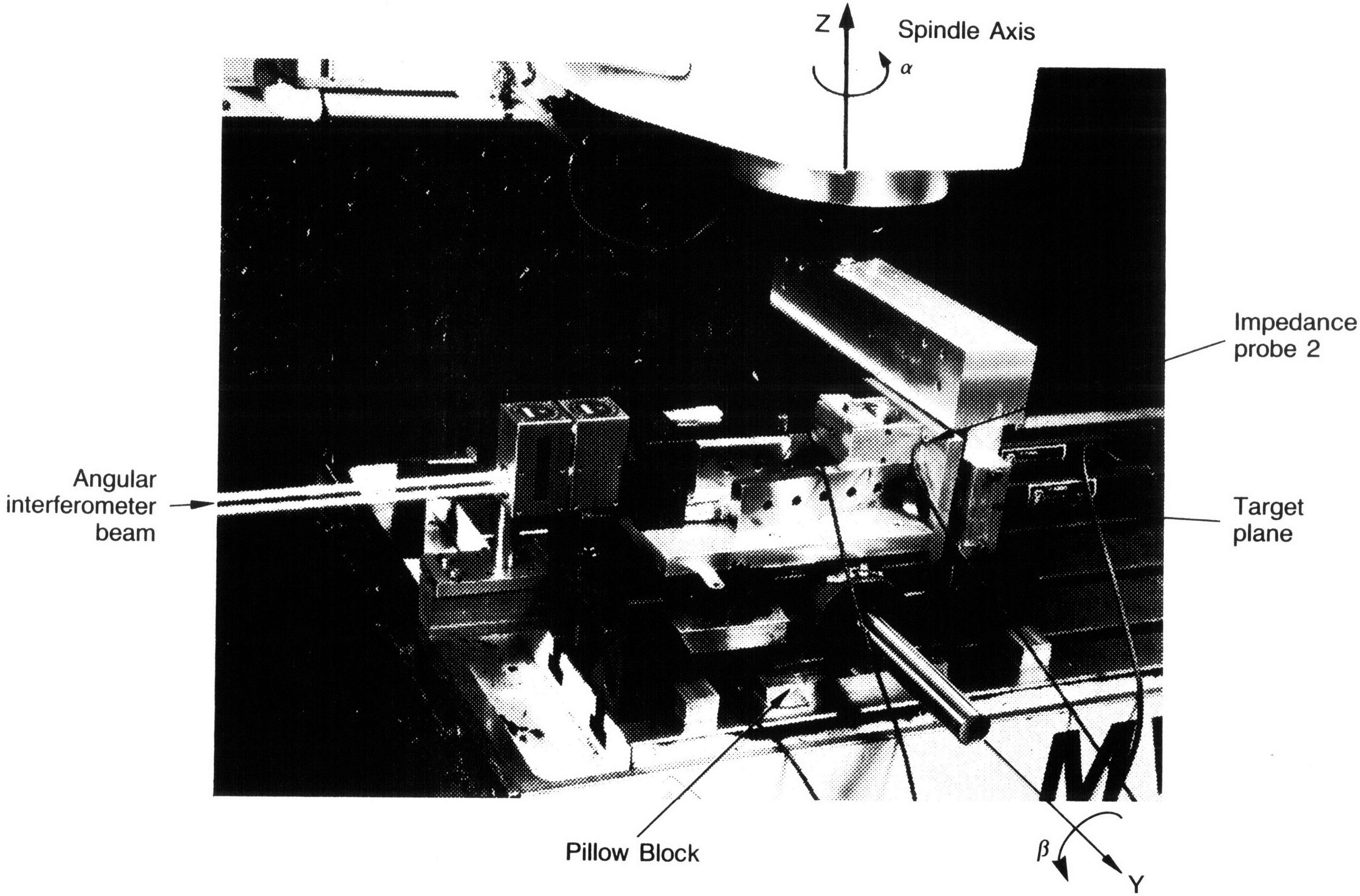

Figure 7.30 Experimental setup for determining relative Y position between impedance probes

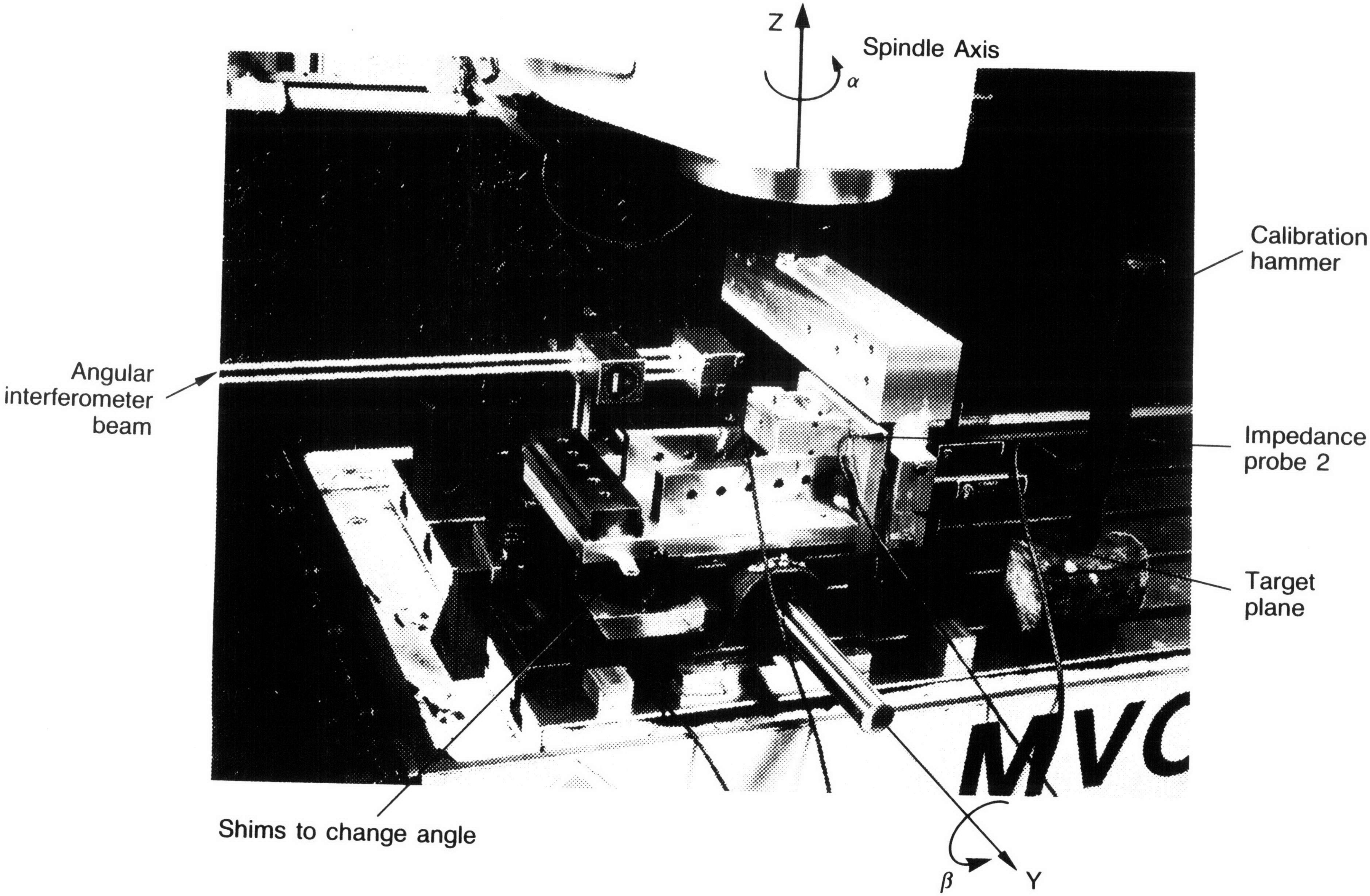

Figure 7.31 **Experimental setup for determining relative X position between impedance probes**

A similar algorithm was used for the distances between probes 1 and 2, and probes 1 and 3. The results and the variations of the readings are shown in Figure 7.29. All the results were very good (considering that we are measuring off a cosine, which gives a bigger error, but then the results are used in a cosine which is not as sensitive to error) except those for D_{23} which was measured off the angle α induced by the spindle. Over several runs, D_{23} was always bad and could not seem to be corrected. A possible explanation for this is offered below.

A test parameter to be checked is the effect of the spindle and probe axes not being perpendicular by a small angle ε. The effect is to cause the intended angle β to be $\beta(1 - \cos\varepsilon)$ and for a rotation $\alpha = \beta\varepsilon$ The former is negligible (tenths of microradians), while the latter can cause some serious errors if care is not taken. The effect of the induced angle α is to cause an error $\sigma_{\alpha\beta\ell i}$ in the probe readings ℓ_i on the order of:

$$\sigma_{\alpha\beta\ell i} = \varepsilon\beta(a + b) \qquad (7.12).$$

For this experiment, if $\delta\ell_i$ is to be kept below the accuracy of the sensors (5 μin (.13 μm)), then using system values of β = .05"/3", (a + b) = 3" (.4233 mm, 76 mm), the tolerance on ε is 100 μradians, or .0005"/5". As noted above, the axes were held parallel to within .0005"/5". Note that if two sets of angular optics were available, then both α and β could be measured simultaneously and the problem of axis alignment could be avoided. Using Equation 5.2 and 7.11 with the error in α equal to 100 μradians (and difference in sensor readings equal to .05" (1.3 mm)), the error in D_{21} is .0179". If the beam (that held the target plate) attached to the spindle had even this slight wobble, it would account for the large error in D_{23}.

7.5.3 Determination of Impedance Probe Stability and Repeatability

Factors affecting probe stability are methods of mounting, supply voltage, distance from the surface to be measured, and room temperature. A valuable lesson in precision calibrations when you are trying to get more out of a sensor than the manufacturer even knows is possible, is never assume that what the manufacturer says is correct (better to have no maps in uncharted waters and be careful, then to plow into a reef!). These factors are discussed in detail below.

When the impedance probe system was first assembled on the POSOR plate, the threaded bodies of the probes were screwed into tapped holes in the plates, and the nuts (supplied with the probes) were gently tightened down to lock them in place. This was a big mistake, because the nuts apparently stressed the probe housing enough to cause them to be unstable (on the order of 100 µin (2.5 µm)). As was found out after the experiment, the probes should have been screwed into the POSOR plate, and then epoxied in place. The stability data for the probes in the former state (which the experiment was run in) is given below followed by measurements (taken after the measuring beam experiment was completed) with the probes epoxied in place.

The linearization and repeatability tests were actually combined. Five runs were made one evening, and five runs were made the next morning. Curves from the 10 sets of coefficients generated by least squares routine were then plotted as shown in Figures 7.32, 7.33, and 7.34 (curves are numbered chronologically). The curves show almost a pure drift. Whether the drift is due to the electronics or stress on the probe case by the locking nuts at this point was not known. But as experiments (done at a later date with the locking nuts removed) showed, probe 1 was insensitive to voltage supply drift compared to the other probes. Thus the results shown in Figures 7.32, 7.33, and 7.34 (which show all three probes drifting about the same amount) seem to indicate that the drift was due to the distortion of the housing. The linearization coefficients were the averaged coefficients of those used to obtain Figures 7.32, 7.33, and 7.34. The error σ_{ℓ} for the linearization curves is therefore on the order of 100 μin.

To determine the "true" stability of the probes, a "cap test" was done. For the cap test, the probes were epoxied into an aluminum block with the distance from the probe tip to the target fixed at .02" (.51 mm). The first tests were made to determine the sensitivity of the probes to a change in the voltage supply. The results are given in Table 7.11. Similar changes in the voltage supply at different mean levels (10 and 12 volts) produced similar results. For the gain setting of .05"/volt (1.27mm/volt), probes 1, 2, and 3 are stable to .000028, .002582, .002422 inches per one volt change in supply voltage (.7, 64.6, 60.6 μm/volt) respectively. To see if the superior performance of probe 1 was due to the probe or to the electronics, the oscillator -

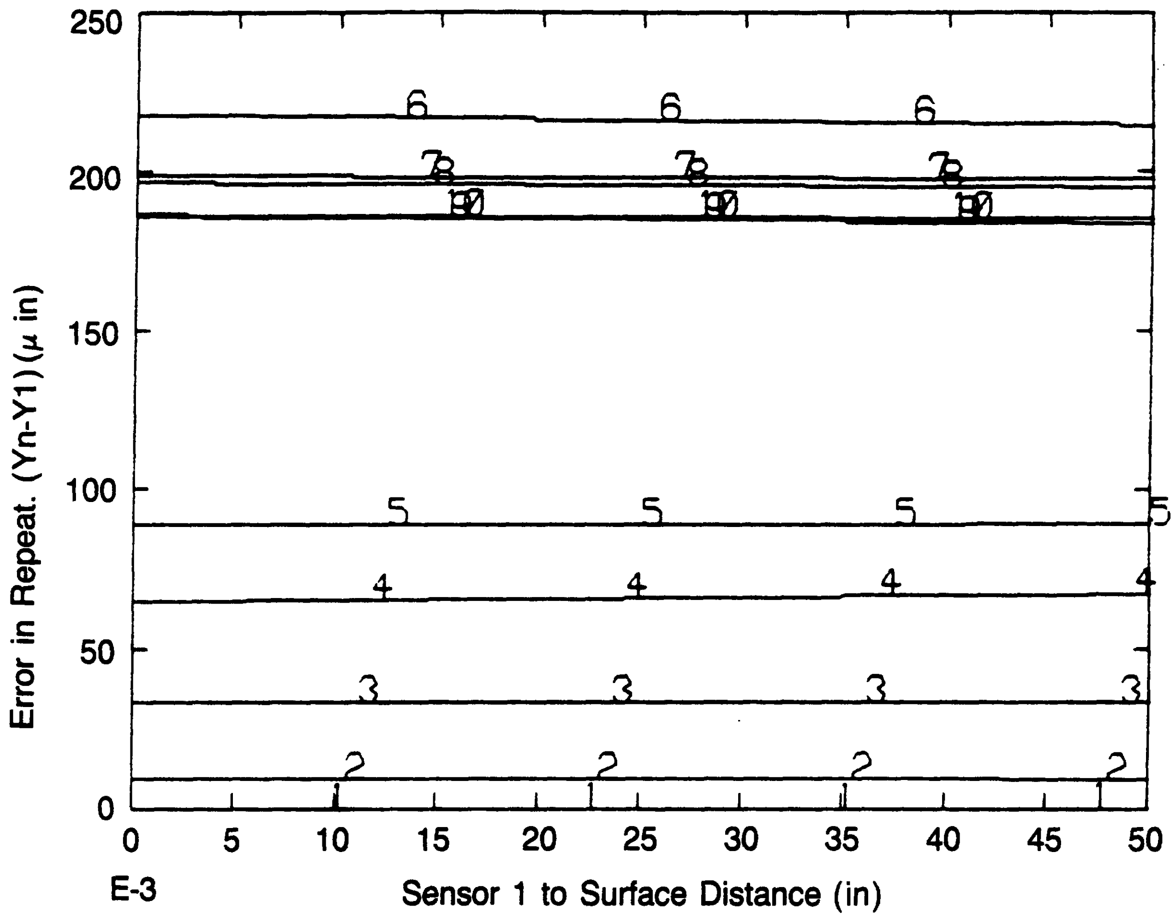

Figure 7.32 Repeatability of impedance probe 1, measured by subtracting linearized results from first pass from all subsequent passes

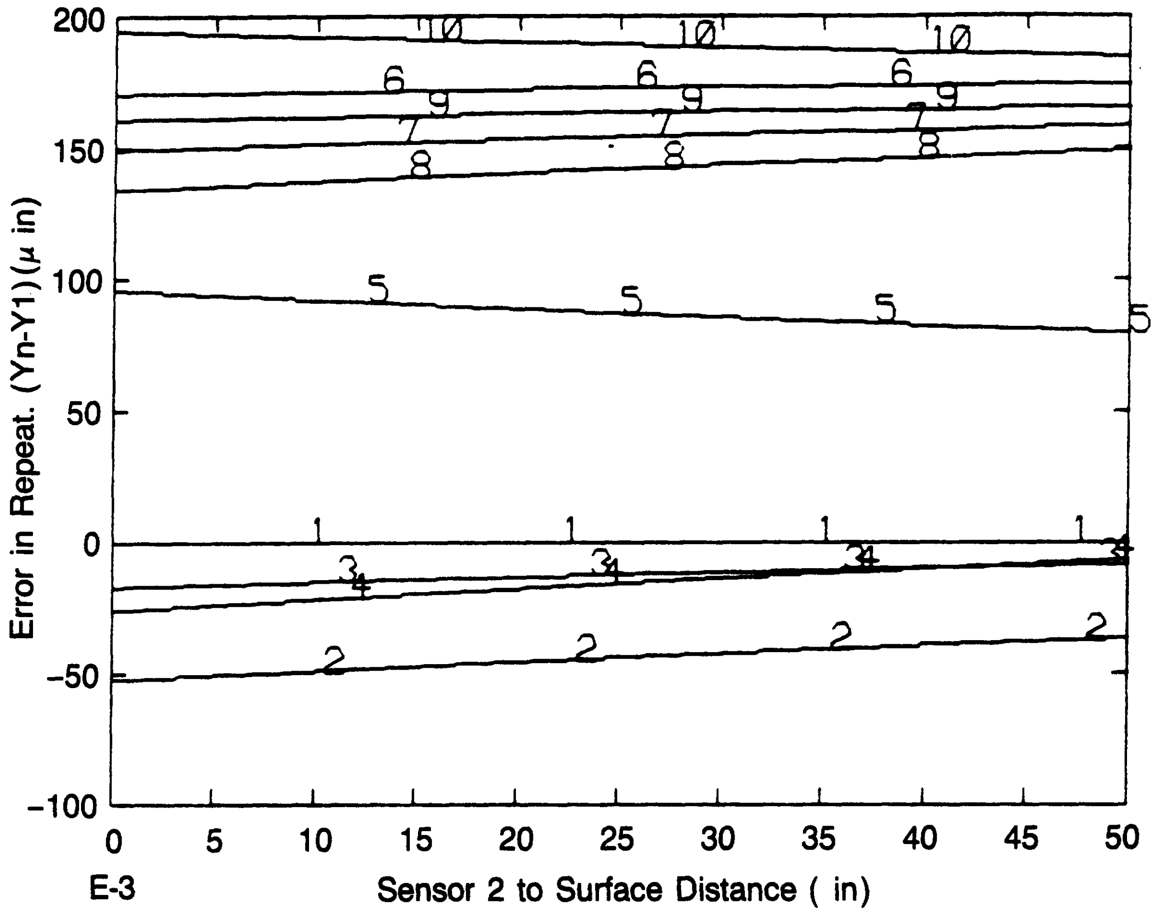

Figure 7.33 Repeatability of impedance probe 2, measured by subtracting linearized results from first pass from all subsequent passes

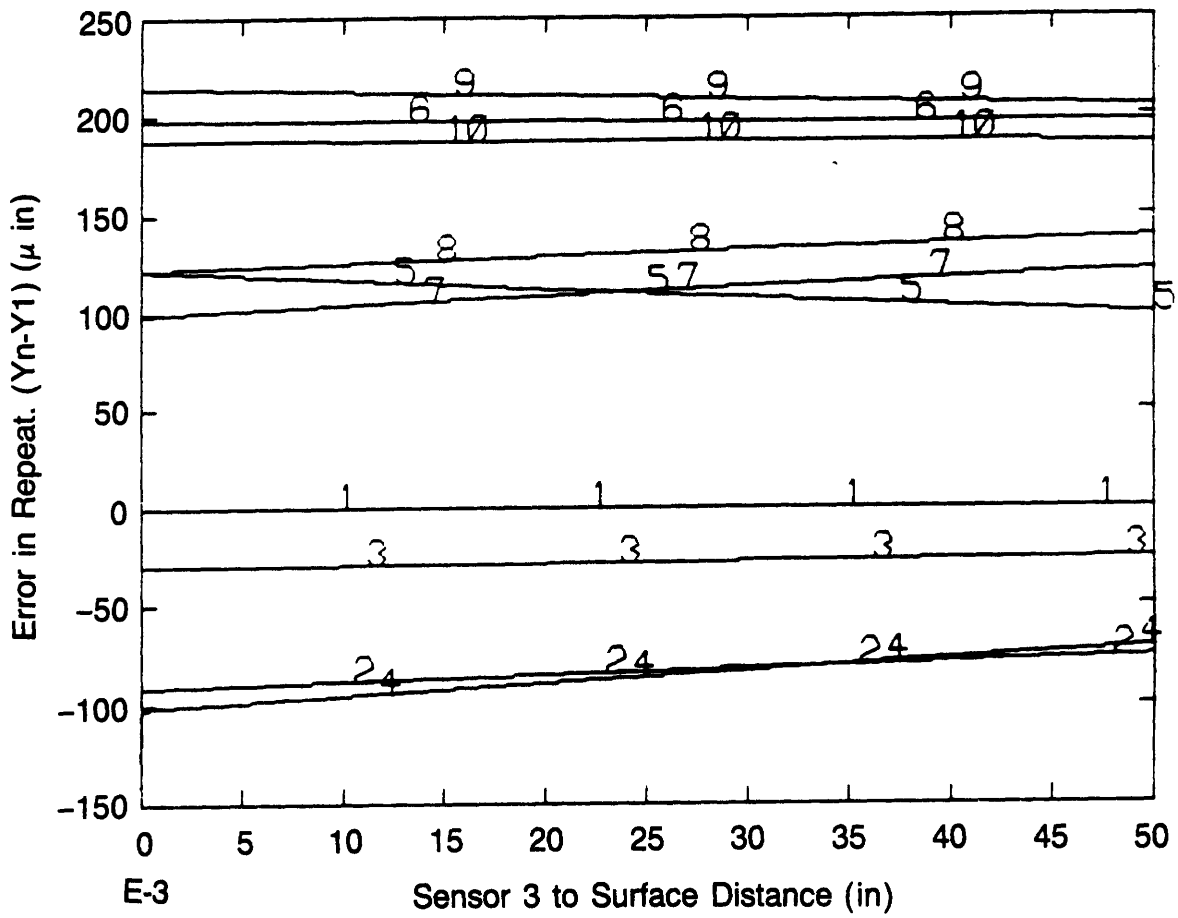

Figure 7.34 Repeatability of impedance probe 3, measured by subtracting linearized results from first pass from all subsequent passes

Table 7.11 Results of Impedance Probe Tests to Determine Sensitivity to Supply Voltage Variations

Probe output voltages

	V	σ_V	σ_{Vmax}	σ_{Vmin}
Before Voltage Change: (293 readings)				
Supply:	11.3824	.00091	.00174	-.00136
Probe:				
1	.419050	.000041	.000070	-.000090
2	.784706	.000196	.000334	-.000366
3	.550081	.000138	.000209	-.000261
After Voltage Change: (212 readings)				
Supply:	11.0169	.00072	.00373	-.00077
Probe:				
1	.418846	.000022	.000084	-.000056
2	.765835	.000209	.001345	-.000425
3	.532376	.000107	.000594	-.000196

Note: the temperature was constant to within .05°F during the experiment.

demodulator boxes were switched but the results stayed the same. Probes 2 and 3 are probably the norm with probe 1 being the exception

The variations on the before and after tests, shown in Table 7.11, are also typical of the long term performance of the probes (assuming the supply voltage does not change). Thus the probes 1, 2, and 3, can be stable to 2.1, 9.8, and 6.9 μin (.05, .26, and .17 μm) respectively.

7.5.4 Summary of Physical Characteristics of the Calibrated Impedance Probe System

The net effect of all the "errors" (system limits) are listed in Table 7.12. The worst errors were due to the nuts stressing the threaded case, the voltage drift in the electronics, and the errors in calculating the probe spacings a, b, and c. Solutions for both of these problems, however, were presented above (epoxy the sensors in place, stabalize the electronics, and use two angular interferometers), so for future systems these errors can be avoided. For the tests to determine measuring beam system performance, discussed in Chapter 8, the voltage shift errors will be compensated for digitally, which will also account for small changes due to the threaded nuts stressing the case.

Two types of error are apparent, the random component and the steadily increasing component. The former is due to the error in the linearization curves (≈5 μin) and the instability of the probe electronics as shown in Figure 7.32, 7.33, and 7.34. For probes 1, 2, and 3, these errors are 5, 20, and 24 μin (.13, .5, and .63 μin)

Table 7.12 Results of Impedance Probe System Calibration:

Total Error Budget

Perturbation Error	Value (in)	Induced $\sigma_{\ell_{0,0}}$ (μin)	Induced $\sigma_{\ell_{-1,1.5}}$ (μin)	Induced σ_{α} (μrad)	Induced σ_{β} (μrad)
Errors that increase with the degree of freedom measured:					
Linear errors:					
σ_a	.013561	113	188	76	38
σ_b	.017283	143	0.	97	48
σ_c	.007313	0.	20	0.	41
Probe orientation errors:					
$\sigma_{\alpha\beta\ell i} \to \sigma_{\ell} = 5\ \mu in$		4	4	2	7
$\sigma_{\varepsilon Xi} \to \sigma_{\ell} = 4\ \mu in$		3	3	2	7
$\sigma_{\varepsilon Yi} \to \sigma_{\ell} = 4\ \mu in$		3	3	2	7
Voltage supply errors:					
σ_{ℓ_1}	18 μin	0	6	0	6
σ_{ℓ_2}	21 μin	11	17	7	4
σ_{ℓ_3}	16 μin	8	3	5	3
Root mean square values:					
		182	189	123	75

Table 7.12 Continued

Perturbation Error	Value (in)	Induced $\sigma_{\ell_{0,0}}$ (μin)	Induced $\sigma_{\ell_{-1,1.5}}$ (μin)	Induced σ_α (μrad)	Induced σ_β (μrad)
Random errors:					
σ_{ℓ_1}	7 μin	0	3	0	3
σ_{ℓ_2}	21 μin	11	17	7	4
σ_{ℓ_3}	25 μin	13	4	8	4
Root mean square values:					
		17	18	11	6

respectively. The latter is due to "fixed errors" in the physical parameters of the system, as well as error in determining the zeroes voltage drift of the probes. Due to the nature of the error calculations (Equation 5.2) these latter types of errors will increase from zero to the maximum value as the measured degree-of-freedom increases.

The root mean square of the errors indicates that the impedance probe system will have angular errors of σ_α = 132 μradians and σ_β = 111 μradians. The errors in calculated distance between the plates at the origin and at a lateral effect diode are $\sigma_{\ell_{0,0}}$ = 196 μin (5μm) and $\sigma_{\ell_{-1,1.5}}$ = 205 μin (5 μm) respectively. These values of course are subject to the stability of the electronics and the probes. The meaning of these values with respect to the final system tests will be discussed in Chapter 8.

References

[7.1] Hewlett Packard Corp. 5528A Laser Measurement System User's Guide, 1982, pp 19-1 - 19-57

[7.2] Hewlett Packard Corp. 3421A Data Aquisition/Control Unit, Operating, Programming, and Configuration Manual p109

(this page left blank)

Chapter 8

Experiments to Evaluate Measuring Beam Performance

8.1 Introduction

This chapter will discuss tests used to evaluate the performance of the measuring beam system that has been the subject of this thesis. Two questions are to be addressed here: 1) how well can the error analysis of Chapter 5 combined with the calibration test results of Chapter 7 predict system behavior? and 2) how well the concept of the POSOR works (can it measure six degrees of freedom simultaneously)? To help answer these questions, tests based on single degree-of-freedom and multi-degree-of-freedom motions are performed.

In the sections that follow, the test setup is described, followed by a discussion of the individual tests and algorithms used to process the data from the POSOR. Detailed test results are presented and errors are compared to the values predicted by the analysis methods of Chapter 5 and the calibration results of Chapter 7. A summary of the results is presented to correlate the results from the various tests. Recommendations and conclusions are then presented.

8.2 Test Setup for Evaluating Measuring Beam System Performance

The test system consists of the measuring beam support structure (shown schematically in Figure 6.1) and the POSOR device which was calibrated as described in Chapter 7. A photograph of the test setup for evaluating the performance of the measuring beam system is shown in Figure 8.1. The major components are: measuring beam components, two axis stage, twist stage, dial indicators, and a CNC vertical machining center. The degrees of freedom that were imposed on the measuring beam were ΔX, ΔY, ΔZ, $\Delta\alpha$, $\Delta\beta$, and $\Delta\Theta$ as shown in Figures 8.1 and 8.3.

The mechanics and function of the measuring beam components were discussed in detail in Chapters 3 and 6. As shown in Figure 8.1, the measuring beam system is set up on the bed of a three axis CNC vertical machining center which will be used as a coordinate measuring machine. The POSOR is at the far right of the figure, and it is shown in greater detail in Figure 8.2. The light source plate (target plate) is used as the stationary reference axes for the POSOR. The stand which holds the target plate is bolted and epoxied to the bed of the machine. The measuring beam is supported at each end by the two and four degree-of-freedom gimbals respectively. The two degree-of-freedom gimbal (angular degrees of freedom about the Y and Z axes shown in Figure 8.1) is located near the POSOR and is mounted on a twist stage. The four degree-of-freedom gimbal (angular degrees of freedom about the X, Y, and Z axes and linear degree-of-freedom along the X axis as shown in Figure 8.1) is attached to a two axis stage. As shown in Figure 8.3, the far end of

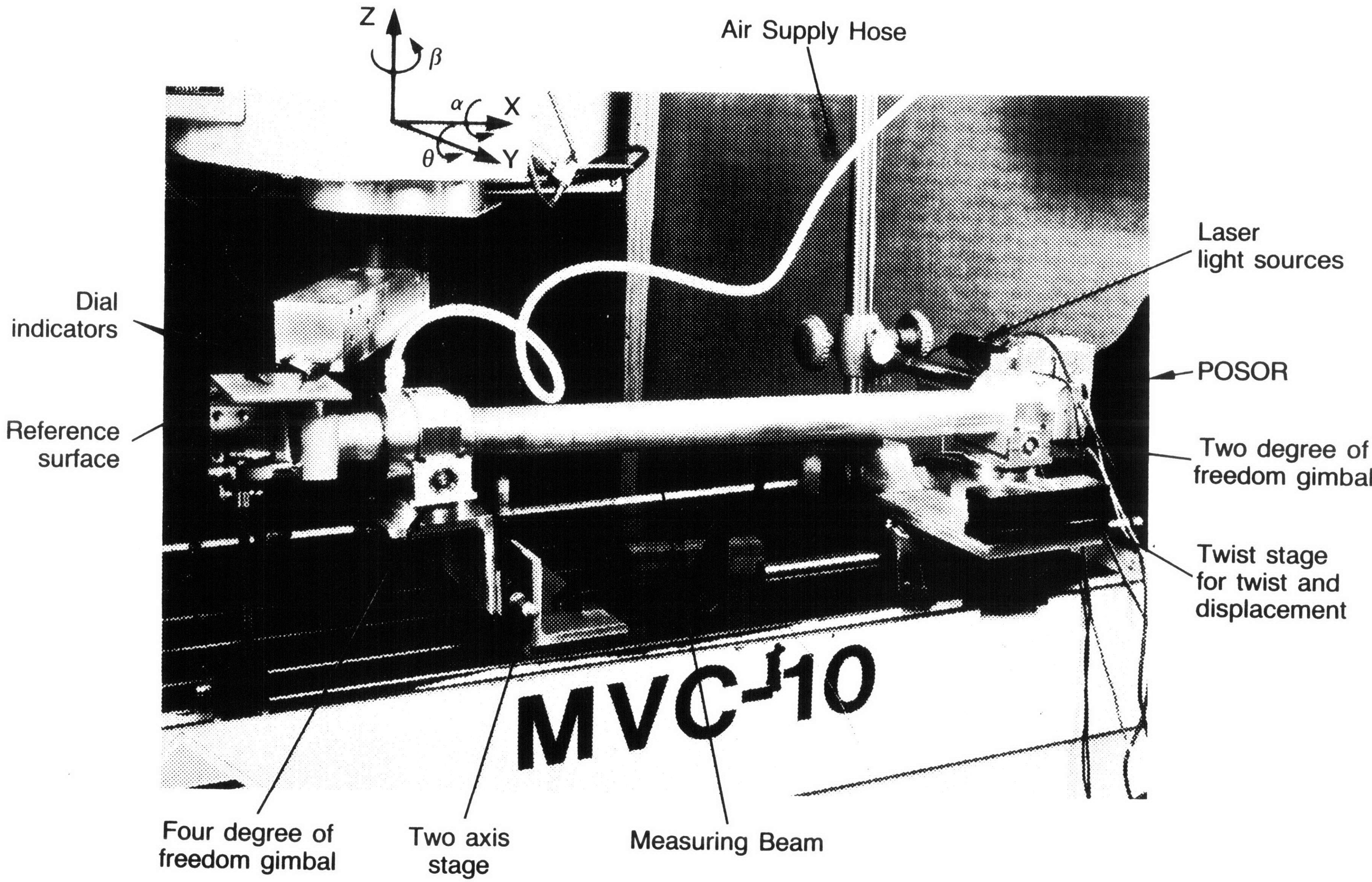

Figure 8.1 Test setup for evaluating measuring beam system performance

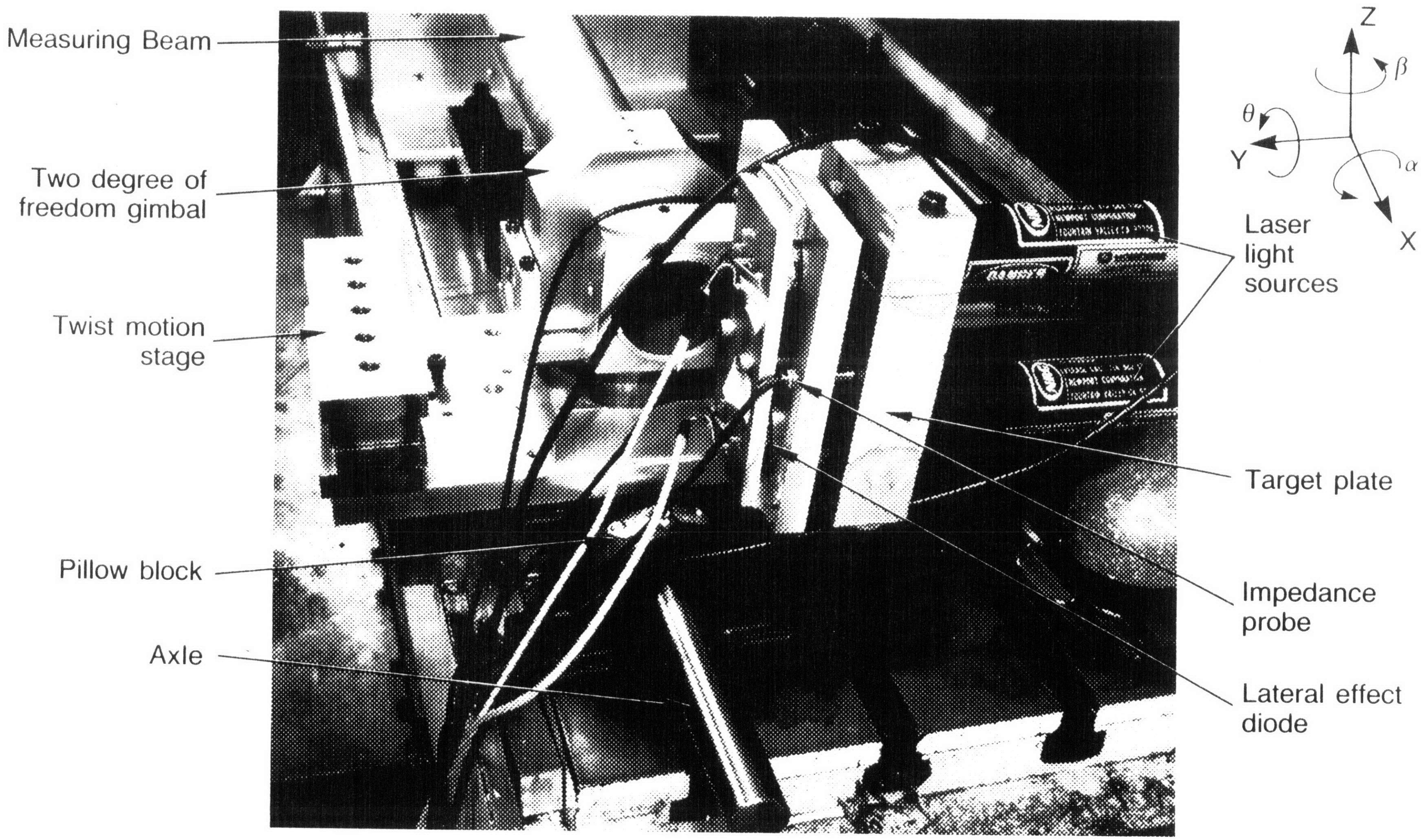

Figure 8.2 Measuring beam system's POSOR

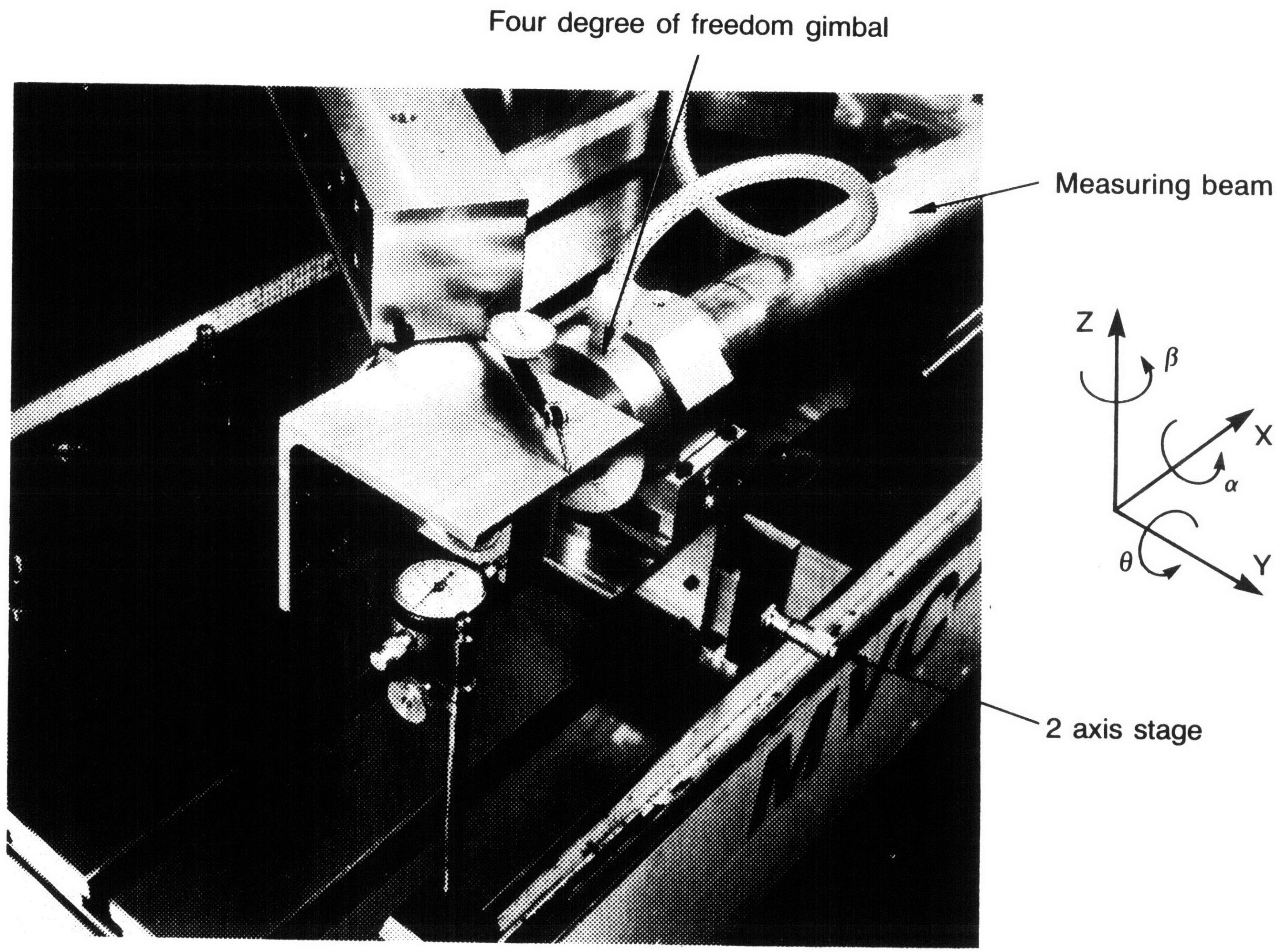

Figure 8.3 Dial indicators on machine tool spindle mount used to measure coordinates of measuring beam

the measuring beam has an angle plate attached to it which acts as a reference surface.

The target plate is supported by a stand that was epoxied and bolted to the machine tool bed. All the motions measured by the POSOR are with respect to the target plane. Any error in orientation of the target plate with respect to the vertical machining center XZ axes would be amplified by the length of the measuring beam for translation motions. In securing the support stand for the target plate, the target plate could not be made "exactly" parallel to the vertical machining center XZ axes; thus in order to determine the orientation of the target plane with respect to the vertical machining center, an initial calibration test was made using the POSOR. This test is discussed in the following section.

The measuring beam's support gimbals were held by stages which were used to synthesize structural beam deflections and one large degree-of-freedom (in the Z direction). The twist stage was located beneath the two degree-of-freedom gimbal near the POSOR. It consisted of the bearing/axle assembly that was used in the test to determine the distance between the impedance probes (see Figures 7.30, and 7.31). This stage was moved by a jack screw and its motion simulated the twist of a structural beam and bearing runout (motion α, ΔY, and ΔZ shown in Figure 8.1). The four degree-of-freedom gimbal was supported by a two axis stage which moved in the Y and Z directions shown in Figure 8.1. These motions simulated out-of-plane bending of a structural beam and the large degree-of-freedom motion about a joint. Thus with these two stages, the equivalent of six degree-of-freedom motions could be imposed on the system.

In order to measure the motions of the endpoint of the measuring beam, an angle plate was attached to one end of the measuring beam to serve as a reference surface. Dial indicators, held by a beam attached to the machine spindle, used this angle plate as a reference surface to position the spindle. This allowed the vertical machining center to be used as a coordinate measuring machine.

A line was scribed on the angle plate which was 31.500" (.800 m) from the centroid of the two degree-of-freedom gimbal. Thus when the twist stage was anchored in place, motions of the endpoint of the measuring beam would trace out a section of a sphere. Hence the angles β and Θ would be directly related to the displacements in the Y and Z directions respectively. Since the total incremental translations were on the order of .3", the cosine error resulting from an error in the length (31.5") of .010" (.254 mm) would be .0001" (.0025 mm).

The accuracy of the digital readout of the vertical machining center along any axis was 0.0002" (measured with a laser interferometer during calibration tests). The accuracy to which the angle α could be determined was based on two Z axis measurements taken 3.5" apart on the angle plate and was 81 μrad; however, when the twist stage was not moved, α should not have changed by more than the runout in the two degree-of-freedom bearings divided by their spacing. Hence α should have been stable to $50\times10^{-6}/3 = 17$ μrad. Because of this, for the translation tests, α measurements were not made. The angles β and Θ were accurate to 6 μradians each (based on the assumption that the twist stage held still while a measurement accurate to .0002" was made at the angle plate).

8.3 General Description of Tests Used to Evaluate Performance of the Measuring Beam System.

This section will present the tests designed to evaluate the performance of the measuring beam system. First the initial setup (initialization) is described. Methods of compensating for zero drift in the probes is then discussed. The method of performing the motion tests is discussed followed by a description of each test.

8.3.1 Test Setup Calibration and Determination of Associated Errors

An initial calibration of the system was done to determine the orientation of the target plane with respect to the machining center axes. Without compensation for these angles, pure Θ rotation of the POSOR plates with respect to each other would seem to cause Y and α motions at the end of the measuring beam. To determine these angles, the tip of the measuring beam was moved in the Z direction and the degrees of freedom α, β, and Θ were measured by the machining center and the POSOR. To negate the effect of probe zero-drift, only a Z motion was imposed on the measuring beam; thus the change in gap between the POSORs was small (on the order of .0020" (.0508 mm)) and the differential error due to zero-drift on the probe linearization curves (see

Equation 5.2 and Figure 7.28 and the following paragraph) was on the order of 10 μin (.26 μm). For the small angles imposed, the error between the readings from the machining center and the POSOR increased linearly with the imposed motion. The target plane orientation angles are those which bring the error to zero along the entire range of motion. These angles were determined iteratively, using a digital computer.

The orientation angles α_X and β_Z about the X and Z axes were found to be 2.55° and 3.18° respectively. This orientation resembles a cosine error to the angle Θ. To the probes, these angles seemed like an error in flatness of the target plate with respect to the vertical machining center YZ axes. This error in flatness was a function of the probe position over the target plate, which was dependent primarily on the sine of the angle θ. Hence, the target plane orientation angles were determined to a degree of accuracy that only induced errors in α and β on the order of the POSOR errors. Greater accuracy could have been achieved by performing numerous runs and averaging values, but time constraints prevented doing this.

For all the remaining tests, the calibration orientation angles were incorporated into the analysis programs. With regard to other system errors, the machining center could only measure the angle α with an accuracy of 81 μrad (distance between touch off points was 3.5" and the accuracy of the readings was only 0.0002"). However, when the twist stage was not moved, α ought not to have changed by more than the runout in the two degree-of-freedom bearings divided by their spacing. Hence α

will be stable to $50\times10^{-6}/3 = 17\ \mu$rad. The other error in the determination of the angles α and β was the zero-drift of the probes (see section 7.5.3). As shown in Figures 7.32, 7.33, and 7.34, the probes were subject to pure drift. Analysis of the electronic circuit showed that standard accuracy components were used in its design, so presumably this problem could be remedied by using hybrid circuits. Methods for compensating for the zero-drift in this experiment are discussed below.

Physically, the zero drift of the probes could only be determined by "zeroing" the probes using gauge blocks, which was accurate to .02 volts. The zero-drifts were found by using gauge blocks to position the POSOR plates the same distance apart as when the probes were calibrated. The probe outputs were read and compared to the voltages at calibration. This measurement is only as accurate as the probes could be zeroed: .001"/.05"/volt = .02 volts (Figure 7.28 shows the gain of the probes to be about .05"/volt). Probe 1 did not drift, while probes 2 and 3 zero points were found to have drifted by .20 and .30 volts respectively.

To determine the effect of this drift in detecting incremental motion, representative values of the probe output voltages along with zero-drifts were substituted into the probe linearization equations (coefficients given in Table 7.10). The error created by the zero-drift problem was then evaluated using Equation 5.2. Representative voltages (with the tolerances associated with finding the new zero points) of .1, .12, .8, and .82 were substituted into the three probe linearization polynomials. For this .7 volt range, which corresponds to .035" motion (.889 mm) the error in incremental motion for probes 1, 2, and 3 was

351, 264, and 175 μin (8.8, 6.6, and 4.4 μm) respectively. This error is unacceptable, and the reliability of the method is also doubtful (can one really bring the probes that close to the initial calibration point?).

Since the dominant error component in the α and β POSOR measurements should be random (see Table 7.12), the errors due to zero-drift would mask the ability of the tests to determine how well the POSOR could work. Since the zero-drift merely represents a shift on the linearization curve (an origin shift), and the shift could not be detected with great enough accuracy by direct measurement, the zero-drifts for the probes were found (digitally) by minimizing the mean square error. This will only remove the increasing error component (discussed in 7.5.4), the random component and any cross coupling terms between the α and β angles will be unaffected. Appendix 8A lists the programs (they use the equations developed in Chapter 5) used to determine the degrees of freedom measured by the POSOR. These programs were modified with the addition of DO LOOPS to allow combinations of the three zero-drifts to be tried until the least squares error in the calculated α and β were found. The accuracy of the computations was .001 volts, which leads to errors of 18, 21, and 16 μin for probes 1, 2, and 3 respectively. These errors correspond to about 5 μrad error in angles α and β measured by the POSOR which is less than the accuracy of the angles measured by the machining center.

Since the POSOR tests were run over a period of three days, the zero-drifts were expected to change and thus had to be found for each test. Changes during the test could not be determined, but are expected to be small (test is one hour verses 24 hour waits). The values of the zero shifts found for the different tests are given in Table 8.1. The zero-drifts are subtle, but the linearization equations are very sensitive.

8.3.2 Description of the Tests Performed to Evaluate POSOR Performance

The goal of the POSOR is to be able to measure six degrees of freedom simultaneously using only displacement measuring sensors that look at the relative motion between two plates. In order to evaluate this concept, the ability of the system to detect single degree-of-freedom motions was first considered. Then multi-degree-of-freedom tests were studied. The tests performed were named according to the axes along (or about) which the end of the measuring beam was moved. The names of the tests also coincided with the names of the FORTRAN programs used to analyze the data (these programs are listed in Appendix 8A).

The tests were performed in the following manner. Initial readings were taken from the vertical machining center and the POSOR. The incremental step(s) were made, and the measuring process was repeated. The measuring process with the vertical machining center used dial indicators to tell when the surface of the angle plate was touched by the vertical machining center coordinate system. Readings were taken on the angle plate at three points whose positions with respect to the longitudinal axis (parallel to the machining center's X axis) of the

Table 8.1 Summary of Ranges of Sensor Motions

	Test				
	ZMO	YMO	YZMO	TWIS	GEN
Lateral effect diode measurements: (in)					
X_{d1s}	.4499	.4556	.4547	.4539	.4557
X_{d1f}	.4474	.4484	.4471	.4523	.4502
Y_{d1s}	.2237	.2219	.2222	.2176	.2468
Y_{d1f}	.2481	.2235	.2402	.2248	.2867
X_{d2s}	.3869	.3917	.3910	.3901	.4092
X_{d2f}	.4017	.3852	.3956	.3891	.4322
Y_{d2s}	.2290	.2292	.2292	.2251	.2335
Y_{d2f}	.2527	.2285	.2448	.2293	.2929
Impedance probe measurements: (in)					
Probe 1	.0021	.0208	.0198	.0394	.0126
Probe 2	.0014	.0092	.0091	.0452	.0128
Probe 3	.0019	.0093	.0091	.0284	.0102
Impedance probe voltage shifts:					
Probe 1	0.00	0.000	-.060	-.185	-.148
Probe 2	0.20	0.100	0.180	0.118	0.245
Probe 3	0.30	0.240	0.140	0.071	0.403

measuring beam were known to within .001" (.025 mm). From these readings, the α, Y, and Z motions were found. In addition, when the twist stage was stationary, the angles β and Θ were determined. The maximum value of the X reading was about .001" (.025 mm), and since there was no error amplification associated with determining it, this trivial motion was not recorded. The tests are discussed below.

Test ZMO was performed in order to determine how well the POSOR could measure the angle Θ which was induced by introducing a motion along the Z axis using the two axis stage. The range of motion was .3" (7.6 mm). For this test, the twist stage was intentionally not moved. As the two axis stage was moved in the Z direction, it caused slight motion in the Y direction, but no rotation α was induced because the aerostatic bearing in the four degree-of-freedom gimbal isolated the measuring beam from all but Y and Z motions of stage. Any rotation α detected by the POSOR would be due to wobble in the twist stage (which was shown above to be on the order of 17 μrad). Thus the measuring beam pivoted about the two degree-of-freedom gimbal axes and measured motions (along the Y and Z axes) of the end of the measuring beam corresponded directly to the angles β and Θ. As discussed above, the α and β results from this experiment were used to determine the orientation angles of the target plate.

Test YMO was performed in order to determine how well the POSOR could measure the angle β which was induced by introducing a motion along the Y axis using the two axis stage. The range of motion was .3" (7.6 mm). Again, the twist stage was held stationary so any rotation α

detected by the POSOR would be due to wobble in the twist stage. Once again, the measuring beam pivoted about the two degree-of-freedom gimbal axes, and measured motions (along the Y and Z axes) of the end of the measuring beam corresponded directly to the angles β and Θ.

Test YZMO was the first look at how the POSOR performed when more than one degree-of-freedom was moved. The range of motion was .3"×.3" (7.6×7.6 mm) along the Y and Z axes of the machining center. The YZ motion caused the angles Θ and β to be simultaneously introduced. The twist stage was not moved during this test.

Test TWIS was performed in order to determine how well the POSOR could measure the angle α and "bearing runout". The range of motion was α = .3° and runout = .005" (.13 mm). These motions were induced by tilting the twist stage while keeping the two axis stage fixed. The motion of the twist stage was rotational (about the X axis), and translational (along the Y and Z axes). POSOR performance was evaluated by measuring the angle α and the Y and Z motions at the end of the measuring beam and comparing it to that predicted by the algorithm discussed below.

Test GEN was performed to evaluate POSOR performance when all axes were moved simultaneously. The range of motion was α = .3°, Z = .3" (7.6 mm), and Y = .01" (.25 mm). The Y motion at the end of the measuring beam was small because the twist motion had also moved the probes close to the target plane. POSOR performance was evaluated by measuring the angle α and the Y and Z motions at the end of the measuring beam and comparing the values to those predicted by the data processing algorithm.

8.3.3 Algorithm to Process Sensor Output

This section will describe the programs written to analyze the output from the sensors of the POSOR and the vertical machining center. Programs used to control the Klinger stage and the data acquisition unit are particular to the data acquisition system used and will not be presented. Data was first gathered on the Hewlett Packard system and then transferred to a VAX 11/780 computer. All final analysis was done using FORTRAN programs which are given in Appendix 8A.

The analysis of the tests is based on detecting incremental motions between the start and the end of the test. To start the test, all initial readings were made, and the initial values were calculated. At each step, the readings were made, the values calculated, and the initial values were subtracted from the calculated values. In the operation of a "real" robot, the robot motions would also be defined with respect to an initial home point.

GEN.FOR is typical of the data analysis programs. It is listed in Appendix 8A and will be outlined here. The program first reads the data and then opens files for tables and plots. The initial conditions are calculated using Equations 5.3 - 5.5 and 5.28 - 5.32. The first step is to add the probe offset voltages and then linearize the probe readings. The angles α and β are then found. A linear interpolation routine

(DLINE) is used to evaluate the light spot position on the diodes. Once the XY coordinates of the light spot are known, the distance between the plates at that point is calculated so that, with the next motion, the change in distance can be used to determine the shift of the light spot due to light source orientation errors. The angle Θ is then found and the X, Y, and Z position of the target plane's origin with respect to the coordinate system of the impedance probes (see for example Figure 5.2). The next set of data points are then processed similarly, except the initial conditions are subtracted.

The following subroutines are included in GEN.FOR, all are well annotated and are listed in Appendix 8A:

1) Subroutine CONSTANT.FOR contains all the linearization constants for the lateral effect diodes. These constants are used by the interpolation subroutine DLINE.FOR.

2) Subroutine DIMEN.FOR contains the physical constants of the POSOR system such as diode axes offsets, orientation angles, etc.

3) Subroutine PROBLIN.FOR accepts the three probe voltages and returns the linearized distance values.

4) Subroutine ALBET accepts the linearized probe distance values and using data on probe spacing from DIMEN, it calculates and returns the angles α and β.

5) Subroutine DIST.FOR accepts the probe readings, angles α and β, system geometric constants and an X,Y position. It then calculates and returns the distance between the plates at the given X, Y coordinates.

6) Subroutine DLINE.FOR is an interpolation routine used to determine the linearized position of a light spot on a photodiode. As

discussed in Chapter 7, the diode linearization curves vary across the diodes. When the light spot falls between curves an interpolation of the curve values is necessary. DLINE.FOR determines which curves bound the light spot and calculates the linearized values for the light spot using each of the bounding curves. These values are then linearly weighted according to how close the light spot lies to the curve. A few iterations are required to determine the linear weighting factor.

The accuracy of the interpolation routine was determined by assuming a linearization curve grid spacing twice that of the actual spacing and then comparing the interpolated values at the center of each enlarged grid section to the "actual" values (found by substituting the same point into the linearization curve that actually passed through that point). Since the grid area was four times as large as the grid on the diode, the error associated with the actual grid would be on the order of one-fourth that found by the above method. Figures 8.4 - 8.7 show how the error varies with position on the diode. As expected, the linear weighting of the values produces the least error near the center of the diode (where the diode itself is most linear). Note that these errors were incorporated into the total light source-lateral effect diode system error budget given in Chapter 7.

The amount of time to process the data could not be judged on the VAX; however, an estimate will be made based on an Intel 86/30 board. If a math processor is used, floating point can be as fast as integer arithmetic in the chip. One 16 bit addition takes about 4 μs, and one 16 bit integer multiply or divide takes about 30 μs. Eight ninth-order

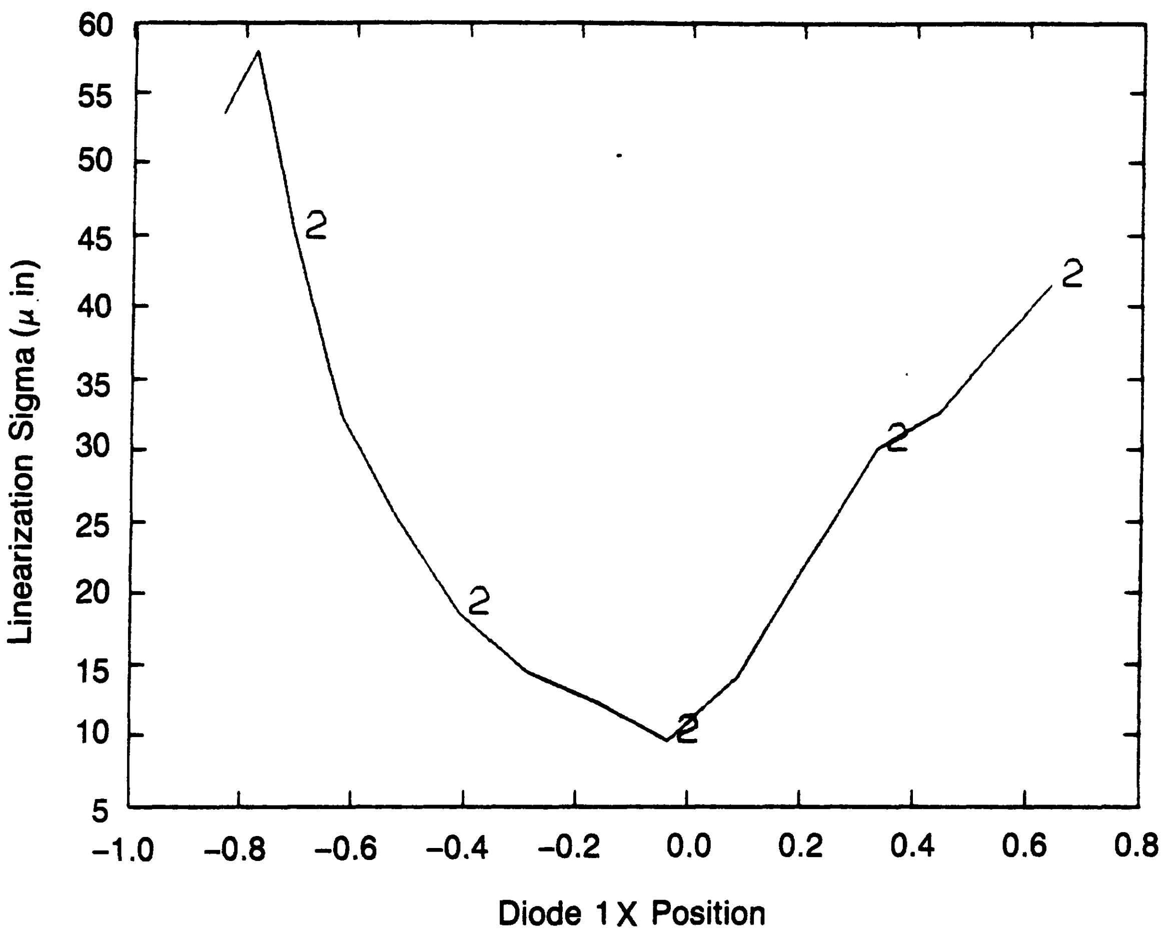

Figure 8.4 Interpolation error associated with analysis routine DLINE. FOR.

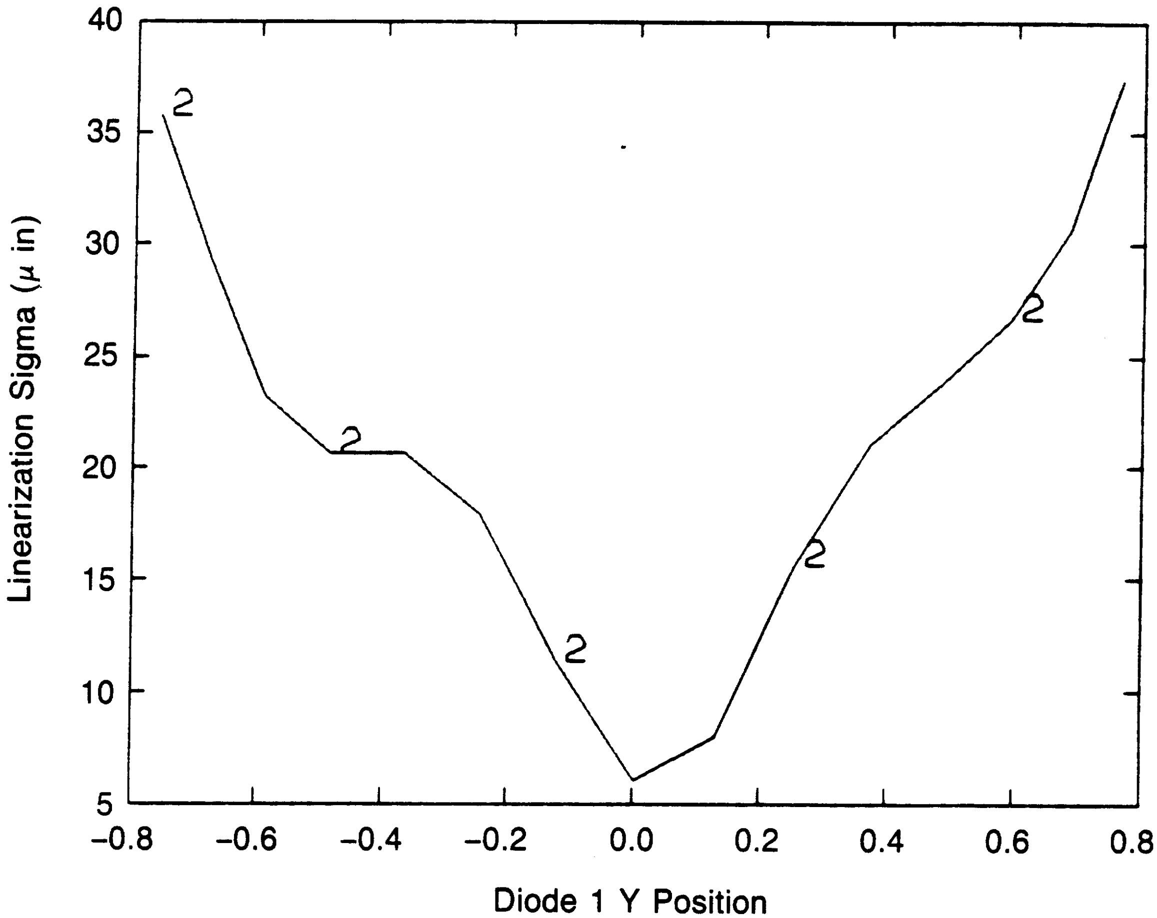

Figure 8.5 Interpolation error associated with analysis routine DLINE. FOR.

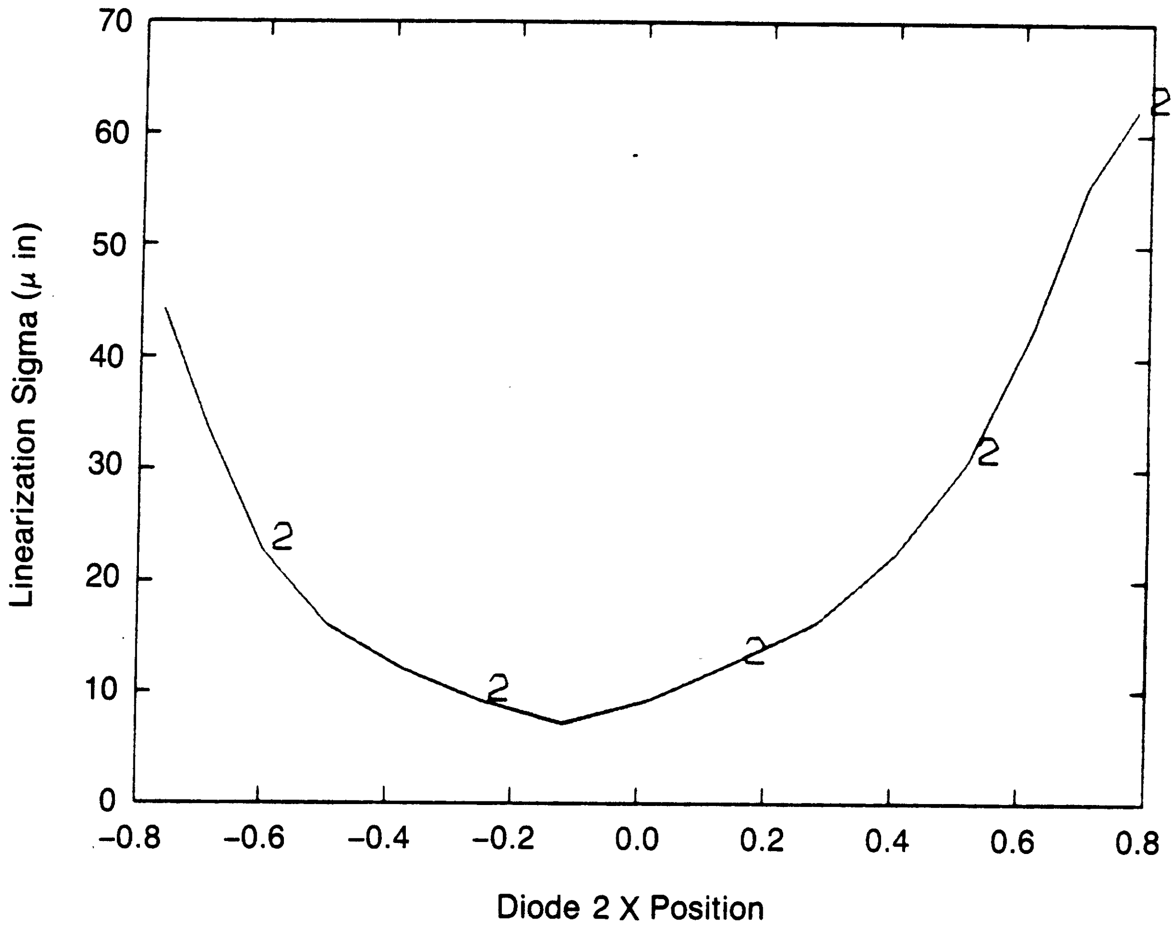

Figure 8.6 **Interpolation error associated with analysis routine DLINE. FOR.**

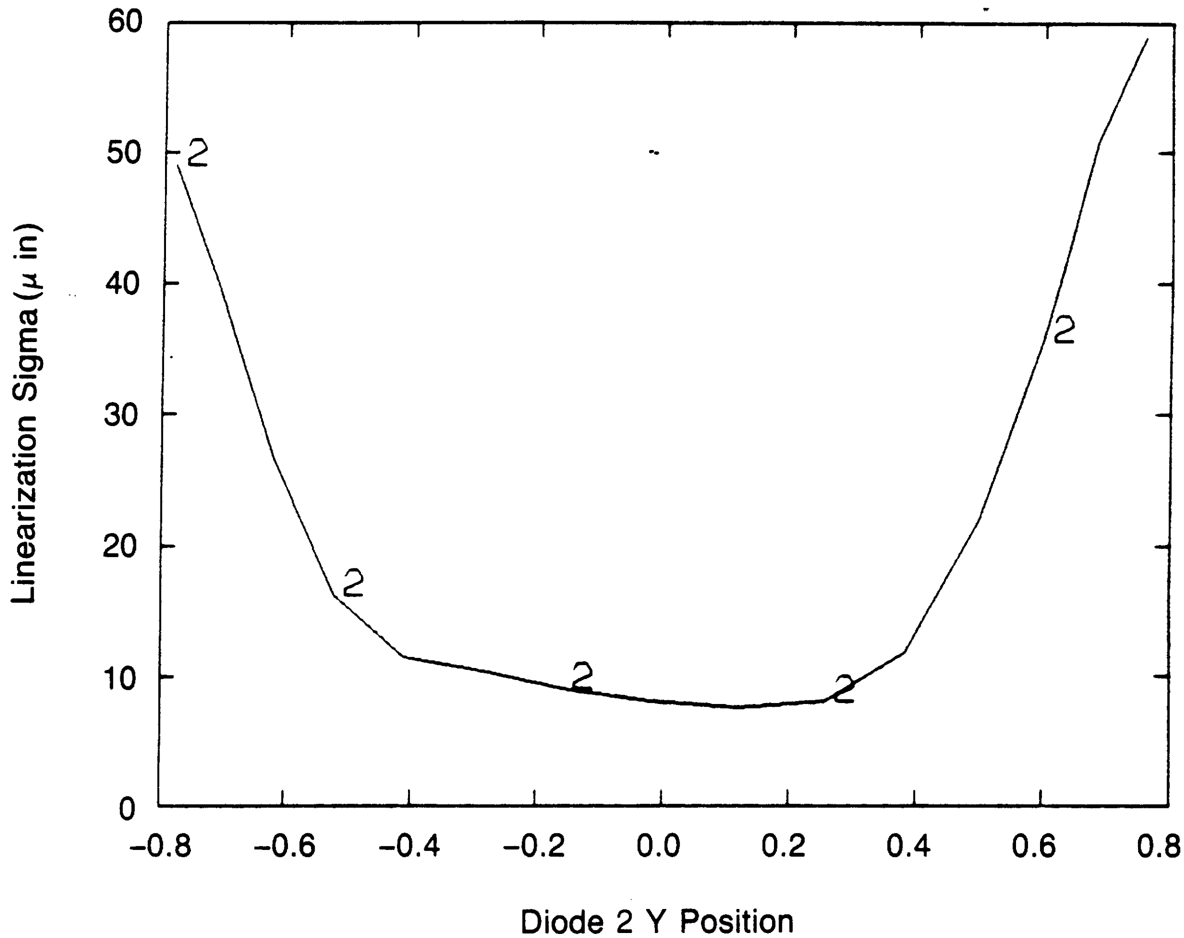

Figure 8.7 Interpolation error associated with analysis routine DLINE. FOR

and three fourth-order polynomials need to be evaluated. Assuming that the support calculations equal 10% of the number of major calculations, 430 multiplications and divisions need to be made. This will take on the order of .013 seconds. The analog to digital converters (11 at 100 μs including filtering) will add another .002 seconds. Thus at least one dedicated micro-processor would be required for each joint in order to analyze all the data.

8.4 Results of Measuring Beam System Tests

This section will present results for each of the tests described above along with an analysis of the errors. The errors will be analyzed using the equations formulated in Chapter 5 and the ranges of motion of the sensors during the tests (see Table 8.1). With regard to the motions made, The X axis lies along the length of the measuring beam and the twist about its length is α. The vertical motion of the measuring beam is along the Z axis, and the angle Θ about the Y axis causes Z axis motion at the tip of the measuring beam. Side to side motion of the measuring beam is along the Y axis, and the angle β causes Y axis motion at the tip of the measuring beam.

As noted earlier, all tests are based on incremental motion; detailed values for system variables (from the analysis programs) are presented in Appendix 8B. The "in the neighborhood of" errors based on the system error budget values obtained in Chapter 7 are given below.

For the light source-lateral effect diode system, Table 7.9 lists the following expected root mean square values for errors in measuring the X (corresponds to X_d), Z (corresponds to Y_d) and Θ motions between the POSOR plates: σ_X = 1572 μin (39.3 μm), σ_Z = 207 μin (5.2 μm), and σ_Θ = 111 μradians. The error in the angle θ will be amplified by the distance from the POSOR coordinate system origin to the end of the measuring beam (33.4" or .85 m) when predicting Z motions. Thus the total expected Z error for the POSOR is σ_Z = 3914 μin (98 μm).

Note that the ninth order curve fit (see section 7.4.2) used to linearize the diodes will have eight peaks and valleys with a distance between a peak and a valley of about .025" (.635 mm). The standard deviation of the error in straightness for the stage was found to be .0004" (10 μm). The period of this error is on the order of .01" (.254 mm) (see Figure 7.3) which can result in a peak to valley error of .0004" (10 μm) in the linearization curve, because the ninth-order curve will map the stage error as well as the diode response. Thus in addition to the errors accounted for in Table 7.9, a 189 μrad error over .025" (.635 mm) motion across the diode could occur. For purposes of estimating this error, Table 8.1 lists the linearized diode positions of the light spots on the diodes at the start and the end of each test. For analyzing the test results, the errors given in Table 7.9 and by the calibration stage straightness effects will be scaled by the distance the light spots traveled across the diodes.

For the impedance probe system, Table 7.12 lists the expected increasing and random error components for the distance between coordinate systems and the angles α and β. For error that increases with the degree-of-freedom being measured (see Equation 5.2, and Section 5.5), the errors are: $\sigma_{\ell 0,0}$ = 182 μin (4.6 μm), σ_{α} = 123 μrad, and σ_{β} = 75 μrad. The random error components are: $\sigma_{\ell 0,0}$ = 17 μin (.4 μm), σ_{α} = 11 μrad, and σ_{β} = 6 μrad. The error in the angle β will be amplified by the distance from the POSOR coordinate system origin to the end of the measuring beam (33.4" or .85 m) when predicting Y motions. Thus the total expected increasing and random Y errors for the POSOR are σ_Y = 2505 μin (63 μm), and σ_Y = 200 μin (98 μm) respectively. Table 8.1 lists the range of motion of the probes for use in evaluating the increasing error component.

As an aid to help in visualizing the motions being measured, keep Figure 8.1 ready for quick reference.

8.4.1 Results of the Vertical Motion (Z) Motion Test

The Z motion test (vertical motion which corresponds to deflections of a beam and large angular motions) served two purposes: 1) evaluation of the POSOR when subjected only to the degree-of-freedom Θ, and 2) determination of the orientation of the target plane with respect to the vertical machining center coordinate system. The range of Z motion, .3" (7.6 mm), was induced in 20 steps using the two axis stage. The orientation angle determination results were discussed earlier. The Θ angle results are shown in Figure 8.8.

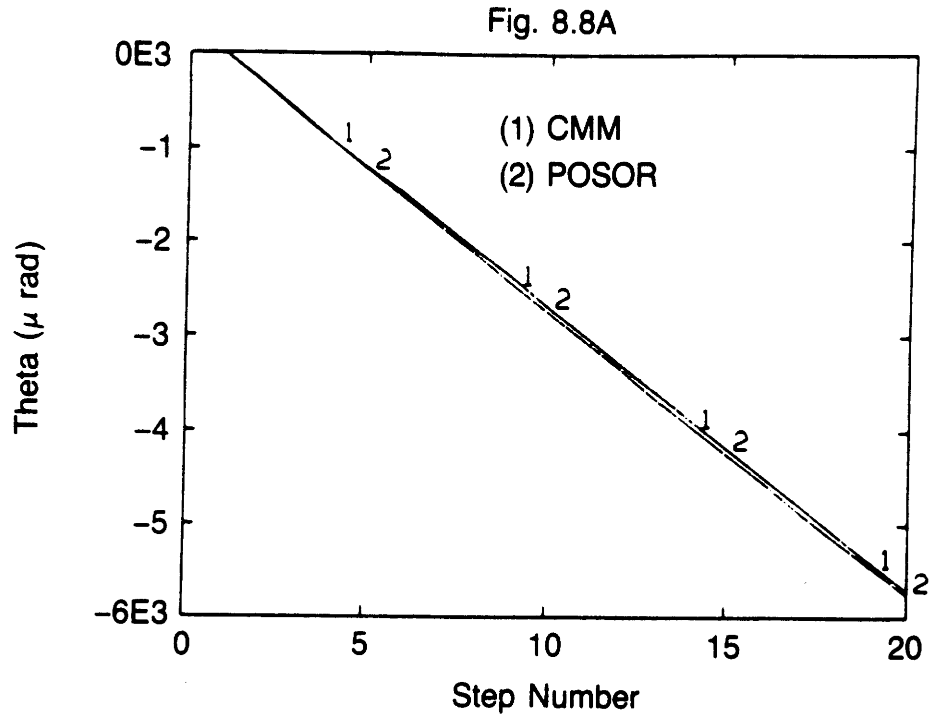

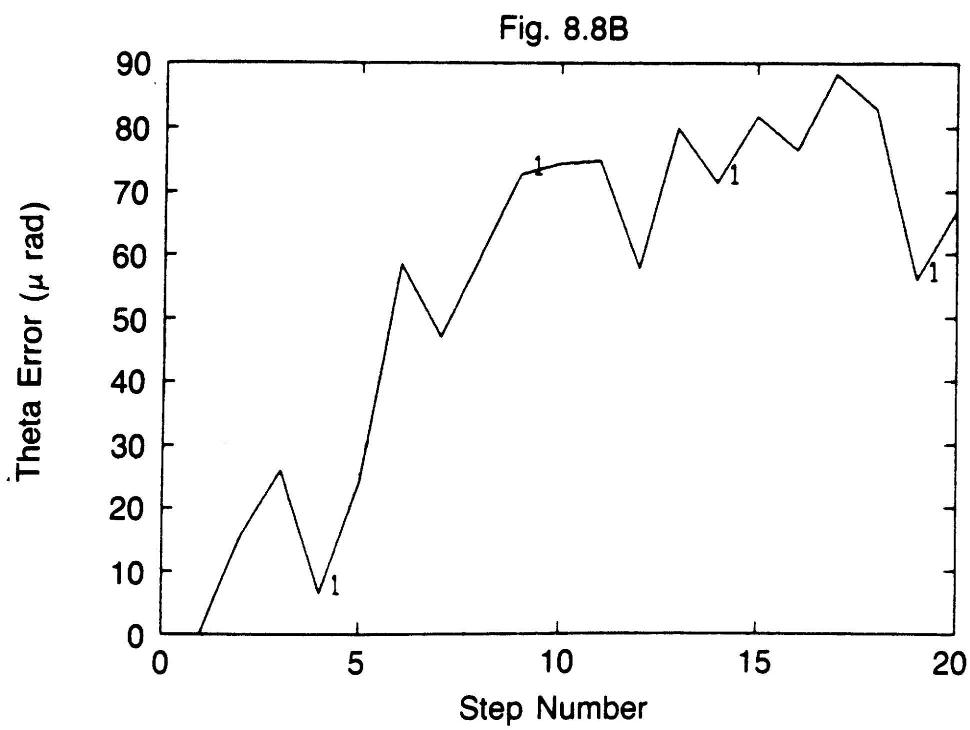

Figure 8.8 Motion θ of measuring beam during test ZMO

Figure 8.8 shows the angle Θ as measured by the machining center and the POSOR. The error starts at zero and increased to 68 μrad over a range of 5756 μrad. The standard deviation of the error was 66 μrad. From Table 8.1, the average X_d motion was .009" (.229) mm. Thus the error induced by the straightness of the calibration stage was a maximum of 68 μrad. The predicted error due to the factors listed in Table 7.9 (such as distance between the diodes, etc.) was 111 μrad over .5" (12.7 mm) of travel across the diodes. For this test, .020" (.51 mm) was traversed which lead to an error of 4 μrad. Note that the error was not steadily increasing, but jumped to a constant offset at about the fifth step. This may have been due to a foreign object (gunk) changing the location of the center of intensity of the light source.

8.4.2 Results of the Side to Side (Y) Motion Test

The Y motion test was used to evaluate the POSOR's performance with respect to β motions only (motions of the tip of the measuring beam in the Y direction which corresponds to sideways motion of a beam). The .3" (7.6 mm) range of Y motion was induced in 15 steps using the two axis stage. The probe zero-drift voltages were found (digitally as described above) to be 0.000, 0.100, and 0.240 volts for probes 1, 2, and 3 respectively. The results of this test are shown in Figures 8.9 - 8.11.

Figure 8.9 shows the angle α measured by the POSOR without and with the probe zero-drift voltages. From Equations 5.21 and 5.22, and Table 8.1, the increasing error component should be 0 μrad. The accuracy of

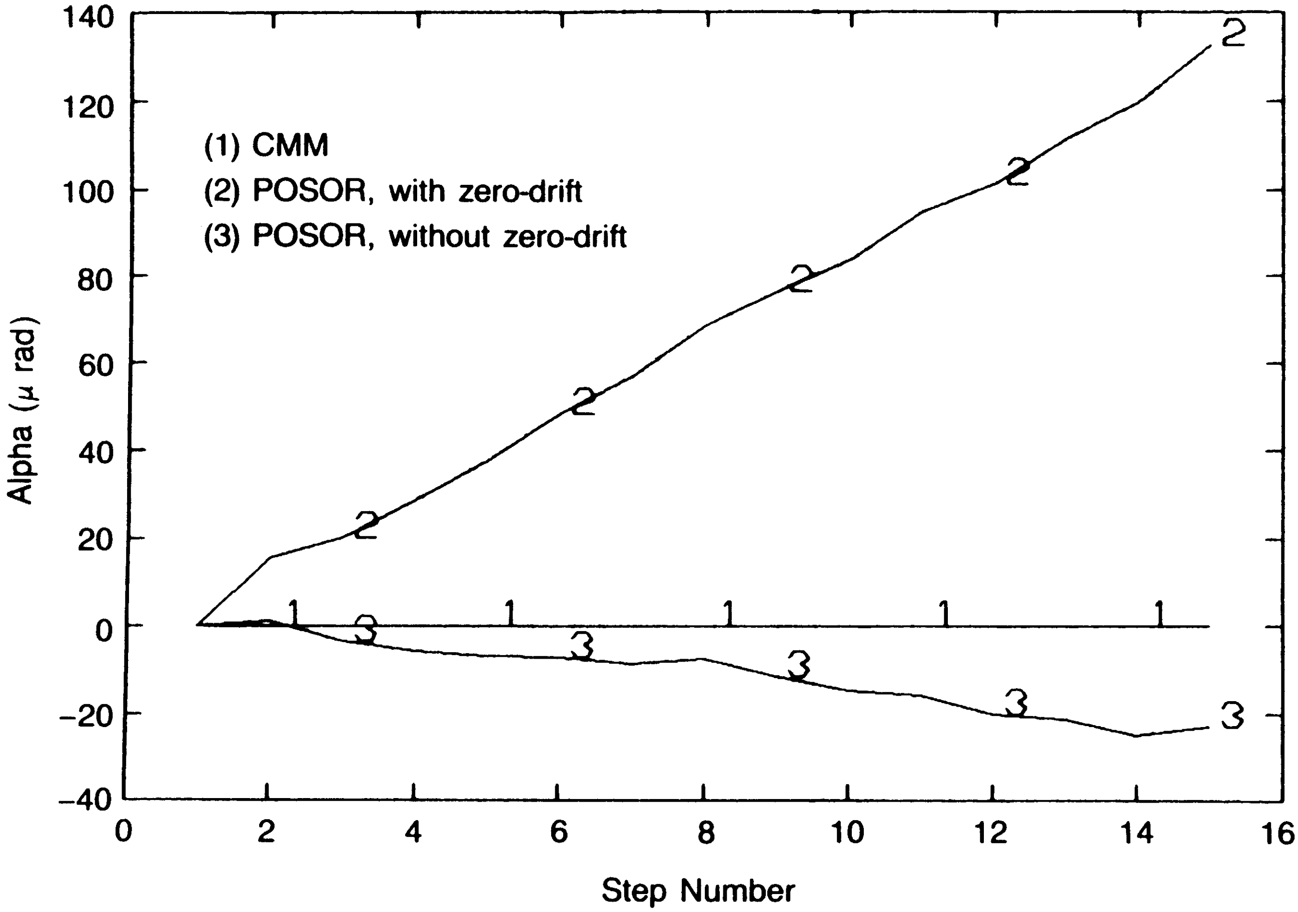

Figure 8.9 **Motion α of measuring beam during test YMO. Voltage drifts are $V_1 = 0.000$, $V_2 = 0.100$, and $V_3 = 0.240$ volts**

the twist stage is 17 μrad. Figure 8.10 shows the value of α measured by the POSOR increasing to about 25 μrad. The expected random error is 11 μrad, so α is within the predicted bounds.

Figure 8.10A shows the angle β as measured by the machining center and by the POSOR without and with the probe zero-drift voltages respectively. Figure 8.10B shows the error found by subtracting curve 1 in Fig. 8.10A from curves 2 and 3. For the zero-drift compensated measurement, the error appears to be random with a standard deviation of 4 μrad over a range of 4318 μrad. The expected random error component is 6 μ rad. From Equations 5.21 and 5.22 and Table 8.1, the increasing error component is found to be 13 μrad.

Both the α and the β curves show the large effect that small shifts in the zero voltage have on POSOR performance. Thus it becomes graphically apparent that stable electronics must be obtained before a high accuracy POSOR can be built.

Figure 8.11 shows the angle Θ as measured by the machining center and the POSOR. The error starts at zero and increases to 230 μrad over a range of 13 μrad. The standard deviation of the error is 179 μrad. From Table 8.1, the X_d motion is on the order of .007" (.178 mm) which indicates an error induced by the straightness of the calibration stage could be a maximum of 53 μrad. The predicted error due to the factors listed in Table 7.9 (such as distance between the diodes, etc.) is 111 μrad over .5" (12.7 mm) of travel across the diodes. For this test, only .007" (.18 mm) was traversed which leads to an error of 2 μrad.

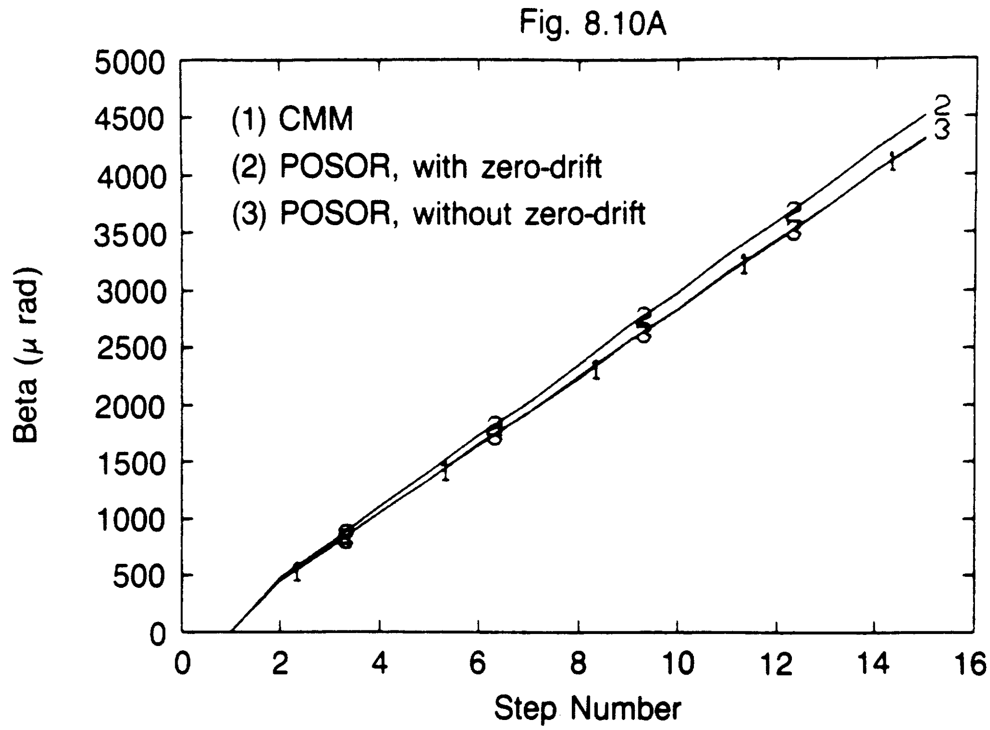

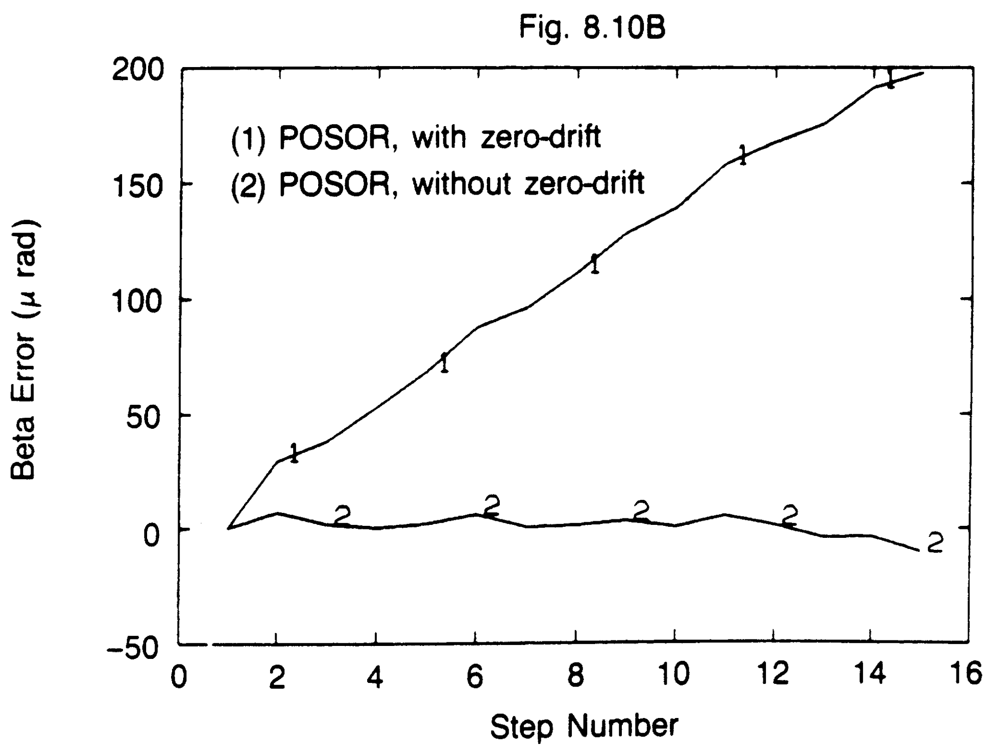

Figure 8.10 **Motion β of measuring beam during test YMO. Voltage drifts are V_1 = 0.000, V_2 = 0.100 and V_3 = 0.240 volts**

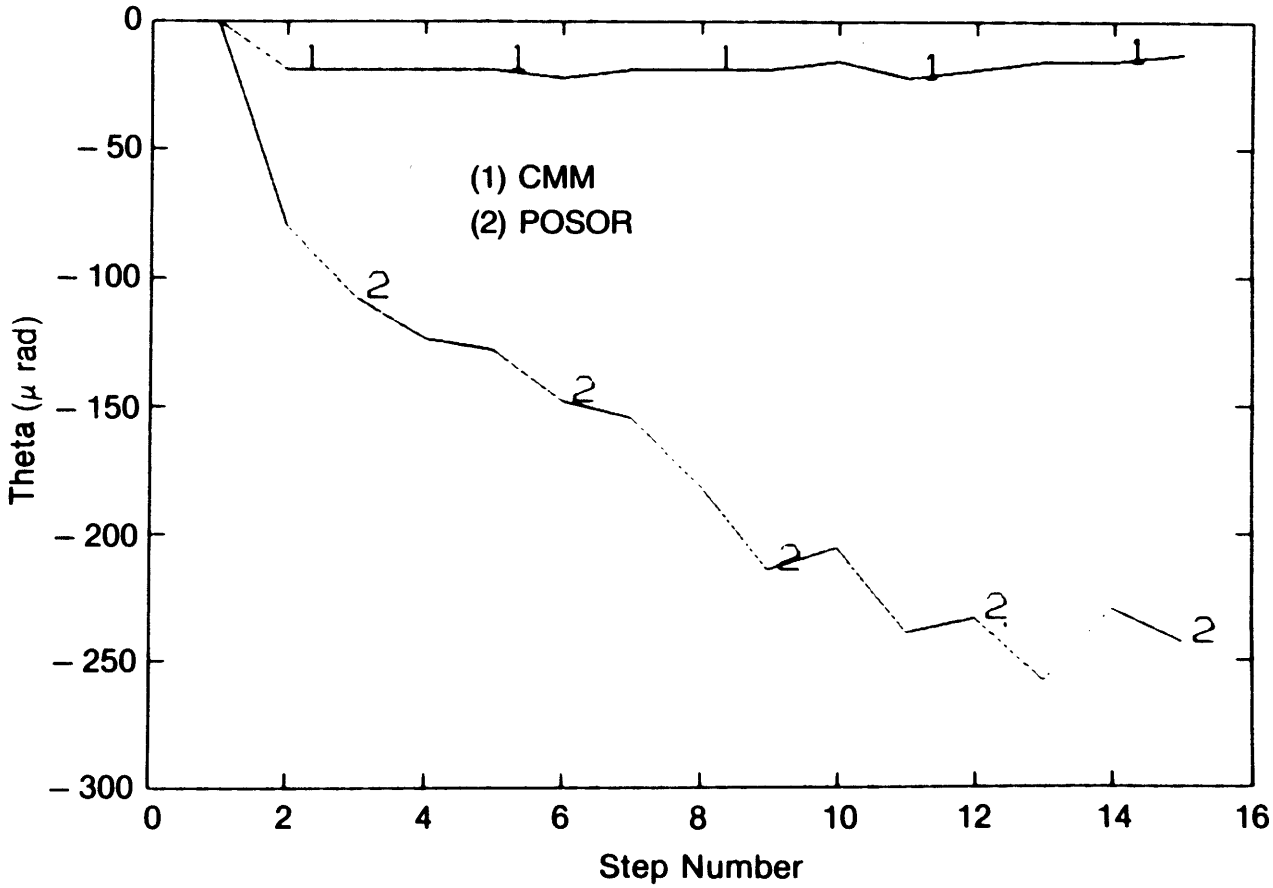

Figure 8.11 Motion θ of measuring beam during test YMO

This places the measured error within 4.3 standard deviations of that predicted. Another contribution to the error could be due to foreign material reflecting the light beam.

8.4.3 Results of the Diagonal (Y and Z) Motion Test

The YZ motion test was used to evaluate the POSOR's performance with respect to β and Θ motions. The ranges of the Y and Z motions were both .3" (7.6 mm) and were made in 13 steps using the two axis stage. The probe zero-drift voltages were found to be -0.060, 0.180, and 0.140 volts for probes 1, 2, and 3 respectively. The results of this test are shown in Figures 8.12 - 8.14.

Figure 8.12 shows the angle α measured by the POSOR without and with the probe zero-drift voltages. From Equations 5.21 and 5.22, and Table 8.1, the increasing error component should be 0 µrad. The accuracy of the twist stage is 17 µrad. The expected random error is 11 µrad. Figure 8.12 shows the value of α rising and falling within these bounds with a standard deviation of 3 µrad, so α is well within the predicted bounds.

Figure 8.13A shows the angle β as measured by the machining center and by the POSOR without and with the probe zero-drift voltages. Figure 8.13B shows the error found by subtracting curve 1 in Fig. 8.13A from curves 2 and 3. The error in the zero-drift compensated curve appears to be random with a standard deviation of 7 µrad over a range of 3700 µrad. The expected random error component is 6 µrad. From Equations

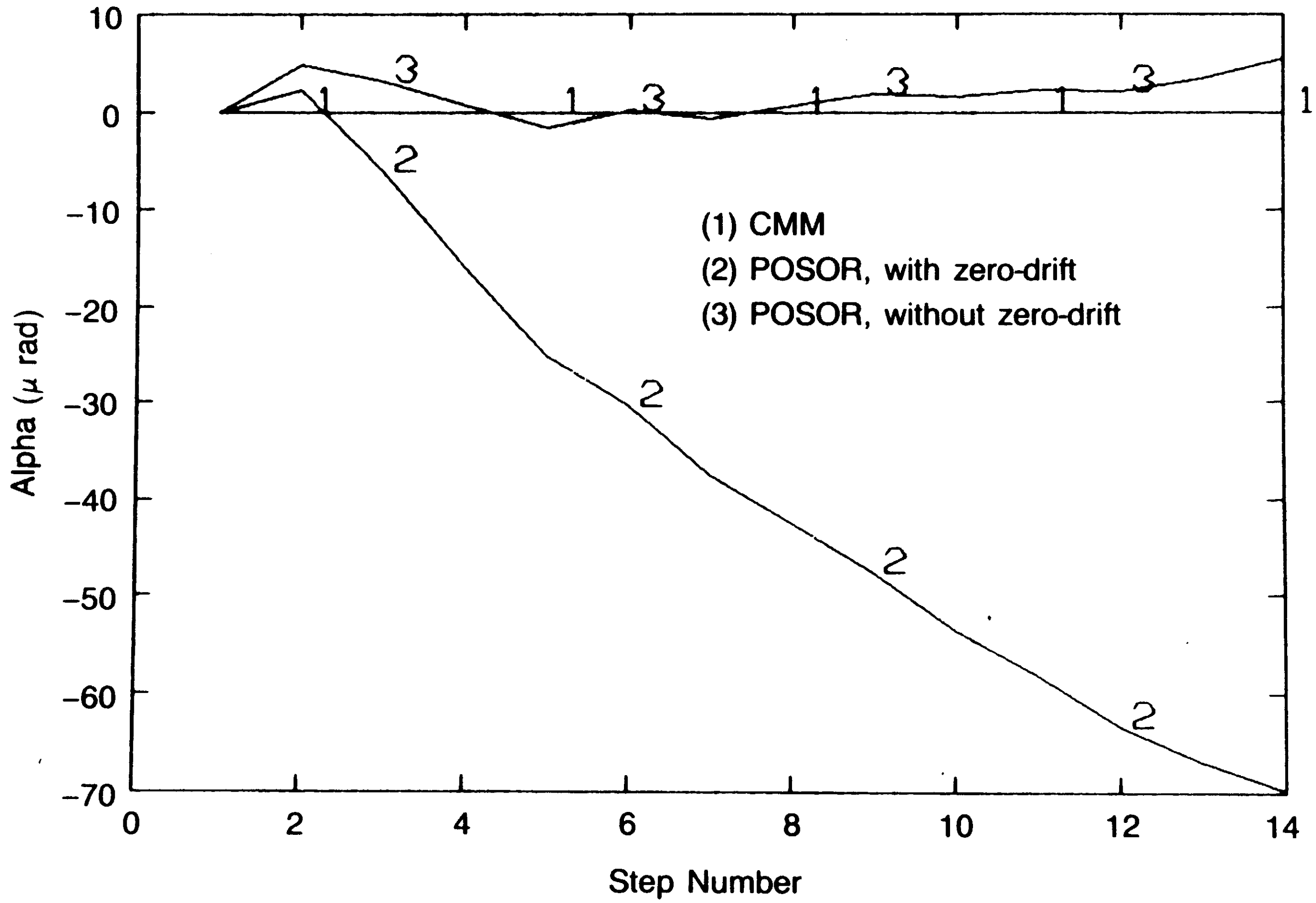

Figure 8.12 **Motion α of measuring beam during test YZMO. Voltage drifts are $V_1 = -0.060$, $V_2 = 0.180$, and $V_3 = 0.140$ volts**

Fig. 8.13A

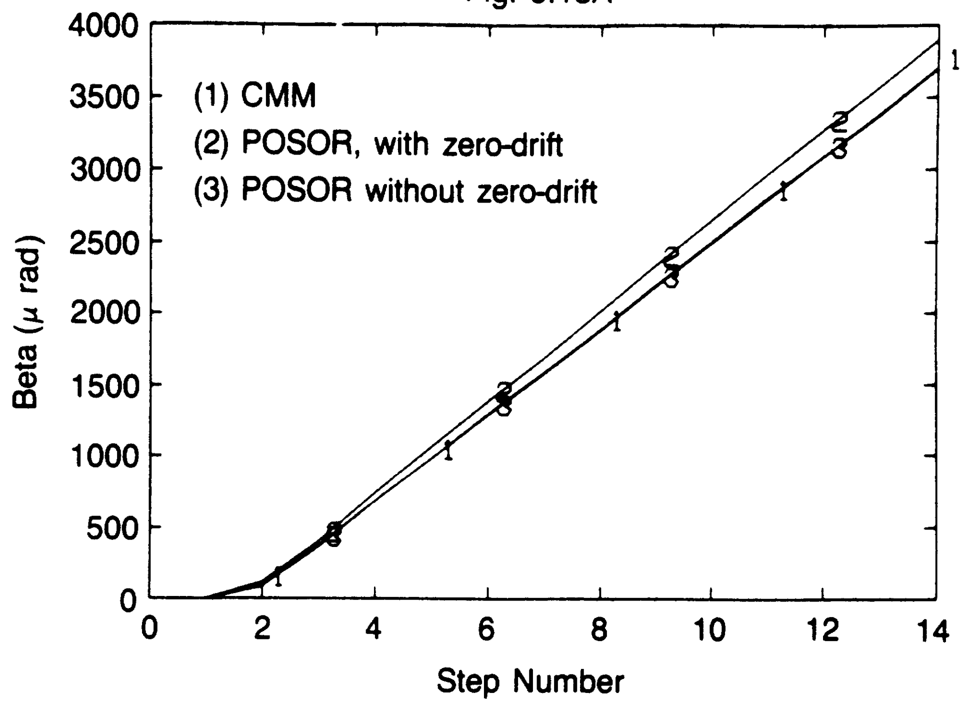

Fig. 8.13B

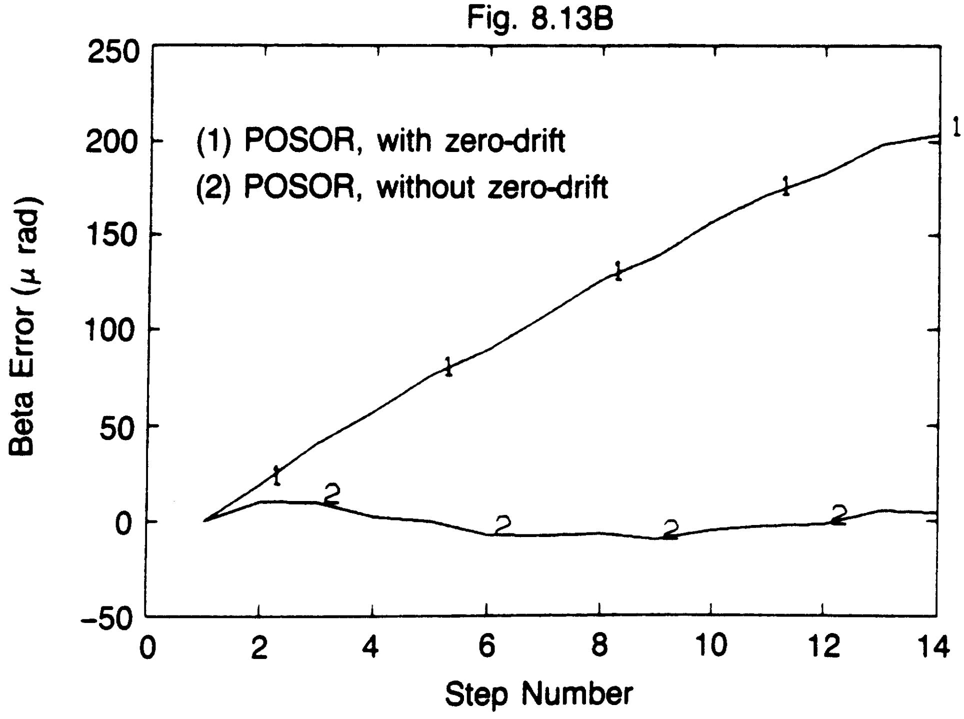

Figure 8.13 Motion β of measuring beam during test YZMO. Voltage drifts are V_1 = -0.060, V_2 = 0.180, and V_3 = 0.140 volts

5.21 and 5.22 and Table 8.1, the increasing error component is found to be 13 μrad. Thus the motion is tracked quite well.

The results for the α and β motions show that they are uncoupled. Once again it is shown that the zero offset voltages are critical to the performance of the system. The stability of the zero-drift is not good for these experiments, but development of hybrid circuits can be expected to alleviate this problem.

Figure 8.14A shows the angle Θ as measured by the machining center and the POSOR. Figure 8.14B shows the error starts at zero and increases to 112 μrad over a range of 3920 μrad. The standard deviation of the error is 92 μrad. From Table 8.1, the X_d motion is on the order of .006" (.152) mm. Thus the error induced by the straightness of the calibration stage could be a maximum of 45 μrad. The predicted error due to the factors listed in Table 7.9 (such as distance between the diodes, etc.) is 111 μrad over .5" (12.7 mm) of travel across the diodes. For this test, only .02" (.51 mm) was traversed which leads to an error of 4 μrad. Thus the error would have to be due to the straightness of the calibration stage, and it is within 2.5 standard deviations of the predicted error.

8.4.4 Results of the Twisting (α) Motion Test

The TWIS motion test (motion α about the X axis, and small motions along the Y and Z axes which correspond to twist of a beam about its length) was used to evaluate the POSOR's performance with respect to Θ

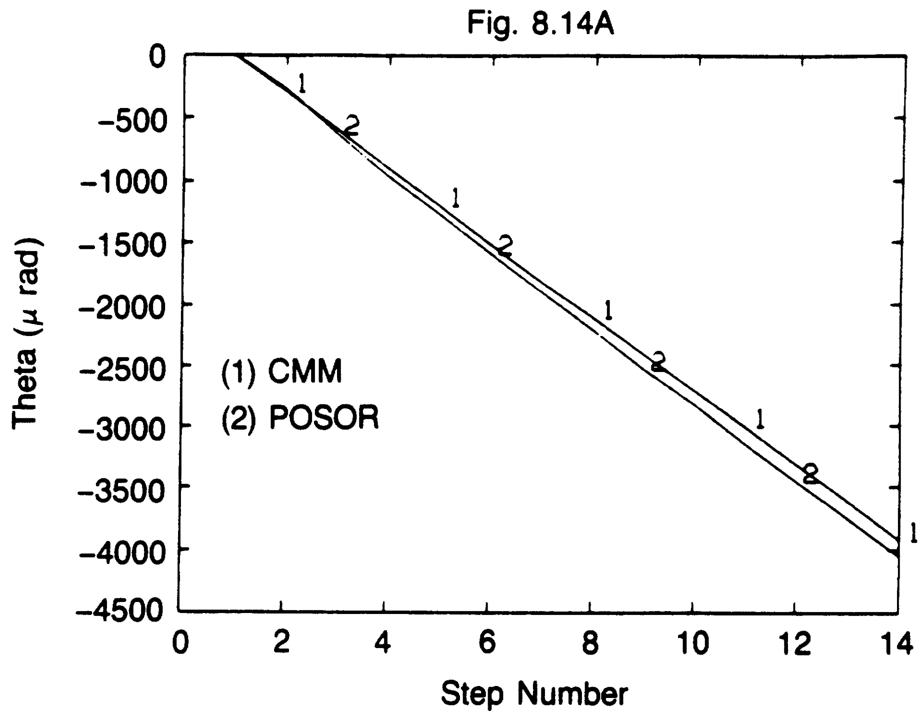

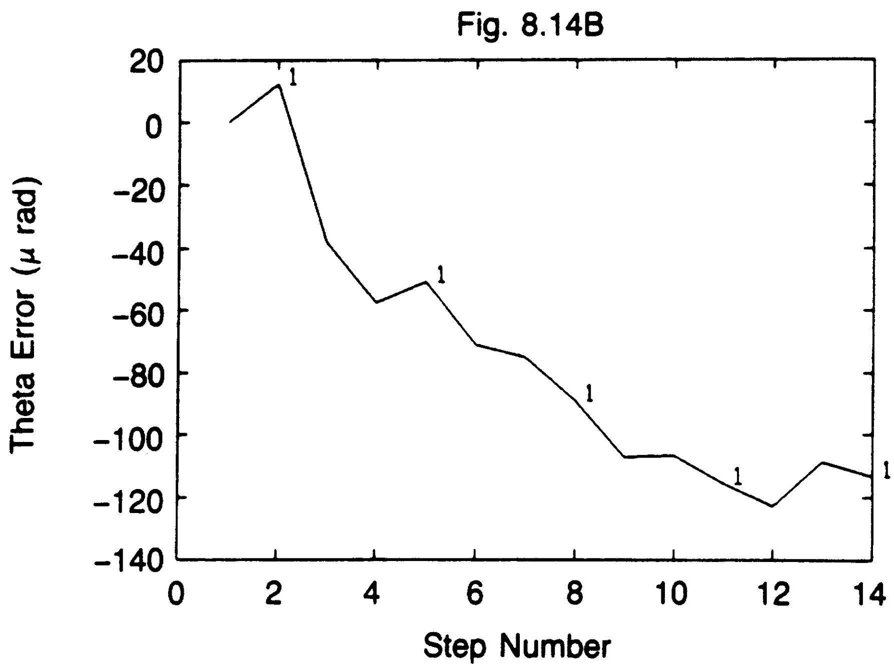

Figure 8.14 Motion θ of measuring beam during test YZMO.

and runout motions. The range of the α motions was .3° and the runout (Y and Z motion) was on the order of .005" (.13 mm). The motions were made in 15 steps using the twist stage. For both the TWIS and GEN tests, since the two degree-of-freedom gimbal was no longer steady, the vertical machining center could not be used to measure the angles β and θ effectively. Instead, the Y and Z motions of the end of the measuring beam were measured. These motions consisted of components due to the rotations β and θ, and of components due to translation of the twist stage as it was rotated. The probe zero offset voltages were found to be -.060, 0.180, and 0.140 volts for probes 1, 2, and 3 respectively. The results of the TWIS test are shown in Figures 8.15 - 8.17.

Figure 8.15A shows the angle α measured by the POSOR without and with the probe zero-drift voltages. Figure 8.15B shows the error found by subtracting curve 1 in Fig. 8.15A from curves 2 and 3. From Equations 5.21 and 5.22 and Table 8.1, the increasing error component (due to uncertainties in the values of the distances between the probes) should be at most 44 μrad. The accuracy of the twist stage is 17 μrad. The expected random error due to the POSOR is 11 μrad, and that due to the machining center is 81 μrad, so the root mean square random error is 83 μrad. Figure 8.20 shows the error in α increasing until constant at steps 2 - 10, and then becoming more random. The standard deviation of the measured error is 53 μrad over a range of 5796 μrad. Thus the measurement of α is as accurate as can be expected.

Figure 8.16A shows the motion Y as measured by the machining center and by the POSOR without and with the probe zero-drift voltages. Figure

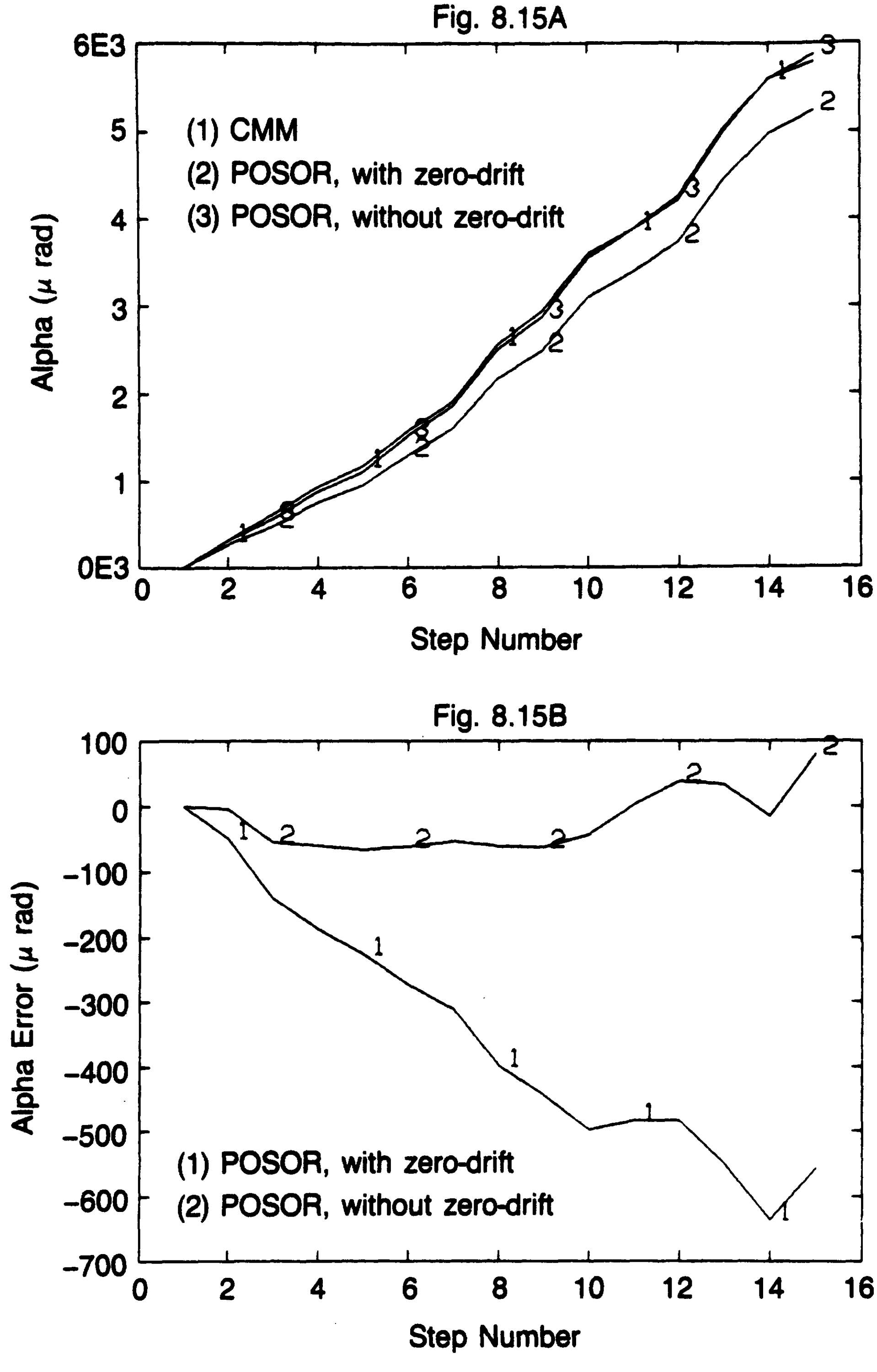

Figure 8.15 **Motion α of measuring beam during test TWIS. Voltage drifts are $V_1 = -0.185$, $V_2 = 0.118$, and $V_3 = 0.071$ volts.**

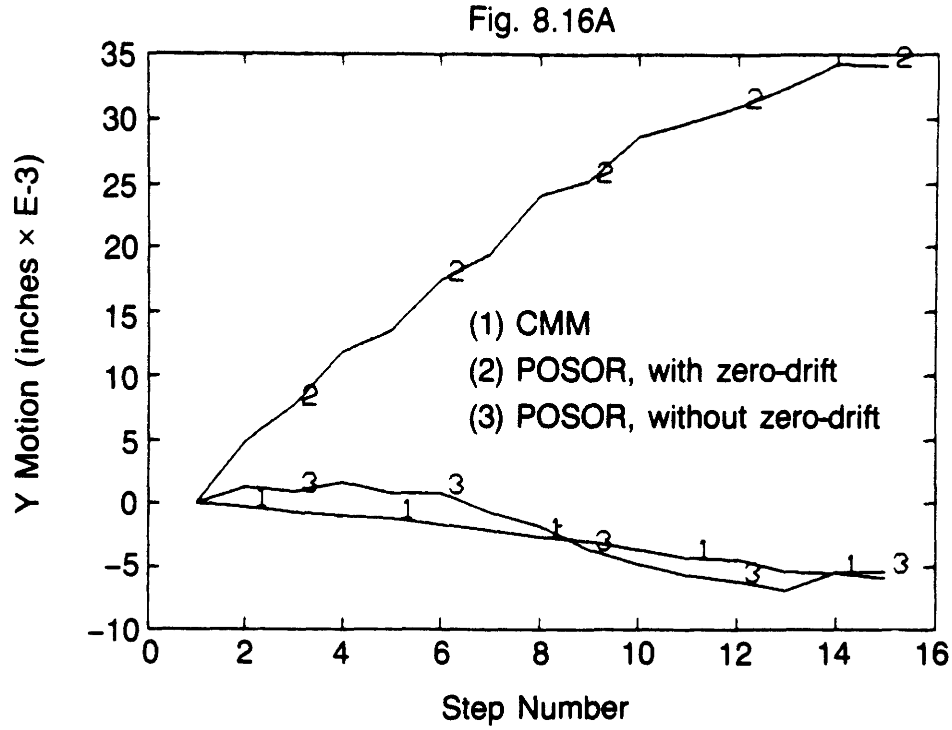

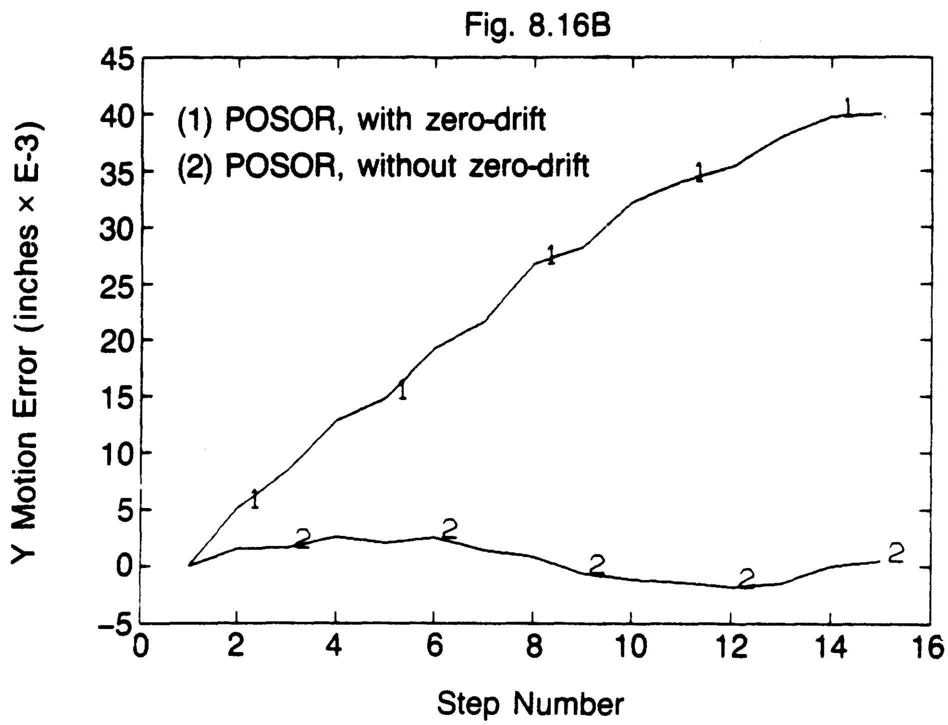

Figure 8.16 Motion Y of measuring beam during test TWIS. Voltage drifts are V_1 = -0.185, V_2 = 0.118, and V_3 = 0.071 volts

8.16B shows the error found by subtracting curve 1 in Fig. 8.16A from curves 2 and 3. The error appears to be pseudo random with a standard deviation of .001627" (40.7 μm) over a range of .005933" (148 μm). The expected random error component is 200 μin (5 μm). From Equations 5.21 and 5.22, and Table 8.1, the increasing error component is found to be 735 μin (18.3 μm). It is difficult to say what is causing the large error, but "human" error doesn't seem plausible because of the smoothness of the curve. A possible explanation is that the probes are less stable at larger gaps, so a shift other than the zero (but probably of the same order) could have occurred.

Figure 8.17 shows the motion Z as measured by the machining center and the POSOR. The error between them rises and falls with a maximum amplitude of about .007" (.178 mm). This could be explained by the light spot moving up a peak in a linearization curve, and then back down the other side. From Table 8.1, the full range of X motion is .0055" (.140 mm) for diode 1, and .0230" (.584 mm) for diode 2. Thus the peak of the up and down error that could be caused would be .0004"×33.4"/3" = .0045" (.113 mm). The average distance moved across the diodes was .027" (.685 mm), so the error contribution from Table 7.9 would only be .0002" (5 μm). Another cause for the error may be foreign material on the diode but this does not seem likely. Similarly, the β motion was constant, so any reflection effects would also be constant; thus the cause must have been related to the calibration stage effects. Hence the error is within 1.6 standard deviations of the predicted error.

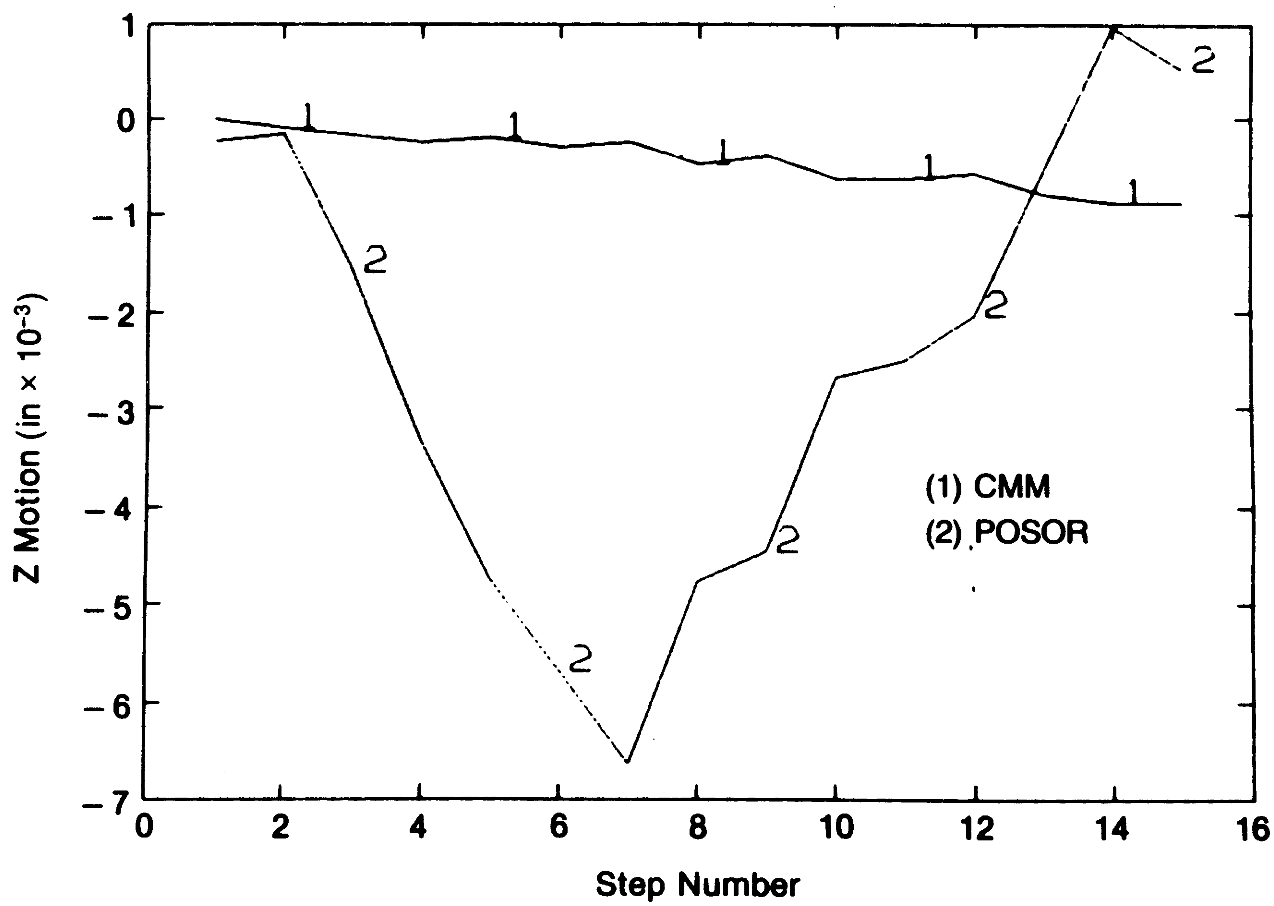

Figure 8.17 Motion Z of measuring beam during test TWIS

8.4.5 Results of the General (Y, Z, and α) Motion Test

The GEN motion test was used to evaluate the POSOR's performance when subjected to combined α, Y, and Z motions. The ranges of the α, Y, and Z motions were .3°, .005", and .3" (.13 mm and 7.6 mm) respectively. The motions were made in 10 steps using both the two axis and twist stages. The probe zero offset voltages were found to be -.148, 0.245, and 0.403 volts for probes 1, 2, and 3 respectively. The results of this test are shown in Figures 8.18 - 8.20.

Figure 8.18A shows the angle α measured by the POSOR without and with the probe voltage offsets. Figure 8.18B shows the error found by subtracting curve 1 in Fig. 8.18A from curves 2 and 3. From Equations 5.21 and 5.22 and Table 8.1, the increasing error component should be 6 μrad. The accuracy of the twist stage is 17 μrad. The expected random error due to the POSOR is 11 μrad, and that due to the machining center is 81 μrad, so the root mean square random error is 83 μrad. Figure 8.25 shows the error in α rising then falling with a standard deviation of 91 μrad over a range of 1565 μrad. Thus the measurement of α is as accurate as can be expected.

Figure 8.19A shows the motion Y as measured by the machining center and by the POSOR without and with the voltage offsets respectively. Figure 8.19B shows the error found by subtracting curve 1 in Fig. 8.19A from curves 2 and 3. The error appears to be random with a standard deviation of 506 μin (12.7 μm) over a range of 7242 μin (181 μm). The

Fig. 8.18A

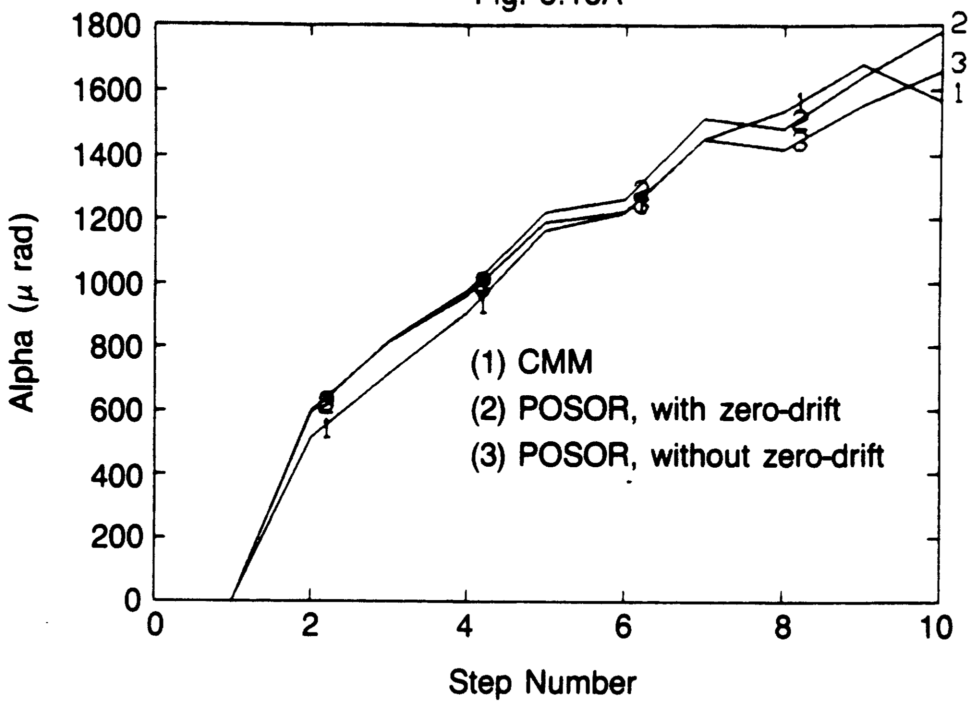

Fig. 8.18B

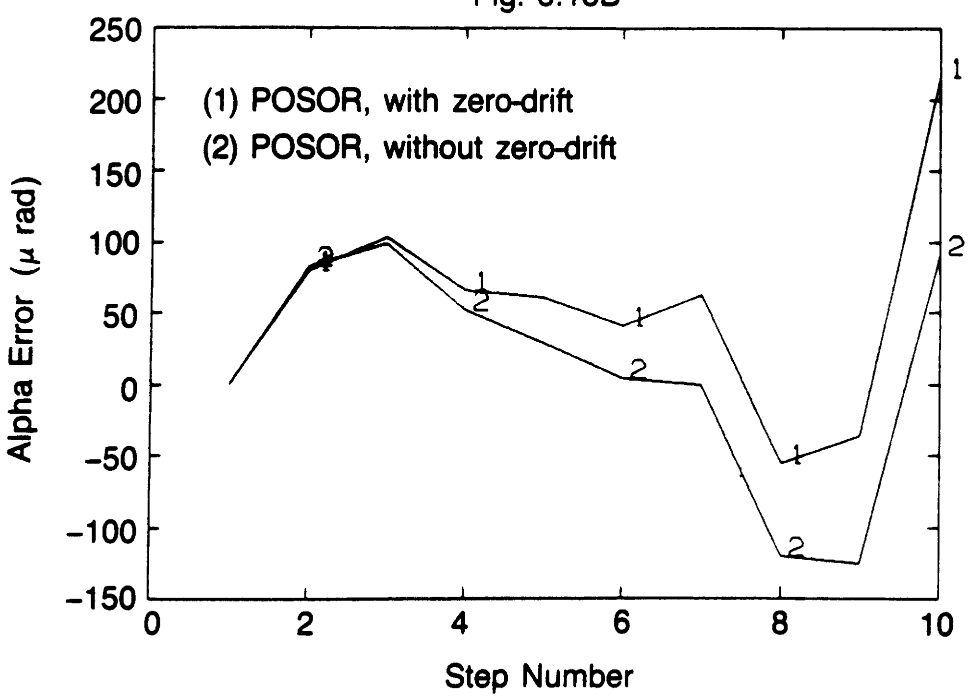

Figure 8.18 Motion α of measuring beam during test GEN. Voltage drifts are V_1 = -0.148, V_2 = 0.245, and V_3 = 0.403 volts

Fig. 8.19A

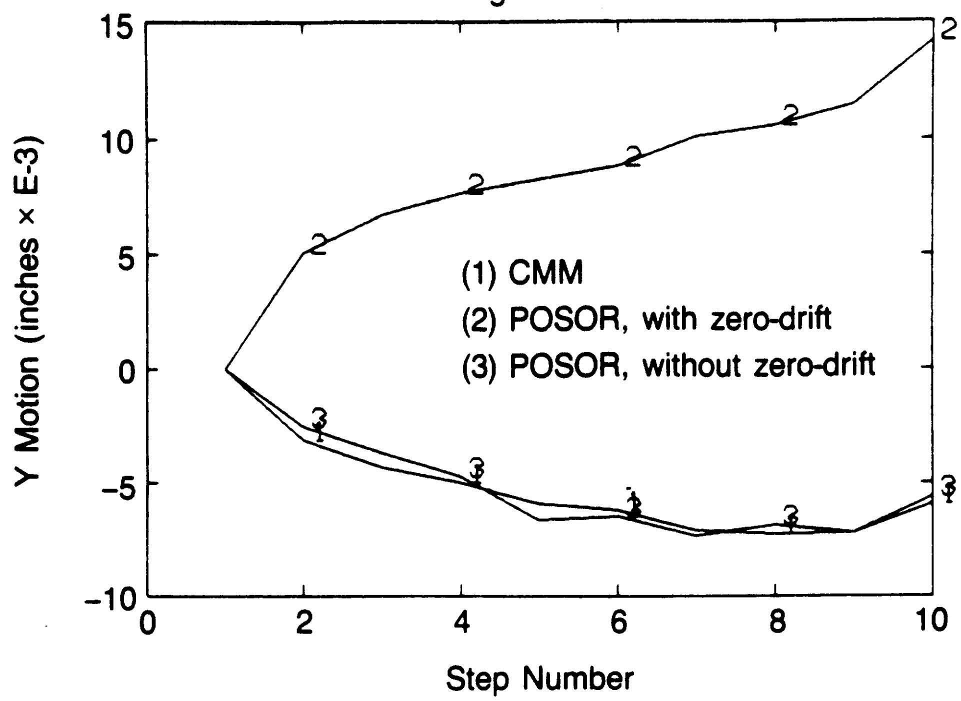

Fig. 8.19B

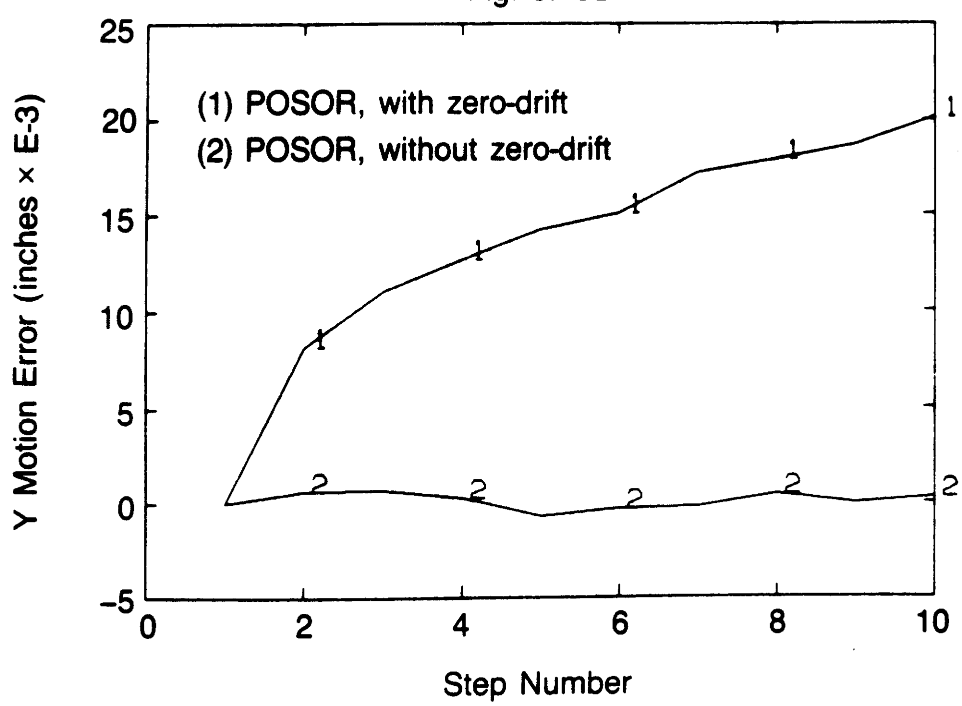

Figure 8.19 Motion Y of measuring beam during test GEN. Voltage drifts are V_1 = -0.148, V_2 = 0.245, and V_3 = 0.403 volts

expected random error component is 200 μin (5 μm). From Equations 5.21 and 5.22 and Table 8.1, the increasing error component is found to be 167 μin (4.2 μm). Thus the error is within two standard deviations of the predicted error. Note that this error is smaller than for the TWIS test, even though the range of α motion is larger because the probe readings (distance traveled by the probes) shown in Table 8.1 are lower.

Figure 8.20A shows the motion Z as measured by the machining center and by the POSOR without and with the voltage offsets respectively. Figure 8.20B shows the error found by subtracting curve 1 in Fig. 8.20A from curves 2 and 3. The error grows continuously to a maximum of .0155", and the standard deviation of the error is .0085" (.216 mm). From Table 8.1, the X_d motion on diode 1 is .0055" (.140 mm) and on diode 2 is .0230" (.584 mm). Thus the error induced by the straightness of the calibration stage could be a maximum of 120 μrad, which would be amplified by the measuring beam to .004008" (.102 mm). The predicted error due to the factors listed in Table 7.9 (such as distance between the diodes, etc.) is 111 μrad over .5" (12.7 mm) of travel across the diodes. For this test, the average distance traveled across the diodes was .0270" (.686 mm), which leads to an error of 6 μrad, which is amplified to .000200" (5 μm) at the endpoint. Thus over the length of the measuring beam, the error should be at most .0040". The endpoint error is within 3.9 standard deviations of the predicted error.

Fig. 8.20A

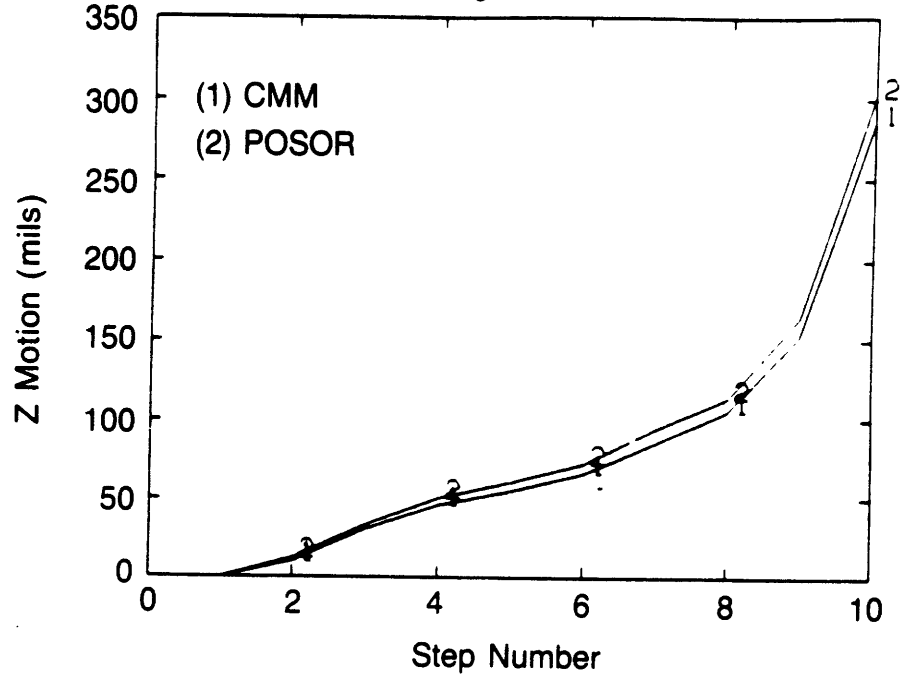

Fig. 8.20B

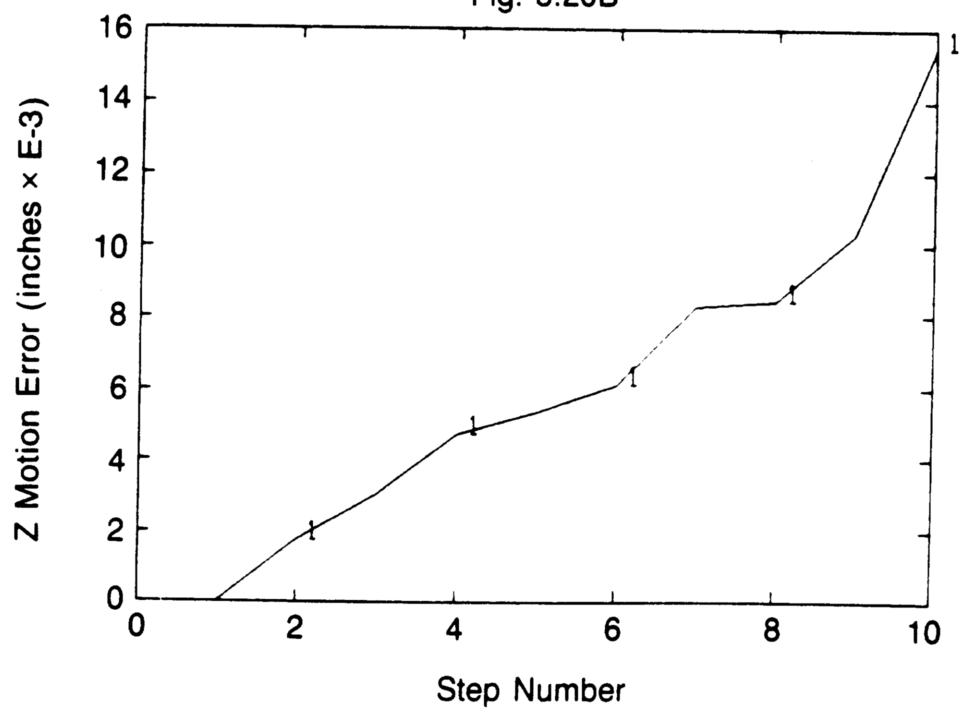

Figure 8.20 Motion Z of measuring beam during test GEN

8.5 Summary of Results, and Recommendations

The results are best summarized by looking at Table 8.2 which lists the results of the measurements, the observed errors, and the predicted errors. The POSOR measured the angles α and β quite well (within the predicted limits of accuracy of the test setup) except for the β motion during the TWIS test. These good results, however, depended on the determination (digitally) of the small (a few tenths of a volt) voltage shifts in the probes' zeroes. These voltages are listed in Table 8.1. There is no clear trend, just a casual drift from the first test (ZMO) to the last test (GEN). Note that test ZMO was performed on the first day, tests YMO and YZMO on the second day, and tests TWIS and GEN on the third day.

The Θ measurements, which were measured by the lateral effect diode system, were poor (but predictable) and the cause was traceable to the calibration stage. Thus all the tests produced errors that were within a few standard deviations of those predicted. Based on these results, the methodology of the error analysis of Chapter 5 appears correct, and the POSOR's performance for the multi degree-of-freedom tests was similar to that of the single degree-of-freedom tests. This indicates that there is little coupling between the measured degrees of freedom.

From the error analysis presented in Chapter 5, the dominant errors were shown to be due to sensor inaccuracies. With regard to the impedance probes, it was the zero drift problem which caused 90% of the

Table 8.2 Summary of Test Results to Evaluate Measuring Beam System Performance*

Test

Values (inches and μrad where appropriate)

	ZMO	YMO	YZMO	TWIS	GEN
α_{max}		<17	<17	5796	1565
σ_{α}		15	3	53	91
Predicted:					
$\sigma_{\alpha rand.}$		11	11	83	83
$\sigma_{\alpha incr.}$		<17	<17	<17	<17
β_{max}		4318	3700	178	217
σ_{β}		4	7	49	15
Predicted:					
$\sigma_{\beta rand.}$		6	6	6	6
$\sigma_{\beta incr.}$		13	13	22	5
Y_{max}		.144221	.123580	.005933	.007242
σ_{Y}		.000134	.000234	.001627	.000506
Predicted:					
$\sigma_{Yrand.}$		.000200	.000200	.000200	.000200
$\sigma_{Yincr.}$		.000434	.000434	.000735	.000167

Table 8.2 (Continued)

Test

Values (inches and μrad where appropriate)

	ZMO	YMO	YZMO	TWIS	GEN
Θ_{max}	5447	22	3920	26	8554
$\varepsilon_{\Theta max}$	68	230	123	191	464
σ_{Θ}	66	179	92	102	274
Predicted:					
$\sigma_{\Theta rand.}$	4	2	4	6	120
$\sigma_{\Theta incr.}$	68	53	45	135	6
Z_{max}	.181930	.000735	.139280	.000876	.285700
ε_{Zmax}	.002037	.007682	.004108	.006388	.015499
σ_{Z}	.001637	.005979	.003073	.003420	.009146
Predicted:					
$\sigma_{Zrand.}$	.000134	.000067	.000134	.000200	.000200
$\sigma_{Zincr.}$	.002271	.001770	.001503	.004500	.004005

* For tests ZMO, YMO, and YZMO, Z and Y motions are obtained by multiplying Θ and β by 33.4" respectively. For tests TWIS and GEN, Θ and β are obtained by dividing Z and Y by 33.4" respectively.

system error. This error, however, was compensated for in the analysis programs. With regard to the lateral effect diode system, the error introduced by the calibration stage accounted for 95% of the system error that was predicted. It is also believed that foreign matter on the diodes (which can cause reflections and shift the center of intensity of the light source) accounted for a significant part of the error in the experiments.

In view of the above, the following recommendations are made concerning the future development of POSOR devices:

For the impedance probe system:

1) The oscillator demodulator unit must be replaced with a unit that has no adjustable pots, and does not drift if bumped. More stable electrical components should also be chosen.

2) The relative probe positions must be found while the angles α and β are simultaneously measured with angular interferometers.

3) The probes must be secured in a stress free way (epoxied, instead of held with nuts)

For the lateral effect diode system:

1) This type of system is suitable for use only in laboratory environments (the diodes are very susceptible to contamination).

2) Stick mirror interferometers (allow direct measurement of simultaneous X and Y stage motion) should be used to measure the stage motion directly when mapping the diodes, so Abbe's offset error can be reduced to microinches.

3) Stable laser light must be used as opposed to laser diodes; however, it can be delivered to the required region by fiber optic cables.

Finally, note that the average endpoint error measured by the impedance system was .000625" (16 μm), and that of the lateral effect diode system was .008929" (.226 mm). If one still ponders how the measuring beam system would work in a real live robot, consider that the measuring beam was 30" (.762 m) long and the POSOR was only 3" (.0762 m) in diameter. Thus even if scaled up to a robot with a 90" reach, the system in question would be one to two orders of magnitude more accurate than any existing robot. Accordingly, as the conclusion to this thesis, Chapter 9 will discuss the conceptual design of a robot that uses bumpy ring POSORs and 5 μin (.13 μm) accuracy impedance probes (easy to obtain) to achieve .0005" (.0127 mm) feedback signal accuracy and payload to weight ratios on the order of five to one.

APPENDIX 8A

FORTRAN Analysis Programs

```
cccccccccccccccccccccccccccccccccccccccccccccccccccccccccccccccccccccccc
c
c       DIMEN.FOR by Alex Slocum, Feb. 1, 1985. To load POSOR
c       dimensions
c
cccccccccccccccccccccccccccccccccccccccccccccccccccccccccccccccccccccccc
      SUBROUTINE DIMEN
      COMMON/DIMEN/ a, b, c, dYsep, dXsep, sig1, sig2, rho1, rho2
      a = 1.499336
      b = 1.536081
      c = 2.992550
      dYsep = 3.0120189
      dXsep = -.0517803
      rho1 = -.746148
      rho2 = .789712
      sig1 = .003996
      sig2 = .002762
      RETURN
      END
```

```
cccccccccccccccccccccccccccccccccccccccccccccccccccccccccccccccccccc
c
c     ALBET.FOR by Alex Slocum, Jan 21, 1985. To determine inclination
c     angles of receiving plane, ALPHA, and BETA.
c
cccccccccccccccccccccccccccccccccccccccccccccccccccccccccccccccccccc
      SUBROUTINE ALBET(ALPH, BET)
      COMMON/DIMEN/ a, b, c, DYSEP, DXSEP, sig1, sig2, rho1, rho2
      COMMON/PROBE/ D1, D2, D3, ALPHA, BETA
      ALPHA = ATAN( (D2 - D3)/(a + b) )
      ALPH = ALPHA
      BETA = ATAN( ( D1 - (D2*b + D3*a)/(a+b) )/c )
      BET = BETA
      RETURN
      END
```

```
cccccccccccccccccccccccccccccccccccccccccccccccccccccccccccccccccccccc
c
c     DIST.FOR by Alex Slocum, Jan 21, 1985. To determine distance
c     from receiving plane to transmitting plane, at a given XY.
c
cccccccccccccccccccccccccccccccccccccccccccccccccccccccccccccccccccccc
      SUBROUTINE DIST(X, Y, D)
      COMMON/DIMEN/ a, b, c, DYSEP, DXSEP, sig1, sig2, rho1, rho2
      COMMON/PROBE/ D1, D2, D3, ALPHA, BETA
      D = D3 + (b + Y)*TAN(ALPHA) - X*TAN(BETA)
      RETURN
      END
```

```
CCCCCCCCCCCCCCCCCCCCCCCCCCCCCCCCCCCCCCCCCCCCCCCCCCCCCCCCCCCCCCCCCCCCCCC
C
C     PROBLIN.FOR by Alex Slocum, Jan 21, 1985, to linearise probe
C     readings.
C
CCCCCCCCCCCCCCCCCCCCCCCCCCCCCCCCCCCCCCCCCCCCCCCCCCCCCCCCCCCCCCCCCCCCCCC
      SUBROUTINE PROBLIN(D1D, D2D, D3D)
      COMMON/PROBE/ D1, D2, D3, ALPHA, BETA
      D1 = -.00611858209203+
     *     -.0537873565289*D1D+
     *     -.00135681621391*D1D**2+
     *     -.0125007816348*D1D**3+
     *     0.00402206672115*D1D**4
      D2 = 0.00966953730103+
     *     -.0569624082221*D2D+
     *     0.00344398406400*D2D**2+
     *     -.0102412224730*D2D**3+
     *     0.000811112121339*D2D**4
      D3 = 0.0173366419656+
     *     -.0588980712953*D3D+
     *     0.0103716249546*D3D**2+
     *     -.01005977491680*D3D**3+
     *     0.00546089798025*D3D**4
      RETURN
      END
```

```
      SUBROUTINE DLINE(ID, X, Y, XC, YC)
      COMMON/COEFF/ AX(2,15,10), AY(2,15,10)
      COMMON/POINT/ POSX(15), POSY(15)
      XCP = 10.     !INITILISE VALUES
      YCP = 10.
      XCP2 = 10.
      YCP2 = 10.
      XC = AX(ID,7,1)     !Assume curve 7 for initial calculation
      DO 4 I = 2, 10
         XC = XC + AX(ID,7,I)*X**(I-1)
4     CONTINUE
C        Use the calculated X value to find curve for Y
2000  IPY = 1
      DPY = POSY(1) - XC
      DO 5 I = 1, 15
         IF( ABS(POSY(I)-XC).LT.ABS(DPY) ) THEN
            DPY = POSY(I) - XC
            IPY = I
         ENDIF
5     CONTINUE
      IF( (DPY.GT.0.).AND.(IPY.GT.1) ) THEN       ! Set direction
         IW = -1
      ELSE
         IW = 1
      ENDIF
      IF (IPY.EQ.15) IW = -1
C       Determine linear interpolation constant
      R1 = DPY/( POSY(IPY) - POSY(IPY+IW) )
C       Calculate the two Ys to use in interpolation
      YC1 = AY(ID,IPY,1)
      YC2 = AY(ID,IPY+IW,1)
      DO 7 I = 2, 10
         YC1 = YC1 + AY(ID,IPY,I)*Y**(I-1)
         YC2 = YC2 + AY(ID,IPY+IW,I)*Y**(I-1)
7     CONTINUE
      YC = YC1 + R1*(YC2-YC1)
C       Use the calc. Y to find the X curve
      IPX = 1
      DPX = POSX(1) - YC
      DO 15 I = 1, 15
         IF( ABS(POSX(I)-YC).LT.ABS(DPX) ) THEN
            DPX = POSX(I) - YC
            IPX = I
         ENDIF
15    CONTINUE
      IF( (DPX.GT.0.).AND.(IPX.GT.1) ) THEN       ! Set direction
         IW = -1
      ELSE
         IW = 1
      ENDIF
      IF (IPX.EQ.15) IW = -1
C       Determine linear interpolation constant
      R1 = DPX/( POSX(IPX) - POSX(IPX+IW) )
C       Calculate the two Xs to use in interpolation
      XC1 = AX(ID,IPX,1)
      XC2 = AX(ID,IPX+IW,1)
      DO 111 I = 2, 10
         XC1 = XC1 + AX(ID,IPX,I)*X**(I-1)
         XC2 = XC2 + AX(ID,IPX+IW,I)*X**(I-1)
111   CONTINUE
      XC = XC1 + R1*(XC2-XC1)
C        If X and Y didn't change in present cycle, return to main
      IF ( (XC .EQ. XCP).AND.(YC .EQ. YCP) ) GOTO 1000
```

```
c       If X and Y same as cycle-2, oscillating, average and retry
      IF ( (XC .EQ. XCP2).AND.(YC .EQ. YCP2) ) THEN
         XLAS = (XC+XCP)/2.
         YLAS = (YC+YCP)/2.
      ENDIF
      XCP2 = XCP      !Update loop values
      YCP2 =YCP
      XCP = XC
      YCP = YC
      GOTO 2000       ! Go thru another iteration
1000  RETURN
      END
```

```
cccccccccccccccccccccccccccccccccccccccccccccccccccccccccccccccccccc
C
C     ZMO.FOR by Alex Slocum, Feb. 1, 1985. To determine Theta motion
C     of measuring beam.
C
cccccccccccccccccccccccccccccccccccccccccccccccccccccccccccccccccccc
      REAL X(20), Y(20), Z(20), L1(20), L2(20), L3(20), ALPH(3,20),
     *   BET(3,20), THET(3,20),
     *   DX1(20), DX2(20), DY1(20), DY2(20)
      COMMON/COEFF/ AX(2,15,10), AY(2,15,10)
      COMMON/POINT/ POSX(15), POSY(15)
      COMMON/DIMEN/ a, b, c, DYSEP, DXSEP, sig1, sig2, rho1, rho2
      COMMON/PROBE/ D1, D2, D3, ALPHA, BETA
      CHARACTER*40, XLAB, ALPHLAB, BETLAB, THETLAB
      OPEN(UNIT = 1, NAME = 'ZMO.INP', STATUS = 'OLD')
      OPEN(UNIT = 2, NAME = 'ZMO.OUT', STATUS = 'NEW')
      XLAB = 'Step Number'      !Plot titles.
      ALPHLAB = 'Alpha (u rad)'
      BETLAB = 'Beta (u rad)'
      THETLAB = 'Theta (u rad)'
      CALL CONSTANT          ! Load linearization polynomials.
      CALL DIMEN             ! Load POSOR dimensions.
C
C              Read data.
C
      DO 5 I = 1, 20
         READ(1,10) Y(I), Z(I), X(I)
10       FORMAT(3F8.5)
5     CONTINUE
      DO 6 I = 1, 20
         READ(1,11) L1(I), L2(I), L3(I)
11       FORMAT(3F12.7)
6     CONTINUE
      DO 7 I = 1, 20
         READ(1,12) DX1(I), DY1(I), DX2(I), DY2(I)
12       FORMAT(4F12.7)
7     CONTINUE
C
C          Calculate initial conditions.
C
      L2(1) = L2(1) + .2        !Add offset due to electronics shift
      L3(1) = L3(1) + .3        !from voltage calibrated at.
      CALL PROBLIN( L1(1), L2(1), L3(1) )!Linearize probe readings.
      CALL ALBET(ALPHO, BETO) ! Det. initial ALPHA, BETA
      CALL DLINE(1, DX1(1), DY1(1), X1, Y1) !Linearize diode 1 readings.
      XD1 = -.566 - X1 !Det. global XY coordinates of LASERS on diodes.
      YD1 = 1.8 - Y1
      CALL DLINE(2, DX2(1), DY2(1), X2, Y2) !Linearize diode 2 readings.
      XD2 = -.566 - X2
      YD2 = -1.2 - Y2
      CALL DIST(XD1, YD1, DL1o)  !Det. initial dist. from LASERs to diodes.
      CALL DIST(XD2, YD2, DL2o)
      THETO = ATAN( (Y1-Y2-DYSEP)/(X1-X2-DXSEP) ) !Det. initial THETA.
      ALPH(3,1) = 1.    !Set plot X axis motion step number.
      BET(1,1) = -ATAN(Y(1)/31.43)  !Det. initial measured BETA.
      BET(3,1) = 1.
      THET(1,1) = -ATAN(Z(1)/31.43)  !Det. initial measured THETA.
      THET(3,1) = 1.
      WRITE(2,13)    !Write table header.
13    FORMAT(///5x,'Z Motion Results With LASER Angle Offsets'
     *//5x,'All angles are in radians'//
     *5X,'ALPH(1,I) ALPH(2,I) BET(1,I)  BET(2,I)  THET(1,I) THET(2,I)'/
     */5X,'   0.         0.        0.         0.         0.        0. ')
```

```
C
C      Loop over data to find ALPHA, BETA, THETA.
C
       DO 100 I = 2, 20
          ALPH(3,I) = REAL(I)  !Set plot X axis motion step number.
          BET(1,I) = -ATAN(Y(I)/31.43)- BET(1,1)  !Det. measured BETA.
          BET(3,I) = REAL(I)
          THET(1,I) = -ATAN(Z(I)/31.43)- THET(1,1)  !Det. measured THETA.
          THET(3,I) = REAL(I)
          L2(I) = L2(I) + .2   !Add voltage offsets to probes.
          L3(I) = L3(I) + .3
          CALL PROBLIN( L1(I), L2(I), L3(I) )!Linearize probe readings.
          D1 = D1 + .133333*SIN(THET(2,I-1)) !Add POSOR flatness terms.
          D2 = D2 + .083333*SIN(THET(2,I-1))
          D3 = D3 - .083333*SIN(THET(2,I-1))
          CALL ALBET(ALPH(2,I), BET(2,I)) !Det. ALPHA, BETA.
          ALPH(2,I) = ALPH(2,I) - ALPHO   !Det. net ALPHA, BETA.
          BET(2,I) = BET(2,I) - BETO
          CALL DLINE(1, DX1(I), DY1(I), X1, Y1) !Linearize diode 1 readings.
          XD1 = -.566 - X1  !Det. global XY coordinates of LASERS on diodes.
          YD1 = 1.8 + Y1
          CALL DLINE(2, DX2(I), DY2(I), X2, Y2) !Linearize diode 2 readings.
          XD2 = -.566 - X2
          YD2 = -1.2 + Y2
          CALL DIST(XD1, YD1, DL1t) !Det. dist. from LASERs to diodes.
          CALL DIST(XD2, YD2, DL2t)
          DL1 = DL1t - DL1o  !Det. net LASER path length change.
          DL2 = DL2t - DL2o
          X1 = X1 + DL1*SIG1*COS(RHO1+THET(2,I-1)) !LASER angle offsets.
          Y1 = Y1 - DL1*SIG1*SIN(RHO1+THET(2,I-1))
          X2 = X2 + DL2*SIG2*COS(RHO2+THET(2,I-1))
          Y2 = Y2 + DL2*SIG2*SIN(RHO2+THET(2,I-1))
          RNUM = (Y1 - Y2 - DYSEP )*COS(ALPH(2,I))
          DNUM = (X1 - X2 - DXSEP)*COS(BET(2,I))
          THET(2,I) = ATAN(RNUM/DNUM) - THETO !Det. net THETA.
          WRITE(2,127) ALPH(1,I), ALPH(2,I), BET(1,I), BET(2,I),
     *     THET(1,I), THET(2,I)   !Record the answers.
127       FORMAT(5X,6(F8.6,2X))
100    CONTINUE
       DO 300 I = 2, 20      !Loop for standard deviations and plots.
          DIFB = BET(2,I) - BET(1,I)
          DIFA = ALPH(2,I) - ALPH(1,I)
          DIFT = THET(2,I) - THET(1,I)
          SUMA = SUMA + DIFA**2
          SUMB = SUMB + DIFB**2
          SUMT = SUMT + DIFT**2
          ALPH(1,I) = ALPH(1,I)/1.E-6    !Convert to microrads
          ALPH(2,I) = ALPH(2,I)/1.E-6
          BET(1,I) = BET(1,I)/1.E-6
          BET(2,I) = BET(2,I)/1.E-6
          THET(1,I) = THET(1,I)/1.E-6
          THET(2,I) = THET(2,I)/1.E-6
300    CONTINUE
       SIGA = SQRT(SUMA/18.)    !Det. sigmas.
       SIGB = SQRT(SUMB/18.)
       SIGT = SQRT(SUMT/18.)
       WRITE(2,117) SIGA, SIGB, SIGT
117    FORMAT(4X,'SIGA = ', F10.6,' SIGB = ',F10.6,' SIGT = ',F10.6)
       PRINT*, 'SIGA = ', SIGA,' SIGB = ',SIGB,' SIGT = ', SIGT
       ALPH(1,1) = 0.   !Set plot to start at GO.
       BET(1,1) = 0.
       THET(1,1) = 0.
       CALL QPICTR(ALPH,3,20,QY(1,2), QX(3), QXLAB(XLAB), QYLAB(ALPHLAB)
```

```
*    ,QLABEL(4) )     !Plot them points up.
 CALL QPICTR(BET,3,20,QY(1,2), QX(3), QXLAB(XLAB), QYLAB(BETLAB)
*    ,QLABEL(4) )
 CALL QPICTR(THET,3,20,QY(1,2), QX(3), QXLAB(XLAB), QYLAB(THETLAB)
*    ,QLABEL(4) )
 STOP                !Fineesh.
 END                 !Its Miller time
```

```
cccccccccccccccccccccccccccccccccccccccccccccccccccccccccccccccccccc
C
C     YMO.FOR by Alex Slocum, Feb. 1, 1985. To determine Beta motion
C     of measuring beam.
C
cccccccccccccccccccccccccccccccccccccccccccccccccccccccccccccccccccc
      REAL X(15), Y(15), Z(15), L1(15), L2(15), L3(15), ALPH(3,15),
     *   BET(3,15), THET(3,15),
     *   DX1(15), DX2(15), DY1(15), DY2(15)
      COMMON/COEFF/ AX(2,15,10), AY(2,15,10)
      COMMON/POINT/ POSX(15), POSY(15)
      COMMON/DIMEN/ a, b, c, DYSEP, DXSEP, sig1, sig2, rho1, rho2
      COMMON/PROBE/ D1, D2, D3, ALPHA, BETA
      CHARACTER*40, XLAB, ALPHLAB, BETLAB, THETLAB
      OPEN(UNIT = 1, NAME = 'YMO.INP', STATUS = 'OLD')
      OPEN(UNIT = 2, NAME = 'YMO.OUT', STATUS = 'NEW')
      XLAB = 'Step Number'      !Plot titles.
      ALPHLAB = 'Alpha (u rad)'
      BETLAB = 'Beta (u rad)'
      THETLAB = 'Theta (u rad)'
      CALL CONSTANT        ! Load linearization polynomials.
      CALL DIMEN           ! Load POSOR dimensions.
C
C             Read data.
C
      DO 5 I = 1, 15
         READ(1,10) Y(I), Z(I), X(I)
10       FORMAT(3F8.5)
5     CONTINUE
      DO 6 I = 1, 15
         READ(1,11) L1(I), L2(I), L3(I)
11       FORMAT(3F12.7)
6     CONTINUE
      DO 7 I = 1, 15
         READ(1,12) DX1(I), DY1(I), DX2(I), DY2(I)
12       FORMAT(4F12.7)
7     CONTINUE
C
C          Calculate initial conditions.
C
      L2(1) = L2(1) + .2       !Add offset due to electronics shift
      L3(1) = L3(1) + .3       !from voltage calibrated at.
      CALL PROBLIN( L1(1), L2(1), L3(1) )!Linearize probe readings.
      CALL ALBET(ALPHO, BETO) ! Det. initial ALPHA, BETA
      CALL DLINE(1, DX1(1), DY1(1), X1, Y1) !Linearize diode 1 readings.
      XD1 = -.566 - X1 !Det. global XY coordinates of LASERS on diodes.
      YD1 = 1.8 - Y1
      CALL DLINE(2, DX2(1), DY2(1), X2, Y2) !Linearize diode 2 readings.
      XD2 = -.566 - X2
      YD2 = -1.2 - Y2
      CALL DIST(XD1, YD1, DL1o)  !Det. initial dist. from LASERs to diodes.
      CALL DIST(XD2, YD2, DL2o)
      THETO = ATAN( (Y1-Y2-DYSEP)/(X1-X2-DXSEP) ) !Det. initial THETA.
      ALPH(3,1) = 1.   !Set plot X axis motion step number.
      BET(1,1) = -ATAN(Y(1)/31.43)  !Det. initial measured BETA.
      BET(3,1) = 1.
      THET(1,1) = -ATAN(Z(1)/31.43)  !Det. initial measured THETA.
      THET(3,1) = 1.
      WRITE(2,13)   !Write table header.
13    FORMAT(///5x,'Y Motion Results With LASER Angle Offsets'
     *//5x,'All angles are in radians'//
     *5X,'ALPH(1,I) ALPH(2,I) BET(1,I)  BET(2,I)  THET(1,I) THET(2,I)'/
     */5X,'  0.         0.        0.         0.        0.         0. ')
```

```
C
C     Loop over data to find ALPHA, BETA, THETA.
C
      DO 100 I = 2, 15
         ALPH(3,I) = REAL(I)  !Set plot X axis motion step number.
         BET(1,I) = -ATAN(Y(I)/31.43)- BET(1,1)  !Det. measured BETA.
         BET(3,I) = REAL(I)
         THET(1,I) = -ATAN(Z(I)/31.43)- THET(1,1)  !Det. measured THETA.
         THET(3,I) = REAL(I)
         L2(I) = L2(I) + .2   !Add voltage offsets to probes.
         L3(I) = L3(I) + .3
         CALL PROBLIN( L1(I), L2(I), L3(I) )!Linearize probe readings.
         D1 = D1 + .133333*SIN(THET(2,I-1)) !Add POSOR flatness terms.
         D2 = D2 + .083333*SIN(THET(2,I-1))
         D3 = D3 - .083333*SIN(THET(2,I-1))
         CALL ALBET(ALPH(2,I), BET(2,I)) !Det. ALPHA, BETA.
         ALPH(2,I) = ALPH(2,I) - ALPHO   !Det. net ALPHA, BETA.
         BET(2,I) = BET(2,I) - BETO
         CALL DLINE(1, DX1(I), DY1(I), X1, Y1) !Linearize diode 1 readings.
         XD1 = -.566 - X1  !Det. global XY coordinates of LASERS on diodes.
         YD1 = 1.8 + Y1
         CALL DLINE(2, DX2(I), DY2(I), X2, Y2) !Linearize diode 2 readings.
         XD2 = -.566 - X2
         YD2 = -1.2 + Y2
         CALL DIST(XD1, YD1, DL1t) !Det. dist. from LASERs to diodes.
         CALL DIST(XD2, YD2, DL2t)
         DL1 = DL1t - DL1o  !Det. net LASER path length change.
         DL2 = DL2t - DL2o
         X1 = X1 + DL1*SIG1*COS(RHO1+THET(2,I-1)) !LASER angle offsets.
         Y1 = Y1 - DL1*SIG1*SIN(RHO1+THET(2,I-1))
         X2 = X2 + DL2*SIG2*COS(RHO2+THET(2,I-1))
         Y2 = Y2 + DL2*SIG2*SIN(RHO2+THET(2,I-1))
         RNUM = (Y1 - Y2 - DYSEP )*COS(ALPH(2,I))
         DNUM = (X1 - X2 - DXSEP)*COS(BET(2,I))
         THET(2,I) = ATAN(RNUM/DNUM) - THETO !Det. net THETA.
         WRITE(2,127) ALPH(1,I), ALPH(2,I), BET(1,I), BET(2,I),
     *     THET(1,I), THET(2,I)   !Record the answers.
127      FORMAT(5X,6(F8.6,2X))
100   CONTINUE
      DO 300 I = 2, 15     !Loop for standard deviations and plots.
         DIFB = BET(2,I) - BET(1,I)
         DIFA = ALPH(2,I) - ALPH(1,I)
         DIFT = THET(2,I) - THET(1,I)
         SUMA = SUMA + DIFA**2
         SUMB = SUMB + DIFB**2
         SUMT = SUMT + DIFT**2
         ALPH(1,I) = ALPH(1,I)/1.E-6    !Convert to microrads
         ALPH(2,I) = ALPH(2,I)/1.E-6
         BET(1,I) = BET(1,I)/1.E-6
         BET(2,I) = BET(2,I)/1.E-6
         THET(1,I) = THET(1,I)/1.E-6
         THET(2,I) = THET(2,I)/1.E-6
300   CONTINUE
      SIGA = SQRT(SUMA/13.)    !Det. sigmas.
      SIGB = SQRT(SUMB/13.)
      SIGT = SQRT(SUMT/13.)
      WRITE(2,117) SIGA, SIGB, SIGT
117   FORMAT(4X,'SIGA = ', F10.6,' SIGB = ',F10.6,' SIGT = ',F10.6)
      PRINT*, 'SIGA = ', SIGA,' SIGB = ',SIGB,' SIGT = ', SIGT
      ALPH(1,1) = 0.   !Set plot to start at GO.
      BET(1,1) = 0.
      THET(1,1) = 0.
      CALL QPICTR(ALPH,3,15,QY(1,2), QX(3), QXLAB(XLAB), QYLAB(ALPHLAB)
```

```
*    ,QLABEL(4) )      !Plot them points up.
 CALL QPICTR(BET,3,15,QY(1,2), QX(3), QXLAB(XLAB), QYLAB(BETLAB)
*    ,QLABEL(4) )
 CALL QPICTR(THET,3,15,QY(1,2), QX(3), QXLAB(XLAB), QYLAB(THETLAB)
*    ,QLABEL(4) )
 STOP                  !Fineesh.
 END                   !Its Miller time
```

```
cccccccccccccccccccccccccccccccccccccccccccccccccccccccccccccccccccc
c
c       YZMO.FOR by Alex Slocum, Feb. 1, 1985. To determine Theta and
c       Beta motion of measuring beam.
c
cccccccccccccccccccccccccccccccccccccccccccccccccccccccccccccccccccc
        REAL X(14), Y(14), Z(14), L1(14), L2(14), L3(14), ALPH(3,14),
     *     BET(3,14), THET(3,14),
     *     DX1(14), DX2(14), DY1(14), DY2(14)
        COMMON/COEFF/ AX(2,15,10), AY(2,15,10)
        COMMON/POINT/ POSX(15), POSY(15)
        COMMON/DIMEN/ a, b, c, DYSEP, DXSEP, sig1, sig2, rho1, rho2
        COMMON/PROBE/ D1, D2, D3, ALPHA, BETA
        CHARACTER*40, XLAB, ALPHLAB, BETLAB, THETLAB
        OPEN(UNIT = 1, NAME = 'YZMO.INP', STATUS = 'OLD')
        OPEN(UNIT = 2, NAME = 'YZMO.OUT', STATUS = 'NEW')
        XLAB = 'Step Number'       !Plot titles.
        ALPHLAB = 'Alpha (u rad)'
        BETLAB = 'Beta (u rad)'
        THETLAB = 'Theta (u rad)'
        CALL CONSTANT         ! Load linearization polynomials.
        CALL DIMEN            ! Load POSOR dimensions.
c
c               Read data.
c
        DO 5 I = 1, 14
           READ(1,10) Y(I), Z(I), X(I)
10         FORMAT(3F8.5)
5       CONTINUE
        DO 6 I = 1, 14
           READ(1,11) L1(I), L2(I), L3(I)
11         FORMAT(3F12.7)
6       CONTINUE
        DO 7 I = 1, 14
           READ(1,12) DX1(I), DY1(I), DX2(I), DY2(I)
12         FORMAT(4F12.7)
7       CONTINUE
c
c            Calculate initial conditions.
c
        L2(1) = L2(1) + .2       !Add offset due to electronics shift
        L3(1) = L3(1) + .3       !from voltage calibrated at.
        CALL PROBLIN( L1(1), L2(1), L3(1) )!Linearize probe readings.
        CALL ALBET(ALPHO, BETO) ! Det. initial ALPHA, BETA
        CALL DLINE(1, DX1(1), DY1(1), X1, Y1) !Linearize diode 1 readings.
        XD1 = -.566 - X1 !Det. global XY coordinates of LASERS on diodes.
        YD1 = 1.8 - Y1
        CALL DLINE(2, DX2(1), DY2(1), X2, Y2) !Linearize diode 2 readings.
        XD2 = -.566 - X2
        YD2 = -1.2 - Y2
        CALL DIST(XD1, YD1, DL1o)  !Det. initial dist. from LASERs to diodes.
        CALL DIST(XD2, YD2, DL2o)
        THETO = ATAN( (Y1-Y2-DYSEP)/(X1-X2-DXSEP) ) !Det. initial THETA.
        ALPH(3,1) = 1.   !Set plot X axis motion step number.
        BET(1,1) = -ATAN(Y(1)/31.43)  !Det. initial measured BETA.
        BET(3,1) = 1.
        THET(1,1) = -ATAN(Z(1)/31.43)  !Det. initial measured THETA.
        THET(3,1) = 1.
        WRITE(2,13)   !Write table header.
13      FORMAT(///5x,'YZ Motion Results With LASER Angle Offsets'
       *//5x,'All angles are in radians'//
       *5X,'ALPH(1,I) ALPH(2,I) BET(1,I)  BET(2,I)  THET(1,I) THET(2,I)'/
       */5X,'  0.        0.        0.        0.        0.        0. ')
```

```
C
C      Loop over data to find ALPHA, BETA, THETA.
C
       DO 100 I = 2, 14
          ALPH(3,I) = REAL(I)  !Set plot X axis motion step number.
          BET(1,I) = -ATAN(Y(I)/31.43)- BET(1,1)  !Det. measured BETA.
          BET(3,I) = REAL(I)
          THET(1,I) = -ATAN(Z(I)/31.43)- THET(1,1)  !Det. measured THETA.
          THET(3,I) = REAL(I)
          L2(I) = L2(I) + .2   !Add voltage offsets to probes.
          L3(I) = L3(I) + .3
          CALL PROBLIN( L1(I), L2(I), L3(I) )!Linearize probe readings.
          D1 = D1 + .133333*SIN(THET(2,I-1)) !Add POSOR flatness terms.
          D2 = D2 + .083333*SIN(THET(2,I-1))
          D3 = D3 - .083333*SIN(THET(2,I-1))
          CALL ALBET(ALPH(2,I), BET(2,I)) !Det. ALPHA, BETA.
          ALPH(2,I) = ALPH(2,I) - ALPHO   !Det. net ALPHA, BETA.
          BET(2,I) = BET(2,I) - BETO
          CALL DLINE(1, DX1(I), DY1(I), X1, Y1) !Linearize diode 1 readings.
          XD1 = -.566 - X1  !Det. global XY coordinates of LASERS on diodes.
          YD1 = 1.8 + Y1
          CALL DLINE(2, DX2(I), DY2(I), X2, Y2) !Linearize diode 2 readings.
          XD2 = -.566 - X2
          YD2 = -1.2 + Y2
          CALL DIST(XD1, YD1, DL1t) !Det. dist. from LASERs to diodes.
          CALL DIST(XD2, YD2, DL2t)
          DL1 = DL1t - DL1o  !Det. net LASER path length change.
          DL2 = DL2t - DL2o
          X1 = X1 + DL1*SIG1*COS(RHO1+THET(2,I-1)) !LASER angle offsets.
          Y1 = Y1 - DL1*SIG1*SIN(RHO1+THET(2,I-1))
          X2 = X2 + DL2*SIG2*COS(RHO2+THET(2,I-1))
          Y2 = Y2 + DL2*SIG2*SIN(RHO2+THET(2,I-1))
          RNUM = (Y1 - Y2 - DYSEP )*COS(ALPH(2,I))
          DNUM = (X1 - X2 - DXSEP)*COS(BET(2,I))
          THET(2,I) = ATAN(RNUM/DNUM) - THETO !Det. net THETA.
          WRITE(2,127) ALPH(1,I), ALPH(2,I), BET(1,I), BET(2,I),
     *     THET(1,I), THET(2,I)   !Record the answers.
127       FORMAT(5X,6(F8.6,2X))
100    CONTINUE
       DO 300 I = 2, 14     !Loop for standard deviations and plots.
          DIFB = BET(2,I) - BET(1,I)
          DIFA = ALPH(2,I) - ALPH(1,I)
          DIFT = THET(2,I) - THET(1,I)
          SUMA = SUMA + DIFA**2
          SUMB = SUMB + DIFB**2
          SUMT = SUMT + DIFT**2
          ALPH(1,I) = ALPH(1,I)/1.E-6    !Convert to microrads
          ALPH(2,I) = ALPH(2,I)/1.E-6
          BET(1,I) = BET(1,I)/1.E-6
          BET(2,I) = BET(2,I)/1.E-6
          THET(1,I) = THET(1,I)/1.E-6
          THET(2,I) = THET(2,I)/1.E-6
300    CONTINUE
       SIGA = SQRT(SUMA/12.)     !Det. sigmas.
       SIGB = SQRT(SUMB/12.)
       SIGT = SQRT(SUMT/12.)
       WRITE(2,117) SIGA, SIGB, SIGT
117    FORMAT(4X,'SIGA = ', F10.6,' SIGB = ',F10.6,' SIGT = ',F10.6)
       PRINT*, 'SIGA = ', SIGA,' SIGB = ',SIGB,' SIGT = ', SIGT
       ALPH(1,1) = 0.   !Set plot to start at GO.
       BET(1,1) = 0.
       THET(1,1) = 0.
       CALL QPICTR(ALPH,3,14,QY(1,2), QX(3), QXLAB(XLAB), QYLAB(ALPHLAB)
```

```
*    ,QLABEL(4) )     !Plot them points up.
 CALL QPICTR(BET,3,14,QY(1,2), QX(3), QXLAB(XLAB), QYLAB(BETLAB)
*    ,QLABEL(4) )
 CALL QPICTR(THET,3,14,QY(1,2), QX(3), QXLAB(XLAB), QYLAB(THETLAB)
*    ,QLABEL(4) )
 STOP                 !Fineesh.
 END                  !Its Miller time
```

```
cccccccccccccccccccccccccccccccccccccccccccccccccccccccccccccccccc
c
c      TWIS.FOR by Alex Slocum, Feb. 1, 1985. To determine motion
c      of measuring beam.
c
cccccccccccccccccccccccccccccccccccccccccccccccccccccccccccccccccc
      REAL Z1(15), Y(15), Z2(15), L1(15), L2(15), L3(15), ALPH(3,15),
     *THET(15), ZM(3,15), YM(3,15), DX1(15), DX2(15), DY1(15), DY2(15)
      COMMON/COEFF/ AX(2,15,10), AY(2,15,10)
      COMMON/POINT/ POSX(15), POSY(15)
      COMMON/DIMEN/ a, b, c, DYSEP, DXSEP, sig1, sig2, rho1, rho2
      COMMON/PROBE/ D1, D2, D3, ALPHA, BETA
      CHARACTER*40, XLAB, ALPHLAB, YLAB, ZLAB
      OPEN(UNIT = 1, NAME = 'TWIS.INP', STATUS = 'OLD')
      OPEN(UNIT = 2, NAME = 'TWIS.OUT', STATUS = 'NEW')
      XLAB = 'Step Number'    !Plot titles.
      YLAB = 'Y Motion (mils)'
      ZLAB = 'Z Motion (mils)'
      ALPHLAB = 'Alpha (u rad)'
      CALL CONSTANT          ! Load polynomials.
      CALL DIMEN             ! Load POSOR dimensions.
c
c             Read data.
c
      DO 5 I = 1, 15
         READ(1,10) Z1(I), Z2(I), Y(I)
10       FORMAT(3F8.5)
5     CONTINUE
      DO 6 I = 1, 15
         READ(1,11) L1(I), L2(I), L3(I)
11       FORMAT(3F12.7)
6     CONTINUE
      DO 7 I = 1, 15
         READ(1,12) DX1(I), DY1(I), DX2(I), DY2(I)
12       FORMAT(4F12.7)
7     CONTINUE
c
c        Calculate initial conditions.
c
      L2(1) = L2(1) + .2   !Add offset due to electronics shift
      L3(1) = L3(1) + .3   !from voltage calibrated at.
      CALL PROBLIN( L1(1), L2(1), L3(1) )!Linearize probe readings.
      CALL ALBET( ALPH(2,1), BETO ) !Det. initial ALPHA, BETA.
      CALL DLINE(1, DX1(1), DY1(1), X1, Y1) !Linearize diode readings.
      XD1 = -.566 - X1  !Det. global XY coordinates of LASERs on diodes.
      YD1 = 1.8 - Y1
      CALL DLINE(2, DX2(1), DY2(1), X2, Y2) !Linearize diode 2 readings.
      XD2 = -.566 - X2
      YD2 = -1.2 - Y2
      CALL DIST(XD1, YD1, DL1o)  !Det. initial dist. from LASERs to diodes.
      CALL DIST(XD2, YD2, DL2o)
      CALL DIST(0., 0., YM(2,1)) !Det. initial dist. between coord. systems.
      THETO = ATAN( (Y1 - Y2 - DYSEP)/(X1 - X2-DXSEP)) !Det. initial theta.
      ALPH(1,1) = ATAN( ( Z1(1) - Z2(1) )/3.5 ) !Det. initial measured Alpha.
      ALPH(3,1) = 1.  !Set plot X axis motion step number.
      ZM(1,1) = Z2(1) + 1.022*( Z1(1) - Z2(1) )/3.5  !Det initial Z and Y
      ZM(2,1) = - (Y1+Y2)/2.   !measured positions.
      ZM(3,1) = 1.
      YM(3,1) = 1.
c
c     Loop over data to find ALPHA, Y, Z.
c
      DO 100 I = 2, 15
```

```
         ALPH(3,I) = REAL(I)  !Set plot X axis motion step number.
         YM(3,I) = REAL(I)
         ZM(3,I) = REAL(I)
         ALPH(1,I) = ATAN((Z1(I) - Z2(I))/(3.5-Y(I))) - ALPH(1,1) !Alpha.
         L2(I) = L2(I) + .2  !Add voltage offsets to probes.
         L3(I) = L3(I) + .3
         CALL PROBLIN( L1(I), L2(I), L3(I) )  !Linearize probe readings.
         D1 = D1 + .133333*SIN(THET(I-1)) !Add POSOR flatness terms.
         D2 = D2 + .083333*SIN(THET(I-1))
         D3 = D3 - .083333*SIN(THET(I-1))
         CALL ALBET(ALPH(2,I), BETA) !Det. ALPHA, BETA from POSOR readings.
         ALPH(2,I) = ALPH(2,I) - ALPH(2,1)   !Subtract initial readings.
         BET = BETA - BETO
         CALL DLINE(1, DX1(I), DY1(I), X1, Y1) !Linearize diode 1 readings
         XD1 = -.566 - X1  !Set. global XY coordinates of LASERs on diodes.
         YD1 = 1.8 - Y1
         CALL DLINE(2, DX2(I), DY2(I), X2, Y2) !Linearize diode 2 readings.
         XD2 = -.566 - X2
         YD2 = -1.2 - Y2
         CALL DIST(XD1, YD1, DL1t)  !Det. dist. from LASERs to diodes.
         CALL DIST(XD2, YD2, DL2t)
         CALL DIST(0., 0., DY)  !Det dist. between POSOR coord. systems.
         DL1 = DL1t - DL1o   !Det. net motion.
         DL2 = DL2t - DL2o
         X1 = X1 + DL1*SIG1*COS(RHO1+THET(I-1))  !Laser angle offsets.
         Y1 = Y1 - DL1*SIG1*SIN(RHO1+THET(I-1))
         X2 = X2 + DL2*SIG2*COS(RHO2+THET(I-1))
         Y2 = Y2 + DL2*SIG2*SIN(RHO2+THET(I-1))
         RNUM = (Y1 - Y2 - DYSEP )*COS(ALPH(2,I))
         DNUM = (X1 - X2 - DXSEP)*COS(BET)
         THET(I) = ATAN(RNUM/DNUM) - THETO   !Det. net Theta from POSOR.
         YM(1,I) = Y(I) + 1.34*ALPH(1,I)   !Det. net measured Y motion.
         YM(2,I) = - DY + 33.4*BET + YM(2,1)  !Det. net POSOR Y motion.
         ZM(1,I) = Z2(I) + 1.022*( Z1(I) - Z2(I))/(3.5-Y(I)) - ZM(1,1)
         ZM(2,I) = - (Y1+ Y2)/2. - ZM(2,1) - 36.1*THET(I)
100   CONTINUE
      WRITE(2,13)
13    FORMAT(///5xX,'Twist Motion Results'//
     * 5X,'All dimensions are in inches and radians'//
     * 5X,'ALPH(1,I)  ALPH(2,I)  ZM(1,I)   ZM(2,I)   YM(1,I)   YM(2,I)'
     *//5x,'    0.        0.        0.        0.        0.        0.')
      DO 300 I = 2, 15  !Loop for statistics.
       WRITE(2,127) ALPH(1,I),ALPH(2,I),ZM(1,I),ZM(2,I),YM(1,I),YM(2,I)
127    FORMAT( 4X, 6(F9.6,1X) )
         DIFA = ALPH(2,I) - ALPH(1,I)
         DIFZ = ZM(2,I) - ZM(1,I)
         DIFY = YM(2,I) - YM(1,I)
         SUMA = SUMA + DIFA**2
         SUMZ = SUMZ + DIFZ**2
         SUMY = SUMY + DIFY**2
         ALPH(1,I) = ALPH(1,I)/1.E-6    !Convert to microrads.
         ALPH(2,I) = ALPH(2,I)/1.E-6
         ZM(2,I) = ZM(2,I)/.001   !Convert to mils.
         ZM(1,I) = ZM(1,I)/.001
         YM(2,I) = YM(2,I)/.001
         YM(1,I) = YM(1,I)/.001
300   CONTINUE
      SIGA = SQRT(SUMA/13.)   !Det. sigmas.
      SIGZ = SQRT(SUMZ/13.)
      SIGY = SQRT(SUMY/13.)
      WRITE(2,117) SIGA, SIGZ, SIGY
117    FORMAT(4X,'SIGA = ', F10.6,' SIGZ = ',F10.6,' SIGY = ',F10.6)
      PRINT*, 'SIGA = ', SIGA,' SIGZ = ',SIGZ,' SIGY = ', SIGY
```

```
      ALPH(1,1) = 0.
      ZM(1,1) = 0.
      YM(1,1) = 0.
      CALL QPICTR(ALPH,3,15,QY(1,2), QX(3), QXLAB(XLAB), QYLAB(ALPHLAB)
     *   ,QLABEL(4) )     !Plot them babies up.
      CALL QPICTR(ZM,3,15,QY(1,2), QX(3), QXLAB(XLAB), QYLAB(ZLAB)
     *   ,QLABEL(4) )
      CALL QPICTR(YM,3,15,QY(1,2), QX(3), QXLAB(XLAB), QYLAB(YLAB)
     *   ,QLABEL(4) )
      STOP                    !Fineesh
      END                      !Its Miller time
```

```
cccccccccccccccccccccccccccccccccccccccccccccccccccccccccccccccccccccc
C
C      GEN.FOR by Alex Slocum, Feb. 1, 1985. To determine motion
C      of measuring beam.
C
cccccccccccccccccccccccccccccccccccccccccccccccccccccccccccccccccccccc
       REAL Z1(10), Y(10), Z2(10), L1(10), L2(10), L3(10), ALPH(3,10),
      *THET(10), ZM(3,10), YM(3,10), DX1(10), DX2(10), DY1(10), DY2(10)
       COMMON/COEFF/ AX(2,15,10), AY(2,15,10)
       COMMON/POINT/ POSX(15), POSY(15)
       COMMON/DIMEN/ a, b, c, DYSEP, DXSEP, sig1, sig2, rho1, rho2
       COMMON/PROBE/ D1, D2, D3, ALPHA, BETA
       CHARACTER*40, XLAB, ALPHLAB, YLAB, ZLAB
       OPEN(UNIT = 1, NAME = 'GEN.INP', STATUS = 'OLD')
       OPEN(UNIT = 2, NAME = 'GEN.OUT', STATUS = 'NEW')
       XLAB = 'Step Number'    !Plot titles.
       YLAB = 'Y Motion (mils)'
       ZLAB = 'Z Motion (mils)'
       ALPHLAB = 'Alpha (u rad)'
       CALL CONSTANT         ! Load polynomials.
       CALL DIMEN            ! Load POSOR dimensions.
C
C              Read data.
C
       DO 5 I = 1, 10
          READ(1,10) Z1(I), Z2(I), Y(I)
10        FORMAT(3F8.5)
5      CONTINUE
       DO 6 I = 1, 10
          READ(1,11) L1(I), L2(I), L3(I)
11        FORMAT(3F12.7)
6      CONTINUE
       DO 7 I = 1, 10
          READ(1,12) DX1(I), DY1(I), DX2(I), DY2(I)
12        FORMAT(4F12.7)
7      CONTINUE
C
C          Calculate initial conditions.
C
       L2(1) = L2(1) + .2    !Add offset due to electronics shift
       L3(1) = L3(1) + .3    !from voltage calibrated at.
       CALL PROBLIN( L1(1), L2(1), L3(1) )!Linearize probe readings.
       CALL ALBET( ALPH(2,1), BETO ) !Det. initial ALPHA, BETA.
       CALL DLINE(1, DX1(1), DY1(1), X1, Y1) !Linearize diode readings.
       XD1 = -.566 - X1  !Det. global XY coordinates of LASERs on diodes.
       YD1 = 1.8 - Y1
       CALL DLINE(2, DX2(1), DY2(1), X2, Y2) !Linearize diode 2 readings.
       XD2 = -.566 - X2
       YD2 = -1.2 - Y2
       CALL DIST(XD1, YD1, DL1o)  !Det. initial dist. from LASERs to diodes.
       CALL DIST(XD2, YD2, DL2o)
       CALL DIST(0., 0., YM(2,1)) !Det. initial dist. between coord. systems.
       THETO = ATAN( (Y1 - Y2 - DYSEP)/(X1 - X2-DXSEP)) !Det. initial theta.
       ALPH(1,1) = ATAN( ( Z1(1) - Z2(1) )/3.5 ) !Det. initial measured Alpha.
       ALPH(3,1) = 1.  !Set plot X axis motion step number.
       ZM(1,1) = Z2(1) + 1.022*( Z1(1) - Z2(1) )/3.5  !Det initial Z and Y
       ZM(2,1) = - (Y1+Y2)/2.   !measured positions.
       ZM(3,1) = 1.
       YM(3,1) = 1.
C
C      Loop over data to find ALPHA, Y, Z.
C
       DO 100 I = 2, 10
```

```
         ALPH(3,I) = REAL(I)  !Set plot X axis motion step number.
         YM(3,I) = REAL(I)
         ZM(3,I) = REAL(I)
         ALPH(1,I) = ATAN((Z1(I) - Z2(I))/(3.5-Y(I))) - ALPH(1,1) !Alpha.
         L2(I) = L2(I) + .2  !Add voltage offsets to probes.
         L3(I) = L3(I) + .3
         CALL PROBLIN( L1(I), L2(I), L3(I) )  !Linearize probe readings.
         D1 = D1 + .133333*SIN(THET(I-1)) !Add POSOR flatness terms.
         D2 = D2 + .083333*SIN(THET(I-1))
         D3 = D3 - .083333*SIN(THET(I-1))
         CALL ALBET(ALPH(2,I), BETA) !Det. ALPHA, BETA from POSOR readings.
         ALPH(2,I) = ALPH(2,I) - ALPH(2,1)   !Subtract initial readings.
         BET = BETA - BETO
         CALL DLINE(1, DX1(I), DY1(I), X1, Y1) !Linearize diode 1 readings
         XD1 = -.566 - X1  !Set. global XY coordinates of LASERs on diodes.
         YD1 = 1.8 - Y1
         CALL DLINE(2, DX2(I), DY2(I), X2, Y2) !Linearize diode 2 readings.
         XD2 = -.566 - X2
         YD2 = -1.2 - Y2
         CALL DIST(XD1, YD1, DL1t)  !Det. dist. from LASERs to diodes.
         CALL DIST(XD2, YD2, DL2t)
         CALL DIST(0., 0., DY)  !Det dist. between POSOR coord. systems.
         DL1 = DL1t - DL1o   !Det. net motion.
         DL2 = DL2t - DL2o
         X1 = X1 + DL1*SIG1*COS(RHO1+THET(I-1))  !Laser angle offsets.
         Y1 = Y1 - DL1*SIG1*SIN(RHO1+THET(I-1))
         X2 = X2 + DL2*SIG2*COS(RHO2+THET(I-1))
         Y2 = Y2 + DL2*SIG2*SIN(RHO2+THET(I-1))
         RNUM = (Y1 - Y2 - DYSEP )*COS(ALPH(2,I))
         DNUM = (X1 - X2 - DXSEP)*COS(BET)
         THET(I) = ATAN(RNUM/DNUM) - THETO   !Det. net Theta from POSOR.
         YM(1,I) = Y(I) + 1.34*ALPH(1,I)   !Det. net measured Y motion.
         YM(2,I) = - DY + 33.4*BET + YM(2,1)  !Det. net POSOR Y motion.
         ZM(1,I) = Z2(I) + 1.022*( Z1(I) - Z2(I))/(3.5-Y(I)) - ZM(1,1)
         ZM(2,I) = - (Y1+ Y2)/2. - ZM(2,1) - 36.1*THET(I)
100   CONTINUE
      WRITE(2,13)
13    FORMAT(///5xX,'General Motion Results'//
     * 5X,'All dimensions are in inches and radians'//
     * 5X,'ALPH(1,I)  ALPH(2,I)   ZM(1,I)   ZM(2,I)   YM(1,I)   YM(2,I)'
     *//5x,'    0.        0.        0.        0.        0.        0.')
      DO 300 I = 2, 10  !Loop for statistics.
       WRITE(2,127) ALPH(1,I),ALPH(2,I),ZM(1,I),ZM(2,I),YM(1,I),YM(2,I)
127    FORMAT( 4X, 6(F9.6,1X) )
         DIFA = ALPH(2,I) - ALPH(1,I)
         DIFZ = ZM(2,I) - ZM(1,I)
         DIFY = YM(2,I) - YM(1,I)
         SUMA = SUMA + DIFA**2
         SUMZ = SUMZ + DIFZ**2
         SUMY = SUMY + DIFY**2
         ALPH(1,I) = ALPH(1,I)/1.E-6    !Convert to microrads.
         ALPH(2,I) = ALPH(2,I)/1.E-6
         ZM(2,I) = ZM(2,I)/.001    !Convert to mils.
         ZM(1,I) = ZM(1,I)/.001
         YM(2,I) = YM(2,I)/.001
         YM(1,I) = YM(1,I)/.001
300   CONTINUE
      SIGA = SQRT(SUMA/8.)    !Det. sigmas.
      SIGZ = SQRT(SUMZ/8.)
      SIGY = SQRT(SUMY/8.)
      WRITE(2,117) SIGA, SIGZ, SIGY
117    FORMAT(4X,'SIGA = ', F10.6,' SIGZ = ',F10.6,' SIGY = ',F10.6)
      PRINT*, 'SIGA = ', SIGA,' SIGZ = ',SIGZ,' SIGY = ', SIGY
```

```
      ALPH(1,1) = 0.
      ZM(1,1) = 0.
      YM(1,1) = 0.
      CALL QPICTR(ALPH,3,10,QY(1,2), QX(3), QXLAB(XLAB), QYLAB(ALPHLAB)
     *   ,QLABEL(4) )     !Plot them babies up.
      CALL QPICTR(ZM,3,10,QY(1,2), QX(3), QXLAB(XLAB), QYLAB(ZLAB)
     *   ,QLABEL(4) )
      CALL QPICTR(YM,3,10,QY(1,2), QX(3), QXLAB(XLAB), QYLAB(YLAB)
     *   ,QLABEL(4) )
      STOP                    !Fineesh
      END                      !Its Miller time
```

```
SUBROUTINE CONSTANT
COMMON/COEFF/ AX(2,15,10), AY(2,15,10)
COMMON/POINT/ POSX(15), POSY(15)
AX(1, 1, 1) = 0.2980584
AX(1, 1, 2) = 0.2601558
AX(1, 1, 3) = 0.0296409
AX(1, 1, 4) = 0.0763846
AX(1, 1, 5) = -.0280014
AX(1, 1, 6) = 0.0198545
AX(1, 1, 7) = -.0775906
AX(1, 1, 8) = -.0546077
AX(1, 1, 9) = 0.1299897
AX(1, 1,10) = 0.1771148
AX(1, 2, 1) = 0.2969800
AX(1, 2, 2) = 0.2647132
AX(1, 2, 3) = 0.0332551
AX(1, 2, 4) = 0.0532803
AX(1, 2, 5) = -.0542051
AX(1, 2, 6) = 0.0728458
AX(1, 2, 7) = 0.0161345
AX(1, 2, 8) = -.0306525
AX(1, 2, 9) = 0.0249807
AX(1, 2,10) = 0.0770690
AX(1, 3, 1) = 0.2963723
AX(1, 3, 2) = 0.2700339
AX(1, 3, 3) = 0.0315351
AX(1, 3, 4) = 0.0310375
AX(1, 3, 5) = -.0746478
AX(1, 3, 6) = 0.1180483
AX(1, 3, 7) = 0.1776002
AX(1, 3, 8) = 0.0501811
AX(1, 3, 9) = -.2227452
AX(1, 3,10) = -.1505706
AX(1, 4, 1) = 0.2962838
AX(1, 4, 2) = 0.2745650
AX(1, 4, 3) = 0.0186398
AX(1, 4, 4) = 0.0218596
AX(1, 4, 5) = 0.0099047
AX(1, 4, 6) = 0.1618608
AX(1, 4, 7) = -.0545973
AX(1, 4, 8) = -.1005216
AX(1, 4, 9) = 0.0036769
AX(1, 4,10) = 0.0333497
AX(1, 5, 1) = 0.2961553
AX(1, 5, 2) = 0.2707391
AX(1, 5, 3) = 0.0121079
AX(1, 5, 4) = 0.0140342
AX(1, 5, 5) = 0.0274019
AX(1, 5, 6) = 0.1952071
AX(1, 5, 7) = -.0489632
AX(1, 5, 8) = -.1588838
AX(1, 5, 9) = -.0445954
AX(1, 5,10) = 0.0411105
AX(1, 6, 1) = 0.2957592
AX(1, 6, 2) = 0.2820121
AX(1, 6, 3) = 0.0172161
AX(1, 6, 4) = 0.0129517
AX(1, 6, 5) = -.0479863
AX(1, 6, 6) = 0.1619599
AX(1, 6, 7) = 0.2053677
AX(1, 6, 8) = 0.0006622
AX(1, 6, 9) = -.3037178
AX(1, 6,10) = -.1600748
```

```
AX(1, 7, 1) = 0.2954522
AX(1, 7, 2) = 0.2033942
AX(1, 7, 3) = 0.0114025
AX(1, 7, 4) = 0.0163611
AX(1, 7, 5) = 0.0164263
AX(1, 7, 6) = 0.1030085
AX(1, 7, 7) = -.0723609
AX(1, 7, 8) = -.2047517
AX(1, 7, 9) = 0.0511096
AX(1, 7,10) = 0.1673899
AX(1, 8, 1) = 0.2950118
AX(1, 8, 2) = 0.2839868
AX(1, 8, 3) = 0.0175507
AX(1, 8, 4) = 0.0132031
AX(1, 8, 5) = -.0760167
AX(1, 8, 6) = 0.1665000
AX(1, 8, 7) = 0.3164701
AX(1, 8, 8) = 0.0293535
AX(1, 8, 9) = -.4423404
AX(1, 8,10) = -.2595607
AX(1, 9, 1) = 0.2946445
AX(1, 9, 2) = 0.2814013
AX(1, 9, 3) = 0.0170533
AX(1, 9, 4) = 0.0341375
AX(1, 9, 5) = -.0674092
AX(1, 9, 6) = 0.0912947
AX(1, 9, 7) = 0.2392187
AX(1, 9, 8) = 0.0991373
AX(1, 9, 9) = -.3077453
AX(1, 9,10) = -.2101355
AX(1,10, 1) = 0.2941400
AX(1,10, 2) = 0.2787178
AX(1,10, 3) = 0.0075042
AX(1,10, 4) = 0.0223446
AX(1,10, 5) = 0.0433440
AX(1,10, 6) = 0.2621886
AX(1,10, 7) = -.1515501
AX(1,10, 8) = -.4617870
AX(1,10, 9) = 0.1110539
AX(1,10,10) = 0.3534077
AX(1,11, 1) = 0.2936103
AX(1,11, 2) = 0.2740105
AX(1,11, 3) = 0.0106702
AX(1,11, 4) = 0.0314745
AX(1,11, 5) = 0.0131239
AX(1,11, 6) = 0.2470635
AX(1,11, 7) = -.0554172
AX(1,11, 8) = -.4209151
AX(1,11, 9) = 0.0230703
AX(1,11,10) = 0.3041218
AX(1,12, 1) = 0.2931002
AX(1,12, 2) = 0.2676167
AX(1,12, 3) = 0.0030136
AX(1,12, 4) = 0.0557657
AX(1,12, 5) = 0.1169735
AX(1,12, 6) = 0.2078738
AX(1,12, 7) = -.4203070
AX(1,12, 8) = -.5154741
AX(1,12, 9) = 0.4088276
AX(1,12,10) = 0.5256600
AX(1,13, 1) = 0.2924610
AX(1,13, 2) = 0.2630242
AX(1,13, 3) = 0.0199279
```

```
AX(1,13, 4) = 0.0724146
AX(1,13, 5) = -.0025905
AX(1,13, 6) = 0.0305074
AX(1,13, 7) = 0.3120301
AX(1,13, 8) = 0.1932538
AX(1,13, 9) = -.4069523
AX(1,13,10) = -.3243430
AX(1,14, 1) = 0.2917405
AX(1,14, 2) = 0.2500253
AX(1,14, 3) = 0.0163360
AX(1,14, 4) = 0.0998707
AX(1,14, 5) = 0.0050597
AX(1,14, 6) = -.0191397
AX(1,14, 7) = -.0657429
AX(1,14, 8) = 0.0172542
AX(1,14, 9) = 0.0399395
AX(1,14,10) = 0.0402138
AX(1,15, 1) = 0.2913544
AX(1,15, 2) = 0.2599675
AX(1,15, 3) = 0.0068359
AX(1,15, 4) = 0.0352724
AX(1,15, 5) = 0.0735290
AX(1,15, 6) = 0.2849523
AX(1,15, 7) = -.2325023
AX(1,15, 8) = -.5879212
AX(1,15, 9) = 0.1799311
AX(1,15,10) = 0.4600654
AY(1, 1, 1) = 0.2555282
AY(1, 1, 2) = -.2619039
AY(1, 1, 3) = -.0008161
AY(1, 1, 4) = -.0553101
AY(1, 1, 5) = -.0328755
AY(1, 1, 6) = -.0138224
AY(1, 1, 7) = 0.0976970
AY(1, 1, 8) = -.0678674
AY(1, 1, 9) = -.0882047
AY(1, 1,10) = 0.0060002
AY(1, 2, 1) = 0.2548558
AY(1, 2, 2) = -.2618161
AY(1, 2, 3) = -.0090454
AY(1, 2, 4) = -.0513244
AY(1, 2, 5) = 0.0282253
AY(1, 2, 6) = -.1112229
AY(1, 2, 7) = -.0453418
AY(1, 2, 8) = 0.1874387
AY(1, 2, 9) = 0.0250431
AY(1, 2,10) = -.1896955
AY(1, 3, 1) = 0.2539475
AY(1, 3, 2) = -.2663339
AY(1, 3, 3) = -.0088770
AY(1, 3, 4) = -.0303122
AY(1, 3, 5) = 0.0273599
AY(1, 3, 6) = -.1432628
AY(1, 3, 7) = -.0123480
AY(1, 3, 8) = 0.1264988
AY(1, 3, 9) = -.0238405
AY(1, 3,10) = -.0859337
AY(1, 4, 1) = 0.2527574
AY(1, 4, 2) = -.2696145
AY(1, 4, 3) = 0.0033480
AY(1, 4, 4) = -.0475653
AY(1, 4, 5) = -.0461925
AY(1, 4, 6) = -.0282190
```

```
AY(1, 4, 7) = 0.1502071
AY(1, 4, 8) = -.1215042
AY(1, 4, 9) = -.1352405
AY(1, 4,10) = 0.0070029
AY(1, 5, 1) = 0.2523114
AY(1, 5, 2) = -.2750277
AY(1, 5, 3) = -.0063547
AY(1, 5, 4) = -.0293241
AY(1, 5, 5) = 0.0360666
AY(1, 5, 6) = -.0998442
AY(1, 5, 7) = -.0621462
AY(1, 5, 8) = 0.0710273
AY(1, 5, 9) = 0.0356540
AY(1, 5,10) = -.0970046
AY(1, 6, 1) = 0.2516328
AY(1, 6, 2) = -.2810342
AY(1, 6, 3) = 0.0038070
AY(1, 6, 4) = -.0135649
AY(1, 6, 5) = -.0434996
AY(1, 6, 6) = -.1608172
AY(1, 6, 7) = 0.1412556
AY(1, 6, 8) = 0.1747301
AY(1, 6, 9) = -.1260531
AY(1, 6,10) = -.1466413
AY(1, 7, 1) = 0.2514281
AY(1, 7, 2) = -.2825607
AY(1, 7, 3) = 0.0065339
AY(1, 7, 4) = -.0700988
AY(1, 7, 5) = -.0897911
AY(1, 7, 6) = 0.1819176
AY(1, 7, 7) = 0.2942420
AY(1, 7, 8) = -.5255150
AY(1, 7, 9) = -.2683747
AY(1, 7,10) = 0.3266056
AY(1, 8, 1) = 0.2514382
AY(1, 8, 2) = -.2879876
AY(1, 8, 3) = 0.0008783
AY(1, 8, 4) = -.0183051
AY(1, 8, 5) = -.0236987
AY(1, 8, 6) = -.1166476
AY(1, 8, 7) = 0.0517444
AY(1, 8, 8) = 0.1400778
AY(1, 8, 9) = -.0200595
AY(1, 8,10) = -.1747443
AY(1, 9, 1) = 0.2513945
AY(1, 9, 2) = -.2095371
AY(1, 9, 3) = 0.0023684
AY(1, 9, 4) = -.0030069
AY(1, 9, 5) = -.0415000
AY(1, 9, 6) = -.2314313
AY(1, 9, 7) = 0.1014693
AY(1, 9, 8) = 0.4441286
AY(1, 9, 9) = -.0662435
AY(1, 9,10) = -.4366342
AY(1,10, 1) = 0.2514127
AY(1,10, 2) = -.2083015
AY(1,10, 3) = -.0039627
AY(1,10, 4) = -.0306927
AY(1,10, 5) = 0.0057733
AY(1,10, 6) = 0.0068897
AY(1,10, 7) = -.0196668
AY(1,10, 8) = -.2553380
AY(1,10, 9) = 0.0294759
```

```
AY(1,10,10) = 0.1090723
AY(1,11, 1) = 0.2513775
AY(1,11, 2) = -.2054440
AY(1,11, 3) = -.0034795
AY(1,11, 4) = -.0309035
AY(1,11, 5) = -.0090290
AY(1,11, 6) = -.0503598
AY(1,11, 7) = 0.0396569
AY(1,11, 8) = -.0952796
AY(1,11, 9) = -.0207961
AY(1,11,10) = 0.0506657
AY(1,12, 1) = 0.2512127
AY(1,12, 2) = -.2797641
AY(1,12, 3) = -.0015945
AY(1,12, 4) = -.0705772
AY(1,12, 5) = -.0316460
AY(1,12, 6) = 0.1214240
AY(1,12, 7) = 0.1106227
AY(1,12, 8) = -.4442050
AY(1,12, 9) = -.1124995
AY(1,12,10) = 0.3063926
AY(1,13, 1) = 0.2510104
AY(1,13, 2) = -.2750536
AY(1,13, 3) = -.0014689
AY(1,13, 4) = -.0780332
AY(1,13, 5) = -.0166026
AY(1,13, 6) = 0.0912520
AY(1,13, 7) = 0.0456980
AY(1,13, 8) = -.3332716
AY(1,13, 9) = -.0275296
AY(1,13,10) = 0.2165535
AY(1,14, 1) = 0.2507192
AY(1,14, 2) = -.2726530
AY(1,14, 3) = 0.0051293
AY(1,14, 4) = -.0494674
AY(1,14, 5) = -.0656407
AY(1,14, 6) = -.1293776
AY(1,14, 7) = 0.1867055
AY(1,14, 8) = 0.2104615
AY(1,14, 9) = -.1586208
AY(1,14,10) = -.2124476
AY(1,15, 1) = 0.2504454
AY(1,15, 2) = -.2698243
AY(1,15, 3) = 0.0023932
AY(1,15, 4) = -.0509329
AY(1,15, 5) = -.0206994
AY(1,15, 6) = -.1067534
AY(1,15, 7) = 0.0410704
AY(1,15, 8) = 0.1342392
AY(1,15, 9) = -.0248087
AY(1,15,10) = -.1326632
AX(2, 1, 1) = 0.2516077
AX(2, 1, 2) = 0.2629546
AX(2, 1, 3) = -.0232926
AX(2, 1, 4) = 0.0530706
AX(2, 1, 5) = 0.0759379
AX(2, 1, 6) = 0.0286953
AX(2, 1, 7) = -.1549870
AX(2, 1, 8) = -.0092005
AX(2, 1, 9) = 0.1132813
AX(2, 1,10) = 0.0586300
AX(2, 2, 1) = 0.2514069
AX(2, 2, 2) = 0.2620479
```

```
AX(2, 2, 3) = -.0291534
AX(2, 2, 4) = 0.0660380
AX(2, 2, 5) = 0.1250347
AX(2, 2, 6) = 0.0070064
AX(2, 2, 7) = -.2706129
AX(2, 2, 8) = 0.0350477
AX(2, 2, 9) = 0.2069484
AX(2, 2,10) = 0.0169956
AX(2, 3, 1) = 0.2500268
AX(2, 3, 2) = 0.2507211
AX(2, 3, 3) = -.0163294
AX(2, 3, 4) = 0.1072338
AX(2, 3, 5) = 0.0763478
AX(2, 3, 6) = -.1501073
AX(2, 3, 7) = -.1944756
AX(2, 3, 8) = 0.3705694
AX(2, 3, 9) = 0.1555769
AX(2, 3,10) = -.2317767
AX(2, 4, 1) = 0.2488076
AX(2, 4, 2) = 0.2597455
AX(2, 4, 3) = -.0058583
AX(2, 4, 4) = 0.0803161
AX(2, 4, 5) = 0.0235780
AX(2, 4, 6) = -.0137225
AX(2, 4, 7) = -.0663400
AX(2, 4, 8) = 0.1402770
AX(2, 4, 9) = 0.0506081
AX(2, 4,10) = -.0960549
AX(2, 5, 1) = 0.2474329
AX(2, 5, 2) = 0.2576582
AX(2, 5, 3) = -.0010392
AX(2, 5, 4) = 0.1046656
AX(2, 5, 5) = 0.0182279
AX(2, 5, 6) = -.1407164
AX(2, 5, 7) = -.0608417
AX(2, 5, 8) = 0.4403518
AX(2, 5, 9) = 0.0447742
AX(2, 5,10) = -.3238364
AX(2, 6, 1) = 0.2463868
AX(2, 6, 2) = 0.2507332
AX(2, 6, 3) = 0.0039885
AX(2, 6, 4) = 0.0928909
AX(2, 6, 5) = -.0141967
AX(2, 6, 6) = -.1067998
AX(2, 6, 7) = 0.0453659
AX(2, 6, 8) = 0.4048671
AX(2, 6, 9) = -.0577312
AX(2, 6,10) = -.3022132
AX(2, 7, 1) = 0.2454442
AX(2, 7, 2) = 0.2610221
AX(2, 7, 3) = 0.0027464
AX(2, 7, 4) = 0.0811234
AX(2, 7, 5) = -.0027161
AX(2, 7, 6) = -.0979461
AX(2, 7, 7) = 0.0370127
AX(2, 7, 8) = 0.4126629
AX(2, 7, 9) = -.0657022
AX(2, 7,10) = -.2970543
AX(2, 8, 1) = 0.2444817
AX(2, 8, 2) = 0.2629135
AX(2, 8, 3) = 0.0007276
AX(2, 8, 4) = 0.0656676
AX(2, 8, 5) = 0.0166096
```

```
AX(2, 8, 6) = -.0504893
AX(2, 8, 7) = -.0129590
AX(2, 8, 8) = 0.3526464
AX(2, 8, 9) = -.0240396
AX(2, 8,10) = -.2503222
AX(2, 9, 1) = 0.2439011
AX(2, 9, 2) = 0.2647444
AX(2, 9, 3) = 0.0000158
AX(2, 9, 4) = 0.0441674
AX(2, 9, 5) = 0.0125955
AX(2, 9, 6) = 0.0326315
AX(2, 9, 7) = 0.0029260
AX(2, 9, 8) = 0.1696762
AX(2, 9, 9) = -.0376166
AX(2, 9,10) = -.1150427
AX(2,10, 1) = 0.2439945
AX(2,10, 2) = 0.2655633
AX(2,10, 3) = -.0000649
AX(2,10, 4) = 0.0250088
AX(2,10, 5) = 0.0003447
AX(2,10, 6) = 0.1226561
AX(2,10, 7) = 0.0453197
AX(2,10, 8) = -.0144466
AX(2,10, 9) = -.0740992
AX(2,10,10) = 0.0145682
AX(2,11, 1) = 0.2440701
AX(2,11, 2) = 0.2631835
AX(2,11, 3) = -.0013296
AX(2,11, 4) = 0.0324976
AX(2,11, 5) = -.0065224
AX(2,11, 6) = 0.1198218
AX(2,11, 7) = 0.0550911
AX(2,11, 8) = -.0485733
AX(2,11, 9) = -.0729574
AX(2,11,10) = 0.0497322
AX(2,12, 1) = 0.2441230
AX(2,12, 2) = 0.2605130
AX(2,12, 3) = -.0002412
AX(2,12, 4) = 0.0341499
AX(2,12, 5) = -.0132508
AX(2,12, 6) = 0.1535754
AX(2,12, 7) = 0.0509563
AX(2,12, 8) = -.1608723
AX(2,12, 9) = -.0565705
AX(2,12,10) = 0.1367312
AX(2,13, 1) = 0.2430560
AX(2,13, 2) = 0.2564610
AX(2,13, 3) = 0.0017906
AX(2,13, 4) = 0.0596554
AX(2,13, 5) = -.0213490
AX(2,13, 6) = 0.0613017
AX(2,13, 7) = 0.0441417
AX(2,13, 8) = -.0229987
AX(2,13, 9) = -.0348916
AX(2,13,10) = 0.0520762
AX(2,14, 1) = 0.2436372
AX(2,14, 2) = 0.2524012
AX(2,14, 3) = 0.0055349
AX(2,14, 4) = 0.0002985
AX(2,14, 5) = -.0497720
AX(2,14, 6) = -.0014250
AX(2,14, 7) = 0.1062200
AX(2,14, 8) = 0.0237333
```

```
AX(2,14, 9) = -.0011706
AX(2,14,10) = 0.0544401
AX(2,15, 1) = 0.2434057
AX(2,15, 2) = 0.2512256
AX(2,15, 3) = 0.0022527
AX(2,15, 4) = 0.0649102
AX(2,15, 5) = -.0310991
AX(2,15, 6) = 0.0553071
AX(2,15, 7) = 0.0597575
AX(2,15, 8) = -.0902346
AX(2,15, 9) = -.0423222
AX(2,15,10) = 0.1319010
AY(2, 1, 1) = 0.2455057
AY(2, 1, 2) = -.2551262
AY(2, 1, 3) = -.0071268
AY(2, 1, 4) = -.0494301
AY(2, 1, 5) = 0.0064183
AY(2, 1, 6) = -.0045460
AY(2, 1, 7) = -.0007463
AY(2, 1, 8) = 0.0455974
AY(2, 1, 9) = 0.0110062
AY(2, 1,10) = -.0429936
AY(2, 2, 1) = 0.2457513
AY(2, 2, 2) = -.2520208
AY(2, 2, 3) = -.0067263
AY(2, 2, 4) = -.0755741
AY(2, 2, 5) = -.0023173
AY(2, 2, 6) = -.0235333
AY(2, 2, 7) = 0.0183354
AY(2, 2, 8) = -.0640105
AY(2, 2, 9) = -.0030720
AY(2, 2,10) = 0.0398183
AY(2, 3, 1) = 0.2458622
AY(2, 3, 2) = -.2498406
AY(2, 3, 3) = 0.0011828
AY(2, 3, 4) = -.0936006
AY(2, 3, 5) = -.0628654
AY(2, 3, 6) = 0.0213523
AY(2, 3, 7) = 0.1646969
AY(2, 3, 8) = -.1542903
AY(2, 3, 9) = -.1171982
AY(2, 3,10) = 0.1028983
AY(2, 4, 1) = 0.2458847
AY(2, 4, 2) = -.2494340
AY(2, 4, 3) = 0.0004154
AY(2, 4, 4) = -.1000600
AY(2, 4, 5) = -.0320568
AY(2, 4, 6) = 0.0396755
AY(2, 4, 7) = 0.0616606
AY(2, 4, 8) = -.2057250
AY(2, 4, 9) = -.0202060
AY(2, 4,10) = 0.1459976
AY(2, 5, 1) = 0.2455689
AY(2, 5, 2) = -.2509632
AY(2, 5, 3) = 0.0062254
AY(2, 5, 4) = -.1088189
AY(2, 5, 5) = -.0381462
AY(2, 5, 6) = 0.1146172
AY(2, 5, 7) = 0.0427539
AY(2, 5, 8) = -.4005824
AY(2, 5, 9) = -.0044397
AY(2, 5,10) = 0.2955661
AY(2, 6, 1) = 0.2452707
```

```
AY(2, 6, 2) = -.2543307
AY(2, 6, 3) = 0.0142555
AY(2, 6, 4) = -.0970103
AY(2, 6, 5) = -.0621290
AY(2, 6, 6) = 0.0035522
AY(2, 6, 7) = 0.0783962
AY(2, 6, 8) = -.3637751
AY(2, 6, 9) = -.0287000
AY(2, 6,10) = 0.2726349
AY(2, 7, 1) = 0.2449414
AY(2, 7, 2) = -.2560443
AY(2, 7, 3) = 0.0173214
AY(2, 7, 4) = -.0894997
AY(2, 7, 5) = -.0568416
AY(2, 7, 6) = 0.0799210
AY(2, 7, 7) = 0.0523075
AY(2, 7, 8) = -.3008333
AY(2, 7, 9) = -.0088913
AY(2, 7,10) = 0.3030200
AY(2, 8, 1) = 0.2446698
AY(2, 8, 2) = -.2598498
AY(2, 8, 3) = 0.0211945
AY(2, 8, 4) = -.0761800
AY(2, 8, 5) = -.0855583
AY(2, 8, 6) = 0.0243410
AY(2, 8, 7) = 0.1279325
AY(2, 8, 8) = -.2508339
AY(2, 8, 9) = -.0677955
AY(2, 8,10) = 0.1877052
AY(2, 9, 1) = 0.2448007
AY(2, 9, 2) = -.2612718
AY(2, 9, 3) = 0.0243965
AY(2, 9, 4) = -.0793969
AY(2, 9, 5) = -.1416526
AY(2, 9, 6) = 0.0307831
AY(2, 9, 7) = 0.3153132
AY(2, 9, 8) = -.1879231
AY(2, 9, 9) = -.2389352
AY(2, 9,10) = 0.0906702
AY(2,10, 1) = 0.2452132
AY(2,10, 2) = -.2621284
AY(2,10, 3) = 0.0158796
AY(2,10, 4) = -.0774327
AY(2,10, 5) = -.0804841
AY(2,10, 6) = 0.0680255
AY(2,10, 7) = 0.1494961
AY(2,10, 8) = -.3629587
AY(2,10, 9) = -.0914754
AY(2,10,10) = 0.2825083
AY(2,11, 1) = 0.2452883
AY(2,11, 2) = -.2633303
AY(2,11, 3) = 0.0153950
AY(2,11, 4) = -.0598368
AY(2,11, 5) = -.0964094
AY(2,11, 6) = -.0352879
AY(2,11, 7) = 0.2180000
AY(2,11, 8) = -.1049756
AY(2,11, 9) = -.1574961
AY(2,11,10) = 0.0785006
AY(2,12, 1) = 0.2449149
AY(2,12, 2) = -.2634949
AY(2,12, 3) = 0.0079950
AY(2,12, 4) = -.0599353
```

```
AY(2,12, 5) = -.0429517
AY(2,12, 6) = -.0127390
AY(2,12, 7) = 0.0953224
AY(2,12, 8) = -.1400013
AY(2,12, 9) = -.0655084
AY(2,12,10) = 0.0986004
AY(2,13, 1) = 0.2449369
AY(2,13, 2) = -.2636763
AY(2,13, 3) = 0.0045141
AY(2,13, 4) = -.0565367
AY(2,13, 5) = -.0052219
AY(2,13, 6) = -.0000825
AY(2,13, 7) = 0.0009200
AY(2,13, 8) = -.1100754
AY(2,13, 9) = -.0048272
AY(2,13,10) = 0.0668762
AY(2,14, 1) = 0.2441006
AY(2,14, 2) = -.2630669
AY(2,14, 3) = 0.0073298
AY(2,14, 4) = -.0536107
AY(2,14, 5) = -.0043621
AY(2,14, 6) = 0.0109993
AY(2,14, 7) = 0.0004529
AY(2,14, 8) = -.1410259
AY(2,14, 9) = -.0020555
AY(2,14,10) = 0.0672601
AY(2,15, 1) = 0.2440201
AY(2,15, 2) = -.2620487
AY(2,15, 3) = 0.0090259
AY(2,15, 4) = -.0438383
AY(2,15, 5) = 0.0173438
AY(2,15, 6) = -.0205954
AY(2,15, 7) = -.0765727
AY(2,15, 8) = -.0492813
AY(2,15, 9) = 0.0629283
AY(2,15,10) = -.0154113
POSX(1) = -.00000735
POSX(2) = 0.03490995
POSX(3) = 0.07139838
POSX(4) = 0.10704547
POSX(5) = 0.14282370
POSX(6) = 0.17849192
POSX(7) = 0.21413800
POSX(8) = 0.24989880
POSX(9) = 0.28562150
POSX(10) = 0.32126780
POSX(11) = 0.35697468
POSX(12) = 0.39271562
POSX(13) = 0.42843710
POSX(14) = 0.46416833
POSX(15) = 0.49983832
POSY(1) = 0.00002038
POSY(2) = 0.03568660
POSY(3) = 0.07147417
POSY(4) = 0.10728205
POSY(5) = 0.14294950
POSY(6) = 0.17866655
POSY(7) = 0.21442593
POSY(8) = 0.25026213
POSY(9) = 0.28628130
POSY(10) = 0.32185790
POSY(11) = 0.35766665
POSY(12) = 0.39347230
```

```
POSY(13) = 0.42936222
POSY(14) = 0.46532970
POSY(15) = 0.50106002
RETURN
END
```

APPENDIX 8B

FORTRAN Analysis Programs' Output and Input Tables

Z Motion Results With LASER Angle Offsets

All angles are in radians

ALPH(1,I)	ALPH(2,I)	BET(1,I)	BET(2,I)	THET(1,I)	THET(2,I)
0.	0.	0.	0.	0.	0.
0.000000	0.000003	0.000092	0.000165	-.000309	-.000293
0.000000	0.000003	0.000143	0.000213	-.000627	-.000600
0.000000	0.000003	0.000137	0.000206	-.000932	-.000925
0.000000	0.000003	0.000140	0.000205	-.001234	-.001210
0.000000	0.000003	0.000140	0.000208	-.001534	-.001475
0.000000	0.000003	0.000143	0.000212	-.001842	-.001795
0.000000	0.000003	0.000153	0.000218	-.002148	-.002087
0.000000	0.000004	0.000143	0.000211	-.002444	-.002370
0.000000	0.000003	0.000153	0.000220	-.002746	-.002671
0.000000	0.000005	0.000153	0.000216	-.003045	-.002970
0.000000	0.000005	0.000159	0.000224	-.003347	-.003289
0.000000	0.000005	0.000159	0.000221	-.003649	-.003569
0.000000	0.000005	0.000159	0.000223	-.003948	-.003876
0.000000	0.000005	0.000159	0.000222	-.004251	-.004168
0.000000	0.000006	0.000159	0.000221	-.004547	-.004469
0.000000	0.000004	0.000159	0.000222	-.004855	-.004766
0.000000	0.000006	0.000162	0.000223	-.005154	-.005071
0.000000	0.000005	0.000153	0.000214	-.005457	-.005400
0.000000	0.000005	0.000165	0.000219	-.005756	-.005688

SIGA = 0.000004 SIGB = 0.000067 SIGT = 0.000066

Y Motion Results With LASER Angle Offsets

All angles are in radians

ALPH(1,I)	ALPH(2,I)	BET(1,I)	BET(2,I)	THET(1,I)	THET(2,I)
0.	0.	0.	0.	0.	0.
0.000000	0.000012	0.000455	0.000449	-.000019	-.000080
0.000000	0.000017	0.000748	0.000729	-.000019	-.000107
0.000000	0.000024	0.001059	0.001031	-.000019	-.000123
0.000000	0.000029	0.001346	0.001310	-.000019	-.000127
0.000000	0.000036	0.001654	0.001614	-.000022	-.000147
0.000000	0.000041	0.001941	0.001888	-.000019	-.000154
0.000000	0.000048	0.002249	0.002188	-.000019	-.000180
0.000000	0.000052	0.002564	0.002497	-.000019	-.000214
0.000000	0.000055	0.002841	0.002764	-.000016	-.000205
0.000000	0.000059	0.003156	0.003075	-.000022	-.000239
0.000000	0.000061	0.003439	0.003347	-.000019	-.000233
0.000000	0.000064	0.003729	0.003624	-.000016	-.000258
0.000000	0.000066	0.004034	0.003922	-.000016	-.000229
0.000000	0.000071	0.004318	0.004191	-.000013	-.000243

SIGA = 0.000051 SIGB = 0.000076 SIGT = 0.000179

YZ Motion Results With LASER Angle Offsets

All angles are in radians

ALPH(1,I)	ALPH(2,I)	BET(1,I)	BET(2,I)	THET(1,I)	THET(2,I)
0.	0.	0.	0.	0.	0.
0.000000	0.000001	0.000095	0.000106	-.000293	-.000280
0.000000	0.000003	0.000366	0.000376	-.000595	-.000633
0.000000	0.000006	0.000694	0.000695	-.000904	-.000961
0.000000	0.000009	0.000990	0.000986	-.001206	-.001256
0.000003	0.000014	0.001298	0.001284	-.001505	-.001575
0.000000	0.000017	0.001584	0.001565	-.001810	-.001885
0.000000	0.000022	0.001893	0.001868	-.002113	-.002201
0.000000	0.000026	0.002199	0.002163	-.002412	-.002518
0.000000	0.000030	0.002498	0.002457	-.002714	-.002820
0.000000	0.000033	0.002794	0.002745	-.003013	-.003128
0.000000	0.000036	0.003093	0.003032	-.003315	-.003438
0.000000	0.000041	0.003382	0.003314	-.003618	-.003726
0.000000	0.000044	0.003700	0.003614	-.003920	-.004032

SIGA = 0.000027 SIGB = 0.000043 SIGT = 0.000092

Twist Motion Results

All dimensions are in inches and radians

ALPH(1,I)	ALPH(2,I)	ZM(1,I)	ZM(2,I)	YM(1,I)	YM(2,I)
0.	0.	0.	0.	0.	0.
0.000315	0.000327	-0.000078	-0.000155	-0.000278	0.002317
0.000630	0.000600	-0.000156	-0.001593	-0.000655	0.002746
0.000945	0.000919	-0.000234	-0.003350	-0.000933	0.004303
0.001174	0.001145	-0.000200	-0.004745	-0.001226	0.003904
0.001575	0.001558	-0.000290	-0.005681	-0.001690	0.004616
0.001918	0.001913	-0.000240	-0.006647	-0.002130	0.003489
0.002575	0.002564	-0.000468	-0.004769	-0.002649	0.002730
0.002946	0.002936	-0.000389	-0.004466	-0.003052	0.000699
0.003603	0.003605	-0.000618	-0.002700	-0.003672	-0.001303
0.003888	0.003933	-0.000626	-0.002526	-0.004290	-0.002874
0.004230	0.004301	-0.000577	-0.002050	-0.004432	-0.004572
0.004999	0.005036	-0.000791	-0.000593	-0.005401	-0.008739
0.005597	0.005561	-0.000880	0.000951	-0.005500	-0.010866
0.005796	0.005841	-0.000876	0.000500	-0.005933	-0.012965

SIGA = 0.000034 SIGZ = 0.003432 SIGY = 0.004669

General Motion Results

All dimensions are in inches and radians

ALPH(1,I)	ALPH(2,I)	ZM(1,I)	ZM(2,I)	YM(1,I)	YM(2,I)
0.	0.	0.	0.	0.	0.
0.000513	0.000599	0.010124	0.011906	-0.003113	0.000412
0.000712	0.000837	0.030427	0.033489	-0.004347	0.000214
0.000911	0.001026	0.045531	0.050236	-0.004980	-0.000200
0.001167	0.001291	0.055192	0.060504	-0.005937	-0.001457
0.001223	0.001341	0.065950	0.072033	-0.006161	-0.001219
0.001451	0.001590	0.085383	0.093626	-0.007056	-0.001698
0.001536	0.001590	0.105270	0.113683	-0.007242	-0.001239
0.001678	0.001765	0.153215	0.163481	-0.007151	-0.001538
0.001565	0.001956	0.285700	0.301174	-0.005902	-0.000185

SIGA = 0.000176 SIGZ = 0.000540 SIGY = 0.005356

```
0.0000,.0000,.00000000000000    Input for Y motion test
-.0143,.0006,.00050000000
-.0235,.0006,.00100000000
-.0333,.0006,.00100000000
-.0423,.0006,.00150000000
-.0520,.0007,.00190000000
-.0610,.0006,.00210000000
-.0707,.0006,.00250000000
-.0806,.0006,.00270000000
-.0893,.0005,.00300000000
-.0992,.0007,.00350000000
-.1001,.0006,.00350000000
-.1172,.0005,.00400000000
-.1268,.0005,.00420000000
-.1357,.0004,.00500000000
0.265025, 0.573820, 0.698645000
0.221226, 0.557025, 0.682840000
0.193312, 0.546403, 0.672826000
0.162924, 0.534767, 0.661860000
0.134547, 0.523079, 0.651618000
0.103528, 0.511973, 0.640444000
0.075513, 0.501279, 0.630398000
0.044879, 0.489653, 0.619578000
0.012917, 0.477425, 0.608038000
-.014864, 0.466753, 0.597996000
-.046780, 0.454561, 0.586530000
-.075208, 0.443507, 0.576098000
-.103759, 0.432389, 0.565664000
-.134859, 0.420063, 0.554038000
-.162615, 0.408887, 0.543640000
0.5258961, 0.1055493, 0.5167265, 0.0598691000
0.5233254, 0.1037409, 0.5147871, 0.0599276000
0.5218129, 0.1034359, 0.5134477, 0.0601149000
0.5202433, 0.1028542, 0.5119512, 0.0602940000
0.5188677, 0.1030409, 0.5105347, 0.0604921000
0.5173782, 0.1027811, 0.5091540, 0.0607655000
0.5160513, 0.1029191, 0.5078125, 0.0610168000
0.5146401, 0.1020490, 0.5065877, 0.0611718000
0.5131301, 0.1010026, 0.5053252, 0.0613759000
0.5118358, 0.1006219, 0.5038918, 0.0616084000
0.5104271, 0.1012884, 0.5026920, 0.0617422000
0.5091062, 0.1008707, 0.5012554, 0.0620145000
0.5077878, 0.1007933, 0.5000936, 0.0622431000
0.5063668, 0.1003719, 0.4983377, 0.0624885000
0.5051332, 0.0997687, 0.4971743, 0.0627082000
```

Input for X motion test

```
0.,0.,0.000000000000
 -.0029,.0097,.0005000000
 -.0045,.0197,.0008000000
 -.0043,.0293,.0010000000
 -.0044,.0388,.0015000000
 -.0044,.0482,.0015000000
 -.0045,.0579,.0020000000
 -.0048,.0675,.0022000000
 -.0045,.0768,.0025000000
 -.0048,.0863,.0028000000
 -.0048,.0957,.0030000000
 -.0050,.1052,.0035000000
 -.0050,.1147,.0035000000
 -.0050,.1241,.0038000000
 -.0050,.1336,.0040000000
 -.0050,.1429,.0044000000
 -.0050,.1526,.0046000000
 -.0051,.1620,.0050000000
 -.0048,.1715,.0052000000
 -.0052,.1809,.0052000000
 -.0603064, 0.4485775, 0.5809790000
 -.0770996, 0.4421315, 0.5749970000
 -.0833658, 0.4397295, 0.5727470000
 -.0840780, 0.4393675, 0.5724970000
 -.0856986, 0.4386175, 0.5718490000
 -.0875280, 0.4377635, 0.5711170000
 -.0894356, 0.4368975, 0.5703650000
 -.0917258, 0.4358795, 0.5694710000
 -.0924696, 0.4354795, 0.5691870000
 -.0949486, 0.4343655, 0.5681590000
 -.0960986, 0.4337355, 0.5677450000
 -.0982858, 0.4328635, 0.5669630000
 -.0997886, 0.4320795, 0.5662970000
 -.1011668, 0.4315935, 0.5659210000
 -.1026212; 0.4309155, 0.5653410000
 -.1038370, 0.4303555, 0.5649490000
 -.1055232, 0.4296515, 0.5642450000
 -.1069928, 0.4289595, 0.5637610000
 -.1075418, 0.4287075, 0.5635450000
 -.1098108, 0.4276895, 0.5626590000
 0.5096753, 0.0990908, 0.5025747, 0.06061640000
 0.5087637, 0.0946241, 0.5043811, 0.05592760000
 0.5082161, 0.0903313, 0.5066896, 0.05098050000
 0.5078673, 0.0846119, 0.5093981, 0.04618710000
 0.5076118, 0.0797252, 0.5118075, 0.04148390000
 0.5072978, 0.0751392, 0.5139641, 0.03675570000
 0.5069354, 0.0709152, 0.5165533, 0.03191610000
 0.5065991, 0.0665531, 0.5189175, 0.02713590000
 0.5062921, 0.0620368, 0.5212263, 0.02247410000
 0.5060474, 0.0572892, 0.5237539, 0.01783980000
 0.5057414, 0.0524611, 0.5261961, 0.01313030000
 0.5054260, 0.0470861, 0.5288145, 0.00826030000
 0.5050674, 0.0426025, 0.5310149, 0.00361920000
 0.5047574, 0.0378200, 0.5335097, -.00113050000
 0.5044207, 0.0332997, 0.5358220, -.00606290000
 0.5041986, 0.0289869, 0.5383228, -.01069670000
 0.5038933, 0.0243865, 0.5407007, -.01541780000
 0.5035891, 0.0196182, 0.5431366, -.02033030000
 0.5032793, 0.0147135, 0.5457636, -.02507060000
 0.5028819, 0.0100829, 0.5479332, -.02963750000
```

```
0.,0.,0.00000000000000000000        Input for YZ motion test
-.0030,.0092,.0000000000
-.0115,.0187,.0010000000
-.0210,.0284,.0015000000
-.0311,.0379,.0020000000
-.0400,.0473,.0025000000
-.0490,.0569,.0030000000
-.0595,.0664,.0038000000
-.0691,.0758,.0045000000
-.0785,.0853,.0050000000
-.0878,.0947,.0057000000
-.0972,.1042,.0062000000
-.1063,.1137,.0069000000
-.1163,.1232,.0075000000
0.2102445, 0.5537005, 0.600770000000000
0.2078167, 0.5490545, 0.677012000000000
0.1801829, 0.5395375, 0.667202000000000
0.1470519, 0.5271195, 0.655435000000000
0.1163497, 0.5155395, 0.644487000000000
0.0847777, 0.5035455, 0.633239000000000
0.0545757, 0.4920255, 0.622427000000000
0.0218775, 0.4794595, 0.610675000000000
-.0101379, 0.4670695, 0.599111000000000
-.0419265, 0.4548475, 0.587687000000000
-.0730329, 0.4427635, 0.576415000000000
-.1043989, 0.4303815, 0.564843000000000
-.1350127, 0.4182075, 0.553565000000000
-.1675260, 0.4050415, 0.541291000000000
0.5233064, 0.1044348, 0.5147181, 0.05962800000000000
0.5225502, 0.1012764, 0.5165072, 0.05518400000000000
0.5205510, 0.0949525, 0.5177296, 0.05066430000000000
0.5184922, 0.0892724, 0.5186464, 0.04590540000000000
0.5169748, 0.0853361, 0.5197900, 0.04148380000000000
0.5150775, 0.0791531, 0.5208111, 0.03698850000000000
0.5134253, 0.0738756, 0.5219752, 0.03245820000000000
0.5116661, 0.0699895, 0.5230463, 0.02782380000000000
0.5099071, 0.0643969, 0.5241766, 0.02334890000000000
0.5081905, 0.0591802, 0.5251970, 0.01887330000000000
0.5066206, 0.0548011, 0.5264039, 0.01432830000000000
0.5049473, 0.0495837, 0.5275422, 0.00981450000000000
0.5033495, 0.0440359, 0.5285706, 0.00514230000000000
0.5016501, 0.0392138, 0.5296406, 0.00061610000000000
```

Input for twist test

```
0.0000, 0.0167, 0.0000000000
0.0007, 0.0163, -.0007000000
0.0014, 0.0159, -.0015000000
0.0021, 0.0155, -.0022000000
0.0027, 0.0153, -.0028000000
0.0036, 0.0148, -.0038000000
0.0045, 0.0145, -.0047000000
0.0059, 0.0136, -.0061000000
0.0069, 0.0133, -.0070000000
0.0083, 0.0124, -.0085000000
0.0090, 0.0121, -.0095000000
0.0099, 0.0118, -.0101000000
0.0116, 0.0108, -.0121000000
0.0130, 0.0101, -.0130000000
0.0135, 0.0099, -.0137000000
0.6456328, 1.0300160, 0.9827375000
0.6068168, 0.9998375, 0.9605735000
0.5710108, 0.9707895, 0.9380775000
0.5323548, 0.9399115, 0.9158655000
0.5035568, 0.9154755, 0.8976415000
0.4550188, 0.8749515, 0.8696755000
0.4104628, 0.8361495, 0.8420295000
0.3309788, 0.7671635, 0.7956775000
0.2836730, 0.7243115, 0.7667195000
0.1988580, 0.6479275, 0.7173375000
0.1559830, 0.6083255, 0.6919435000
0.1073892, 0.5629135, 0.6631395000
0.0074510, 0.4667115, 0.6026575000
-.0665962, 0.3947715, 0.5581915000
-.1045704, 0.3554275, 0.5341035000
0.5210306, 0.1212534, 0.5116706, 0.0752199000
0.5211347, 0.1231714, 0.5116576, 0.0742988000
0.5211638, 0.1246801, 0.5112694, 0.0733504000
0.5210357, 0.1236513, 0.5107962, 0.0725023000
0.5210075, 0.1230173, 0.5104915, 0.0716667000
0.5209488, 0.1250782, 0.5101086, 0.0705581000
0.5210097, 0.1263188, 0.5098951, 0.0694913000
0.5203880, 0.1222560, 0.5100460, 0.0678227000
0.5200273, 0.1192098, 0.5099828, 0.0667956000
0.5189768, 0.1131524, 0.5097816, 0.0650917000
0.5187543, 0.1113896, 0.5097405, 0.0642458000
0.5183381, 0.1094410, 0.5095864, 0.0633433000
0.5170562, 0.1017410, 0.5091737, 0.0615080000
0.5161645, 0.0975287, 0.5089459, 0.0602525000
0.5159438, 0.0954293, 0.5087635, 0.0595756000
```

Input for general motion test

```
0.0000, -.0030, 0.000000000
0.0114, 0.0058, -.003000000
0.0322, 0.0259, -.005300000
0.0478, 0.0400, -.006200000
0.0501, 0.0502, -.007500000
0.0690, 0.0609, -.007000000
0.0890, 0.0801, -.009000000
0.1091, 0.0999, -.009300000
0.1574, 0.1477, -.009400000
0.2896, 0.2803, -.008000000
0.2270303, 0.4754030, 0.6519115000
0.1366953, 0.3901970, 0.5989675000
0.0978625, 0.3537990, 0.5761755000
0.0669435, 0.3249190, 0.5584235000
0.0248515, 0.2834332, 0.5328515000
0.0151003, 0.2751552, 0.5277055000
-.0269866, 0.2342508, 0.5021925000
-.0311932, 0.2327096, 0.5009565000
-.0625464, 0.2029330, 0.4823605000
-.1069874, 0.1655566, 0.4579625000
0.5262356, 0.0146555, 0.5692912, -.0323221000
0.5247665, 0.0064243, 0.5712507, -.0390311000
0.5235666, -.0004017, 0.5756517, -.0499386000
0.5225134, -.0127527, 0.5791100, -.0580266000
0.5216812, -.0184768, 0.5810053, -.0637285000
0.5211563, -.0239156, 0.5834603, -.0692323000
0.5198256, -.0347666, 0.5877353, -.0797128000
0.5194342, -.0434610, 0.5924465, -.0895966000
0.5173510, -.0670742, 0.6030409, -.1141607000
0.5134793, -.1302746, 0.6331463, -.1802823000
```

Input for general motion test

```
0.0000, -.0030, 0.000000000
0.0114, 0.0058, -.003000000
0.0322, 0.0259, -.005300000
0.0470, 0.0400, -.006200000
0.0501, 0.0502, -.007500000
0.0690, 0.0609, -.007800000
0.0890, 0.0801, -.009000000
0.1091, 0.0999, -.009300000
0.1574, 0.1477, -.009400000
0.2896, 0.2803, -.000000000
0.2270303, 0.4754030, 0.65191150000
0.1366953, 0.3901970, 0.59896750000
0.0970625, 0.3537990, 0.57617550000
0.0669435, 0.3249190, 0.55842350000
0.0240515, 0.2834332, 0.53205150000
0.0151003, 0.2751552, 0.52770550000
-.0269866, 0.2342500, 0.50219250000
-.0311932, 0.2327096, 0.50095650000
-.0625464, 0.2029330, 0.48236050000
-.1069874, 0.1655566, 0.45796250000
0.5262356, 0.0146555, 0.5692912, -.03232210000
0.5247665, 0.0064243, 0.5712507, -.03903110000
0.5235666, -.0004017, 0.5756517, -.04993060000
0.5225134, -.0127527, 0.5791100, -.05802660000
0.5216812, -.0184768, 0.5810053, -.06372850000
0.5211563, -.0239156, 0.5834603, -.06923230000
0.5198256, -.0347666, 0.5877353, -.07971280000
0.5194342, -.0434610, 0.5924465, -.08959660000
0.5173510, -.0670742, 0.6030409, -.11416070000
0.5134793, -.1302746, 0.6331463, -.18028230000
```

(this page left blank)

Chapter 9

Conceptual Design of a High Performance Robot

9.1 Introduction

As shown in the summary of Chapter 8, a measuring beam system can provide accurate joint and endpoint position feedback information necessary for a control system to position a large articulated structure accurately. To illustrate the incorporation of a measuring beam system into a robot design, this chapter will document the preliminary design of a long reach, high accuracy, high payload, articulated robot that uses an internal measuring beam system to provide joint and endpoint absolute position information. Documentation will include conceptual assembly drawings and preliminary calculations for the structural and measuring systems. Thesis conclusions are then presented.

The results of the experiments to determine POSOR performance (summarized in Table 8.2) found that even for the crude system tested, a 30" (.762 m) arm with a 3" (.0762 m) POSOR, could measure endpoint position two to three orders of magnitude better than any large (60" - 90" reach) robot presently available (Note that a 90" arm would use a 9" POSOR). Specifically, the impedance probe triad could measure out of plane bending of a structural beam to within .0006" (.0152 mm)(average of standard deviations of errors from all tests). Even the average errors of the light source lateral effect diode system, with all its calibration problems, were only .0047" (.1194 mm). In view of the above, the following sections will discuss measuring beam system performance that can be expected from future designs (now that 20/20 hindsight is available), and the methods by which a measuring beam system and structural system can be combined to yield a robot that is accurate to .001" (.0254 mm) and has a payload to weight ratio on the order of five to one.

9.2 Conceptual Robot Design

This section will first outline the desired properties for the subject robot. The robot will be designed from the inside out, and from the end to the base. Hence the measuring beam system will first be designed to meet the accuracy requirements, and the structural system will then be designed to fit over the measuring system.

With regard to the overall implementation strategy, cost effectiveness is best achieved from high volume production. Thus since precision is removed from the list of structural component requirements, it becomes economical to design and manufacture an "all purpose robot". This type of robot could be used for materials handling and laser, or for water jet machining or drilling and deburring operations. The materials handling operations require accuracy only for the ease of off-line programming, while the materials processing operations require accuracy for the actual process as well as for ease of off-line programming. Note that a high payload, and payload to weight ratio capability are also useful for quickly moving the robot about.

With regard to the choice of the number of degrees of freedom the robot should have, consider that most manufacturing processes the robot will perform would require only five degrees of freedom. Also many pick and place operations, such as those associated with a turning center, only require a five degree-of-freedom robot. Thus a five degree-of-freedom robot design will be developed and presented below.

To make the robot's performance commensurate with the tools it could replace, robot accuracy along any axis should be on the order of .001" (.025 mm). Point to point accuracy can be on the order of .0017" (.0432 mm). For servicing most large machine tools and for drilling aircraft panels, it should also have a reach of at least 6' (2 m) and a payload of about 100 - 150 pounds (45 - 68 kg).

Figures 9.1 through 9.4 show how a structural system and a measuring system can be combined to yield a high payload, long reach, high accuracy, five axis robot. Bumpy ring POSORs are held at the ends of measuring beams which are supported by wire gimbals. Short measuring beams are cantilevered directly off of their associated structural beams by single posts. The basic construction of the structural system consists of offset box beams joined by turntable (four point contact) bearings with integral gear teeth. This allows the drive motors (electric, pneumatic, or hydraulic) to drive the joints from the outside which prevents interference with the POSORs. The controllability of the robot will depend on the amount of gear backlash and how the control algorithm compensates for it (in some cases a micromanipulator may be needed). The control aspects of the problem are not discussed.

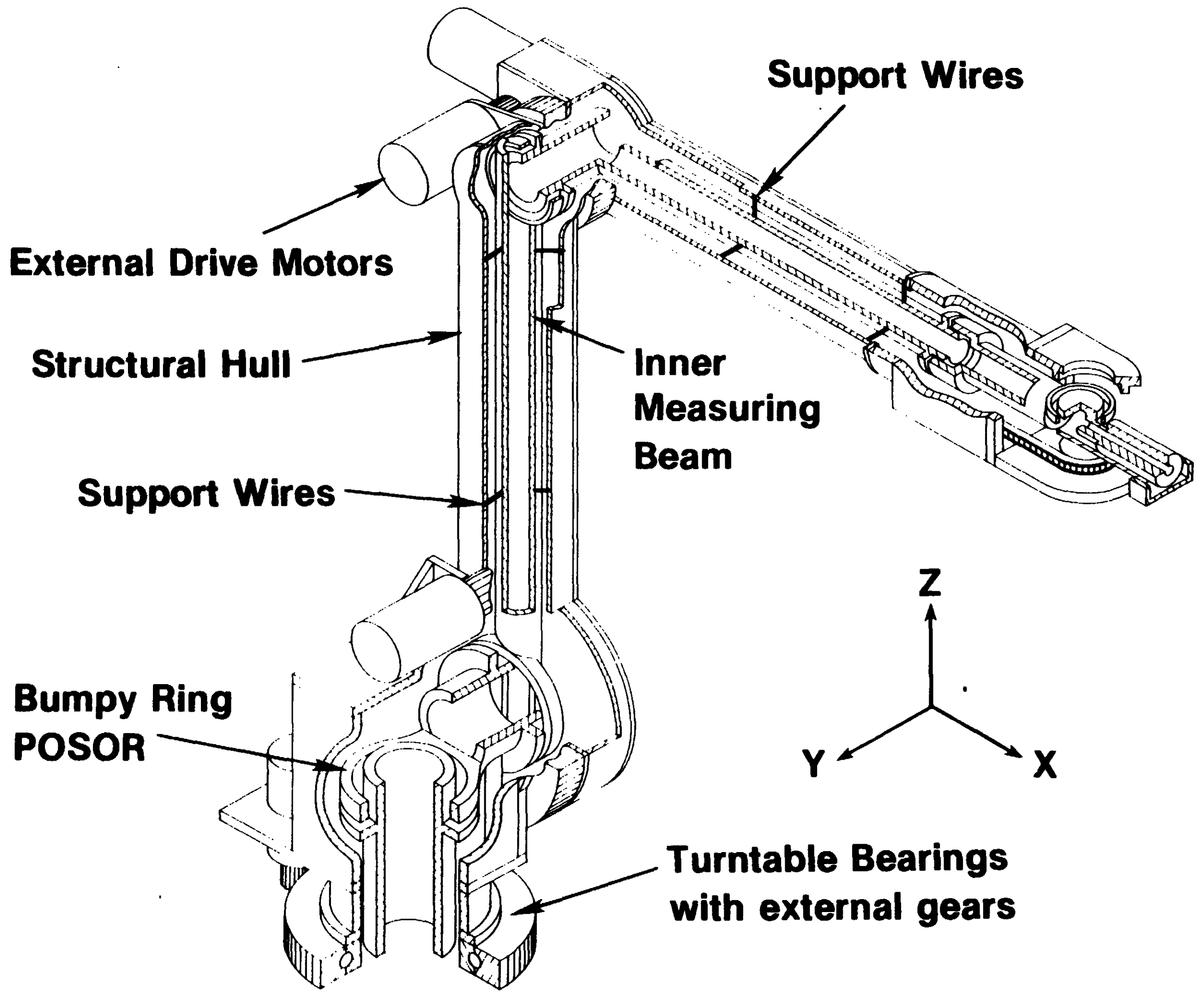

Figure 9.1 Conceptual design of a five degree of freedom, high payload, high accuracy robot. (impedance probes not shown here for clarity)

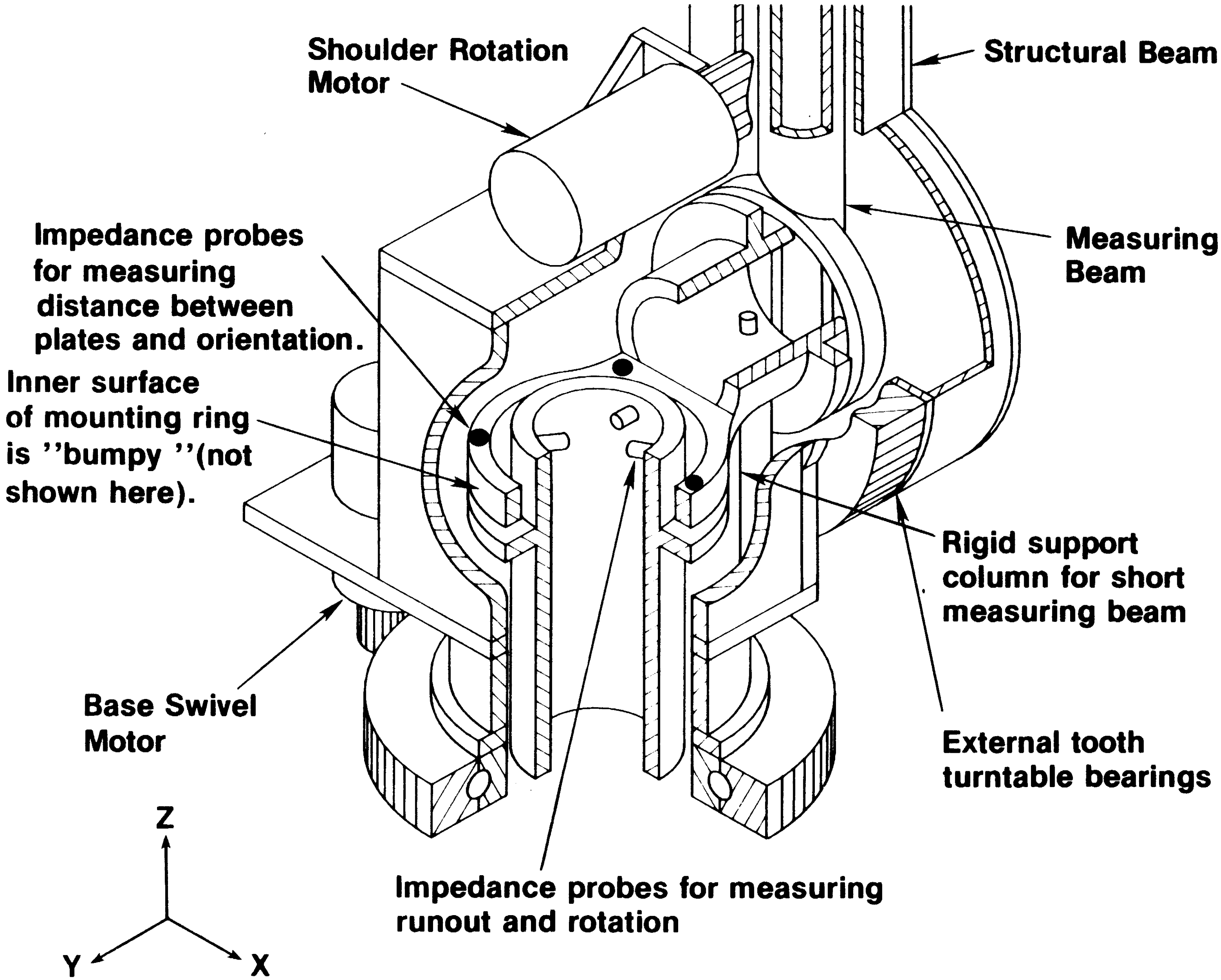

Figure 9.2 Detail of robot's base assembly

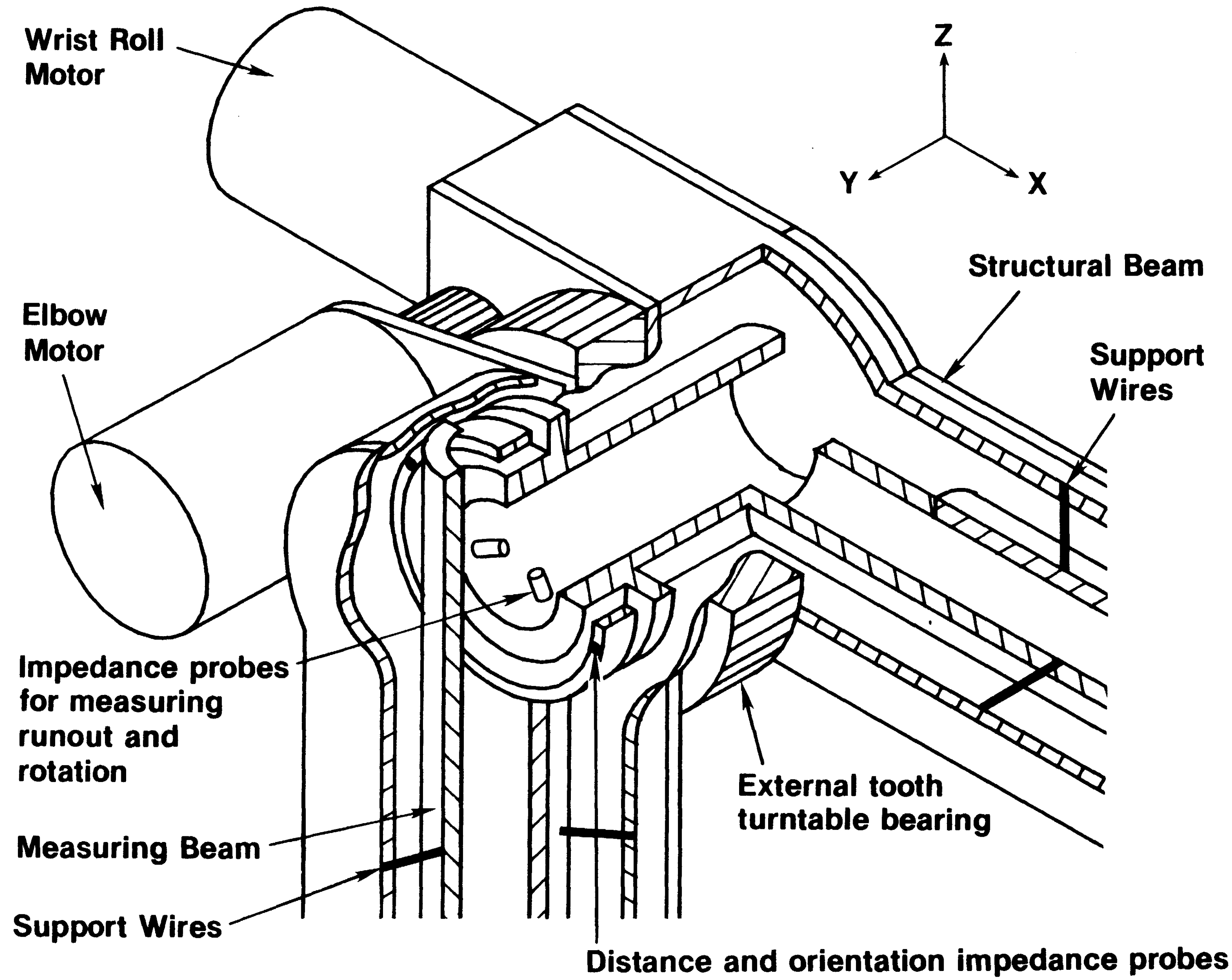

Figure 9.3 Detail of robot's elbow assembly

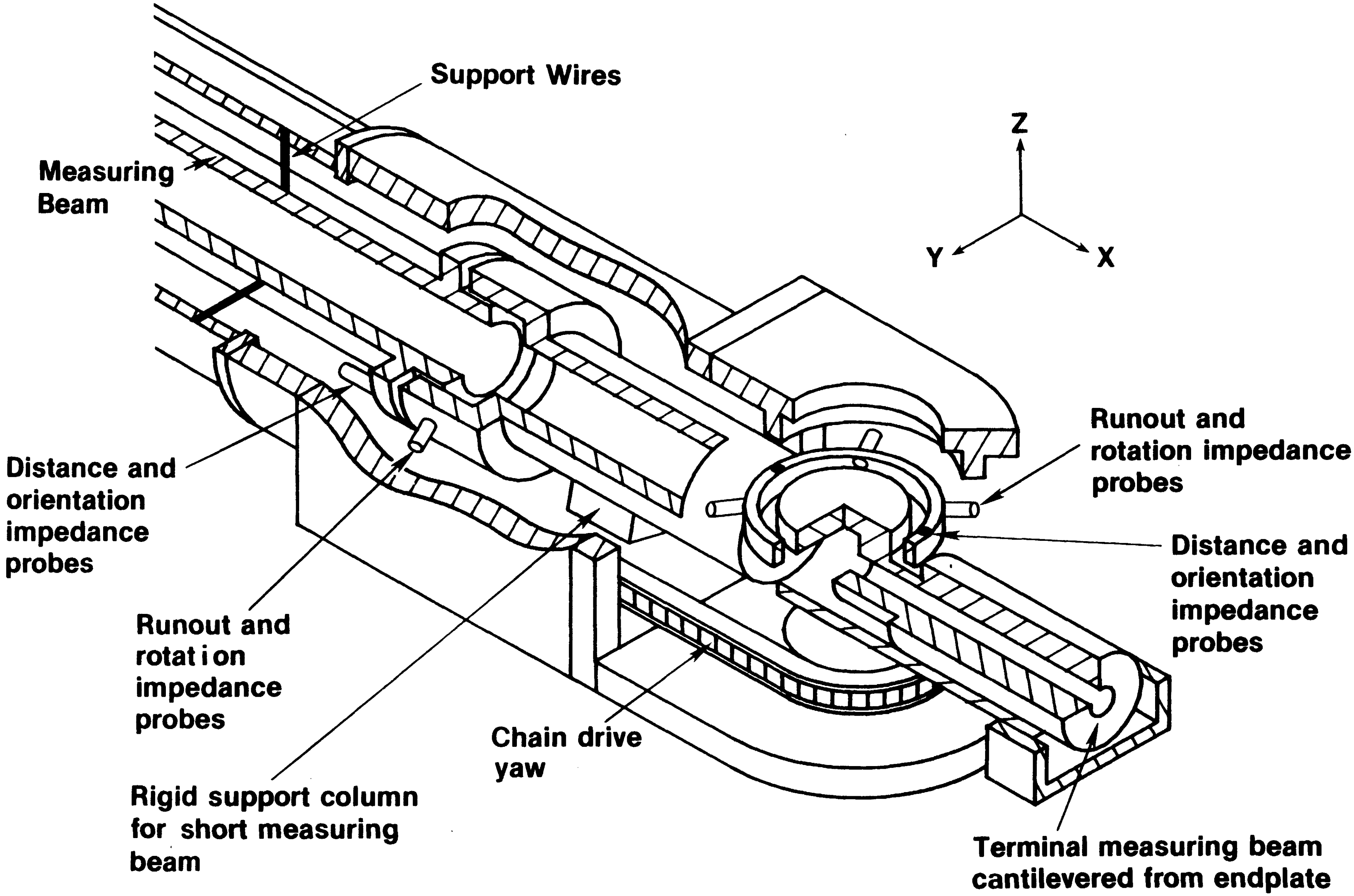

Figure 9.4 Detail of robot's wrist assembly

Following sections will describe the measuring system and the structural system in greater detail.

9.3 Measuring Beam System Design

Factors to consider in the measuring beam system design are the size of the POSORs, the relative inertia of the measuring and structural beams, and the design of the wire gimbals. The latter two issues were discussed in Section 6.2.3. To obtain accuracy on the order of .0017" (.0432 mm), the feedback signal should be five to ten times better, or in the range of .00034" to .00017" (8.5 μm to 4.7 μm). The sizing of the measuring beam components used to achieve this accuracy are discussed below.

9.3.1 POSOR Design

The achievable robot accuracy is dependent on the accuracy of the POSORs, the measuring beam error (non-measurable deflections), and the reach of the robot (angular error amplification factor). Given the desired reach and accuracy design specifications, there are probably many ways to optimize allocations of the total error budget to the various system components. The development of such methods is not discussed here, rather the experience of the designer is relied upon to provide "in the neighborhood" error allocations of error among system components.

The first step is to outline the basic design of the POSORs. It is assumed that bumpy ring POSORs are chosen, and that they will use impedance probes to measure distances as discussed in Chapter 3. Impedance probes are chosen because they are only affected by metallic contamination. Note that capacitance probes are affected by any environmental change which alters the dielectric constant of the gap which they are measuring. For this system, sensor accuracy is assumed to be 5 μin (.13 μm) which is readily achievable. The stability problem encountered in the tests of Chapter 8, can be overcome by using hybrid circuits (recently available from Kaman Instrumentation Corp.). The outside diameter of the bumpy ring sensors is assumed to be inside diameter + 2", so the large degree-of-freedom angular accuracy is 5 μin/(outside diameter - 2). The triad of probes used to determine two small angles is assumed to be on a circle of radius diameter = outside diameter - 1", so the accuracy is 5 μin/[.75×(outside diameter - 1")].

When determining the robot's endpoint error, there are two extreme (largest possible error) configurations for the robot as shown Figures 9.5 and 9.6. The first is with the wrist bent at 90° and the second is with the robot extended fully. In order to meet the reach specification, the measuring beams are sized as shown in Figure 9.7. It is assumed that the terminal link is 8" long and the distance to the center of the end effector is also 8", so link ℓ_5 is 16" (.406 m) long. Translational errors are insignificant compared to joint angle errors.

Figure 9.7 shows the measuring beam system sans structural beams and wire supports. The approximate dimensions for the various links

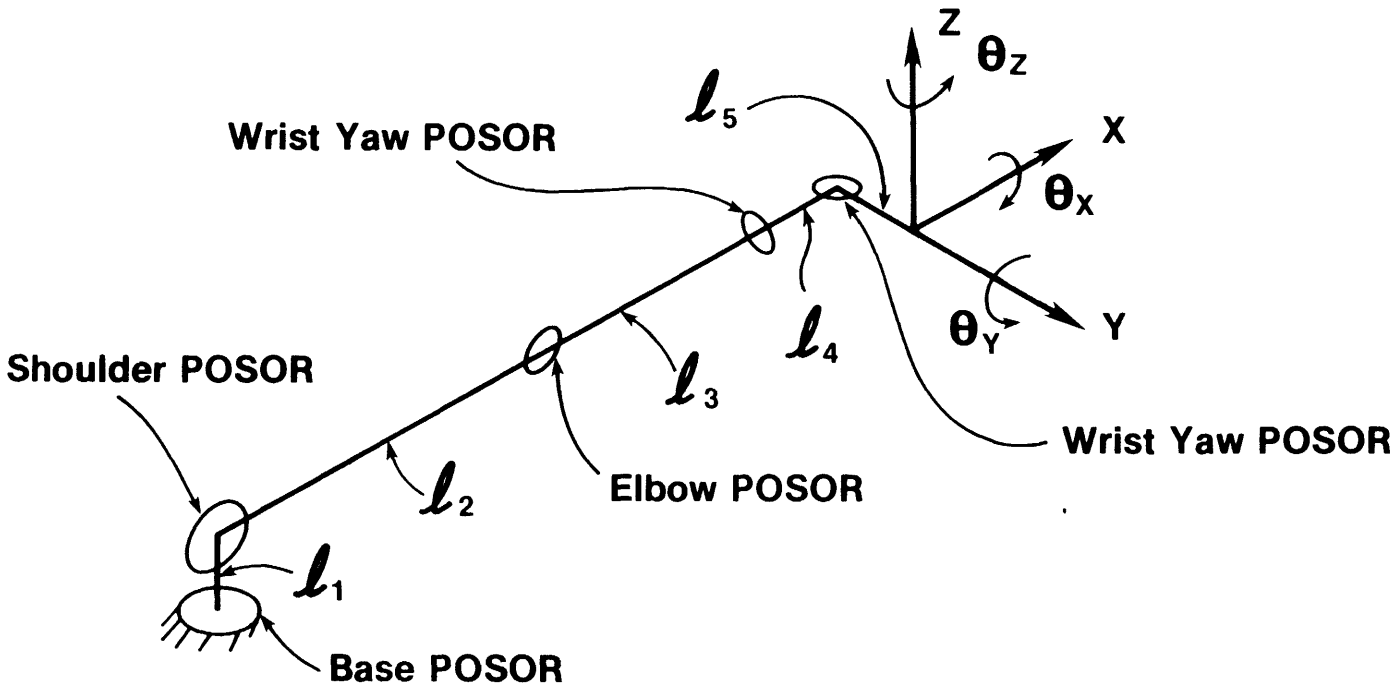

Figure 9.5 Geometry for determining total endpoint error for bent wrist

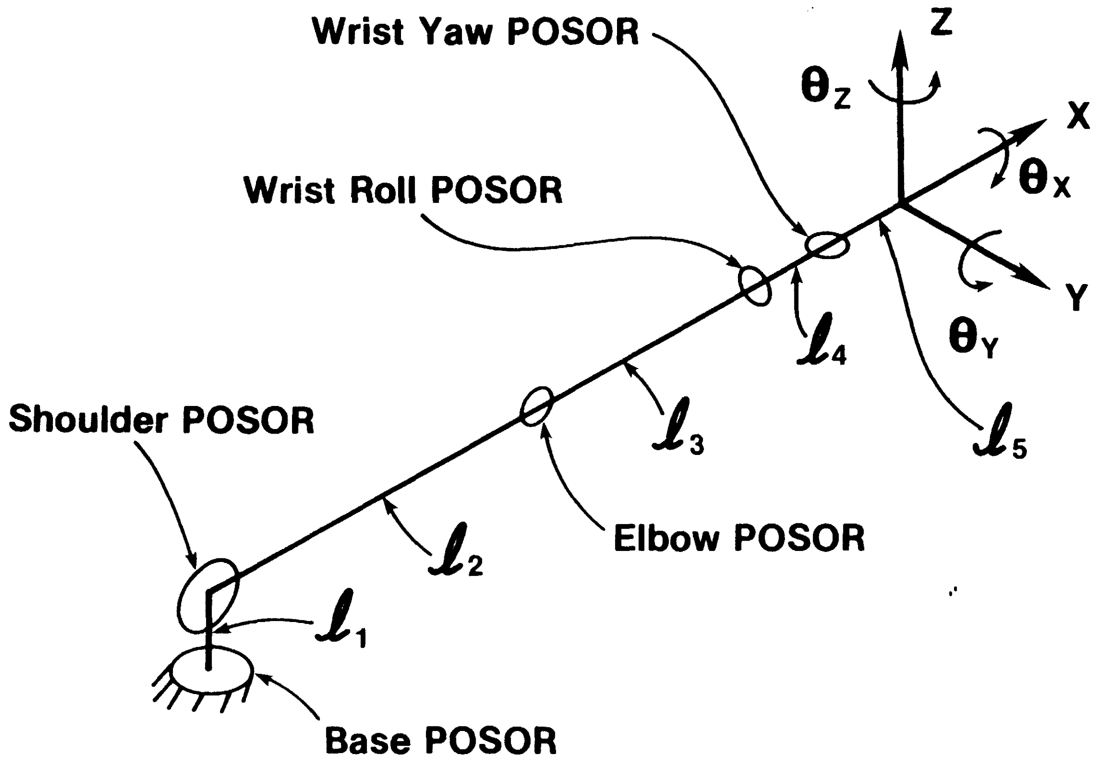

Figure 9.6 Geometry for determining total endpoint error for straight wrist

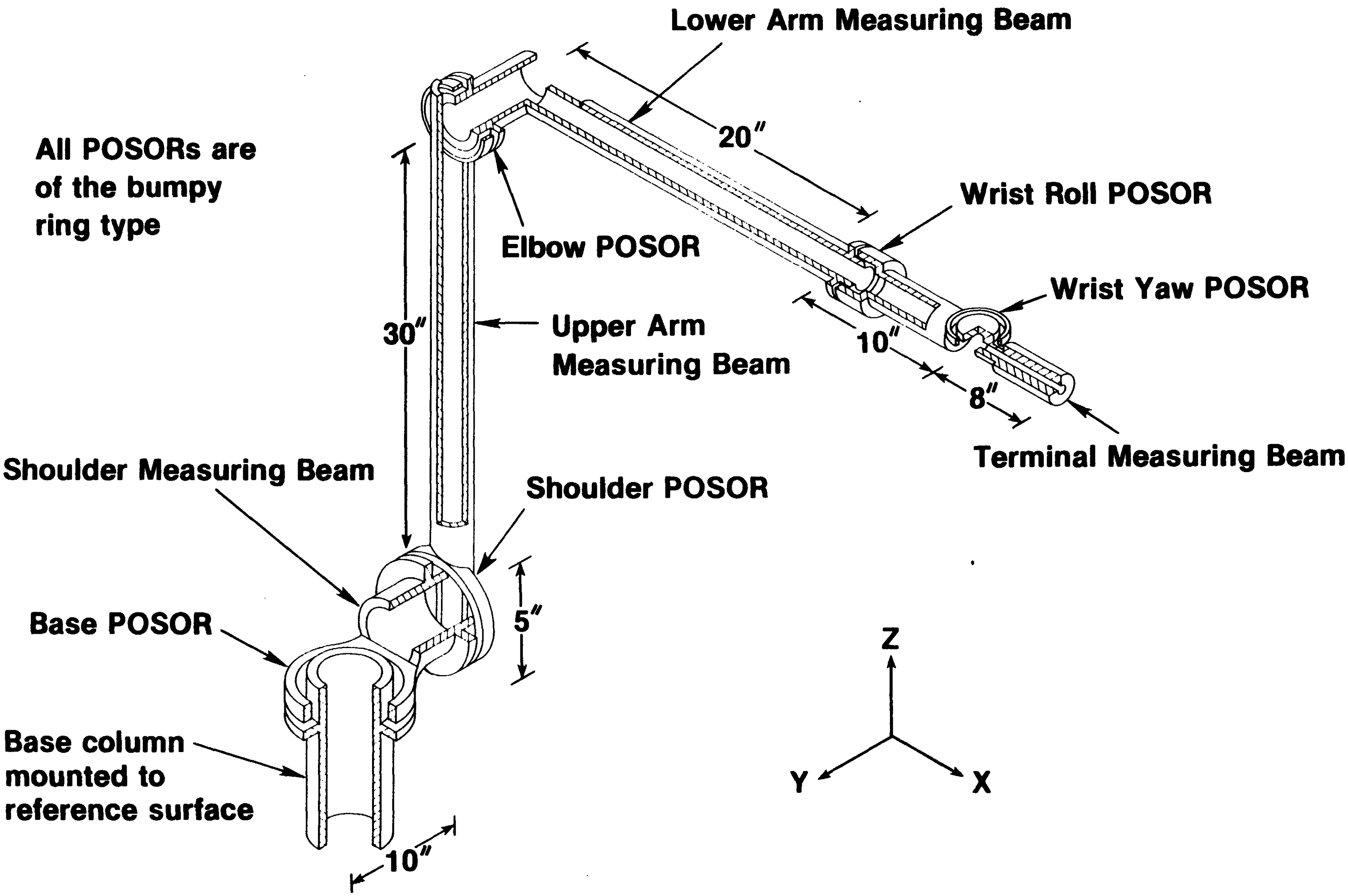

Figure 9.7 Conceptual measuring system assembly for a five degree of freedom, high payload, high accuracy robot (impedance probes and supports not shown here for for clarity)

indicate that the POSORs nearest the base should be as large as possible (they are subject to the greatest error amplification). As the end of the robot is approached, the error amplification decreases and the smaller the POSORs used, the more dexterous the robot will be. Figures 9.8 - 9.10 show the joints in greater detail.

Figure 9.8 shows the detail of the base of the measuring beam system. The first measuring beam is cantilevered off the "floor" which must be structurally isolated from loads imposed by the robot base. A turntable bearing on the order of 22" (.56 m) diameter will be used, so that there is plenty of room for the first two POSORs. The second POSOR is held by a short measuring beam which is held to the robot by a post. The POSORs used in the base are:

Base Swivel and Shoulder Joint POSORs: The maximum allowable POSOR outside diameter at this joint is assumed to be 8" (203 mm). Thus the maximum angular accuracy for the large degree-of-freedom is 5 μin/3" = 1.67 μrad. The worst case accuracy for the small degrees of freedom is 5 μin/5.25" = .95 μrad.

Figure 9.9 shows the detail of the elbow joint of the measuring beam system. The third measuring beam (the upper arm measuring beam) holds the elbow POSOR. The elbow joint will use a turntable bearing on the order of 12" (305 mm) diameter. Note the right angle extension of the lower arm measuring beam which will require the four degree-of-freedom gimbal to be located at this end. The characteristics of the elbow POSOR are:

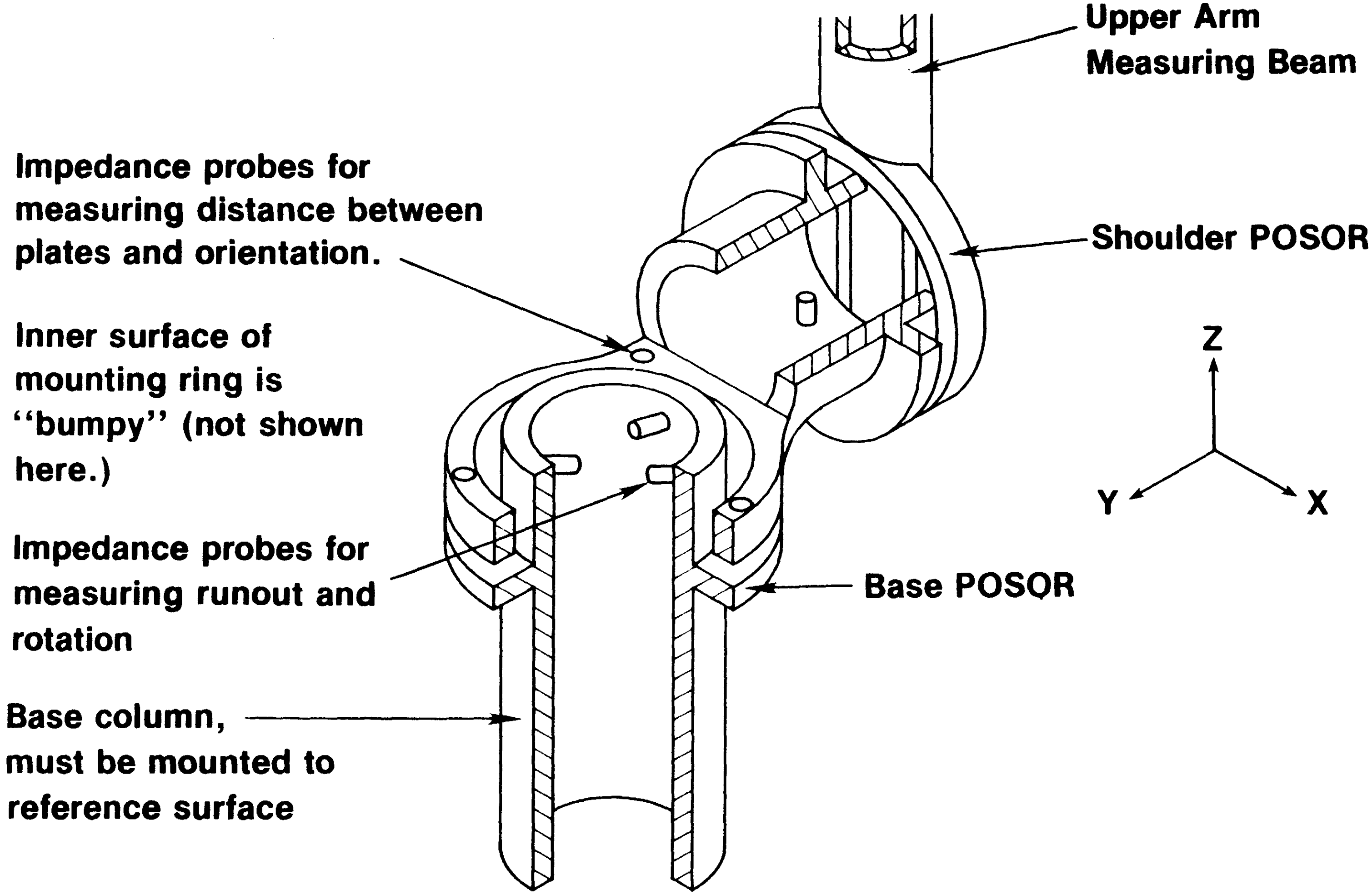

Figure 9.8 Detail of robot's base measuring system assembly

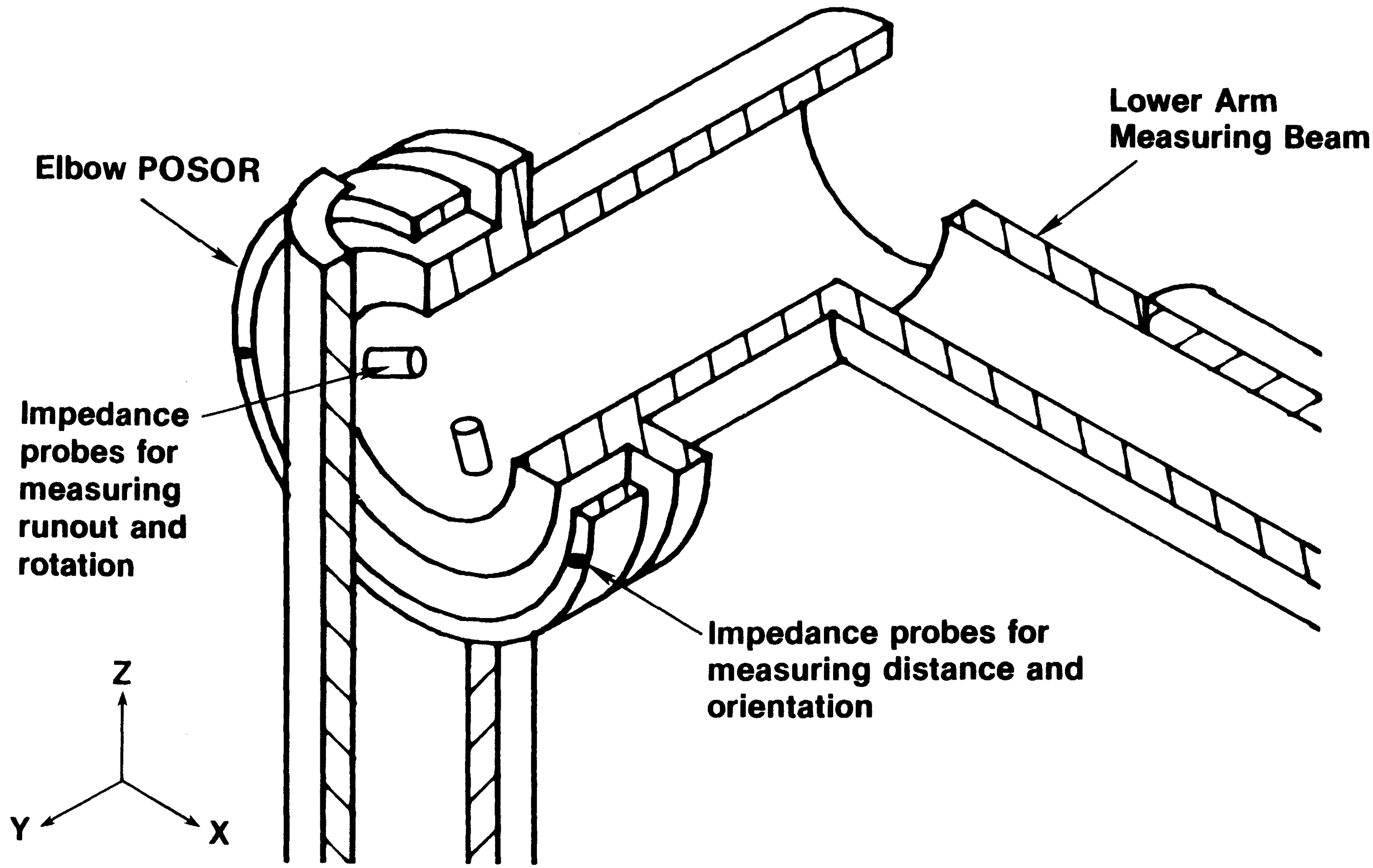

Figure 9.9 Detail of robot's elbow measuring system assembly

Elbow Joint POSOR: The maximum allowable POSOR outside diameter at this joint is assumed to be 6" (152 mm). Thus the maximum angular accuracy for the large degree-of-freedom is 5 μin/2" = 2.50 μrad. The worst case accuracy for the small degrees of freedom is 5 μin/3.75" = 1.33 μrad.

Figure 9.10 shows the lower arm portion of the measuring beam system. This part contains the wrist roll (used to turn a screwdriver) and the wrist yaw (used to wave goodbye). The wrist measuring beam is short enough that it can be supported by a single post, while the terminal measuring beam is short enough to allow it to be cantilevered from the end effector mounting plate. The characteristics of the two POSORs are:

Wrist Roll Joint POSOR: The maximum allowable POSOR outside diameter at this joint is assumed to be 5" (127 mm). Thus the maximum angular accuracy for the large degree-of-freedom is 5 μin/1.5" = 3.33 μrad. The worst case accuracy for the small degrees of freedom is 5 μin/3.00" = 1.67 μrad.

Wrist Yaw Joint POSOR: The maximum allowable POSOR outside diameter at this joint is assumed to be 4" (102 mm). Thus the maximum angular accuracy for the large degree-of-freedom is 5 μin/1" = 5.00 μrad. The worst case accuracy for the small degrees of freedom is 5 μin/2.25" = 2.22 μrad.

The total endpoint error is a function of the individual joint errors and the distances from the joints to the endpoint. For the bent

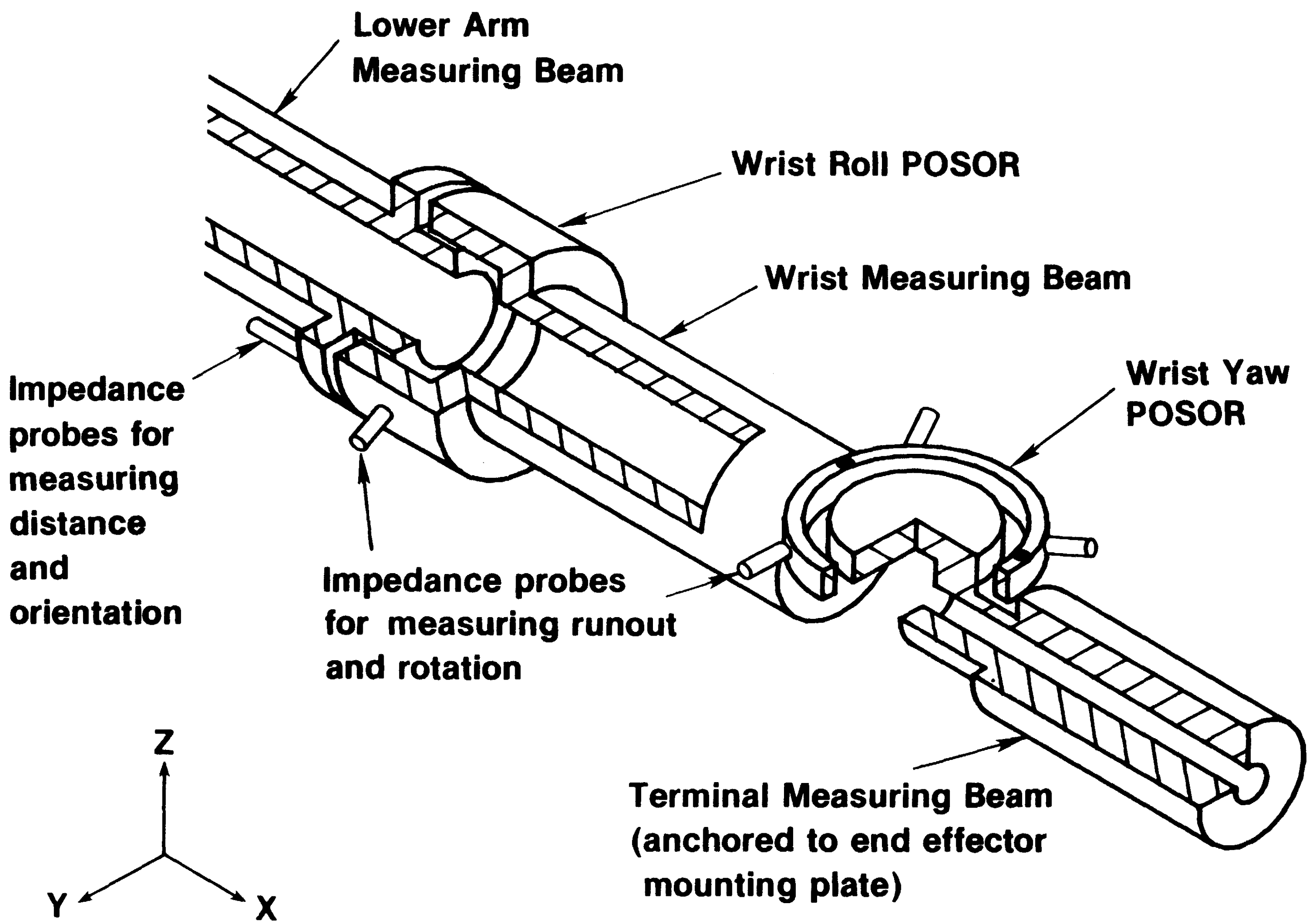

Figure 9.10 Detail of robots wrist measuring system assembly

wrist case shown in Figure 9.5, the root mean square endpoint errors are: ΔX = 73 μin, ΔY = 131 μin, ΔZ = 190 μin (1.83, 3.28, and 4.75 μm). The total displacement error at the endpoint is thus 242 μin (6.05 μm). For the fully extended case shown in Figure 10.3, the total endpoint errors are: ΔX = 36 μin, ΔY = 172 μin, and ΔZ = 204 μin (.90, 4.30, and 5.10 μm). The total endpoint displacement error is thus 269 μin (6.73 μm). For both cases, the root mean square orientation error at the endpoint is α_X = 4.4 μrad, α_Y = 4.2 μrad, and α_Z = 5.8 μrad. To each of these errors must be added calibration errors (relative orientation of POSORs on measuring beams) and errors due to deflection of the measuring beams. These factors are discussed below.

9.3.2 Gimbal and Measuring Beam Design

The sizing of the wire support gimbals and their locations are directly coupled as discussed in 6.2.3. The closer to the ends of the measuring beam the gimbals are placed, the less "runout" there will be in the POSOR, and the greater flexibility allowed in the structural beams. However, the farther apart the gimbals are placed, the more they will deform the measuring beam. Section 6.2.3 found that the gimbals could be located at the ends of a 30" (.762 m) long, 2" (50.8 mm) outside diameter × 1.75" (44.5 mm) inside diameter measuring beam. With the gimbals at the ends, the endpoint error resulting from deflections of the major measuring beams in a 60" (1.52 m) reach robot would be 50 μin (1.3 μm) from the first long measuring beam, and 20 μin (.5 μm) from the second measuring beam. Section 6.2.3.1 showed that the wire support gimbals can be made using .020" (.508 mm) wires approximately .75" (19 mm) long.

In the example of 6.2.3.1, the measuring beams were assumed to be made from aluminum; however, to reduce thermal effects, Super Invar should probably be used. Note however that the target surfaces for the impedance probes should still be made from aluminum, because a ferrite grain structure will affect probe accuracy. If an iron alloy is used for the measuring beams, then the root mean square endpoint error due to measuring beam deformations is on the order of 18 μin (.45 μm).

9.3.3 Summary of Measuring System Accuracy

Assuming that the system is calibrated many times, so averaging can be used, the calibration error should be on the order of 50 μin. Thus the "worst case" endpoint errors (root mean square errors) for the bent wrist case shown in Figure 9.5 are: ΔX = 88 μin, ΔY = 142 μin, and ΔZ = 198 μin (2.20, 3.55, and 4.95 μm). The total displacement error is thus 260 μin (6.49 μm). For the fully extended case shown in Figure 9.6, the total errors are: ΔX = 62 μin, ΔY = 180 μin, and ΔZ = 211 μin (1.55, 4.57, and 5.28 μm). The total displacement error is thus 284 μin (7.10 μm). For both cases, the root mean square orientation errors at the endpoint are on the order of α_X = 6 μrad, α_Y = 6 μrad, α_Z = 7 μrad.

9.4 Structural System Design

The total reach of the robot (to the center of the grip point) was shown in Figure 9.7 to be 76" (1.93 m). The desired payload is on the order of 100 pounds (45 kg) so the robot should be able to apply an endpoint force of 200 pounds (90 kg). For added dexterity, the three main joints should be double jointed to allow the robot to "bend over backwards". The structural system design is presented starting from the endpoint moving back to the base (as the base components must support all the components "in front of them").

The most difficult part of the design is choosing the type of drive system. To meet the payload to weight requirements, hydraulic actuators must be used (Note that a hydraulic pump unit is not much larger than a AC to DC converter used for a large machine tool). If large angular motions at the joints (double jointedness) are to be achieved, then rotary actuators or motors must be used. Linear actuators (backhoe configuration) would provide the most economical and most easily controllable system, but the joint rotations would be limited to about 135°.

For the double jointed configuration, vane actuators or hydraulic motors can be used. The former provide a "direct drive" link while the latter would use a geroler, vane, or radial piston motor. The geroler motor has a torque to weight ratio about 1.5 times that of the other motors (which are also meant for high torque low speed applications).

One possible problem with the use of geroler motors is that they can produce jerky motions at fractional RPMs. No reference was found pertaining to servocontrol of geroler motors, but is assumed here that it is possible. Even if fine motions are not easily obtainable, a micromanipulator could be used.

The robot structure is shown (without the measuring beam system) in Figure 9.11. Following sections describe each joint design in detail.

9.4.1 Wrist Yaw Joint

The wrist yaw joint is the first joint back from the end effector. It is shown in Figure 9.12. It must accommodate a 4" (102 mm) POSOR. The payload is applied 16" (406 mm) from the center of the two bearings. The lower bearing has a sprocket attached to it which is driven by a chain controlled by two hydraulic pistons. The sprocket is 4" (102 mm) D, so two 1" (25.4 mm) bore (effective area) pistons with 8" (203 mm) stroke are required in order to provide $\pm$ 120° yaw motion. The bearings are about 5" (127 mm) apart, so the radial load on each is 640 pounds (290 kg), and the thrust load is about 200 pounds (91 kg). Kaydon Reali-slim KB020XPO four point contact bearings with the following properties are chosen for use: 2.000" inside diameter, 2.625" (67 mm) outside diameter, $^5/_{32}$" (3.97 mm) balls, $^5/_{16}$" (7.94 mm) cross section, static loads: 880 lbs (363 kg) radial, 2200 lbs (998 kg) thrust, and 1020 in-lbs (115 Nt-m) moment. The structural weight of this region including the actuators is on the order of 50 lbs (23 kg).

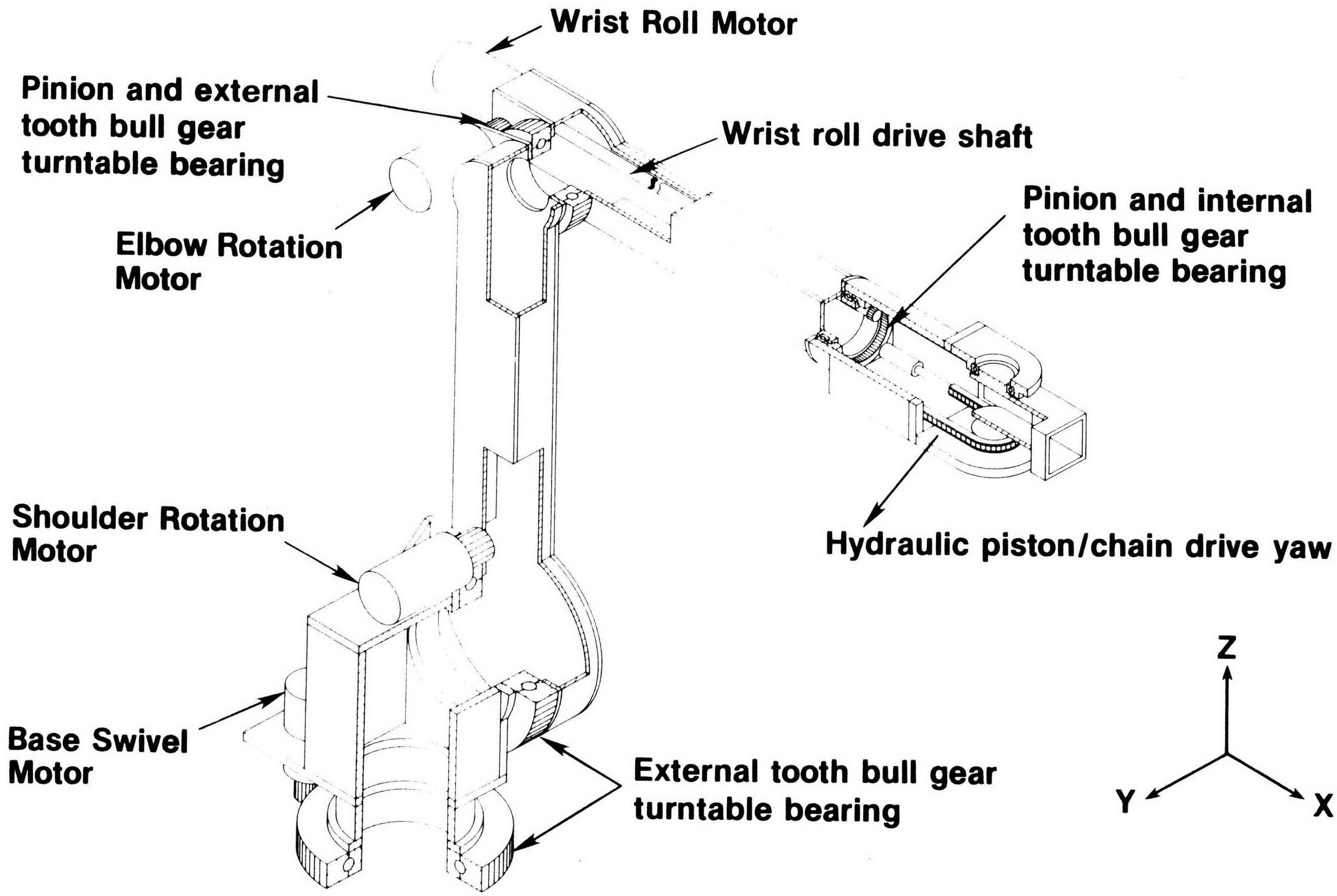

Figure 9.11 Conceptual structural assembly of a five degree of freedom,high payload, high accuracy robot.

9.4.2 Wrist Roll Joint

The wrist roll joint is also shown in Figure 9.12. The moment at this joint is 26"×200lbs + 9"×50lbs = 5650 in-lbs (638 Nt-m). The maximum roll moment is on the order of 16"×200 lbs = 3200 in-lbs (362 Nt-m). A Kaydon four point contact bearing with a 5" (127 mm) pitch diameter internal gear is used for this joint. Bearing KD065XPO has the following properties: 7.500" (190 mm) outside diameter, $^{1}/_{4}$" (6.35 mm) balls, $^{1}/_{2}$" (12.7 mm) cross section, static loads: 3640 lbs (1651 kg) radial, 9090 lbs (4123 kg) thrust, and 12,760 in-lbs (1442 Nt-m) moment. The outside diameter of the wrist will be on the order of 8.5" (216 mm), which allows plenty of room for accommodation of the 5" (127 mm) diameter POSOR. A 1" (12.7 mm) diameter drive shaft will supply 640 in-lbs of torque (stress in shaft ≈ 20 ksi [140 Mpa]) from a Char Lynn 4000 series 6.6 in^3/rev geroler motor located at the elbow. The motor weighs 40 lbs (18 kg) and delivers 1290 in-lbs (146 Nt-m) of torque at 1500 psi (10.5 Mpa) supply pressure, and turns at 110 RPM @ 4 gpm (15 ℓpm) flow. The weight of the wrist roll joint is on the order of 30 lbs (13.6 kg).

9.4.3 Elbow Joint

The elbow joint is shown in Figure 9.13. The major moment at this joint is 39"×50 lbs + 30"×30 lbs + 46"×200 lbs + 15"×10 lbs = 12,200 in-lbs (1379 Nt-m). A 4"×4"×$^{1}/_{8}$" (102×102×3.18 mm) aluminum box beam connects the wrist assembly to the elbow, and has a design stress of 5000 psi (35 Mpa). The minor moment at this joint is due to the structural beam offset which allows the structure to be double jointed, and

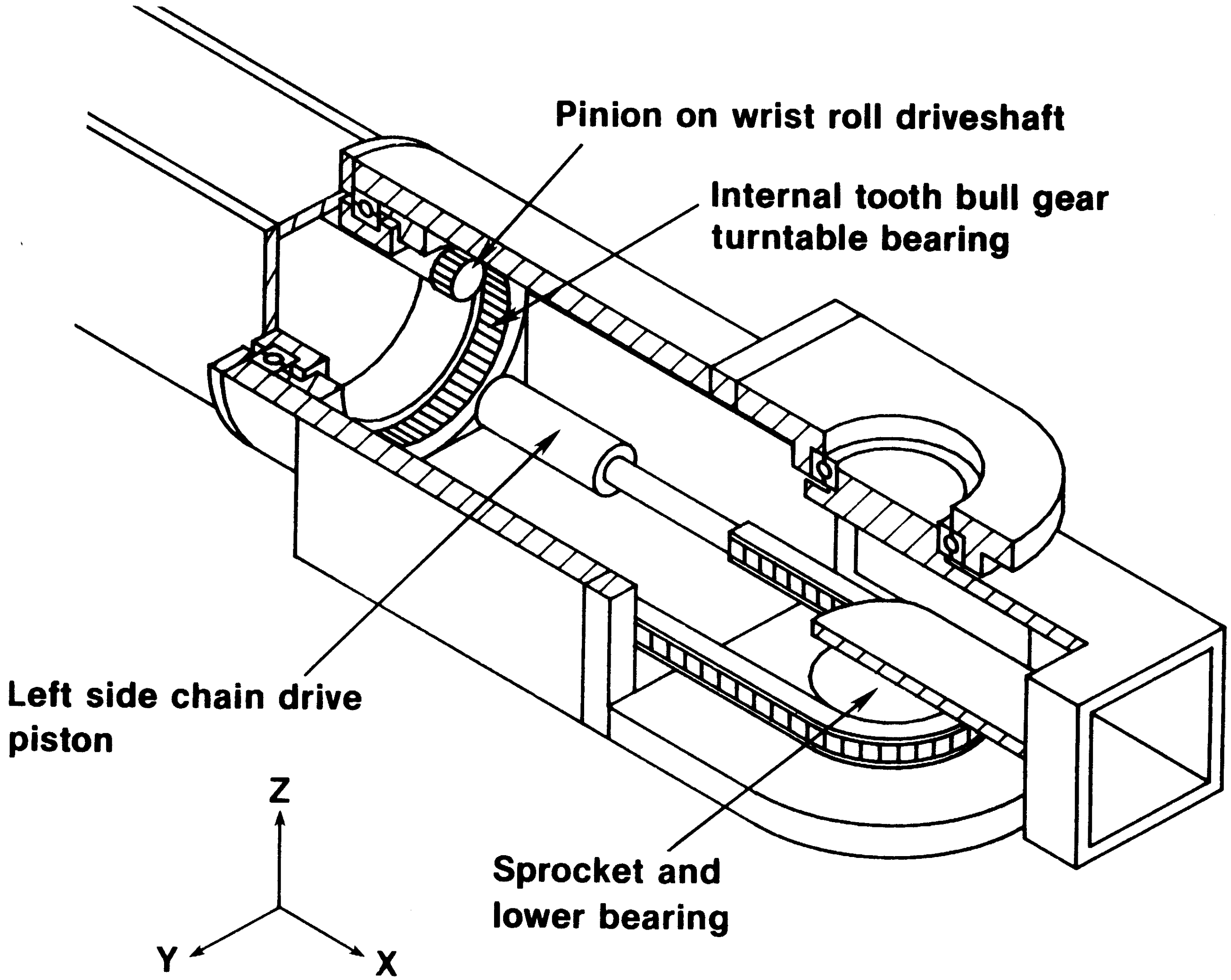

Figure 9.12 Detail of robot's wrist structural assembly

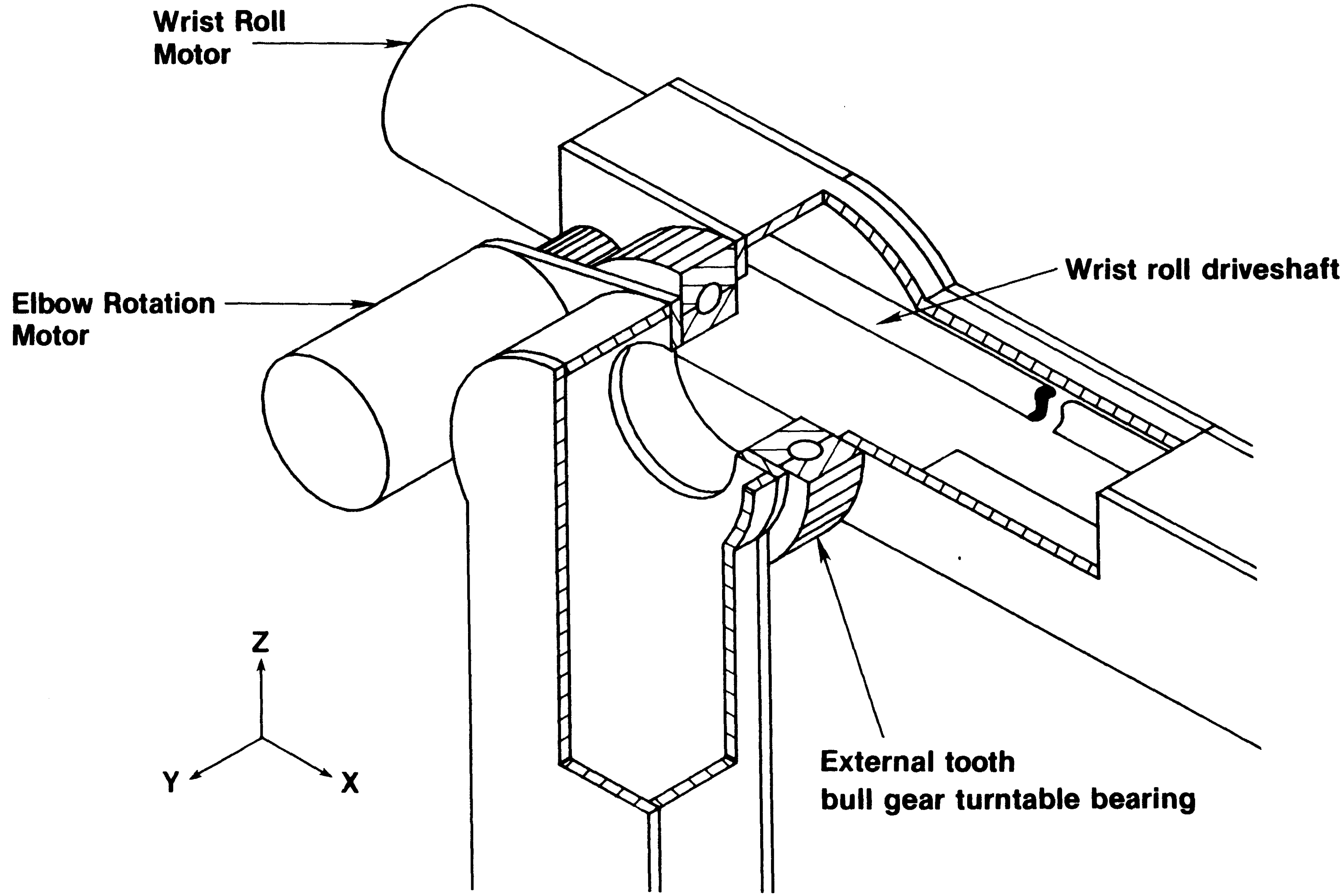

Figure 9.13 Detail of robot's elbow structural assembly

the bent wrist position. This minor moment is on the order of 21"×300 lbs = 6300 in-lbs (712 Nt-m). The geroler motors have a 4000 lb (1814 kg) maximum radial load, so a 3:1 gear ratio is required at this joint. If a 3.5" (89 mm) pitch diameter pinion is used, a 10.5" (267 mm) pitch diameter external tooth bearing/gear assembly will be required at the elbow joint. A Kaydon KD065XPO bearing is chosen, it has the following properties: 6.500" (165 mm) inside diameter, $^{1}/_{4}$" (6.35 mm) balls, $^{1}/_{2}$" (12.7 mm) cross section, static loads: 3640 lbs (1651 kg) radial, 9080 lbs (4082 kg) thrust, and 12,720 in-lbs (1438 Nt-m) moment. A Char Lynn 6000 series 19 in^3/rev motor with 4800 in-lbs (542 Nt-m) torque at 2000 (13.7 MPa) psi supply pressure is used. The motor weighs 57 lbs (25.9 Kg) and turns at 38 RPM @ 4 gpm (15 ℓpm). The weight of the elbow joint (including the motors) is on the order of 150 lbs (68 kg).

9.4.4 Shoulder and Base Swivel Joints

The shoulder joint is shown in Figure 9.14. The major moment at this joint is 68"×50 lbs + 60"×30 lbs + 76"×200 lbs + 45"×10 lbs + 30"×150 lbs + 15"×15 lbs = 25,575 in-lbs (2890 Nt-m). The minor moment is on the order of 25"×400 lbs = 10,000 in-lbs (1130 Nt-m). A 5"×5"×$^{1}/_{8}$" (127×127×3.2 mm) aluminum box beam connects the shoulder and the elbow joints, it has a design stress of 5000 psi (35 MPa). A 6.4:1 gear ratio is required at this joint, which is obtained by using a 3.5" (89 mm) diameter pinion and a 22.4" (569 mm) pitch diameter gear. The gear is integral with the bearing at this joint which is a Keene T8-18E1. This bearing weighs 110 lbs, and has a moment capability of 113,000 ft-lbs (153,000 Nt-m). This is a large over-kill, but it is the

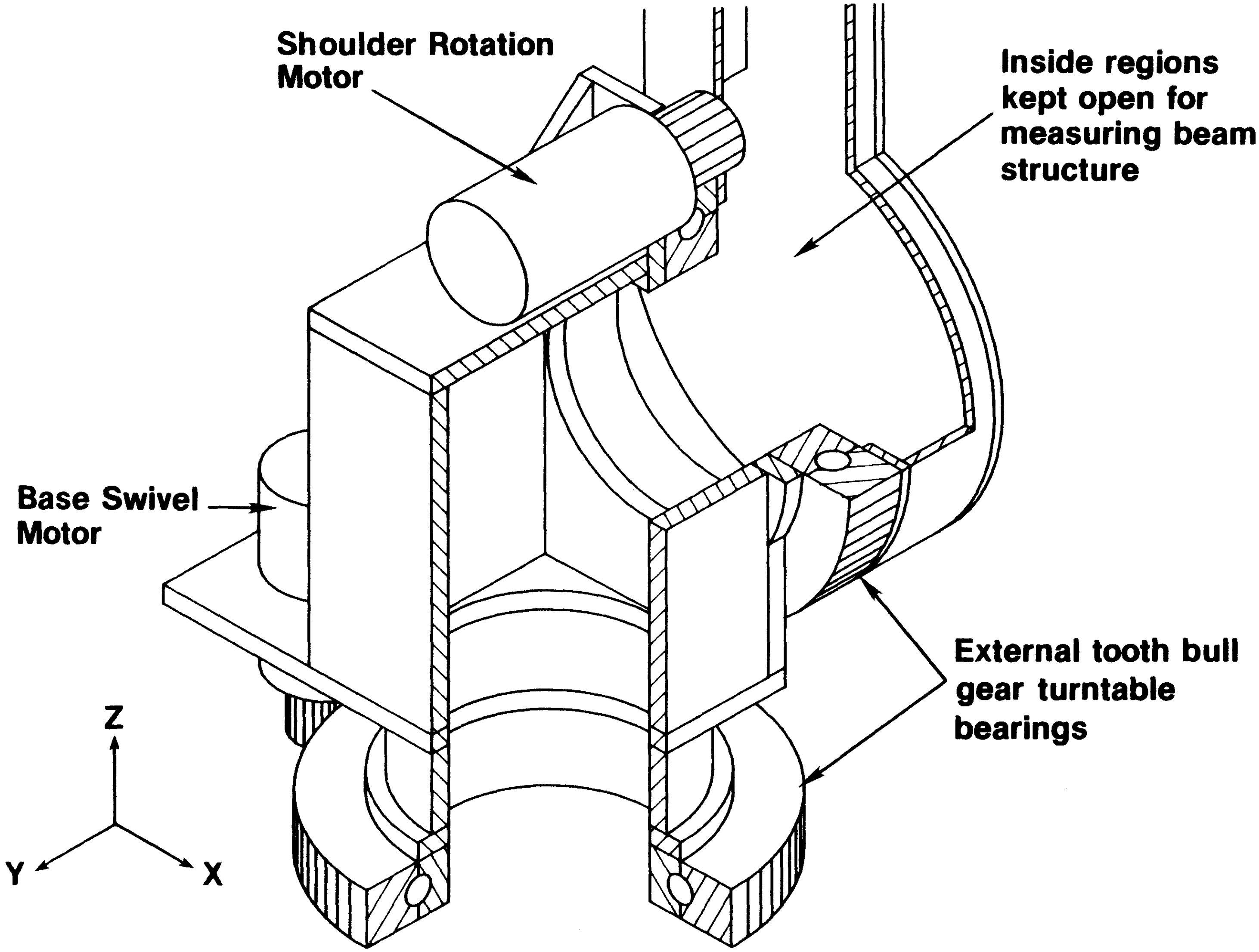

Figure 9.14 Detail of robot's base structural assembly

smallest "large" diameter integral gear bearing available. A Char Lynn 600 series 60 in^3/rev geroler motor with 9550 in-lbs (1079 Nt-m) of torque at 1250 psi (8.6 MPa) is used. The motor weighs 68 lbs (31 kg) and turns at 14 RPM at 4 gpm (15 ℓpm).

The base swivel joint uses the same bearing and motor as the shoulder joint. The housing can be constructed of $^1/_4$" (6 mm) aluminum plate with stiffeners.

9.4.5 Summary of Structural System Design

The conceptual design of a robot with 76" (1.93 m) reach (base to center of end effector) was presented. The robot has a end-force capability of 200 lbs (90.7 kg). The approximate weight consists of: 325 lbs (147 kg) of bearings and gears, 175 pounds (79 kg) of motors, and 300 pounds (136 kg) of structure and miscellaneous items. Thus the payload to weight ratio of this 800 pound (363 kg) robot is 4:1 (static).

The design is double jointed, and its success depends on the ability to control a geroler motor with a hydraulic servoloop. In the event that the latter is not possible, hydraulic cylinders can be used with no loss in payload to weight values, but it will no longer be double jointed (it will become like any other robot).

9.5 Remarks

The accuracy of the endpoint feedback signal was predicted to be .000284" (7.1 μm). The structure, which has a 200 pound (91 kg), weighs 800 pounds (364 kg). Thus an order of magnitude increase in structural performance and a two to three order of magnitude increase in accuracy over existing robots was predicted. This will allow a robot to be built that will be lightweight and fast, with the ability to perform most machining operations (that have low reaction force) with tolerances on the order of .001" (.0254 mm).

(this page left blank)

Chapter 10

Thesis Summary and Conclusions

10.1 Summary of Experiments to Determine POSOR Performance

The results of the experiments to determine POSOR performance are best summarized by Table 8.2. The POSOR measured the angles α and β quite well (within the predicted limits of accuracy of the test setup) except for the β motion during the TWIS test. These good results, however, depended on the determination (digitally) of the small (a few tenths of a volt) voltage shifts in the probes' zeroes.

The Θ measurements, which were measured by the lateral effect diode system, were poor (but predictable) and the cause was traceable to the calibration stage. Thus all the tests produced errors that were within a few standard deviations of those predicted. Based on these results, the methodology of the error analysis of Chapter 5 appears correct, and the POSOR's performance for the multi degree-of-freedom tests was similar to that of the single degree-of-freedom tests. This indicates that there is little coupling between the measured degrees of freedom.

From the error analysis presented in Chapter 5, the dominant errors were shown to be due to sensor inaccuracies. With regard to the impedance probes, it was the zero drift problem which caused 90% of the system error. This error, however, was compensated for in the analysis programs. With regard to the lateral effect diode system, the error introduced by the calibration stage accounted for 95% of the system error that was predicted. It is also believed that foreign matter on the diodes (which can cause reflections and shift the center of intensity of the light source) accounted for a significant part of the error in the experiments.

Finally, note that the average endpoint error measured by the impedance system was .000625" (16 μm), and that of the lateral effect diode system was .008929" (.226 mm). If one still ponders how the measuring beam system would work in a real live robot, consider that the measuring beam was 30" (.762 m) long and the POSOR was only 3" (.0762 m) in diameter. Thus even if scaled up to a robot with a 90" reach, the system in question would be one to two orders of magnitude more accurate than any existing robot.

10.2 Summary of Conceptual Robot Design Parameters

The conceptual design of a robot with 76" (1.93 m) reach (base to center of end effector) was presented. The robot has an end-force capability of 200 lbs (91 kg). The approximate weight consists of: 325 lbs (147 kg) of bearings and gears, 175 lbs (79 kg) of motors, and 300 lbs (136 kg) of structure and miscellaneous items. Thus the payload to weight ratio of this 800 pound (363 kg) robot is 4:1 (static).

The design is double jointed, and its success depends on the ability to control a geroler motor with a hydraulic servoloop. In the event that the latter is not possible, hydraulic cylinders and/or vane actuators can be used with no loss in payload to weight values, but the robot will no longer be double jointed (it will become like any other robot).

The accuracy of the endpoint feedback signal was predicted to be .000284" (7.1 μm). Thus an order of magnitude increase in structural performance and a two to three order of magnitude increase in accuracy over existing robots was predicted

10.3 Thesis Summary

This thesis focused on methods of increasing the accuracy of articulated structures. Sources of measurement error in articulated structures were first identified. Various state of the art motion measuring methods were reviewed and none were found to be entirely suitable for use with articulated structures. Accordingly, a six degree of freedom motion measuring system was developed that relied directly (only) on the stability and accuracy of non-contact displacement measuring sensors. The design is also flexible enough to allow for the introduction of new types of sensors as they become available. A model was tested on a simulated one degree of freedom robot and the measured errors were predicted by the error analysis. On the model tested, which had the same error amplification factor as a robot with a 90" (2.2 m) reach, endpoint error was on the order of .000625" (15.5 μm). Subsequently, the errors present in the test system were identified, and recommendations made to correct them. A conceptual robot design was then presented which showed that a five axis robot with a 76" (1.9 m) reach and 200 pound (91 kg) payload could be designed to have a payload to weight ratio of 4:1 and an endpoint feedback accuracy of .000284" (7.1 μm), which is sufficient for most manufacturing processes the robot may be required to perform. Thus by using the concepts developed, an order of magnitude increase in structural performance and a two to three order of magnitude increase in accuracy over existing robots was attained.

10.4 Thesis Conclusions

Based on the work performed, the following conclusions are made:

1) The POSOR can measure five small and one large degree-of-freedom simultaneously.

2) The POSOR's accuracy can be predicted using equations formulated and data on individual sensor performance.

3) The measuring beam system used to support the POSOR can be designed to support POSORs without deforming beyond a design threshold.

4) The measuring beam and POSOR combination can be used to accurately determine an articulated structure's joint and endpoint orientation and position in real time.

5) A robot that incorporates a measuring beam system can achieve accuracies of .001" (.0254 mm) over a reach of 76" (1.9 m).

6) The fundamental accuracy of the measuring beam system is limited only by the electronics of the system

10.5 Recommendations

In view of the above, the following recommendations are made concerning the future development of POSOR devices:

For the impedance probe system:

1) The oscillator demodulator unit must be replaced with a unit that has no adjustable pots, and does not drift if bumped. More stable electrical components should also be chosen.

2) The relative probe positions must be found while the angles α and β are simultaneously measured with angular interferometers.

3) The probes must be secured in a stress free way (epoxied, instead of held with nuts)

For the lateral effect diode system:

1) This type of system is suitable for use only in laboratory environments (the diodes are very susceptible to contamination).

2) Stick mirror interferometers (allow direct measurement of simultaneous X and Y stage motion) should be used to measure the stage motion directly when mapping the diodes, so Abbe's offset error can be reduced to microinches.

3) Stable laser light must be used as opposed to laser diodes; however, it can be delivered to the required region by fiber optic cables.

In general, the light source-lateral effect diode system is a poor choice. The bumpy ring sensor should be developed.

Finally, it is recommended that controls researchers begin to study how to use the feedback data from the measuring beam system. It is also recommended that a full scale robot be built that uses a measuring beam system for joint and endpoint feedback.